



**SHIBAURA INSTITUTE OF TECHNOLOGY**

Graduate School of Engineering and Science

**AGH UNIVERSITY OF SCIENCE AND TECHNOLOGY**

Faculty of Physics and Applied Computer Science

**DOCTORAL DISSERTATION**

*Properties of Fe-Mn-Si and Ni-Ti shape memory  
alloys prepared by pulsed-current sintering*

**Witold Prendota**

**Supervisor: Prof. Akito Takasaki**

**Supervisor: Prof. Czesław Kapusta**

TOKYO, KRAKOW 2019



*A heartfelt thanks to Prof. Akito Takasaki and Prof. Czesław Kapusta for comprehensive support and assistance during my scientific work.*

*In addition special thanks to:*

- *Family, friends, coworkers, lab members both in Poland and in Japan,*
- *Dr. hab. Janusz Przewoźnik (Faculty of Physics and Applied Computer Science, AGH University of Science and Technology),*
- *Dr. hab. inż. Agnieszka Radziszewska (Faculty of Metals Engineering and Industrial Computer Science, AGH University of Science and Technology),*
- *Prof. Dr. hab. inż. Tadeusz Knych (Faculty of Non-Ferrous Metals, AGH University of Science and Technology),*
- *Dr. hab. inż. Andrzej Mamala, prof. AGH (Faculty of Non-Ferrous Metals, AGH University of Science and Technology),*
- *Prof. Dr. hab. inż. Adam Piestrzyński (Faculty of Geology, Geophysics and Environmental Protection, AGH University of Science and Technology),*
- *Dr. Jan Żukrowski (Faculty of Physics and Applied Computer Science, AGH University of Science and Technology),*
- *Dr. Damian Rybicki (Faculty of Physics and Applied Computer Science, AGH University of Science and Technology),*
- *Prof. Susumu Uematsu (Shibaura Institute of Technology) for support and help in the research work.*
- *Shunsuke Miyazawa, Goto Koki, Yamada Eisuke and Kamil Goc for cooperation in this study.*

*I dedicate this work to my fiancée Justyna Szydło for her faith, patience and support. I love you.*

*The author acknowledges the Swiss Light Source (SLS) in Paul Scherrer Institut (PSI) in Switzerland for provision of beamtime.*



## Abstract

This Thesis presents results of a study of Fe-Mn-Si alloys and Ni-Ti intermetallics which exhibit shape memory effect. Such materials are commonly used in a broad area of applications, such as: engineering or medicine. In particular, Fe-Mn-Si can be used e.g. for constructions, and Ni-Ti - in medicine or micro-electro mechanical devices (MEMS). Within this work, materials prepared with pulsed-current sintering method were studied. Main focus was put on the thorough characterization and description of physical properties of the materials and phases involved as well as on the interplay between them and dependence on the composition and preparation conditions.

As the technological novelty a single-step route for preparation of Ni-Ti shape memory micro foil alloys from pure element foils has been designed. Three starting configurations of elemental foils of properly adjusted thicknesses were used: a simple Ni/Ti as well as sandwich-like Ni/Ti/Ni and Ti/Ni/Ti. A good shape memory recovery effect, reaching 100 %, was obtained for Ni/Ti/Ni configuration derived alloy. A complex characterization of the materials obtained included X-Ray Diffraction, Scanning Electron Microscope with EDS elemental mapping, Differential Scanning Calorimetry, magnetometry, electrical resistivity and magnetoresistance. The results revealed the phases occurring in the material at different preparation conditions with respect to the completeness of the diffusion process leading to the formation of the Ni-Ti shape memory alloy. A comparison was made to the materials prepared from the cold-rolled foils, subsequently annealed which shows a much higher effectiveness of the pulsed-sintering method.

For the Fe-Mn-Si system the materials obtained with mechanical alloying of elemental powders and subsequent pulsed-current sintering process were studied. The same characterization methods as for Ni-Ti system were also used here. Except for them, Mössbauer spectroscopy and the specific heat measurements were carried out. The as annealed and thermally processed samples were studied and the properties of the phases involved were characterized. The study showed that the austenitic fcc phase is ferro or ferri magnetic and exhibits exchange bias behavior, depending on the heating temperature. A linear-like temperature dependencies of the inversed magnetic susceptibility reveal a Curie-Weiss character corresponding to localized moments. A very small magnetic splitting derived from iron Mössbauer spectra indicates that the magnetism is governed by manganese. For the material with 0.1 wt.% carbon added for improvement of shape memory effect a peak at 250 K in the specific heat is observed. It is almost insensitive to the applied magnetic field up to 9 T was observed, indicating transition to antiferromagnetic-like state of the martensite hcp phase. The exchanged bias effect observed for the fcc phase at some thermal treatment conditions samples and a nucleation of reversed domain character of their virgin magnetization curves reveals a nanometric size of the austenitic fcc phase precipitation, not detectable with XRD, in the martensite matrix.



## List of content

Chapter 1. Introduction .....	1
1.1 Shape memory effect .....	4
1.2 Preparation of shape memory alloys.....	11
1.3 Diffusion process .....	12
Chapter 2. Characterization techniques .....	18
2.1 Crystal structure and phase content .....	18
2.2 Microstructure and elemental composition.....	19
2.3 Magnetic properties .....	22
2.4 Heat capacity, electrical and thermal properties.....	25
2.5 Shape Recovery Rate .....	29
Chapter 3. Fe-Mn-Si alloys – results and discussion.....	30
3.1 Preparation of the samples .....	30
3.2 Structural and magnetic properties .....	32
3.3 Summary of results for Fe-Mn-Si alloys .....	61
Chapter 4. Cold rolled and annealed NiTi micro-foils – results and discussion. ....	63
4.1 Annealing process.....	63
4.2 Characterization of materials obtained .....	66
4.3 Summary of results for rolled and annealed NiTi micro-foils.....	80
Chapter 5. Sintering of NiTi micro-foils – results and discussion.....	82
5.1 Annealing process.....	82
5.2 Characterization of micro-foils .....	88
5.2.1 Comparison for different samples types .....	89
5.2.2 Compositional dependence .....	95
5.2.3 Dependence on sintering time.....	101
5.2.4 Dependence on the thickness .....	105
5.2.4 Dependence on the time profile of sintering current .....	109

5.2.5 Magnetic, electrical and thermal properties.....	111
5.3 Summary of results for sintered NiTi micro-foils .....	121
Chapter 6. Conclusions .....	123
References.....	125
List of tables.....	140
List of figures.....	141

## Chapter 1. Introduction

Shape memory alloys are special materials which exhibit shape memory effect. This is a big family of materials, commonly used in broad area of applications, such as: medicine and engineering. Due to differences in their specific properties their applications are different. For example: Fe-Mn-Si can be used e.g. in constructions, and NiTi e.g. in medicine or micro-electro mechanical devices (MEMS).

In 1982 A. Sato discovered SME in Fe-Mn-Si alloy with stress induced martensitic transformation between  $\gamma$  (fcc; austenite;  $Fm\bar{3}m$ ; ) phase and  $\epsilon$  (hcp; martensitic;  $P6_3/mmc$  (N° 194)) [1]. It occurs due to the motion of Shockley partial dislocations in the fcc structure (the Burgers vector  $a/6[11\bar{2}]_{FCC}$  glides between two (111) layers of the fcc lattice). Silicon and manganese atoms randomly interchange iron atoms, which stabilizes the  $\gamma$  phase at high temperatures [2]–[5]. Reverse transformation occurs during heating: from  $\epsilon$  to  $\gamma$  phase [4], [5]. Other alloying elements can be used for the improvement of properties. Some studies showed improvement of properties upon doping carbon, but it is still a controversial subject. Reasons for improvement are that it can stabilize and strengthen the austenite [6][7]. As the phase diagrams suggest, it can produce unwanted particles or support creation  $\alpha'$ -phase which can degrade properties of the alloy [6], [8]–[12]. Magnetic properties of Fe-Mn-Si alloys are reported as mainly antiferromagnetic [13] [14]. In Fe-Mn alloys,  $\epsilon$ -hcp exhibit itinerant electron antiferromagnetism (with increased electrical resistivity),  $\gamma$ -fcc is reported also as antiferromagnetic, with higher magnetic moment, and  $\alpha$ -bcc phase is ferromagnetic [15]. Addition of silicon into Fe-Mn system decreases Néel temperature of austenite, enhances the strength of matrix, reduces the stacking fault energy of austenite [16], increases electrical resistivity, decreases volume per atom of fcc phase [17], increases volume per atom of hcp phase, reduces stabilization of austenite and causes appearance of Kondo-like effect [18]. In contrast to that, increase of Mn content rises the Néel temperature, decreases the driving force of martensitic transformation, increases volume per atom of fcc/hcp phase [17] and has significant impact on the shape memory effect [19][20]. The thermo-induced martensitic transformation from paramagnetic to antiferromagnetic state is reported in [2][12][21]. A complex study of Fe-Mn-Si system with electron spin resonance (ESR) and transmission electron microscopy measurements is reported in [22]. A preference of silicon location in the nearest neighbor shell to iron was postulated. The presence of paramagnetic Curie-Weiss and Pauli-like susceptibility was found and attributed to Mn localized moments and conduction electrons, respectively. These alloys were also studied with neutron diffraction and

magnetometry [23]. Dominant antiferromagnetic structure was found with a possibility for some ferromagnetic component of  $0.6 \mu_B$ . However, magnetic measurements revealed a ferromagnetic moment of  $0.05 \mu_B$  only.

As one can see, the knowledge about the properties of the phases occurring in the Fe-Mn-Si shape memory alloys and the interplay between them is neither unambiguous nor complete. Thus, a thorough study of their structure, magnetism, heat capacity, electrical conductivity and magneto-resistance as well as the influence of carbon doping on them has been undertaken within this Thesis. The materials obtained with mechanical alloying of elemental powders and subsequent pulsed-current sintering process were used.

In order to compare the alloy-like shape memory materials represented by Fe-Mn-Si with a compound-like one, the study was complemented with the investigation of the Ni-Ti system in application to micro-foils also produced by current sintering method. In addition to the study of the properties of the phases and the interplay between them, the technological procedure of a single step production of the NiTi shape memory micro-foils has been designed and tested.

In 1959 William J. Buehler discovered shape memory effect in Ni-Ti compounds, and dr. Frederick E. Wang in 1962 discover theoretical description of the mechanism [24]. Taking into account group of the materials which exhibit shape memory effect, Ni-Ti system is named as an alloy, but it is a compound by crystallographic standards. Transition occurs due to a thermal treatment, which induced crystal structure change: between B19' martensite (monoclinic) and B2 austenite (cubic). Generally their properties depends on the composition and thermo-mechanical treatment. They exhibit biocompatibility properties [25].

Over the years, many publications have been reporting different synthesis approaches for shape memory materials. Synthesis methods depend in a natural way on the size/shape of the desired output material and on the production scale. Thin films can be obtained e.g. by deposition methods [26], [27], [36], [28]–[35]. Another approach includes multilayer deposition of different elements with similar thermal post processing [27], [31]. The most common and simple method in bulk alloy production is induction/arc vacuum furnace. This process involves heating of pure input elements above melting points with simultaneous mixing in the crucible, which can be easily contaminated by spurious elements (e.g. carbon) [37]–[41]. Also simple and less energy consuming methods include pure element powders milling and further sintering [42]–[46]. Hot/cold rolling is excellent way for the mass production of sheets and foils [47], [48], [57]–[59], [49]–[56]. This concerns e.g. nickel and

titanium foils multilayer hot rolling and folding with a composition adjusted by different foil thicknesses [60], [61]. Production of wires can be realized by hot and cold working [62]–[66]. Till now there is a little reports on the current sintering approach regarding NiTi production from pure nickel and titanium foils, in particular to micrometric thickness.

Concerning the Ni-Ti system, in the paper [67] the authors shown that Ni-Ti thin foil can be produced by diffusion bonding of relatively thick nickel and titanium foils. Further processing required etching it from the foils residue. The [68] study also used diffusion bonding method to obtain  $Ti_2Ni/NiTi$  micro-laminated composites, which exhibit shape memory effect, and tensile test show cracks propagation along  $Ti_2Ni$  compound layers. Interesting results were reported by Garay in [69] and further in [70], [71]. In the studies direct current synthesis was used for intermetallic phases creation and to study the current parameters influence on it.

Chapter 1. of this Thesis presents the overview of the data on the shape memory materials studied, including their properties, applications, preparation methods, etc. It also includes literature review of recent trends in their studies. Further, a description of pressure assisted pulsed-current sintering method used for materials preparation is presented. Chapter 2. describes briefly all of the experimental methods and apparata used for materials characterization, i.e.: X-Ray Diffraction (XRD), X-Ray Absorption Near Edge Structure (XANES), Extended X-Ray Absorption Fine Structure (EXAFS), Scanning Electron Microscopy (SEM) with Energy Dispersive Spectroscopy (EDS), Mössbauer Spectroscopy (MS), Differential Scanning Calorimetry (DSC), bending test (for Shape Recovery Rate (SRR) measurement and Physical Properties Measurement System (PPMS). In the last subsections the Heat Capacity, Vibrating Sample Magnetometry (VSM) and resistivity measurement method are described.

Chapter 3. focuses on Fe-Mn-Si type shape memory alloys properties prepared by pulsed-current sintering method. Properties of the Fe-30Mn-6Si (wt.%) after heating up to different temperatures during reverse martensitic transformation and the alloy with small carbon addition (0.1 wt.%) at the cost of the silicon content reduction are studied. The XRD structural characterization at room temperature and at elevated temperatures has been carried out. As the magnetic characterization reported in the literature is rather poor, a detailed magnetic study of the materials has been carried out. It included full susceptibility and magnetization dependences on temperature and the applied field. Also, the specific heat measurements have been carried out for the carbon containing alloy. They were carried out

also at the applied magnetic field up to 90 kOe, in order to determine the character of the observed transition.

Further parts of the Thesis shows a study of the Ni-Ti shape memory compound. In recent years big development in Ni-Ti production has been made, however, there is a little reports on the possibility of pulsed current application in microfoils production, shape memory properties of the materials prepared, possible advantage of this method and its impact on boundary conditions during synthesis. In Chapter 4. a comparison of preparation process of diffusion couples prepared by cold rolling and post thermal treatment with the pulsed current sintering method is presented and compared to other studies. Chapter 5. focuses on the process of optimization with application of novel (as for this purpose) technique – pulse current sintering and its advantages to cold rolling combined with thermal treatment with respect to micro-foil intermetallic production in one-step process. Differences between results obtained with application of pulse and direct current are discussed.

Conclusions are drawn in Chapter 6. to all the results obtained and presented in this Thesis.

This Chapter focuses on literature overview regarding shape memory effect and alloys – especially Fe-Mn-Si and Ni-Ti alloy. Their description involves: shape memory effect mechanism, types of alloys, other properties, preparation methods and applications.

## 1.1 Shape memory effect

Shape Memory Effect (SME) was discovered in 1932 by Olander in Gold-Cadmium alloy [72]. It was firstly known as “rubber like effect”. In 1959 William J. Buehler discovered this effect in Ni-Ti alloys, also known as NITINOL (from Nickel Titanium Naval Ordnance Laboratory). Materials which exhibit such an effect are known as Shape Memory Alloys (SMA) or intelligent materials.

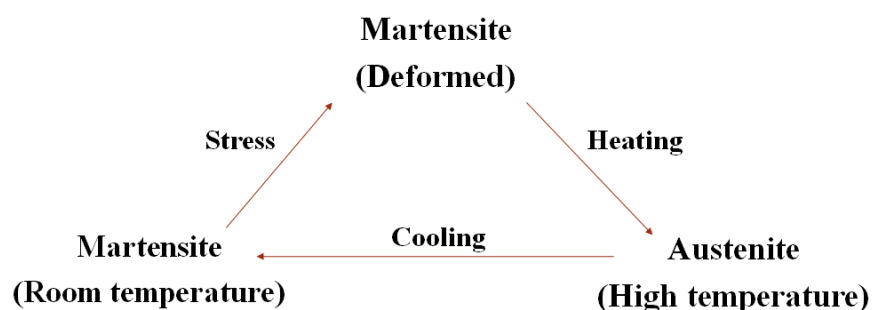


Figure 1. 1: Illustrative representation of the thermally induced shape memory effect in Ni-Ti alloys.

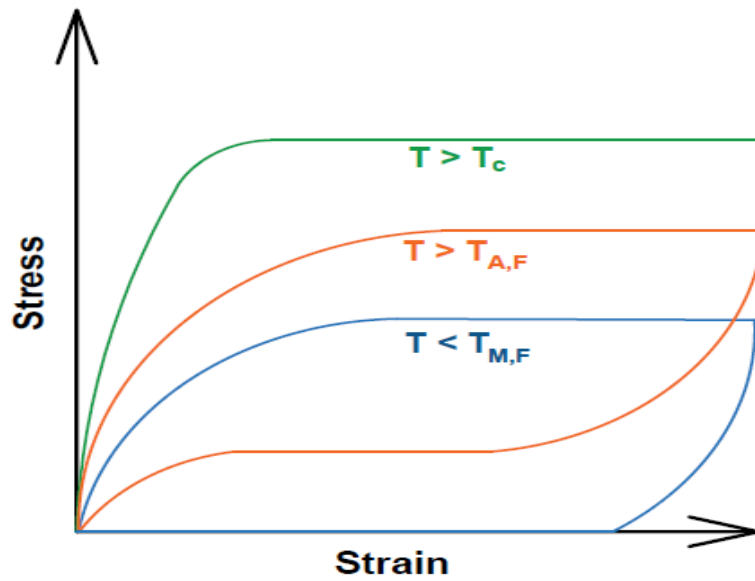


Figure 1. 2: SMA stress-strain curves: green – austenite, blue - martensite and orange - superelastic behavior.

Dr. Frederick E. Wang in 1962 discover theoretical description mechanism of this effect [24]. The effect is based on temperature thermoelastic transformation between martensite (low temperature phase) and austenite (high temperature phase) – see Figure 1. 1. This phenomenon is strictly based on composition. Any deviations from it can drastically change transformation temperature. During heating crystal structure is changing, based on twinning effect between B19' (monoclinic structure) and B2 (cubic) for NiTi compound [73]–[76].

Table 1. 1: Selected Shape Memory Alloys and their important characteristics. Taken from: [77].

<b>Alloy:</b>	<b>Composition range:</b>	<b>Transformation temperature range [°C]:</b>	<b>Transformation hysteresis [°C]:</b>
Ag-Cd	44/49 at.% Cd	-190 to - 5 0	≈ 15
Au-Cd	46.5/50 at.% Cd	30 to 100	≈ 15
Cu-Al-Ni	14/14.5 wt% Al 3/4.5 wt% Ni	-140 to 100	≈ 35
Cu-Sn	≈ 15 at.% Sn	-120 to 30	-
Cu-Zn	38.5/41.5 wt% Zn	-180 to - 1 0	≈ 10
Cu-Zn-X (X = Si, Sn, Al)	a few wt% of X	-180 to 200	≈ 10
In-Ti	18/23 at.% Ti	60 to 100	≈ 4
Ni-Al	36/38 at.% Al	-180 to 100	≈ 10
Ni-Ti	49/51 at.% Ni	- 5 0 to 110	≈ 30
Fe-Pt	≈ 25 at.% Pt	≈ - 130	≈ 4
Mn-Cu	5/35 at.% Cu	-250 to 180	≈ 25
Fe-Mn-Si	32 wt% Mn, 6 wt% Si	-200 to 150	≈ 100

They also exhibit superelastic behavior, which occurs in austenite phase – see Figure 1. 2 (orange curve). After application of external stress the alloy deforms (austenite stress transformation into martensitic phase), but with removal of the force it goes back instantly to the original shape (martensitic phase reverse to austenite phase). Due to small inhomogeneity in the material (presence of  $Ni_4Ti_3$  or  $Ti_2Ni$  particles) additional phase can appear: R-phase (trigonal or rhombohedral distorted austenite phase).  $Ti_2Ni$  particles appear in titanium rich NiTi, and  $Ni_4Ti_3$  in nickel rich alloys [[78], [79], [80], [81]]. It appears during temperature transformations between martensite and austenite ( $M \rightarrow R \rightarrow A$  and  $A \rightarrow R \rightarrow M$ ) [26], [81]–[84].

Table 1. 1 shows examples of alloys in which SME was discovered and their properties. Each alloy possess different properties and they can be used for different applications.

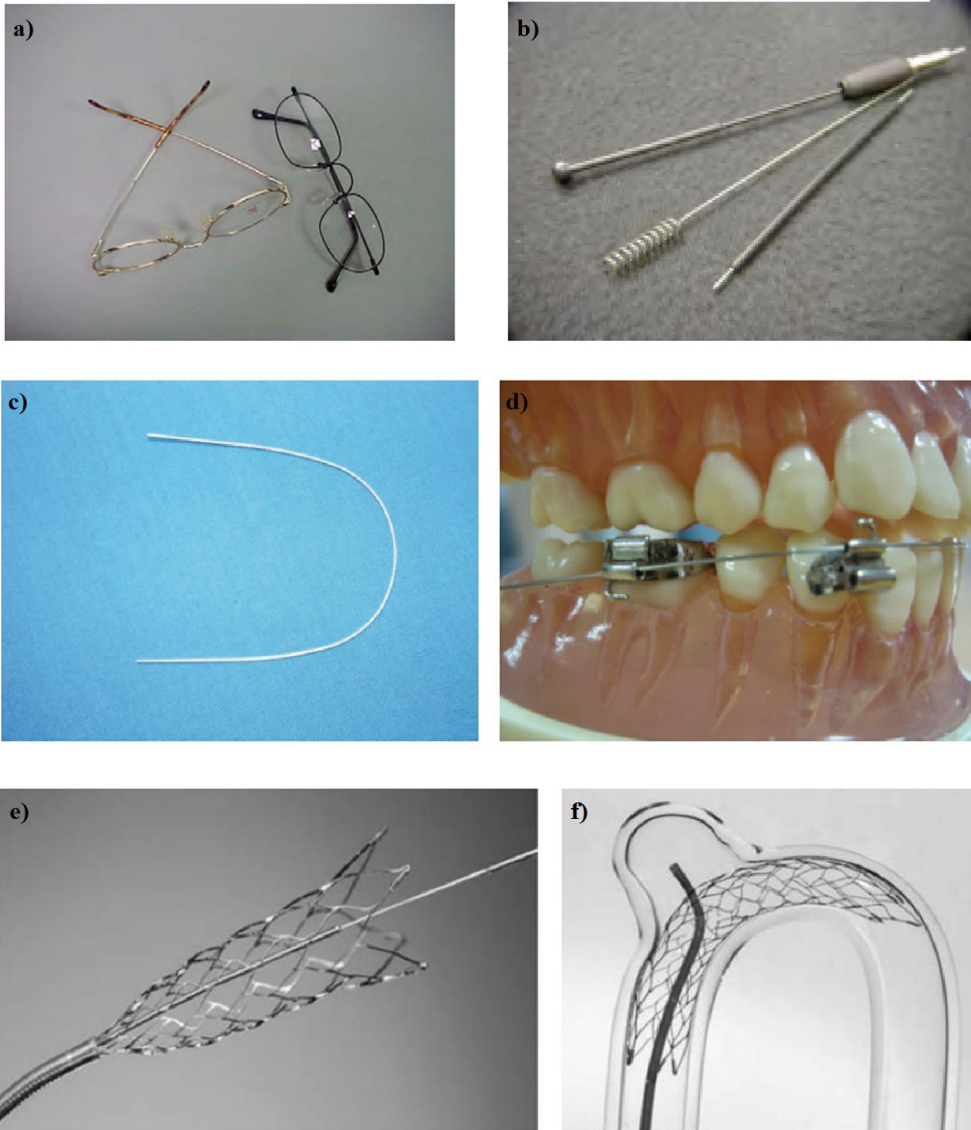


Figure 1. 3: General examples of Ni-Ti applications: a) eyeglass frame, b) cellular phone antenna [85], c), d) orthodontic wires and e), f) neurosurgical stent. Taken from: [86].

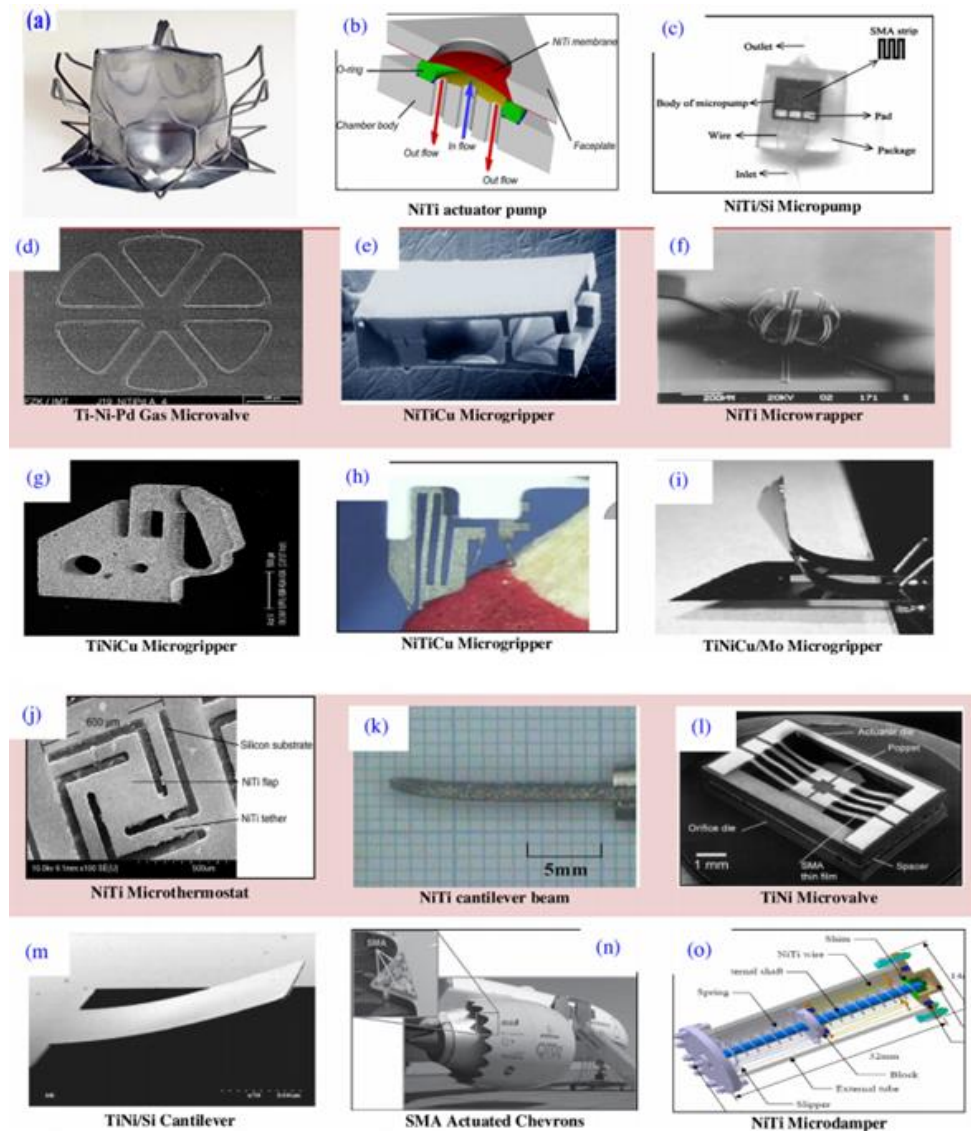


Figure 1. 4: Ni-Ti applications as (micro) devices. Taken from: [87].

Most commonly used alloy exhibiting SME is Ni-Ti. It shows good corrosion resistance (like stainless steel or titanium alloys) [77], [88], [89], super-elasticity and other superior mechanical features [77]. For improvement of this properties thermomechanical treatments procedures are used [90], [91]. Preparation process, on the other hand, is very difficult and costly uses expensive elements and the material is hard-workable, hard-welding (laser welding is effective) [92]–[95]. It is believed that materials based on nickel can be dangerous. Moreover, there are also some concerns regarding elemental release due to critical deformations/destruction. [25], [96]–[98]. There are studies showing NiTi alloys excellent biocompatibility [25], [98], [99]. This is owing to titanium presence on its surface where there is instantaneously created thin titanium oxide ( $\text{TiO}_2$ ) layer, which protects from nickel diffusion into the human body [100]. On the other hand, easy titanium oxidation also makes difficulties during alloys synthesis. Presence of oxygen or other extra element (like carbon)

can influence alloys properties. It changes nickel to titanium ratio due to of oxides/carbides creation, such as:  $\text{Ni}_2\text{Ti}_4\text{O}$ ,  $\text{TiO}$ ,  $\text{TiO}_2$  and  $\text{TiC}$ . This influences e.g. transformation temperatures – higher nickel content decreases transformation temperature. It is believed that 0.1 at% nickel content increases/lowers it by 10K [101]–[104]. There is also a bright side of additives – they can modify or even improve some properties. For example, iron addition into NiTi alloy results in a decrease of phase transformation temperatures. Similar effect can be observed in TiNiCu alloys with zirconium substitution. Chromium and nickel substitutions in Fe-Mn-Si alloy improves corrosion resistance and shape memory effect [105], [106], [115], [107]–[114]. Popularity of the Ni-Ti alloy is also based on many other applications in different industries, such as: biomedicine (e.g. Simon vena cava filter, atrial septal occlusion, surgical endoscopic instruments, orthodontic wires, hingless grasper, drills and paragon stent) [86], [116]–[118], engineering (structural vibration control, seismic isolation, morphing aircraft, robotics, biomimetic, parts of engine, parts of fuselage, etc.) [85], [119]–[121], [121]–[123] and, especially, for this study purpose - in microelectromechanical systems (MEMS; thin film stents, micro-valve, -gripper, etc.) [35], [87], [124], [125] - see Figure 1. 3 and Figure 1. 4. Shape memory alloys are still of a big scientific interest. Recent selected papers focus on ferromagnetic shape memory alloys [126]–[133], their synthesis by laser melting [134], [135], additives [109], [110], [112], [115], [136] and new measurement method for stress-temperature phase diagram [137].

*Table 1. 2: Comparison of selected properties of NiTi and FeMnSiCr alloys. Taken from:[122], [138].*

Alloy:		Young's modulus [GPa]:	Yield strength [MPa]:	Recovery strain [%]:	max. recovery stress [MPa]:	Resistivity [ $\mu\Omega\cdot\text{m}$ ]:
NiTi	austenite	70-98	100-800	8	600-900	0.5-1.1
	martensite	27	50-300			
FeMnSi		140	~200	3.4	400	1.0-1.3

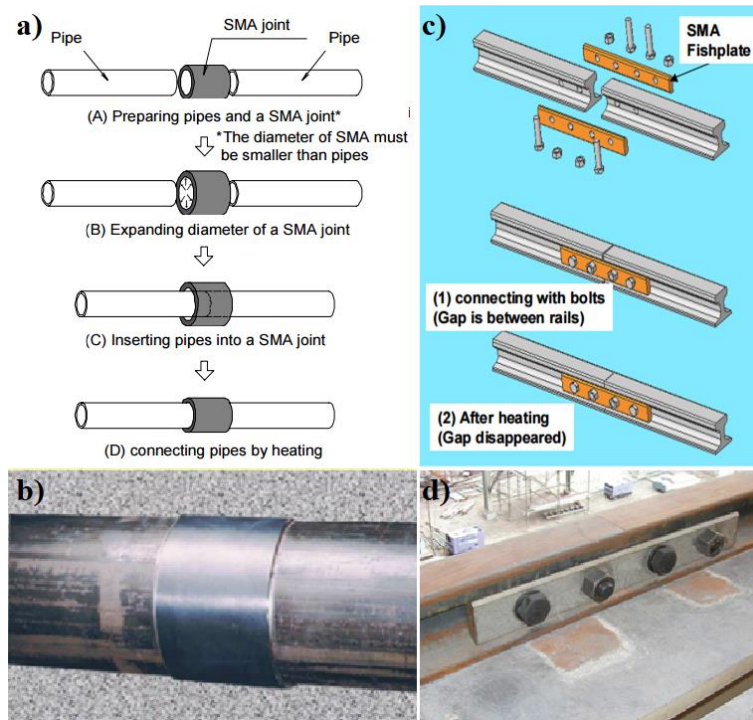


Figure 1. 5: Fe-Mn-Si alloy as: a), b) pipes connecting material and c), d) fishplate connector. Taken from: [139].

In 1982 A. Sato discovered SME in Fe-Mn-Si alloy [1]. Their SME is stress induced martensitic transformation: between  $\gamma$  (fcc; austenite) phase and  $\epsilon$  (hcp; martensitic). It occurs due to the motion of Shockley partial dislocations in the fcc structure (the Burgers vector  $a/6[11\bar{2}]_{\text{FCC}}$  glides between two (111) layers of the fcc lattice). Further silicon and manganese atoms positions are randomly changed between iron atoms in  $\alpha$  (BCC) structure, which stabilized the  $\gamma$  phase in the room temperature [2]–[5]. Reverse transformation occurs during heating: from  $\epsilon$  to  $\gamma$  phase [4], [5]. They are important alloys from the point of view of this study. They exhibit SME in iron composition range: 60-65 wt.%. In comparison with NiTi alloy they are not suitable e.g. for biomedical applications but they are much less expensive (with respect to the elements used). They possess high strength and Young modulus. Alloying with additional elements improve properties. They superior properties in ferrous SMA family have Fe-28%Mn-6Si-5Cr (wt.%) alloy. For high recovery strain (up to 1000 MPa) and corrosion resistance Fe-Ni-Co-Ti alloy should be used [122]. A comparison of chosen properties differences between NiTi and FeMnSiCr are summarized in Table 1. 2. Figure 1. 5 presents example applications as a pipes and fishplates joining material. They can be also applied as e.g. seismic damper (JP Tower Nagoya) [3]. One of the studies show promising results regarding its application as a biodegradable material [140]. Other alloying elements can be also used. Few studies showed improvement of properties upon carbon

addition, but it is still a controversial subject. For example, it was reported that it can stabilize and strengthen the austenite [6]. Based on phase diagrams, it can produce unwanted particles or support creation  $\alpha'$ -phase which can degrade properties [6], [8]–[12].

Magnetic properties of Fe-Mn-Si alloys are reported as antiferromagnetic ones. In Fe-Mn alloys,  $\epsilon$ -hcp exhibits itinerant electron antiferromagnetism (also increased electrical resistivity),  $\gamma$ -fcc is also antiferromagnetic, but with higher magnetic moments, and  $\alpha$ -bcc is ferromagnetic [15]. Addition of silicon into Fe-Mn system decreases Néel temperature of austenite, enhances the strength of matrix, reduces the stacking fault energy of austenite [16], increases electrical resistivity, decreases volume per atom of fcc phase [17], increases volume per atom of hcp phase, reduces stabilization of austenite and causes appearance of Kondo-like effect [18]. In contrast to that, increased Mn content raises Néel temperature, decreases the driving force of martensitic transformation, increases volume per atom of fcc/hcp phase [17], and has impact on the shape memory effect [19][20]. The thermo-induced martensitic transformation from paramagnetic to antiferromagnetic state was reported in [2] [12] [21].

## **1.2 Preparation of shape memory alloys**

Over the years, many publications shows different synthesis approaches for shape memory alloys and the alloys generally. Synthesis methods depend on the size/shape of the desired output material and on the production scale. Taking it into account production of thin films can be obtained by deposition methods such as: pulse laser deposition, magnetron sputtering or chemical vapor deposition. There are many different approaches depending on their thickness and applications e.g. first nickel and next titanium deposition on it with/without heating and further annealing [26], [27], [36], [28]–[35]. Another approach includes multilayer deposition of different elements with similar thermal post processing [27], [31]. The most common and simple method in bulk alloy production is induction/arc vacuum furnace. This process involves heating of pure input elements above melting points with simultaneous mixing in the crucible. Output product possess very good properties, but can easily be contaminated by external elements (e.g. carbon) [37]–[41]. Also simple and less energy consuming methods include pure element powders, which are mixed together and shredded in mills (e.g. rotary mills). Output amorphous powder material is sintered and annealed [42]–[46].

From economic point of view, industrial (mass) production is most favorable. Hot/cold rolling is excellent method for this purpose. It is mainly used in sheets and foils production – plastic working and forming [47], [48], [57]–[59], [49]–[56]. An approach was reported regarding

nickel and titanium foils multilayer, which first were heated and further rolled and folded several times, and composition could be adjusted by different foil thicknesses [60], [61]. In wires production it can be realized by hot and cold working [62]–[66].

### 1.3 Diffusion process

Diffusion process is describing movement of each element atoms: within the same material volume – called self-diffusion and into another material, when an interface is established between materials which are in this case termed diffusion couples. It is described by Fick’s laws. Connection between materials is established by mechanical pressing (e.g. hydraulic press and rolls) or all kinds of welding methods. Element movement speed is characterized by its diffusion coefficient in their material studied. It is specific for each element.

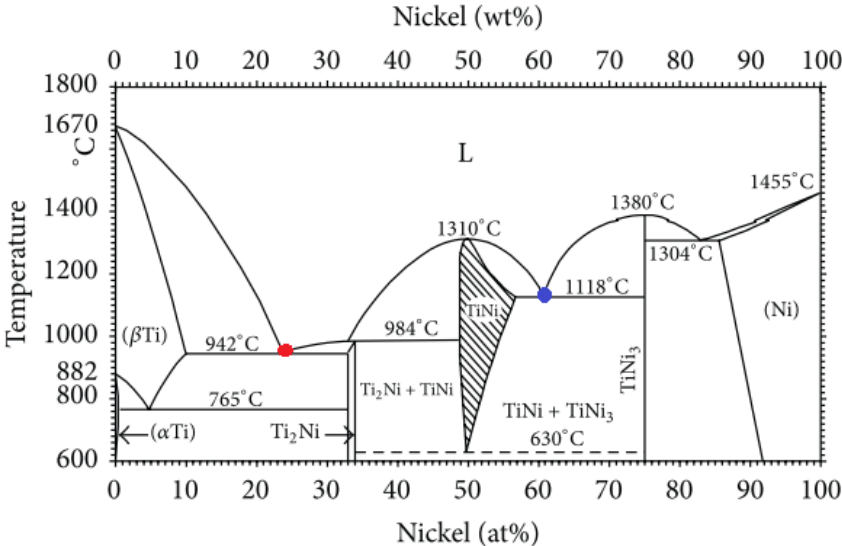


Figure 1. 6: Phase diagram of the Ti–Ni system, taken from: [141]. Red dot – lowest melting point for titanium rich alloy and blue dot - lowest melting point for nickel rich alloy.

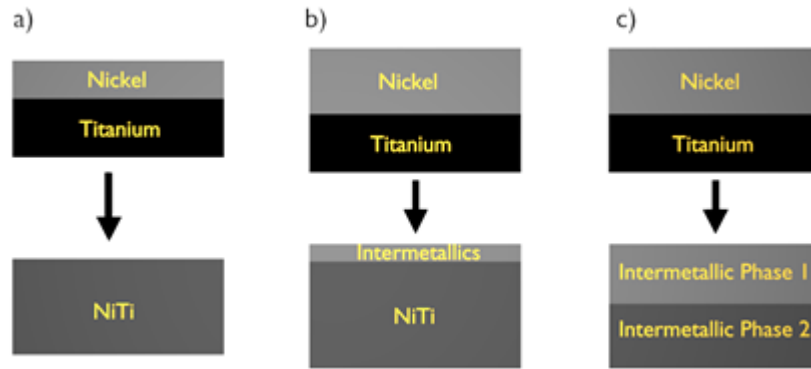


Figure 1. 7: A comparison between: a) well-chosen volume of input materials and b) wrong chosen for similar diffusion time and c) wrong when diffusion process is completed. Based on [67], [69]–[71], [142]–[144].

Diffusion process should be designed basing first on the phase diagram. For Ni-Ti system it is presented in the Figure 1. 6. Diffusion effect consideration in this study focuses on examination of joining methods used and depending on the process time, temperature and composition. NiTi shape memory alloy phase existence can be observed between ~49 - 57 (at.%) [145]. One of the main two goals of this study is to obtain NiTi shape memory alloy in the full material volume from input foils. Based on the phase diagram (NiTi composition range) initial foils should have properly chosen thicknesses, which should be set at the initial stage, before the synthesis – see Figure 1. 7. Next important parameter is the proper temperature of the synthesis. Basing on the phase diagram minimal temperature should be ~630 °C, but not exceed melting point (for nickel 1455 °C, for titanium 1668 °C and for NiTi 1300 °C [146]). Pressing force and annealing time have to be also set. Compressive force holds materials steady, improve their interface (better contact without undesired micro-voids) and increases diffusion rate. Too high force can introduce unnecessary too high internal stress. This is well known method for alloys preparation in powder metallurgy. Material protection during synthesis process is also an important factor. Materials should be surrounded by unreactive atmosphere, which can protect them from contaminations (e.g. oxygen, carbon or nitrogen). For this purpose, best option is high vacuum or high purity argon gas atmosphere. Few studies report on NiTi preparation by diffusion process (hot pressing) from initial material thickness starting from 40 μm and higher [67], [68], [71], [142]. Basing on powder metallurgy it is easier to set initial composition and adjust other parameters to obtain homogenous material in its whole volume. The process is getting harder if it is necessary to obtain full volume alloy based on synthesis time for desirable thickness. Proper chemical (e.g. etchants) or mechanical treatment (e.g. laser cutting) are usually necessary to

include to the process. Disadvantages of this way are unwanted material losses and additional treatments involvement, which makes the process more complex.

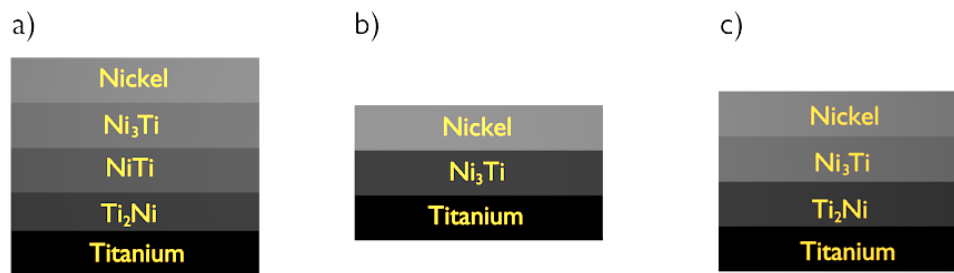


Figure 1. 8: Illustrative representation of phases creation during diffusion process between pure nickel and titanium input materials: a) at the temperature range of NiTi phase. b) and c) lower temperature or too short diffusion time.

During diffusion process different intermetallic phases are created depending on the conditions. For Ni-Ti system phases creation based on composition and temperature are showing in Figure 1. 6. In the diffusion couple at the interface region, at the beginning the Ni<sub>3</sub>Ti phase appearance can be seen. It evolves in time into layers of two phases: Ti<sub>2</sub>Ni and Ni<sub>3</sub>Ti. Between them the layer of the NiTi phase is created – see Figure 1. 8. Ti<sub>2</sub>Ni and Ni<sub>3</sub>Ti phases are used as a “fuel” for NiTi phase volume growth during diffusion process. Their thicknesses and phases content depends strongly on annealing temperature and time [67], [69]–[71], [142]–[144].

Bastin, et al. in the studies [143], [147] presents experimental results of chemical diffusion coefficient in different kinds of diffusion couples (Ti-TiNi, Ti-TiNi<sub>3</sub>, Ti<sub>2</sub>Ni-TiNi<sub>3</sub>, Ti<sub>2</sub>Ni-Ni and TiNi-Ni). They are showing NiTi phase composition range and layer width squared dependence on temperature and time. Simple linear dependences can be seen. For example to obtain NiTi content of  $5 \cdot 10^{-4} \mu\text{m}^2$  at 940 °C, 100 h of annealing is necessary. Width squared strongly falls for lower temperatures – at 850 °C for the same time  $1 \cdot 10^{-4} \mu\text{m}^2$  can be obtained. Based on this, to obtain in such a way a relatively high phase thickness, long annealing time is necessary, which can be counted in days. The example presented showing that to obtain thicker foils layers faster, long annealing at high temperatures has to be used or preparation method has to be changed.

Good alternative for it can be hot pressing/sintering method. Based on their source of heating and design, they can be divided into following types:

- conventional hot pressing a powder metallurgy method used for obtaining dense materials from powders. Initial material is placed in a die (commonly made from graphite) and pressed. Heating is provided by external heater located around die in the pressing chamber [148], [149].

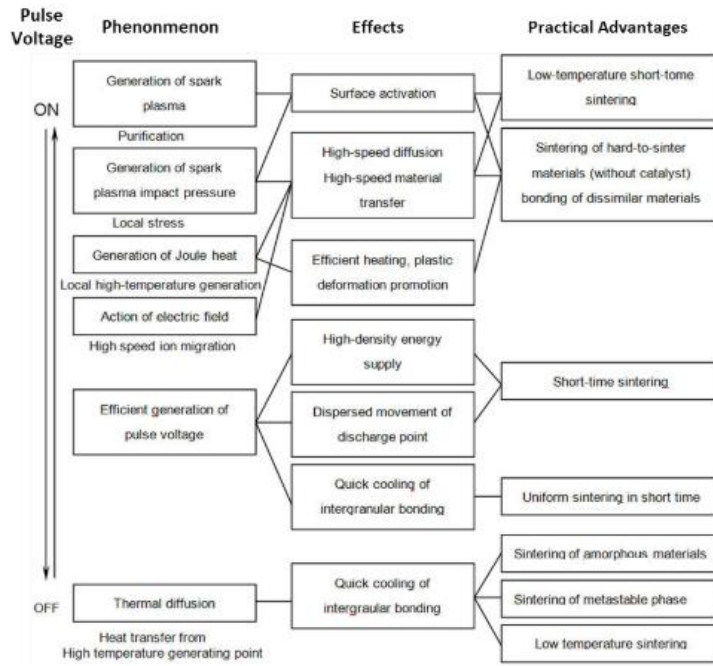


Figure 1. 9: Table summarizing direct current heating effects. Adapted from [150].

- Spark Plasma Sintering (SPS)/Field Assisted Sintering Technology (FAST) Direct hot pressing (also known as Pulsed Electric Current Sintering (PECS)), is a technique which is based on pulsed/un pulsed electric current flow through the sample material and graphite dies under compressive force. It can be used for conductive, partial conductive materials and for some ceramics (heated by high electric current flowing through graphite dies generates high-temperature zone [150]). Temperature is measured on the graphite die surface, close to the sample, by thermocouple. Output is a dense material [151]. Pulsed current heating effects are shown in Figure 1. 9.

- Inductive Hot Pressing is a method based on induction heating of the sample material. It can be used for experiments with high heating rates, with or without applied external compressive force [152].

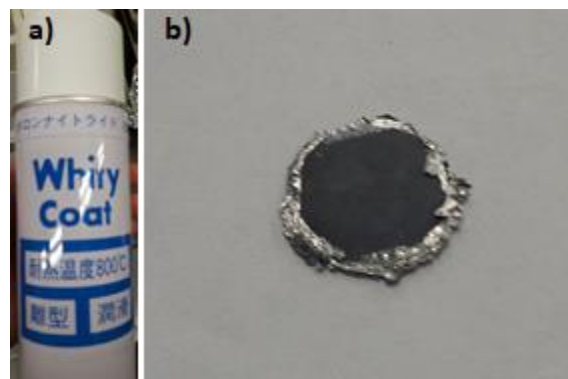


Figure 1. 10: a) Boron Nitride (BN) spray and b) example of output foil obtained after synthesis process.

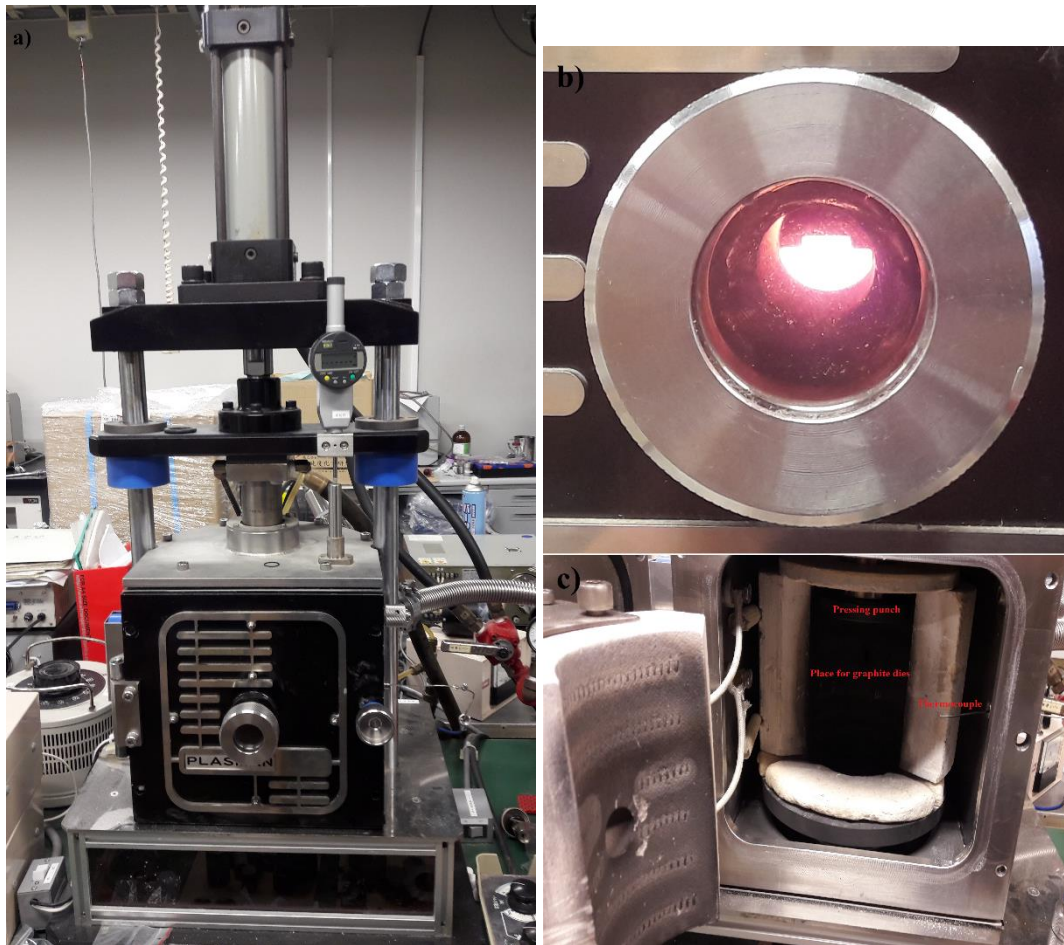


Figure 1. 11: Pulse-current pressure sintering equipment (PLASMAN, SS Alloy): a) main, b) sintering in high temperature and c) chamber inside view.

As it was mentioned before, their application can shorten processing time. For the process, special lubricants have to be used to protect material (sample) surface of sticking to press molds. For the study presented in this thesis boron nitride (BN, White Coat, h-BN, package can be seen in Figure 1. 10 a)) was used for covering both foil surfaces. It can be safely used up to 800 °C and has very high thermal conductivity [153]–[155]. Without it, application of hot pressing techniques to micro-foils would be problematic. Output foil after synthesis process, before cleaning, can be seen in Figure 1. 10 b). Initial unnecessary foils residue can be seen around processed sample area. Protective atmosphere in this study was low vacuum, which is a part of inherent feature of this technological process. Pulse-current pressure sintering machine (pulse width 50%, pulse frequency dependent on the samples and current amperage dependent on desired temperature - maximum 500 A) used in this study is presented in Figure 1. 11.

In the paper [67] the authors shown that Ni-Ti thin foil can be produced by diffusion bonding of relatively higher nickel and titanium foils – between intermetallic phases are

created with NiTi in the center. Further processing required etching it from the foils residue. The [68] study used also diffusion bonding method to obtain Ti<sub>2</sub>Ni/NiTi micro-laminated composites, which exhibit shape memory effect, and tensile test show cracks propagation along Ti<sub>2</sub>Ni compound layers. Interesting research was shown by Garay [69] and further by [70], [71]. In the studies direct current was used to study its influence on intermetallic phases creation. Based on the newest research, it was shown that current does not have directional influence on their growth. However, current can significantly increase the growth rate, as was first shown by Garay [69]. They also observed that a dendritic structure was formed inside of NiTi, which is related to high titanium diffusion. Also the columnar crystals were formed at temperature higher than 882 °C (titanium transformation between  $\alpha$  and  $\beta$ -phase) initially inside the Ni<sub>3</sub>Ti matrix – with further progress of Ti diffusion, the Ni<sub>3</sub>Ti phase vanished and surprisingly pure titanium layer appeared adjacent to Ni.

## Chapter 2. Characterization techniques

### 2.1 Crystal structure and phase content

Basic information regarding crystallographic structure and phase content in the samples is possible to obtain by X-Ray Diffraction (XRD) measurements and their data processing software. Two XRD machines were used: SmartLab, Rigaku Corporation (Technoplaza, Shibaura Institute of Technology) and Siemens/Bruker D5000 – see Figure 2. 1 and Figure 2. 2, respectively for images and characteristics.



Parameter name:	Value:
Anode:	Cu
Voltage [kV]:	20 - 60
Current [mA]:	2 - 60
Step [°]:	0.0001
2Theta max [°]:	4 - 158
Measurement accuracy 2Theta [°]:	0 ± 0.005
Heating stage:	-

Figure 2. 1: Image of: on the left SmartLab, Rigaku Corporation (Technoplaza, Shibaura) [156] and characterization table on the right.



Parameter name:	Value:
Anode:	Cu
Voltage [kV]:	20-55
Current [mA]:	20-60
Step [°]:	0.01
2Theta max [°]:	1 - 160
Heating/Cooling stage:	+
Temperature range [K]:	2- 500
Container:	zero background /amorphous

Figure 2. 2: Image of: on the left Siemens d5000 (SSPD, AGH) and characterization table on the right.

X-Ray Diffraction on polycrystalline samples was performed in Bragg-Brentano geometry and was based on Bragg equation (see equation 2.1). X-rays emitted from source X-rays (commonly Cu anode) are scattering from the sample (with finite penetration depth depending

on the material). Detection is done in the selected angle range and angle step (at the circle around sample).

$$2d\sin\theta = n\lambda \quad (2.1)$$

Where:  $d$  – interplanar distance,  $\theta$  – scattering angle,  $n$  – positive integer and  $\lambda$  – ray wavelength.

Depending on the sample crystallographic structure peaks can appear at appropriate angles in XRD pattern. For amorphous materials low angle diffraction bumps appear. From obtained pattern it is possible to establish e.g. material crystal structure with atom positions, phases content, crystalline size, internal strains and compare their differences between samples. In this study X'Pert High Score Plus (PANalytical) was used to XRD patterns analysis. It provides easy user interface with many possibilities of data processing. Rietveld refinement analysis (which is included in the software) is a powerful tool for many applications. It simulates theoretical curve based on the established model of crystal structure and compares it with measurement data of the sample. Peaks positions are depended on the lattice parameters and space group. The intensities are also characteristic for the real crystal structure.

The X-Ray Absorption Spectroscopy (XAS) provides information on the local structure, chemical state and uniform environment of individual elements. X-Ray Absorption Near Edge Structure (XANES) and Extended X-Ray Absorption Fine Structure (EXAFS) measurements were performed at Swiss Light Synchrotron (SLS) on the super XAS beamline. They were performed in Partial Fluorescence Yield (PFY) mode. Qualitative analysis was performed between samples – Athena software (DEMETER, Bruce Ravel). XANES provides information regarding absorbing atom e.g. chemical environment, oxidation states (energy of absorption edge shifts) and its chemical bonds. It is a complex and demanding method due to lack of a simple theory. EXAFS analysis gives structural information on the nearest and next neighbor shells of individual elements. For example the distance of atoms in those shells from the absorbing atom can be determined [157].

## **2.2 Microstructure and elemental composition**

Scanning Electron Microscopy (SEM) is based on electron interactions with sample surface (in vacuum). The electron beam is created in electron gun and accelerated by high voltage. Surface image is created based on detector used. Secondary Electrons (SE; most common method) and Back-Scattered Electrons (BSE; gives more information regarding material microstructure) are used. There are also specific detectors dedicated to analysis of

material composition with Energy Dispersive Spectroscopy (EDS), and for e.g. crystal structure and its orientation - Electron Back-Scattering Diffraction (EBSD).

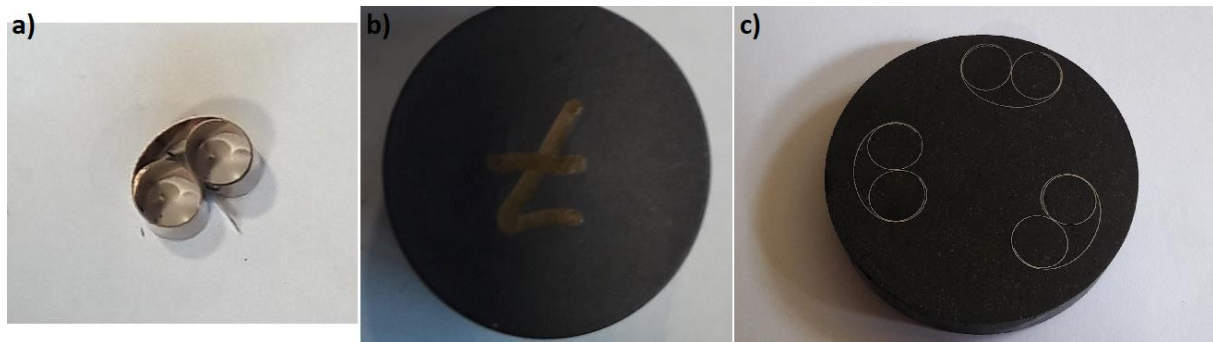


Figure 2. 3: Images of: a) sample between fixation clip, b) resin holder with fixation clip and sample inside and c) resin holder with samples cross-sections after grinding and polishing process.

In this thesis, SEM equipped with EDS was used for microstructure and elemental composition study. Taking into account diffusion occurring between two thin foils, it is important to get information about composition near foils interface and element distribution from it. For this purpose samples cross-sections were prepared and studied. The samples were prepared at Faculty of Metals Engineering and Industrial Computer Science of the AGH University. Pieces of foils were put between 6 mm fixation clip (Struers, see Figure 2. 3 a)) and inserted into graphite resin (KEM 70 Pulver, ATM GMBH, see Figure 2. 3 b)). After 24 hours of drying, resin holder is ready for cutting and grinding process. Starting from 200 and finishing on 3000 of sand paper granulation, holders are ready for polishing process: initially with aluminium oxide and finally with silicon oxide. At the end of the process it is necessary to remove undesirable pollution from the surface by washing with ethanol and drying (Figure 2. 3 c)).



Parameter name:	Value:
Acceleration voltage [kV]:	0.2 – 30
Magnification:	Over 500 000×
BSE:	+
EDS:	+
EBSD:	+
WDS:	+

Figure 2. 4: Image of: on the left FEI Nova NanoSEM 450 Scanning (at Faculty of Metals Engineering and Industrial Computer Science, AGH University of Science and Technology) and characterization table on the right. Taken from [158].



Parameter name:	Value:
Acceleration voltage [kV]:	0.2 - 30
Magnification:	x10 - 1000000
BSE:	+
EDS:	+
EBSD:	+
WDS:	-

Figure 2. 5: Image of: on the left JSM-7100F (JEOL Ltd., at Technoplaza, Shibaura Institute of Technology) and characterization table on the right. [156].

Two types of Scanning Electron Microscope (SEM) were used in this study: FEI Nova NanoSEM 450 Scanning (at Faculty of Metals Engineering and Industrial Computer Science, AGH University of Science and Technology) and JSM-7100F (JEOL Ltd., at Technoplaza, Shibaura Institute of Technology). Their images and characteristics are presented in Figure 2. 4 and Figure 2. 5, respectively. All of them are equipped with Energy Dispersive Detectors (EDS).

For a preliminary sample surface characterization, optical microscope was also involved in this study. Measurements were performed on Opton Axioplan apparatus at Laboratory of

### 2.3 Magnetic properties

Magnetic properties of the samples were studied by Vibrating Sample Magnetometry (VSM) which is a part of Physical Properties Measurement System (PPMS) and Mössbauer Spectroscopy. The measurements were performed in Solid State Physics Department at the AGH University of Science and Technology.

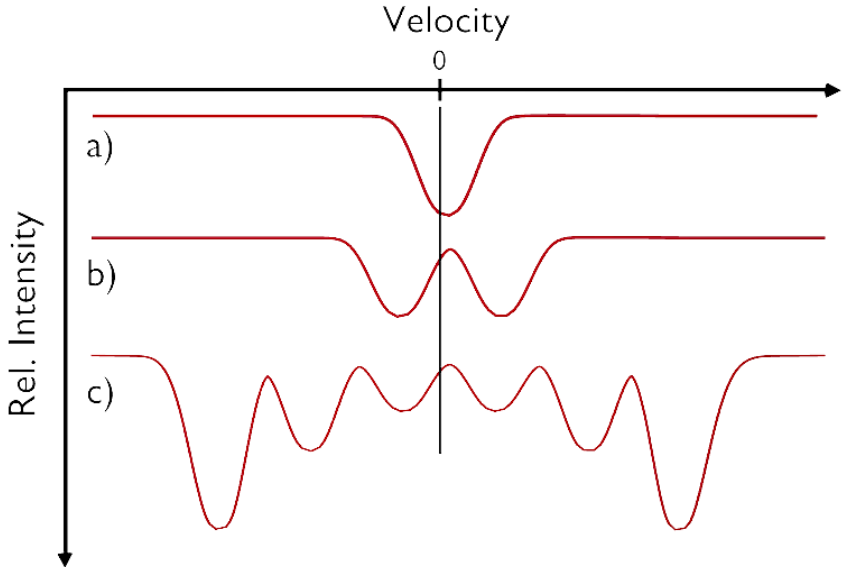


Figure 2. 6: Illustrative representation of Mössbauer spectrums: a) single line (singlet) b) two lines (doublet) and c) six lines (sextet).

Mössbauer Spectroscopy allows for the study of magnetism and structural site location of iron or other Mössbauer element in pure elements, alloys and compounds. It is very sensitive method which can detect changes occurring at nucleus. A source placed on the vibrating stage emits gamma rays which energy is changing due to relativistic Doppler effect. Next they penetrate sample volume where they can be recoilless absorbed by Mössbauer nuclei. Finally, transmitted gamma rays are collected by detector. Those which are recoilless absorbed in the sample are causing a decrease of intensity in the Mössbauer spectrum – the respective absorption lines creation. The following hyperfine interactions parameters are obtained from the spectra: isomer shift (spectrum is shifted due to s-electron density change at nucleus) - see Figure 2. 6 a), quadrupole splitting (due to electric field gradient and nucleus quadrupole moment interaction – see Figure 2. 6 b)) and hyperfine field (Zeeman effect – energy levels splitting due to interactions between magnetic field and nuclear spin - see Figure 2. 6 c)).

Except for the conventional transmission measurement method there is also Mössbauer Spectroscopy technique which is based on inner conversion electrons detection – Conversion Electron Mössbauer Spectroscopy (CEMS). This method characterizes the sample surface properties up to 500 nm.



Figure 2. 7: Mössbauer Spectroscopy sample preparation process.

Sample preparation for this method, involved copper rings, high purity aluminium foil (thickness:  $0.038 \pm 0.007$  mm and purity: 99.9995%), glue and sample powder. The whole process is presented in Figure 2. 7. Copper ring was glued to aluminium foil, filled with sample powder (sealed with another layer of aluminium foil. This way prepared absorber was fixed into sample holder (see Figure 2. 8 a)) and ready for measurement.



Figure 2. 8: a) Sample inside holder, b) gas flow cryostat and c) Mössbauer Spectroscopy measurement setup.

Mössbauer Spectroscopy system used allows for room and low temperature measurements. It consists of: gas flow cryostat with sample holder, connected liquid nitrogen/helium container (depending on required temperature) and turbomolecular pump – see Figure 2. 8 c). Measurements are performed with  $^{57}\text{Co}$  in Rh source.

Analysis of the results was performed with “Mos1” (Dr. J. Żukrowski) and “Origin Pro” (OriginLab Corporation) fitting software.



Figure 2. 9: Images of Physical Properties Measurement System with 9 T superconducting magnet: a) PC with PPMS electronics cabinet and b) Dewar/probe (with mounted VSM module, Quantum Design).

The method used for DC magnetic properties measurements is Vibrating Sample (DC) Magnetometer (VSM) – magnetic moment dependences. Based on the VSM results it is possible to characterize different magnetic types of materials. It is an option of Physical Properties Measurement System (PPMS) manufactured by Quantum Design company (see Figure 2. 9 a)). It allows for measurements at the temperature range from 4 K to 380 K and magnetic field up to 9 T.

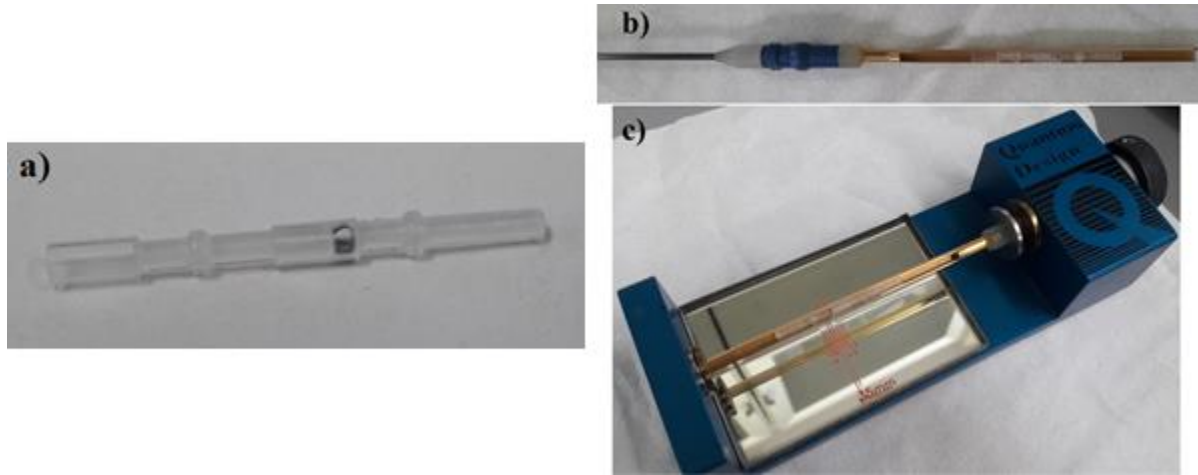


Figure 2. 10: VSM sample holder with inserted sample (foil).

VSM sample preparation involved weighting and inserting the powdered sample into plastic container (see Figure 2. 10 a)), placed then in trough-shaped sample holder (see Figure 2. 10 b)) and adjustment of the sample container position on special stage (see Figure 2. 10 c)). The sample in holder is then placed inside of PPMS probe part – inside of the Evercool cryostat Figure 2. 9 b).

The placed in the coil sample is moved by a linear motor vibrating with an amplitude range of 2 mm at the frequency of 40 Hz, allowing the measurement accuracy better than  $10^{-6}$  emu. The movement is inducing a response in pick up coil in form of voltage changes. It is based on magnetic Faraday induction law (induction phenomenon) and sample magnetic moment  $m$  can be derived from (equation 2.3.1) [159]

$$V = 2\pi f C m A \sin(2\pi f t) \quad (2.3.1)$$

Where:  $V$  – pick up coil voltage,  $A$  – amplitude of oscillations,  $f$  – frequency of oscillations and  $C$  - coupling constant. The coupling constant is determined from calibration measurement.

## 2.4 Heat capacity, electrical and thermal properties

Heat capacity studies were carried out by a two-tau relaxation method at the temperature range 1.85 K – 360 K using a heat capacity option (HC) of the Quantum Design PPMS platform. Care was taken to shape bulk  $\text{Fe}_{0.600}\text{Mn}_{0.286}\text{Si}_{0.110}\text{C}_{0.004}$  (at.) sample to a flat square geometry in order to ensure good thermal contact with the sample platform.

The electrical properties of samples were investigated by using the Resistivity option of Physical Properties Measurement System (PPMS) in Solid State Physics Department at AGH University of Science and Technology – see Figure 2. 9 a). It allows for resistance and

magnetoresistance measurements at the temperature range from 400 K down to 1.8 K and at magnetic field up to 9 T. For this purpose four-point method is used with two voltage and the current connections.

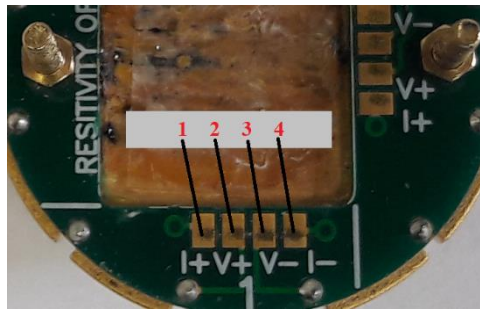


Figure 2. 11: Illustration of four point method: black lines – wires and red numbers – pressing pin positions.

The method is presented in Figure 2. 11 – grey rectangle is the sample, black lines represent a wires connected by pressing pins to the sample. Current wires are in the positions 1 and 4, and voltage wires in 2 and 3. This method measures resistance between points 2 and 3, rest is based on Ohm law. It is commonly used for precise resistance measurement. Magnetoresistance is measured in the same way, but in the presence of required magnetic field.

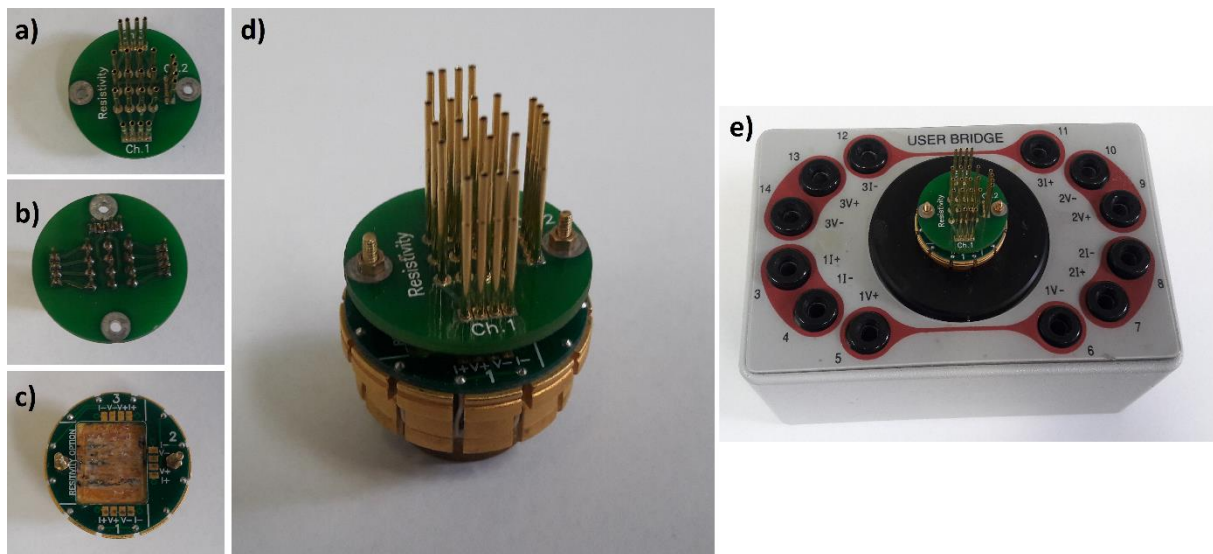


Figure 2. 12: Images of resistivity option sample: puck a), b) upper part (connection pin board from the top and bottom respectively), c) lower part: three channel sample puck, d) assembled and e) in the user bridge board.

Samples dimensions are measured and the samples are placed in the puck, which can be seen in Figure 2. 12 (with different views) - specially designed for this system. It provides fast and easy mounting of up to three samples before measurement. Without the connection board it is necessary to solder each wire to the sample and the puck (in total: four between one

sample and puck). Each pin is separated by 2 mm. The puck with the mounted samples is next inserted into the sample chamber of PPMS system [160].



Parameter name:	Value:
Device name:	DSC-60
Company:	SHIMADZU
Measuring principle:	Heat-flux type
Temperature range [°C]:	-150 - 600
Temperature speed [K/min or K/hour]:	0 - 99
Measuring power range [mW]:	±40
Noise level [μW]:	1
Atmosphere:	air, argon or argon flow

Figure 2. 13: Image of DSC-60 (SHIMADZU) device (on the left) and characterization table (on the right). Taken from [161].

Thermal transformation between martensite and austenite phase was investigated by Differential Scanning Calorimetry (DSC), more precisely - by power compensating DSC (DSC-60, SHIMADZU at Shibaura Institute of Technology – see Figure 2. 13). Sample and references sample are placed in separate pans (each is equipped with heater and thermometer) in aluminium containers with similar weights and under argon flow. It allows for measurements at the temperature range from -150 to 600 °C and power range: ±150 mW with adjustable heating/cooling speed. As a reference sample aluminium oxide ( $Al_2O_3$ ) is used, and for low temperature measurement liquid nitrogen is required. Data analysis is performed on included software “ta60”.

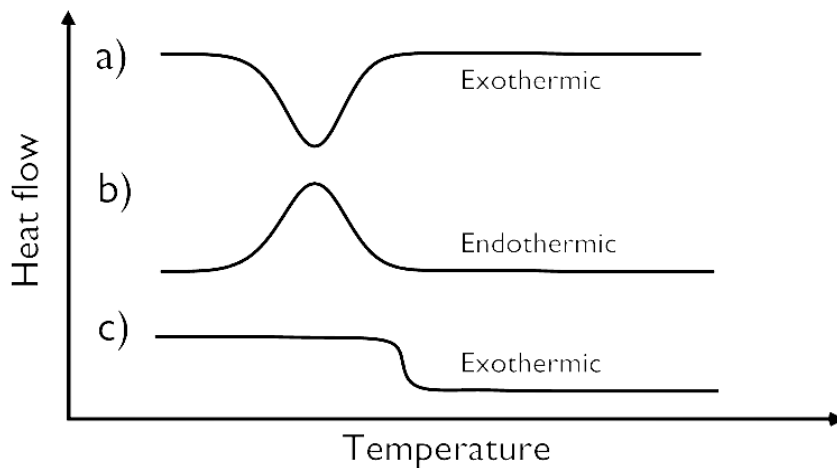


Figure 2. 14: Example of DSC curve with following transitions marked: a) melting, b) crystallization and c) glass transition for exothermal and endothermal reactions.

The principle of the method is based on temperature comparison between pans and any thermal event is compensated by the heater. By measuring the heater power or difference, it allows to distinguish endothermic (power decreases) and exothermic (power increases) reactions, such as: melting point, crystallisation and glass transition – see Figure 2. 14. It is commonly used in kinetic, phase transition and crystallinity determination studies.

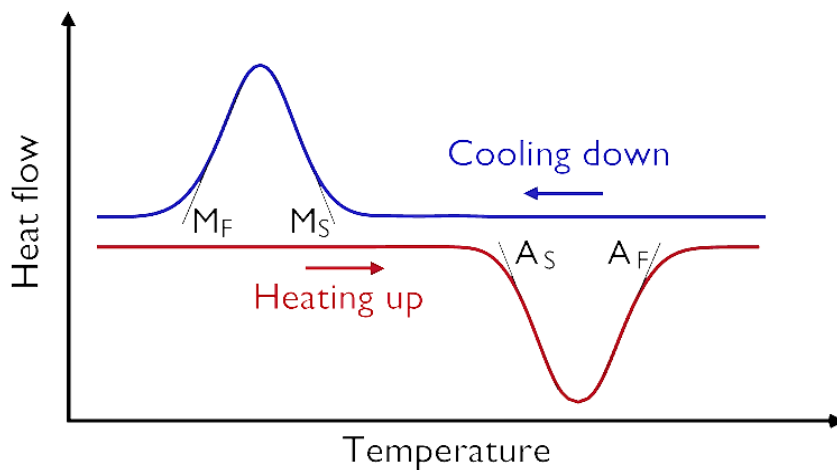


Figure 2. 15: Example of shape memory alloy DSC curve with marked transformation temperatures:  $A_S$  – austenite start,  $A_F$  – austenite finish,  $M_S$  – martensitic start and  $M_F$  – martensitic finish.

Example of DSC curves for martensite-austenite transformation of SMA is presented in the Figure 2. 15. During heating it should appear at some temperature endothermic peak (from martensite to austenite transformation), and during cooling - exothermic peak (from austenite

to martensite). It is important to note that too big heating rate can influence measurement accuracy – it will shift transformation temperature. The contact between sample surface, and pans can also affect measurement accuracy.

## 2.5 Shape Recovery Rate

Shape Recovery Rate (SRR) is a parameter allowing a comparison of shape memory effect in different materials. For this purpose home-made bending test machine was prepared based on study [162] – the scheme is presented in Figure 2. 16.

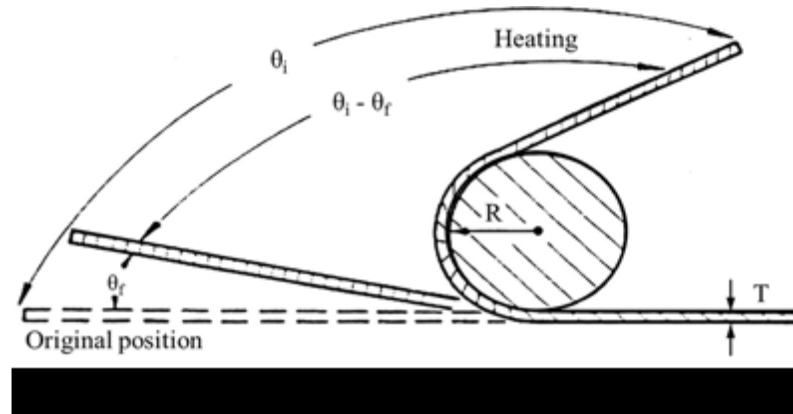


Figure 2. 16: Bending test diagram. Taken from [162].

The SRR can be derived based on following equations:

$$\varepsilon = \frac{T}{2R} \quad (1.2)$$

$$SRR = \frac{(\theta_i - \theta_f)}{\theta_i} \quad (1.3)$$

where:  $\varepsilon$  – bending strain,  $T$  – sample thickness,  $R$  – bending machine rod radius,  $SRR$  – Shape Recovery Rate,  $\theta_i$  – bending angle and  $\theta_f$  – final angle (after heat treatment).

Bending rod diameter was adjusted to the samples thickness for desired bending strain. The system consists of the heater, camera and container with: mineral oil, sample holder and thermometer (placed close to the sample position). Shape recovery (angle change) recorded by a camera placed above the sample and heated to different temperatures in the range from ambient temperature to 120 °C. Sample dimensions were: 5 mm x 2 mm, and the thickness was dependent on the studied sample. Temperature was measured by simple K-type probe within range of: -20 - 1200 °C and accuracy:  $\pm 1$  °C.

## **Chapter 3. Fe-Mn-Si alloys – results and discussion**

In this Chapter results of investigations of Fe-Mn-Si type materials, which exhibit shape memory effect during martensitic transformation are presented and discussed. In the next subchapters results obtained for “heated” samples and with small carbon addition will be presented. It is well known that characteristics of the shape memory alloy can vary significantly, depending on their composition. In Fe-Mn-Si system, alteration of the properties by the addition of elements is possible. In particular, the parent phase reinforcement with a solid solution with carbon addition is known to improve the shape memory characteristic [163].

Study includes samples preparation process, crystal structure (X-Ray Diffraction, X-ray Absorption Near Edge Structure and Extended X-Ray Absorption Fine Structure) and magnetic properties at low and room temperature (Mössbauer Spectroscopy, Conversion Electron Mössbauer Spectroscopy and Vibrating Sample Magnetometry). Also specific heat was measured in the 2 K to 350 K temperature range at zero field and at applied magnetic field up to 90 kOe. Short overview of techniques used can be found in previous Chapter. Samples preparation and the study of their properties were performed in collaboration with Shunsuke Miyazawa (Shibaura Institute of Technology student).

### **3.1 Preparation of the samples**

Sample preparation process is schematically presented in the Figure 3. 1. Several physical and thermal treatments had been used on mixed pure iron (electrolytic Fe (99.9%)), manganese (electrolytic Mn (99.9%)), silicon (atomized Si (99.9%)) and graphite powders (scaly graphite carbon (99.9%)). The alloying process was carried out using a planetary ball mill (Pulverisette 7, Fritsch) with a stainless steel vial (volume = 45 ml). The ball-to-powder weight ratio was 8:1. The powder mixture was milled with stainless steel balls (15 mm diameter) in the atmosphere of Ar gas at a rotational speed of 600 rpm. It allows to obtain fine powder mixture –  $\alpha$ -Fe phase transformation to  $\gamma$ -phase and its stabilization [4]. The mechanically alloyed powder obtained (MA powder) was put into a graphite die and sintered by means of pulse-current pressure sintering equipment (PLASMAN, SS Alloy). The sintering was performed at temperature of 900 °C, rate of rise of temp. 50 °C/min, under an external uniaxial compression pressure of 20 MPa, duration 10 min and in vacuum. The samples obtained were cylindrical with a diameter of 10 mm and a height of about 20 mm. Further, the materials were subjected to

annealing (temperature: 600 °C, rise of temp. 5 °C/min, duration 1 hour and in vacuum under high vacuum conditions (10<sup>-3</sup> Pa)) process. Thermal processing improved crystal structure and the sample in the shape of an elongated pellet was obtained. Further treatment involved deformation compression in uniaxial geometry parallel to the external stress of the sintering (rate: 1mm/min, 4% deformation in room temperature) and subsequent heating at 200, 400, 500 and 600 °C depending on the sample. It gave in total seven samples which were investigated as presented in this Chapter (see Table 3. 1) [4], [5], [164]. More detailed information about used techniques can be found in the Chapter 2.

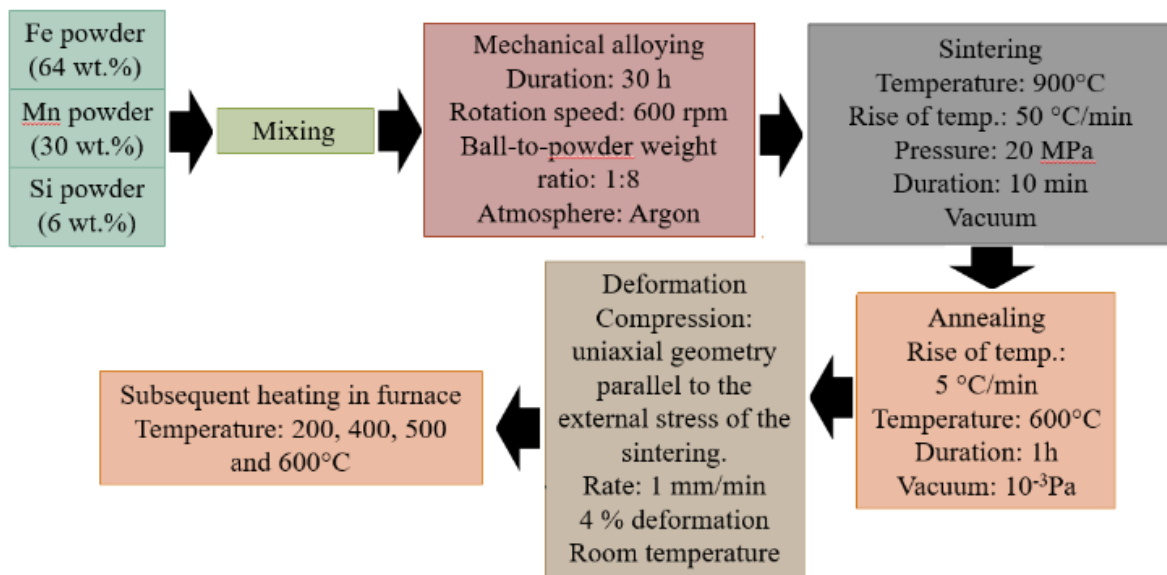


Figure 3. 1: Samples preparation process.

Table 3. 1: Overview of the samples.

Alloy number:	Elements (wt.%):				Description:
	Fe	Mn	Si	C	
1	64	30	6	-	As annealed
2					Heated 200 °C
3					Heated 400 °C
4					Heated 500 °C
5					Heated 600 °C
7			5.9	0.1	0.1 wt.% C

### 3.2 Structural and magnetic properties

In comparison, one material with 0.1 wt.% of carbon addition was chosen due to best shape memory properties – see Figure 3. 2.

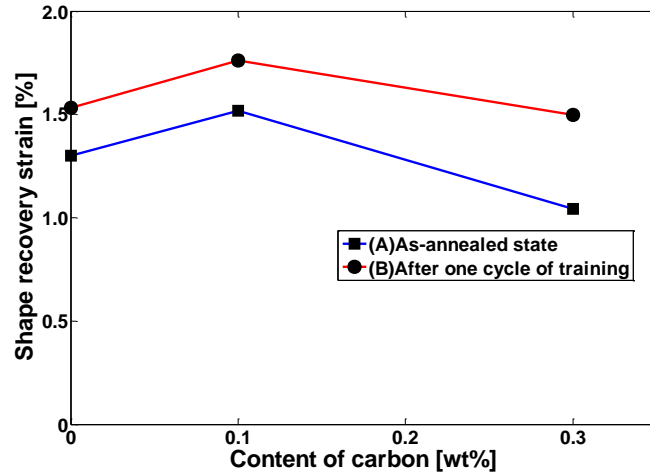


Figure 3. 2: Dependence of shape recovery strain on C content of the alloys. (A) As-annealed state. (B) After one cycle of training, Prendota et al. [163]

Structural properties of the samples prepared were measured with X-Ray Diffraction and X-Ray Absorption Near Edge Structure (XANES)/Extended X-Ray Absorption Fine Structure (EXAFS) method.

Mössbauer spectra for MA10h and MA30h of “0.1 wt.% C” are shown in Figure 3. 3 and Figure 3. 4, respectively.

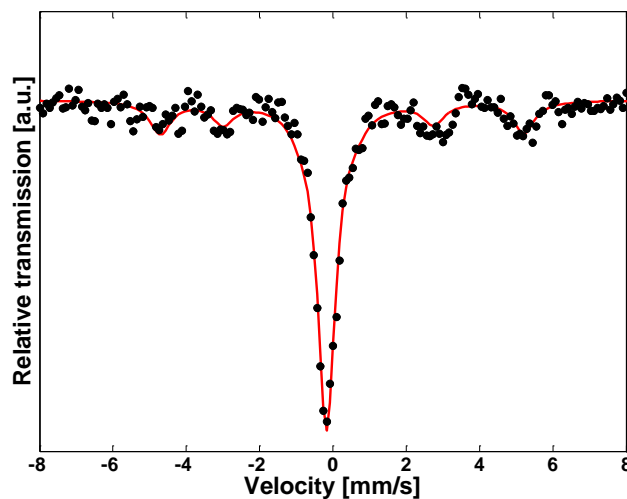


Figure 3. 3: Mössbauer spectra for “0.1 wt.% C” powders after MA for 10 h, Prendota et al. [163].

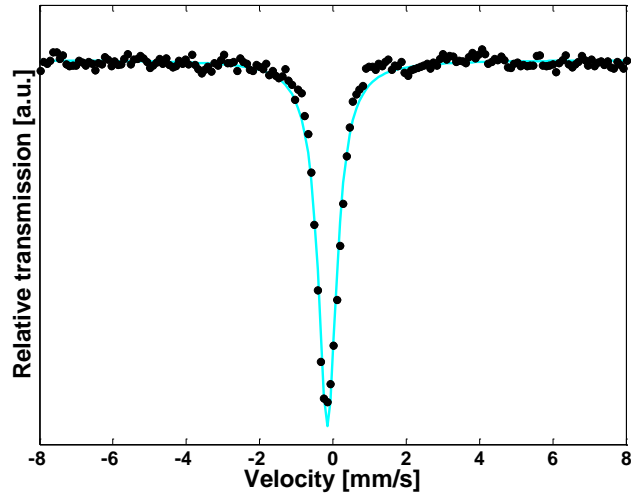


Figure 3. 4: Mössbauer spectra for “0.1 wt.% C” powders after MA for 30h, Prendota et al. [163].

The spectrum after 10 h of MA shows a weak sextet and a dominant single peak, which correspond to the ferromagnetic and the paramagnetic (or diamagnetic) component, respectively. This reveals presence of a mixture of  $\alpha$  and  $\gamma$  phases, showing that MA process was incomplete. For the Mossbauer spectrum of the powder subjected to MA for 30 h, only a single peak is observed and the ferromagnetic component seen for the powder after 10 h of MA, did not appear. Therefore, it can be concluded that the formation of the  $\gamma$  phase is complete for the 30 h of MA.

Figure 3. 5 presents XRD patterns for “As annealed” and “0.1 wt.% C” after 30h of milling.

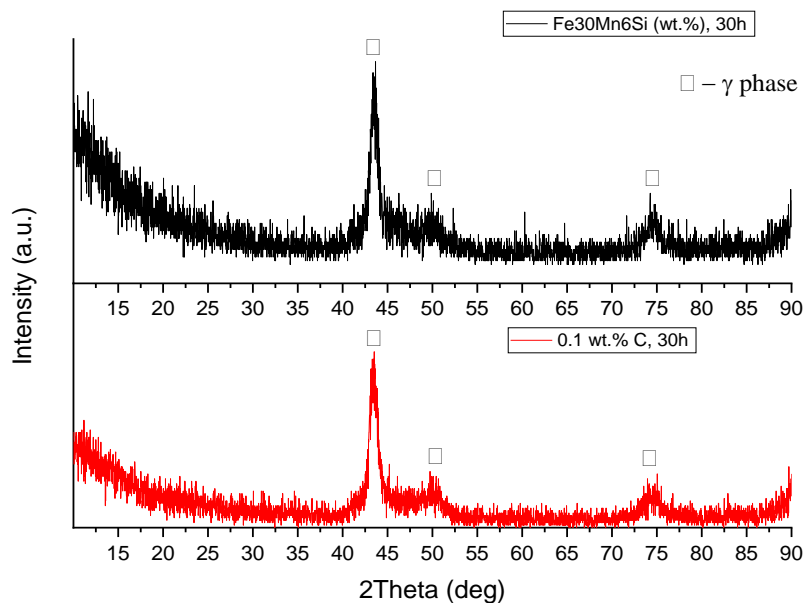


Figure 3. 5: X-Ray Diffraction patterns for “As annealed” (black line) and “0.1 wt.% C” (red line) after 30 h of mechanical alloying.

It provides also confirmation of the  $\gamma$ -phase existence without additional phases – only peaks corresponding to paramagnetic phase can be seen and there is no difference in comparison with the sample without carbon additions.

Figure 3. 6 shows XRD patterns obtained for “As annealed” and Figure 3. 7 for “Heated 600 °C” sample.

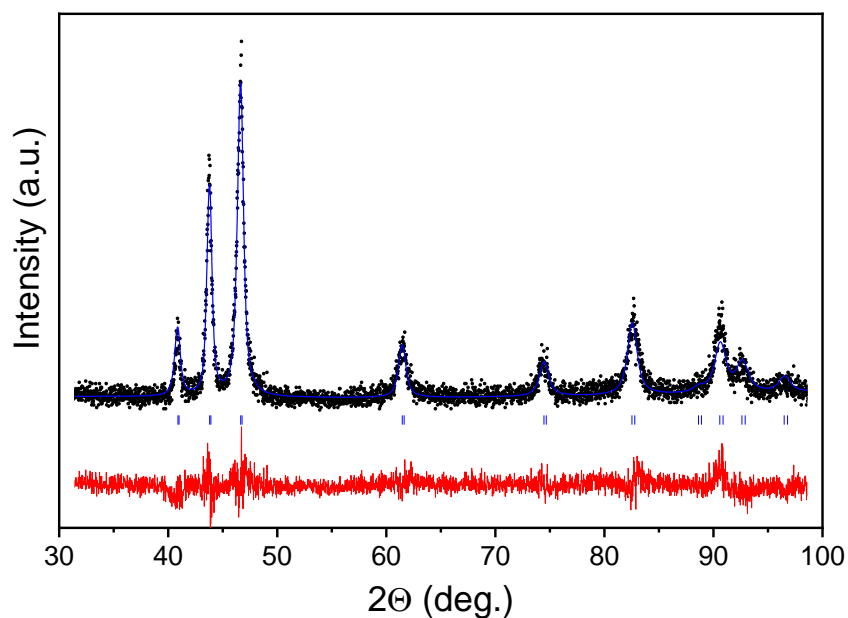


Figure 3. 6: Room temperature X-Ray Diffraction patterns for “As annealed” sample. Detected phase:  $\epsilon$ -hcp (hexagonal close-packed).

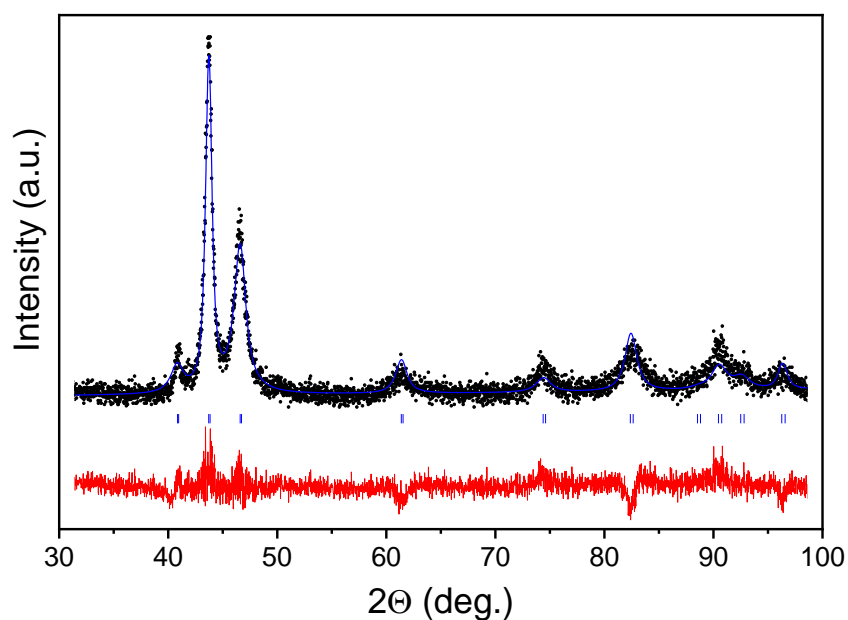


Figure 3. 7: Room temperature X-Ray Diffraction patterns for “Heated 600 °C” sample. Detected phase:  $\epsilon$ -hcp (hexagonal close-packed).

Table 3. 2: Elemental cell parameters obtained after Rietveld refinements for XRD patterns of “As annealed” and “Heated 600 °C” sample.

Sample name:	$\epsilon$ -hcp			
-	Content [%]:	a [Å]:	c [Å]:	V [Å <sup>3</sup> ]:
As annealed	100	2.5465(4)	4.1306(5)	23.197(5)
Heated 600 °C	100	2.5486(8)	4.1378(7)	23.28 (1)

Based on analysis performed, one phase can be distinguished:  $\epsilon$ -hcp (hexagonal close-packed). Elemental cell parameters obtained from Rietveld refinements are summarized in Table 3. 4. Samples differ in peaks relative intensities which may indicate presence of texture. There is no traces of  $\gamma$ -phase content in the diffractograms of the “As annealed” and “Heated 600 °C” samples.

Figure 3. 8 - Figure 3. 10 presents XRD patters with Rietveld refinements for the “0.1 wt.% C” sample at 75, 295 and 423 K.

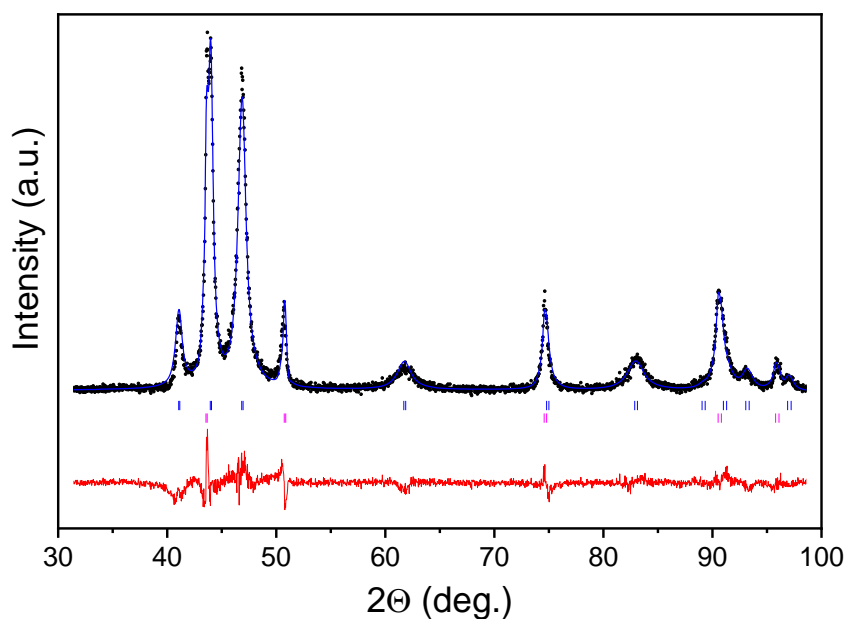


Figure 3. 8: X-Ray Diffraction patterns for “0.1 wt.% C” in 75 K (experimental data - black dots, differential pattern - red line and blue line – fitted pattern).

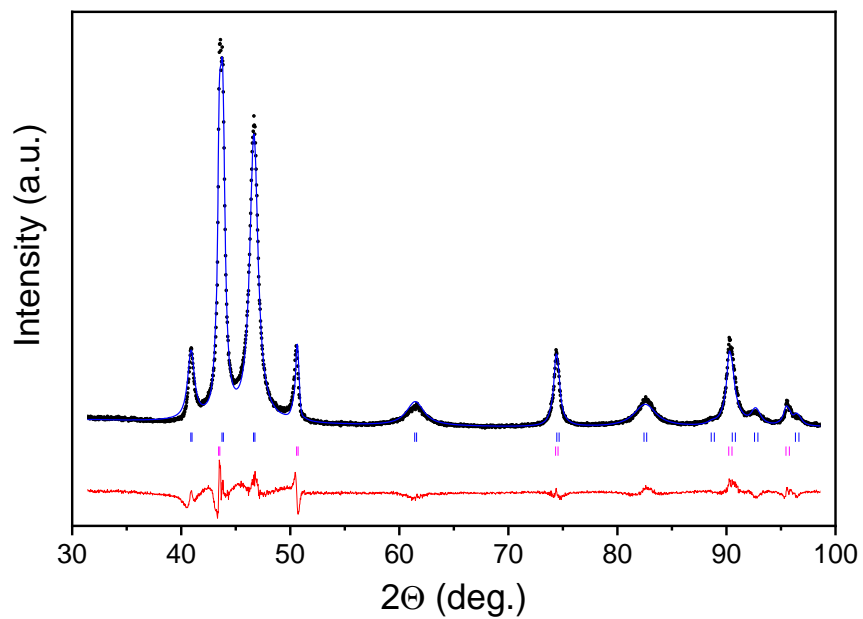


Figure 3. 9: X-Ray Diffraction patterns for “0.1 wt.% C” in 295 K (experimental data - black dots, differential pattern - red line and blue line – fitted pattern).

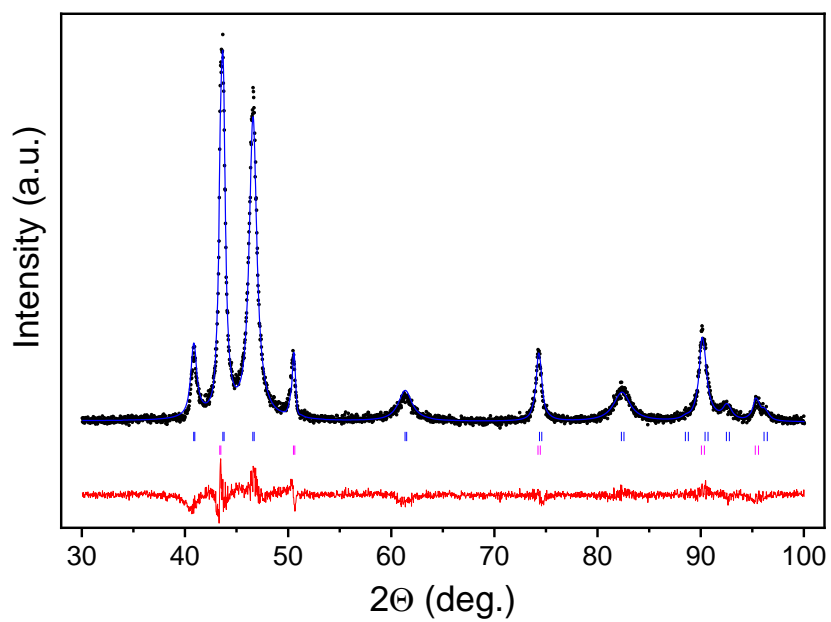


Figure 3. 10: X-Ray Diffraction patterns for “0.1 wt.% C” in 423 K (experimental data - black dots, differential pattern - red line and blue line – fitted pattern).

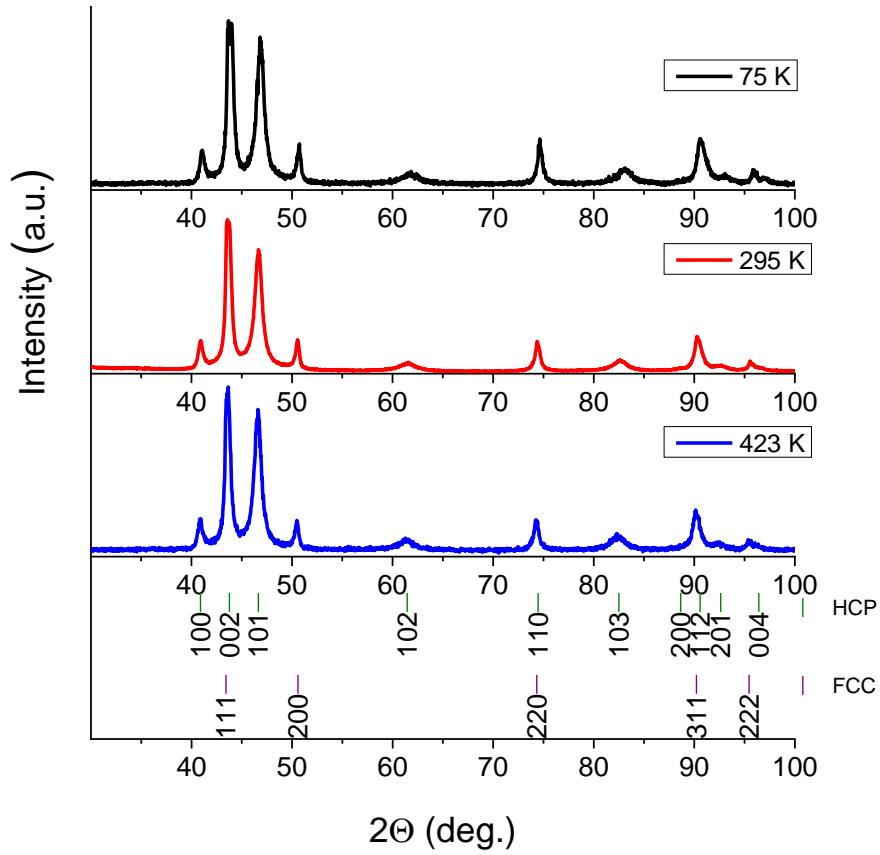


Figure 3. 11: X-Ray Diffraction patterns for “0.1 wt.% C” in 75 (black line), 295 (red line) and 423 K (blue line).

At all temperatures two phases can be distinguished:  $\epsilon$ -hcp (dominant) with some  $\gamma$ -fcc. Their content change slightly between different temperatures, and refinements parameters are summarized in Table 3. 3. Figure 3. 11 shows all the diffraction patterns collected together.

Table 3. 3: Crystallographic unit cell parameters obtained after Rietveld refinements for XRD patterns of “0.1 wt.% C” sample at 75, 295 and 423 K.

Temperature [K]:	$\epsilon$ -hcp			
	Content [%]:	a [Å]:	c [Å]:	V [Å <sup>3</sup> ]:
75	94(5)	2.5488(8)	4.142(1)	23.30(1)
295	90(7)	2.546(1)	4.133(1)	23.205(16)
423	94(6)	2.5490(9)	4.1418(14)	23.305(13)
-	$\gamma$ -fcc			
	Content [%]:	a [Å]:	V [Å <sup>3</sup> ]:	
75	5.8(7)	3.6106(5)	47.07(1)	
295	10.4(1.6)	3.6063(7)	46.900(16)	
423	6(1)	3.6109(7)	47.080(13)	

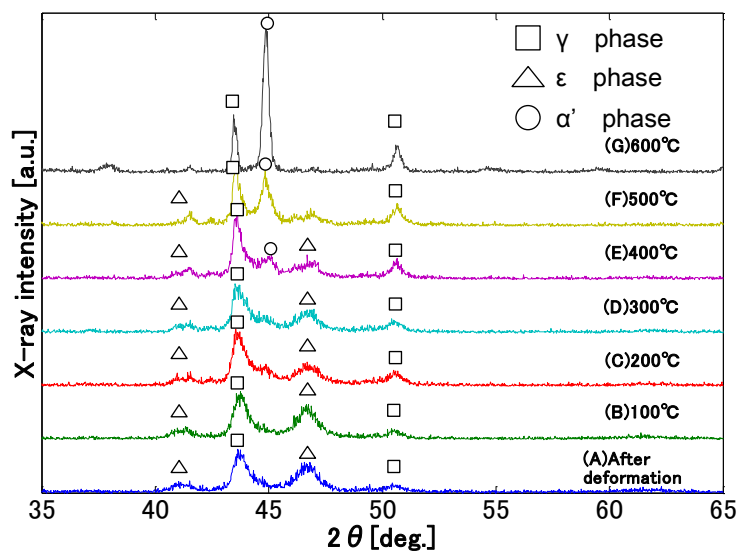


Figure 3. 11: High temperature XRD patterns for “0.1 wt.% C” alloy at several heating temperatures, Prendota et al. [163].

The crystallographic structure of the bulk alloy synthesized from the MA treated powder and subjected to the compressive strain was studied with high-temperature X-ray diffraction. The XRD patterns for “0.1 wt.% C” alloy at several heating temperatures are shown in Figure 3. 11 (A) shows the XRD pattern of the bulk alloy after 4 % deformation. All the peaks are broad and the  $\epsilon$  phase peaks are pronounced. Peaks broadening indicates an increase in lattice strain. Since the  $\epsilon$  phase peaks are relatively large, it suggests that  $\gamma \rightarrow \epsilon$  stress-induced martensitic transformation occurred due to the deformation. With increasing heating

temperature, the intensities of  $\epsilon$  phase peaks decrease and, eventually, the  $\epsilon$  phase peaks disappear when the sample is heated at 600 °C. In contrast to that, the diffraction peaks of the  $\gamma$  phase continue to increase with temperature rise and are pronounced at temperatures higher than 400 °C. Thus, with the heating, the amount of  $\epsilon$  phase is reduced and the  $\gamma$  phase increases its content, suggesting that the  $\epsilon \rightarrow \gamma$  reverse transformation occurred. So, these high temperature X-ray diffraction results indicate, that this alloy can have shape memory.

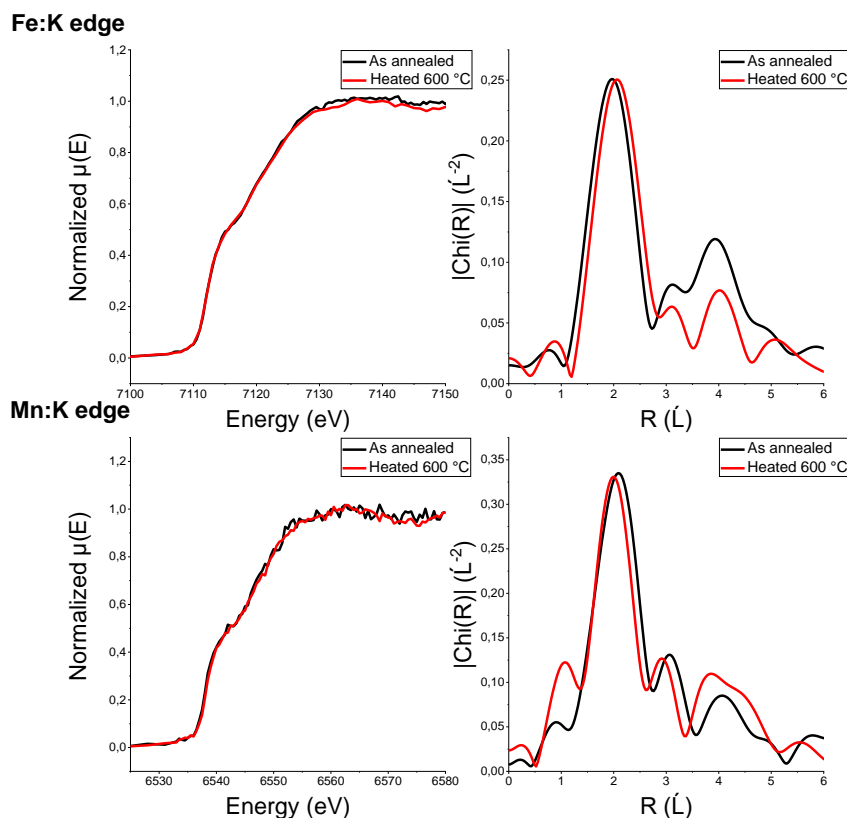


Figure 3. 12: XANES (on the left side) and EXAFS (on the right side) for iron (upper images) and manganese (lower images) K edge measurements of “As annealed” and “Heated 600 °C” samples.

XANES and XAS measurements were performed at Swiss Light Source (SLS) in Paul Scherrer Institut (PSI) in Switzerland. Results obtained are presented in the Figure 3. 12 for the samples “As annealed” and “Heated 600 °C”. The shape of the absorption edge with a characteristic shoulder indicates a metallic state of both Fe and Mn. A lack of differences between samples observed in the XANES region indicates unchanged electronic state of the elements. Fourier transforms for the Fe K-edge EXAFS part reveal peaks at 1.96 and 2.06 Å for the “As annealed” and “Heated 600 °C”, respectively. For the Mn K-edge obtained peaks are as follows: 2.09 (“As annealed”) and 1.99 Å (“Heated 600 °C”). This small change has

opposite tendencies for Fe and Mn and may indicate a slight change of the nearest neighbour shell distances: an increase for Fe and a decrease for Mn.

Magnetic properties characterization involved Mössbauer Spectroscopy (MS) and Vibrating Sample Magnetometry (VSM). MS samples preparation process is shown in Chapter 2, and results of measurements are presented in Figure 3. 13 - Figure 3. 17 and Table 3. 4.

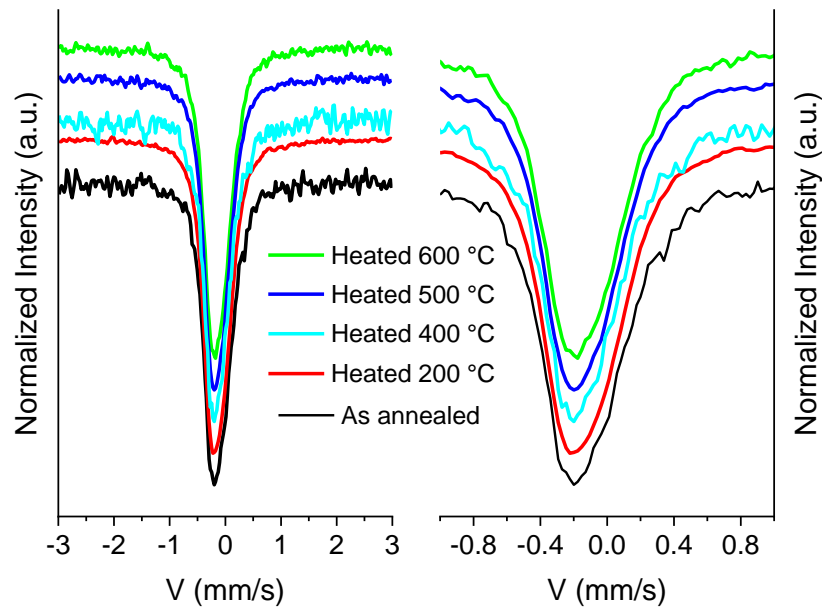


Figure 3. 13: Mössbauer spectra for all samples obtained at room temperature.

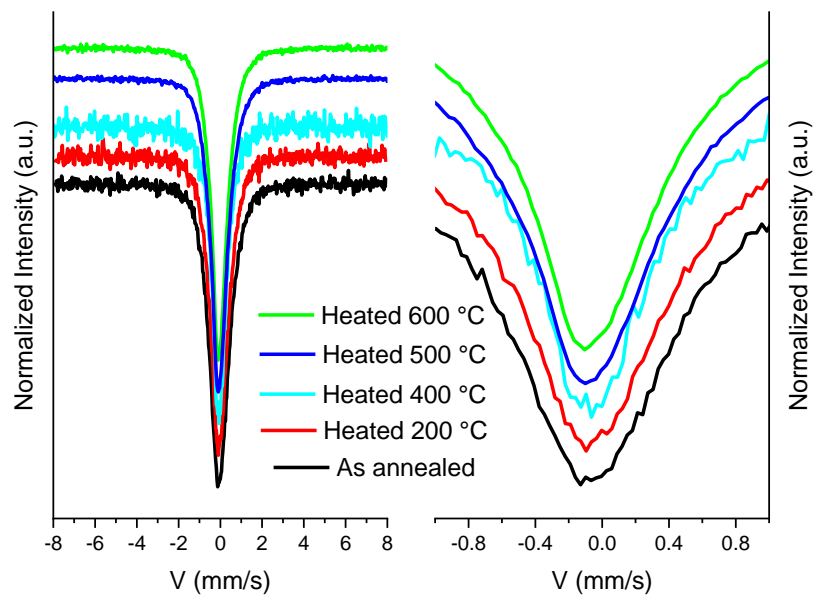


Figure 3. 14: Mössbauer spectra for all samples obtained at low temperature. The right panel shows a zoom of the spectra at low velocity range.

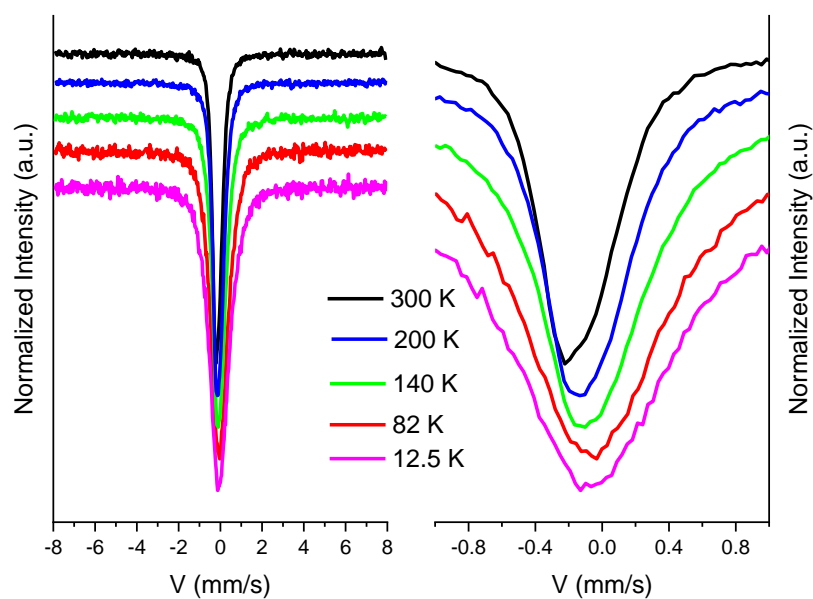


Figure 3. 15: Mössbauer spectra for sample “As annealed” obtained in different temperatures. The right panel shows a zoom of the spectra at low velocity range.

Table 3. 4: Summarized Isomer Shifts and FWHM values for all samples in low and room temperature. At the lower part temperature dependence FWHM of “As annealed” sample.

Sample name:	As annealed		Heated 200 °C		Heated 400 °C		Heated 500 °C		Heated 600 °C	
Temperature [K]:	12.5	300	7.401	300	4.2	300	4.2	300	4.2	300
Isomer Shift Powder [mm/s]:	-0.08	-0.08	-0.07	-0.07	-0.03	-0.08	-0.09	-0.12	-0.09	-0.11
FWHM Powder [mm/s]:	1.05	0.56	1.02	0.79	0.79	0.52	0.91	0.52	0.88	0.71
FWHM Bulk [mm/s]:	-	0.48	-	0.43	-	0.49	-	0.49	-	
Temperature [K]:	12.5		82		140		200		300	
FWHM Powder [mm/s]:	1.05		0.98		0.71		0.59		0.56	

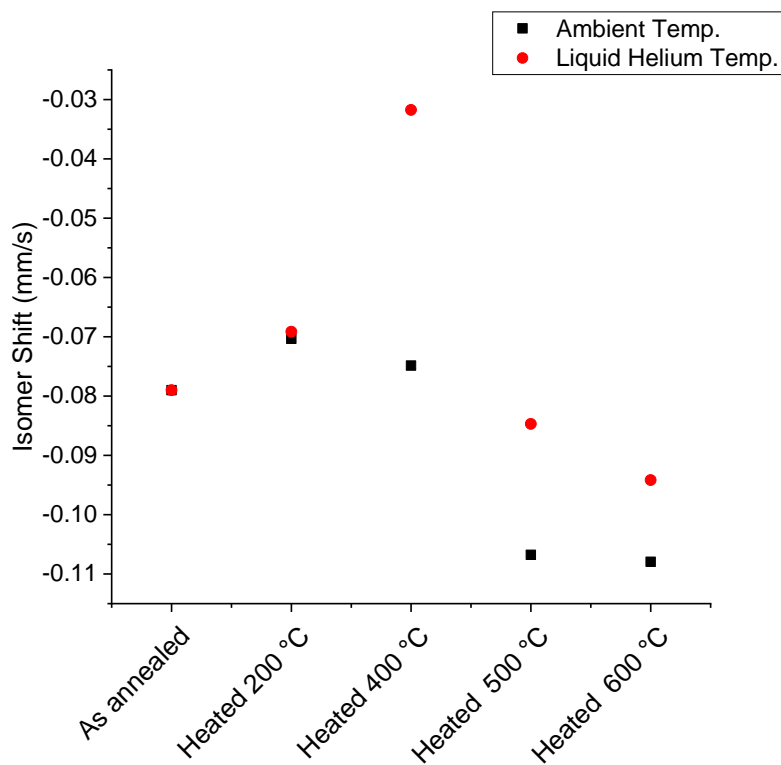


Figure 3. 16: Isomer shift for all samples at ambient (black squares) and liquid helium temperature (red dots).

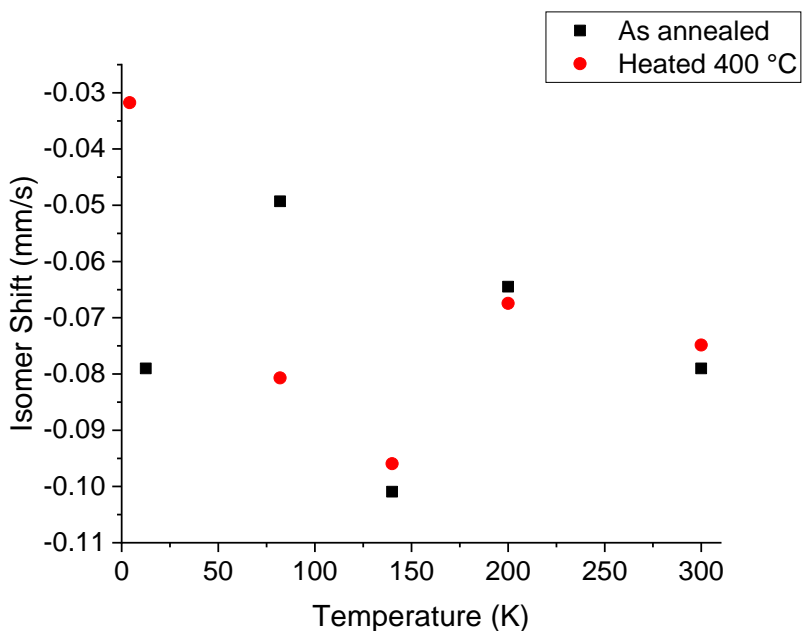


Figure 3. 17: Isomer Shift for “As annealed” and “Heated 600 °C”.

There can be seen only one, slightly broadened line of the  $^{57}\text{Fe}$  spectrum in the whole temperature region for all the samples. It shows a small asymmetry from positive velocity side, so that two component were used for spectrum fitting. Slight line broadening at low

temperatures is observed. The small linewidth with no magnetic splitting visible indicates that Fe bears no magnetic moment in the materials studied. The values of Isomer Shift (IS) summarized in Table 3. 4 are similar for the samples at helium and room temperatures and are also similar to the value obtained in previous work [4]. Only slight variations in mean values of isomer shift (IS) and full width at half maximum (FWHM) indicate a lack of significant differences of electronic and magnetic states between all samples at the low and the room temperature.

A comparison of magnetic properties between the pure (“As annealed”) and with small carbon addition (“0.1 wt.% C”) samples have been also performed. Results obtained from Mössbauer Spectroscopy at room temperature (RT) and 80 K for powdered samples are shown in Figure 3. 18.

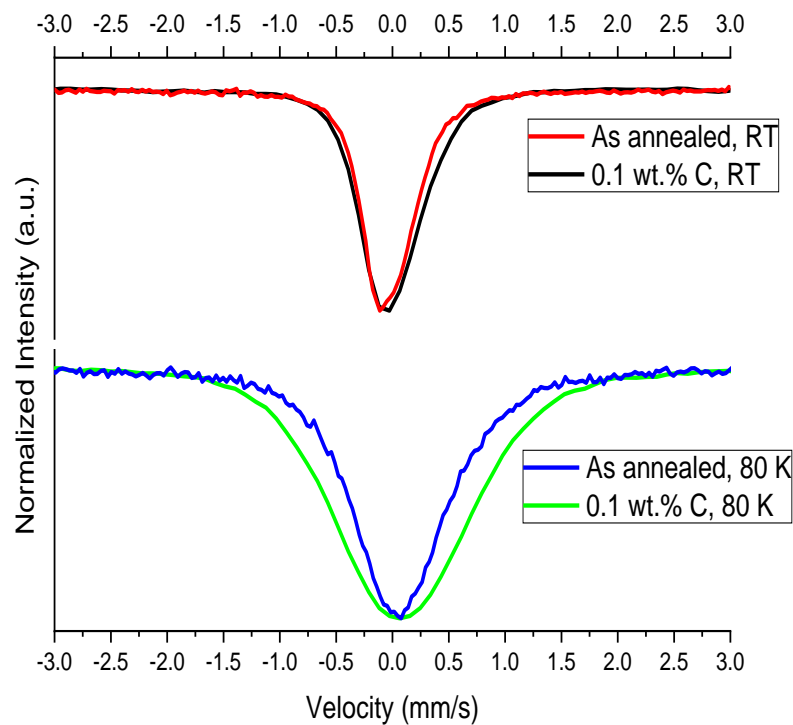


Figure 3. 18: Mössbauer spectra: a) room temperature and b) 80K for “As annealed” and “0.1 wt.% C” alloys.

A single peak is observed for all the spectra. Differences of isomer shift (listed in Table 3. 5) observed at both temperatures indicate, that carbon enters the bulk of the alloy.

Table 3. 5: Isomer shift values at room temperature and 80K.

Sample name:	Isomer shift at room temperature [mm/s]:	Isomer shift at 80 K [mm/s]:
As annealed	-0.06	-0.05
0.1 wt.% C	-0.23	-0.07

This is also consistent with a larger line width observed for the carbon containing sample. For both samples a significant broadening of the spectrum (by more than two times) on lowering the temperature from 293 K to 80 K is observed. It can be attributed to the appearance of a small magnetic field at the Fe site at the lowest temperatures. A much larger linewidth for “0.1 wt.% C” sample is attributed to the effect of carbon entering the bulk of the alloy. The presence of the  $\gamma$ -fcc phase in the material with carbon addition can be attributed to its support to austenite formation.

In the Figure 3. 19 Conversion Electron Mössbauer Spectroscopy results at room temperature for bulk samples are presented.

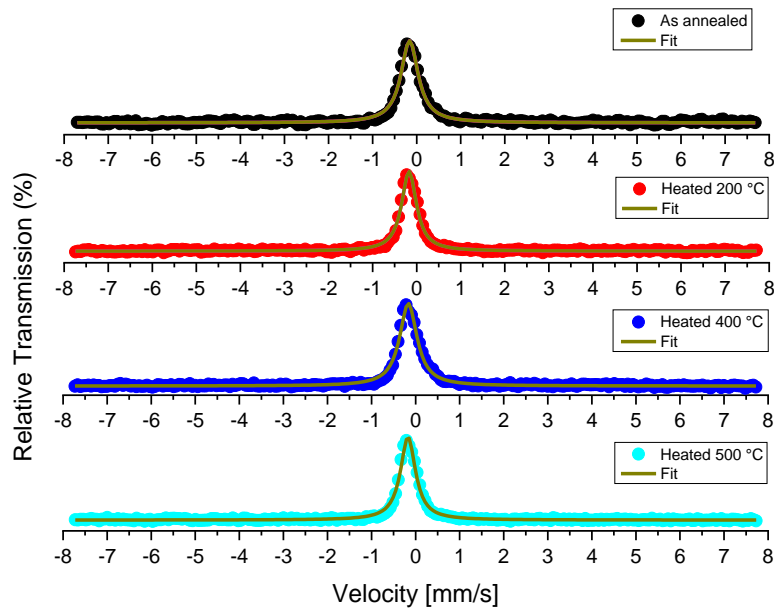


Figure 3. 19: CEMS spectra for “As annealed” (black dots), “Heated 200 °C” (red dots), “Heated 400 °C” (blue dots) and “Heated 500 °C” (cyan dots) sample (dark yellow line –fit).

We can observe the spectra, which can be fitted simply by one line for each sample. They reveal a lack of magnetic moment on Fe at room temperature in all of the heated samples. Isomer Shift values are presented in the Table 3. 4. It can be seen that they slightly change with increasing heating temperature to more negative values. A much larger line width for powdered samples

than for bulk ones can be attributed to defects and strain introduced with preparation of powders done by filing.

Further materials characterization involved magnetometric method. For the “As annealed” sample hysteresis loops at all the temperatures can be observed - see Figure 3. 20 - Figure 3. 22. Figure 3. 21 presents its virgin magnetization curves. For the other heated samples magnetic behaviour looks very similar. A small contribution of ferromagnetic (or ferromagnetic) phase is detected in the samples. Almost linear dependence between magnetic moment and field with the slope increasing with decreasing temperature can also be seen. Thus a dominant antiferromagnetic or paramagnetic behavior can be concluded. Hysteresis loops combining with linear component can be observed at all temperatures. A very small value of saturation magnetization, calculated after linear contribution removal, are summarized in Table 3. 6.

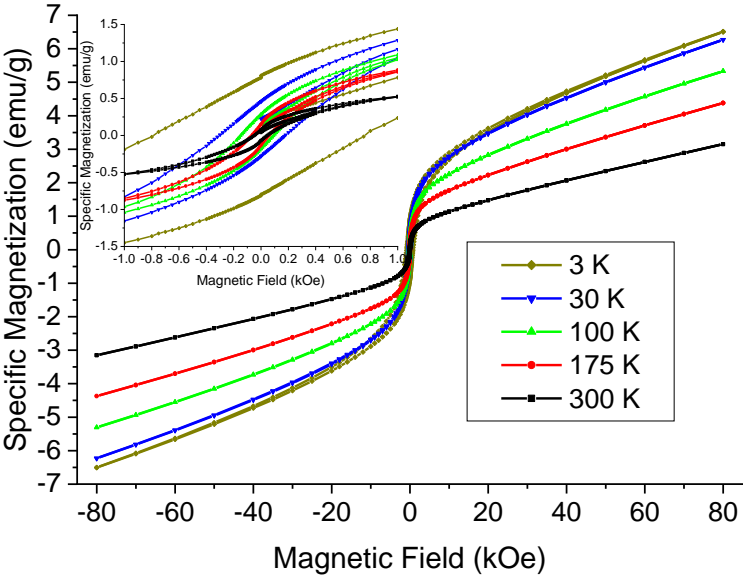


Figure 3. 20: Hysteresis loops for the “As annealed” sample at all the temperatures.

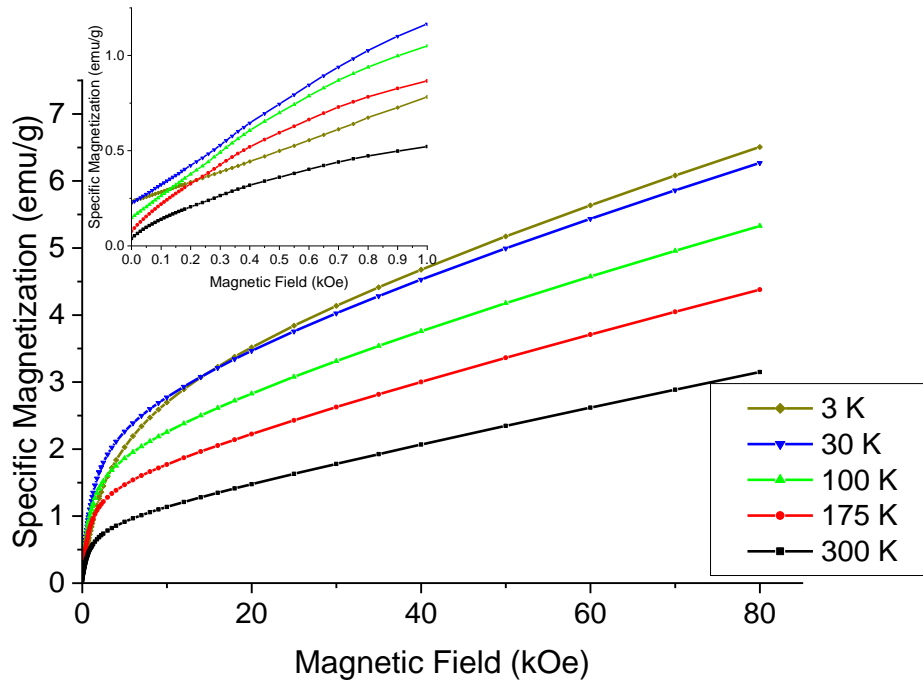


Figure 3. 21: Virgin magnetization curves for the “As annealed” sample at all the temperatures.

The curves show a positive curvature at the origin indicating the nucleation of reverse domains mechanism in the magnetization process. At high temperatures this curvature is much more pronounced than at low temperatures.

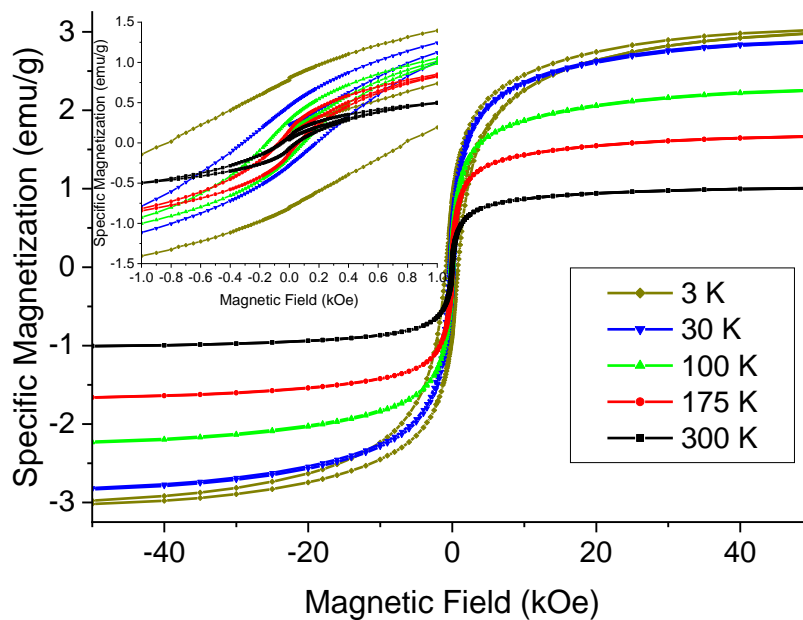


Figure 3. 22: Hysteresis loops for “As annealed” sample at all the temperatures without paramagnetic contribution.

Table 3. 6: Mean values of saturation magnetization at 80 kOe.

Sample No.:	Mean Saturation magnetization at 3K [emu/g]:	Mean Saturation magnetization at 30K [emu/g]:	Mean Saturation magnetization at 100K [emu/g]:	Mean Saturation magnetization at 175K [emu/g]:	Mean Saturation magnetization at 300K [emu/g]:
As annealed	3.00	2.85	2.24	1.66	1
Heated 200°C	1.50	1.34	1.21	0.98	0.74
Heated 500°C	1.84	1.66	1.28	-	0.98
Heated 600°C	3.31	3.13	2.61	2.16	1.74

Remnant magnetization values for “0.1 wt.% C” sample were also derived from hysteresis loops presented in Figure 3. 23, Figure 3. 24, and summarized in Table 3. 7. Intersection with positive and negative axis are included and marked with + and -, respectively. Their average, termed as “mean” is also included.

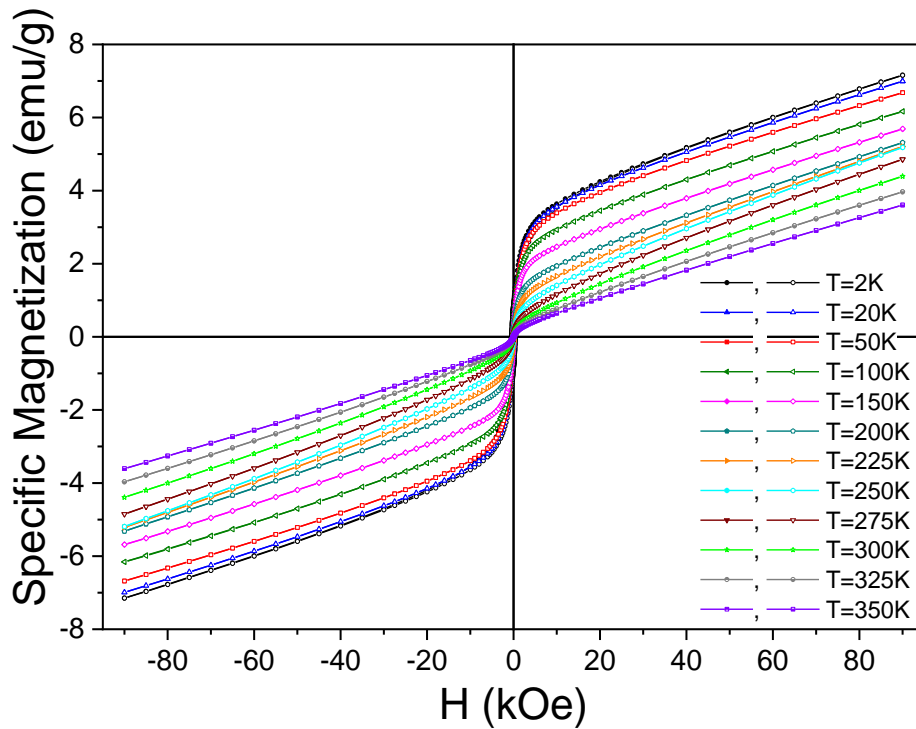


Figure 3. 23: Hysteresis loops for “0.1 wt.% C” sample at all the temperatures.

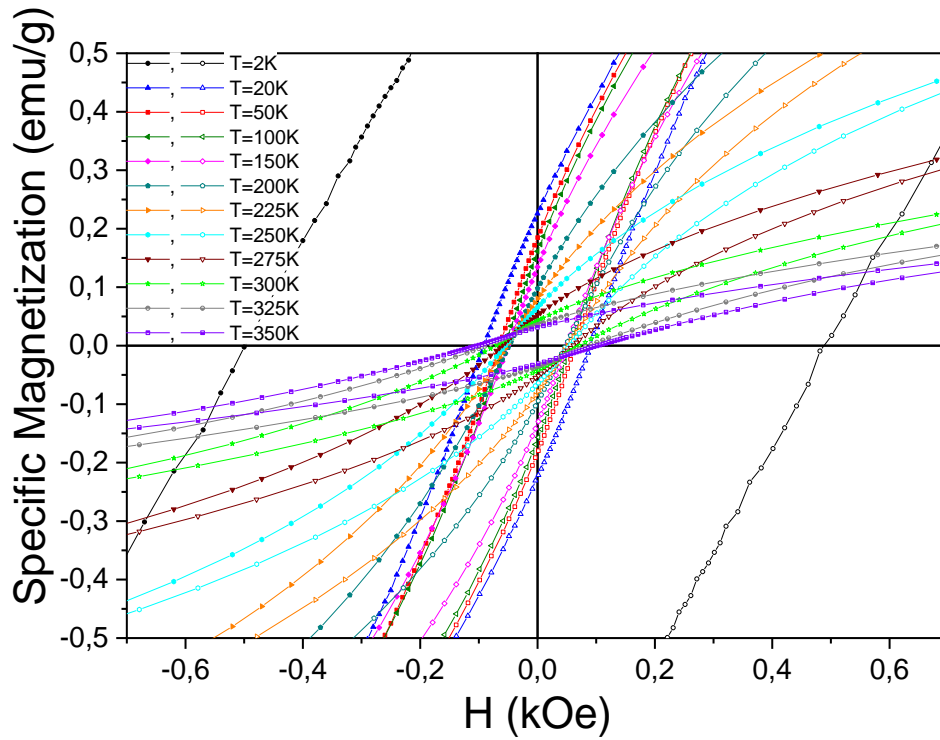


Figure 3. 24: Hysteresis loops for "0.1 wt.% C" sample at all the temperatures - zoomed.

Table 3. 7: Values of remnant- remnant+ and mean remnant magnetization for "0.1 wt.% C" sample.

Temperature [K]:	Remnant Magnetization - [emu/g]:	Remnant Magnetization + [emu/g]:	Mean Remnant Magnetization [emu/g]:
3	0.85	0.85	0.85
20	0.23	0.23	0.23
50	0.20	0.20	0.20
100	0.16	0.16	0.16
150	0.13	0.13	0.13
200	0.097	0.099	0.098
225	0.08	0.08	0.08
250	0.065	0.066	0.0655
275	0.052	0.53	0.291
300	0.043	0.043	0.043
325	0.036	0.036	0.036
350	0.031	0.031	0.031

Linear slope values obtained from magnetization curves for all the samples are shown in Figure 3. 25.

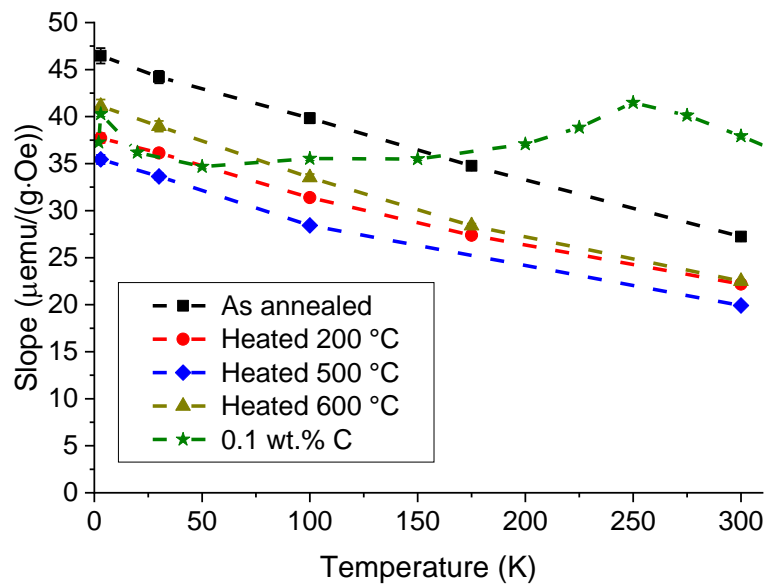


Figure 3. 25: Temperature dependence of slope values for paramagnetic contributions (linear part). Dashed lines are guides for eyes.

The slope, i.e. the values of the magnetic susceptibility increase with decreasing temperature for all the samples except for the carbon doped one, where a peak is observed at 250 K, indicating a magnetic transition there. The part of the magnetic susceptibility increasing with decreasing temperature, according to Gavriljuk et al. [22], can be attributed to localized Mn moments corresponding to the magnetically isolated atoms. Thus, carbon doping decreases the number of such atoms and the Pauli-like temperature independent susceptibility of conduction electrons dominates.

Figure 3. 26 - Figure 3. 30 present temperature dependence of coercivity values for each sample.

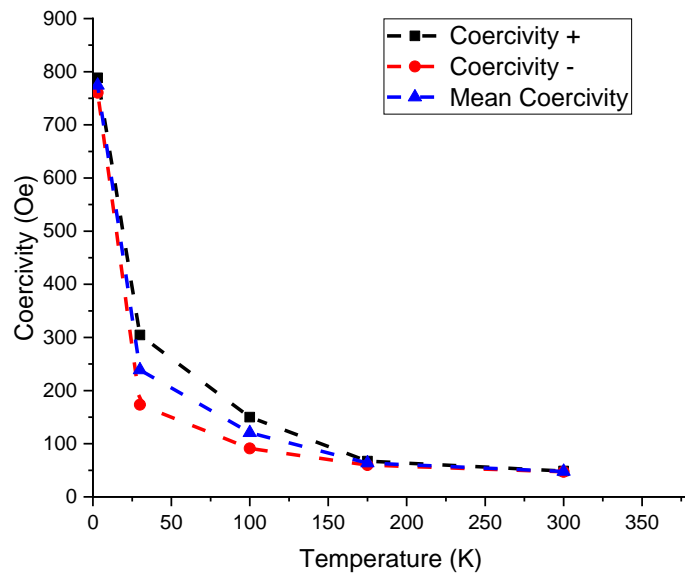


Figure 3. 26: Coercivity values for "As annealed" sample.

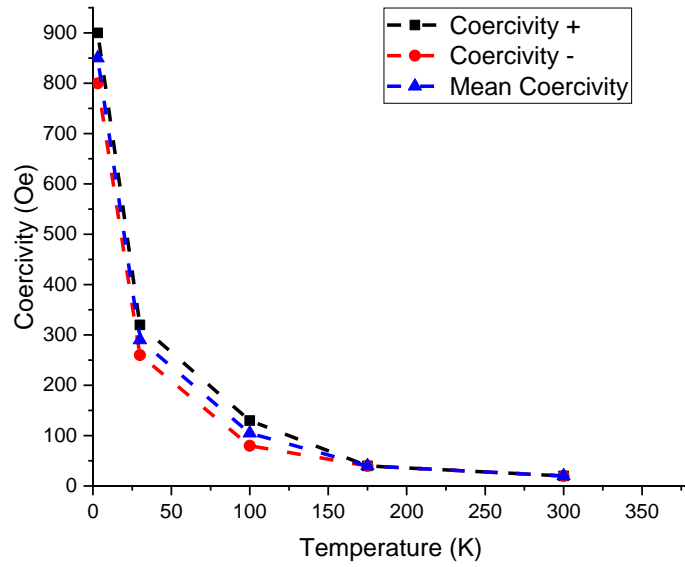


Figure 3. 27: Coercivity values for "Heated 200 °C" sample.

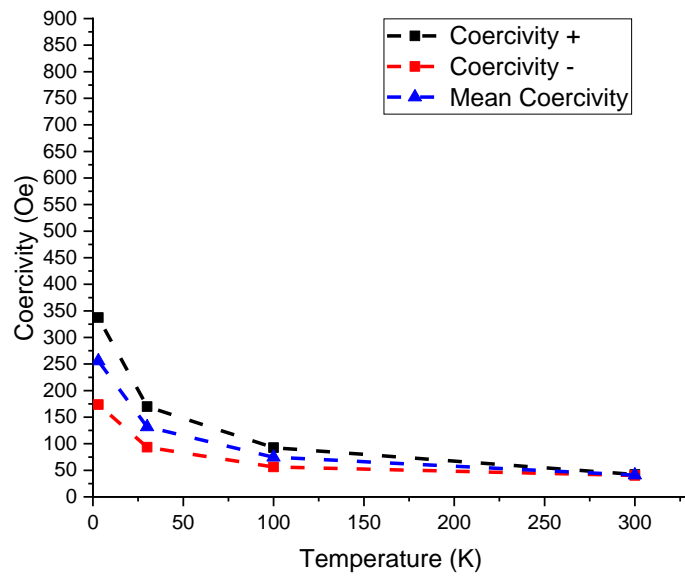


Figure 3. 28: Coercivity values for "Heated 500 °C" sample.

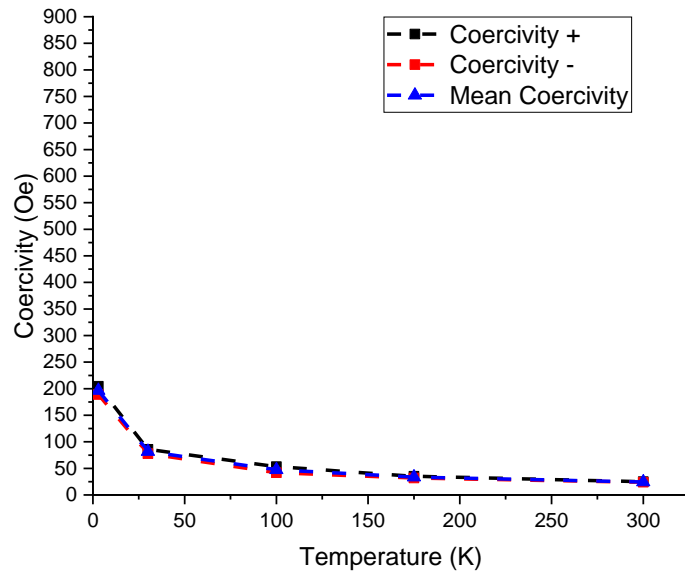


Figure 3. 29: Coercivity values for "Heated 600 °C" sample.

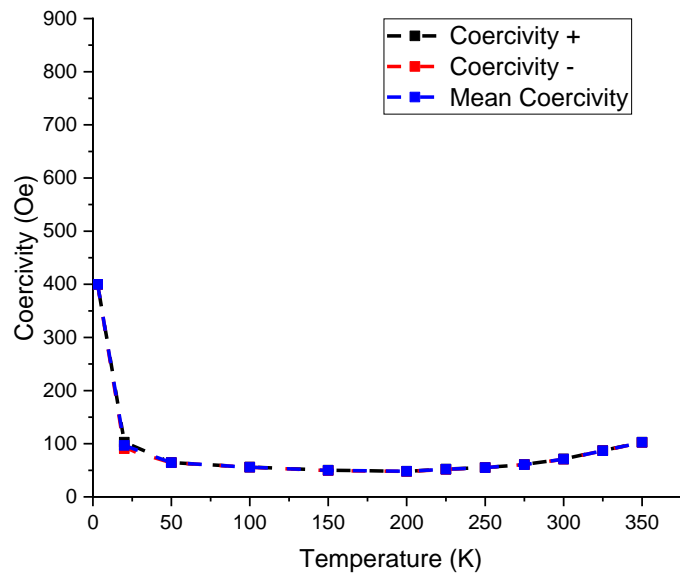


Figure 3. 30: Coercivity values for “0.1 wt.% C” sample.

They show coercivity values obtained from both sides of hysteresis loop as well as their mean value. Their values are asymmetrical for heated samples, except for the 600 °C heated and the “0.1 wt.% C” samples, where they are symmetrical. The asymmetry reveals the presence of the exchange bias effect, which can be attributed to a coupling of this ferro- or ferrimagnetic phase to an antiferromagnetic one. As such the phenomenon is effective at the length scale of nanometers, the regions exhibiting asymmetric hysteresis are of nanometric size. They can be attributed to the austenitic phase precipitations in the antiferromagnetic-like martensite matrix. Mean absolute value of coercivity at low temperature decreases with increase of thermal processing temperature and it shows two times lower values for the “0.1 wt.% C” sample than for the “As annealed” one. The highest asymmetry of the hysteresis loops, i.e. the strongest exchange bias effect is observed at the temperature range of 20 – 175 K. An upturn in the coercivity values at high temperatures for the “0.1 wt.% C” sample is worth noting.

Saturation magnetization values show that the highest temperature differences between low and room temperature, of four times occurs for “0.1 wt.% C” sample. For the “As annealed” sample this change is only two times. Thus it can be concluded that even low temperature treatment has influence on magnetic properties of the samples, which is related to martensitic reverse transformation.

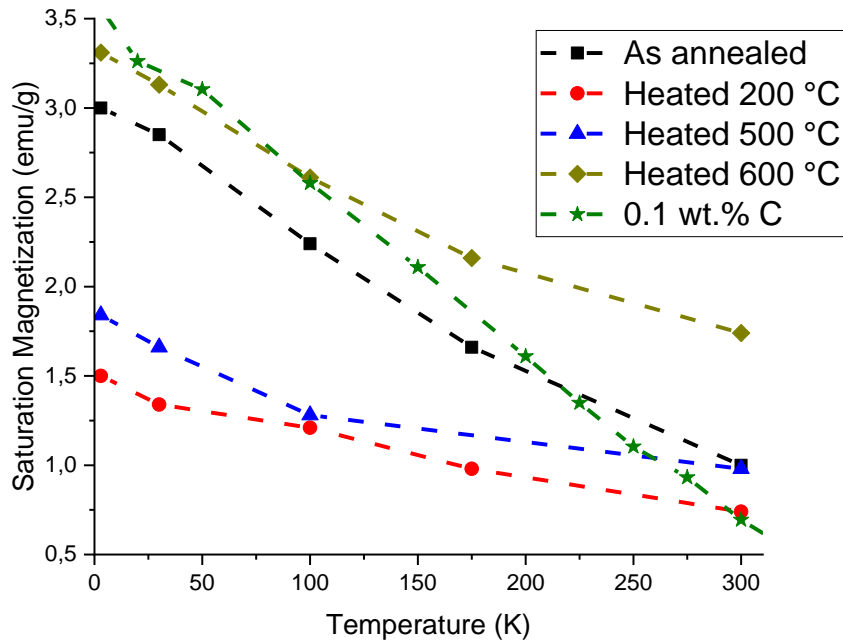


Figure 3.31: Saturation Magnetization corresponding to the field of 80 kOe after subtraction of paramagnetic (linear) contribution from magnetization curves at various temperatures.

For the “0.1 wt.% C” sample the zero field cooled (ZFC) and the field cooled (FC) temperature dependences of the magnetic susceptibility were measured, Figure 3.32.

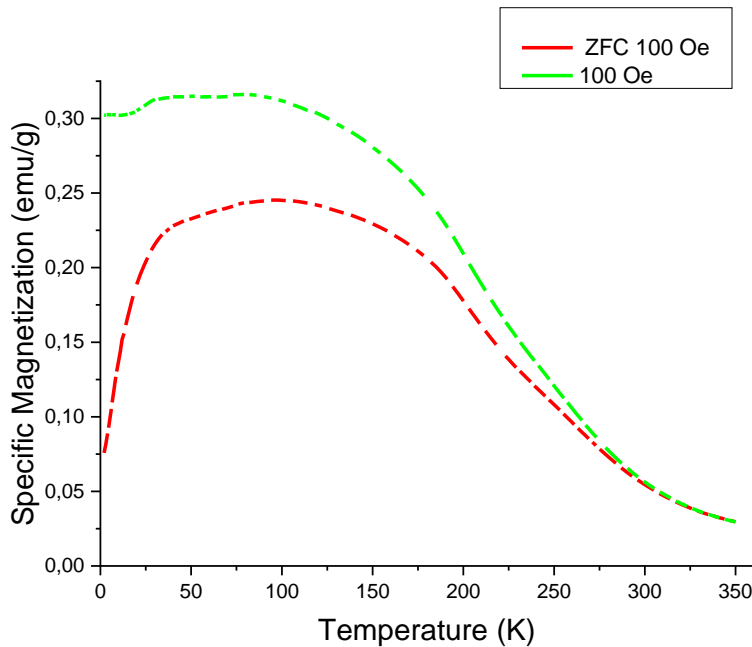


Figure 3.32: ZFC and 100 Oe FC of “0.1 wt.% C”.

The FC and ZFC curves depart at about 300 K, which indicates an onset of the magnetic phase, possibly of a spin-glass character there. Magnetic susceptibility was also measured for

other samples and at higher fields. Dependences of inverse susceptibility are presented in Figure 3. 33 - Figure 3. 36 for different values of the applied magnetic field: 100 Oe, 10 kOe and 80 kOe (for “0.1 wt.% C”: 50, 70 and 90 kOe), respectively.

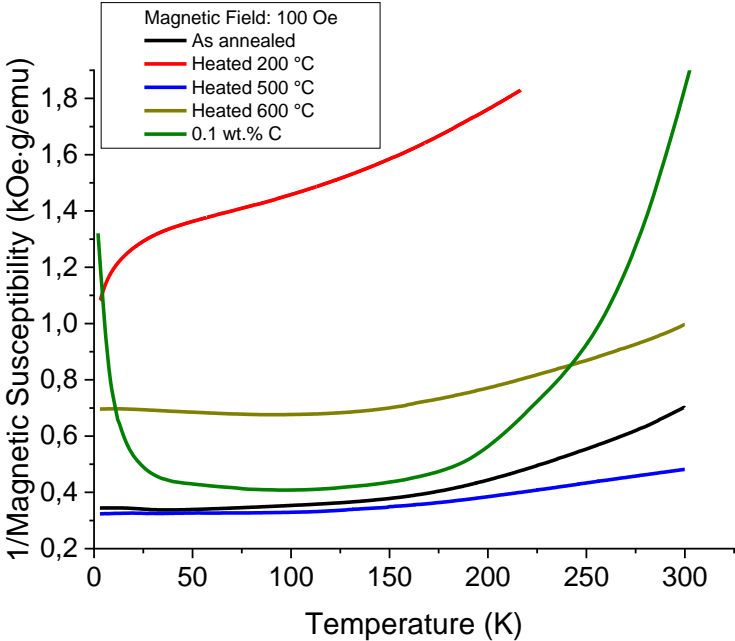


Figure 3. 33: Inverse magnetic susceptibility versus temperature of all samples in the magnetic field of 100 Oe.

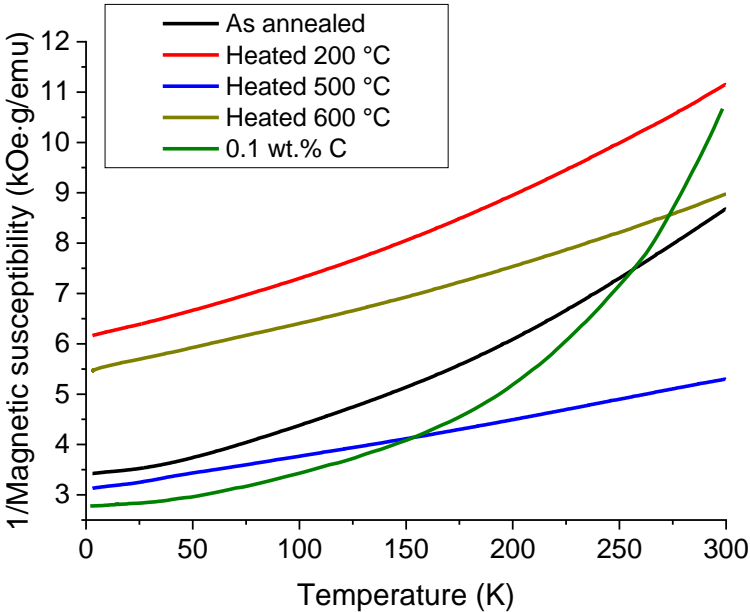


Figure 3. 34: Inverse magnetic susceptibility versus temperature of all samples in the magnetic field of 10 kOe.

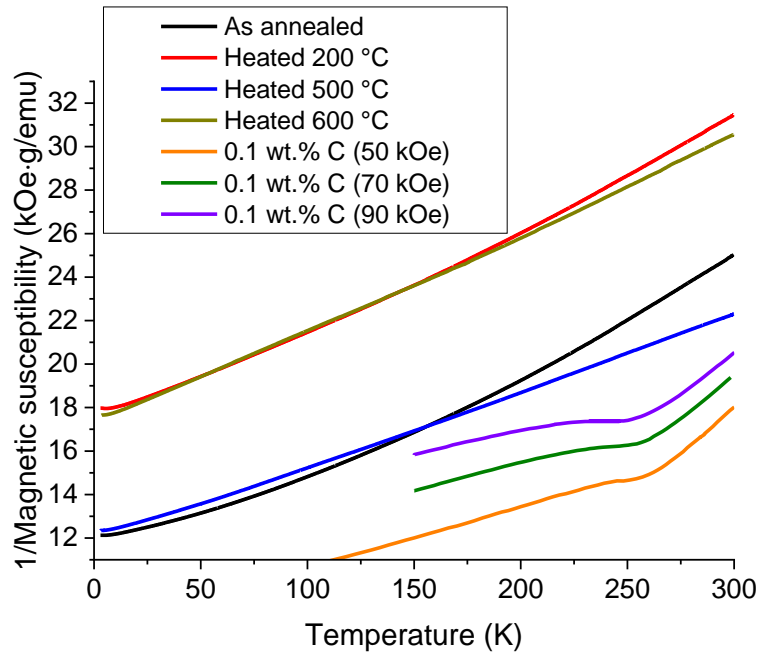


Figure 3. 35: Inverse magnetic susceptibility versus temperature of all samples in the magnetic field of 80 kOe (besides 0.1 wt.% C).

Linear dependence of the inverse susceptibility shows up at higher fields, decreasing with temperature (see Figure 3. 35). The most linear dependences are obtain for samples “Heated 200 °C” and “Heated 600 °C”. Carbon doped material exhibit different magnetic susceptibility dependence in comparison with other samples, with linear dependence of inversed susceptibility at higher temperatures starting from about 325 K. At lower temperatures a dip appears at about 250 K, indicating a magnetic transition. Based on room temperature XRD (see Figure 3. 6 and Figure 3. 7) in “Heated 600 °C” and “as annealed” samples,  $\epsilon$  phase is detected – at higher fields its inverse magnetic susceptibility is almost linear.

The inverse susceptibility curves obtained for various applied magnetic field values for the “0.1 wt.% C” sample are presented in Figure 3. 36.

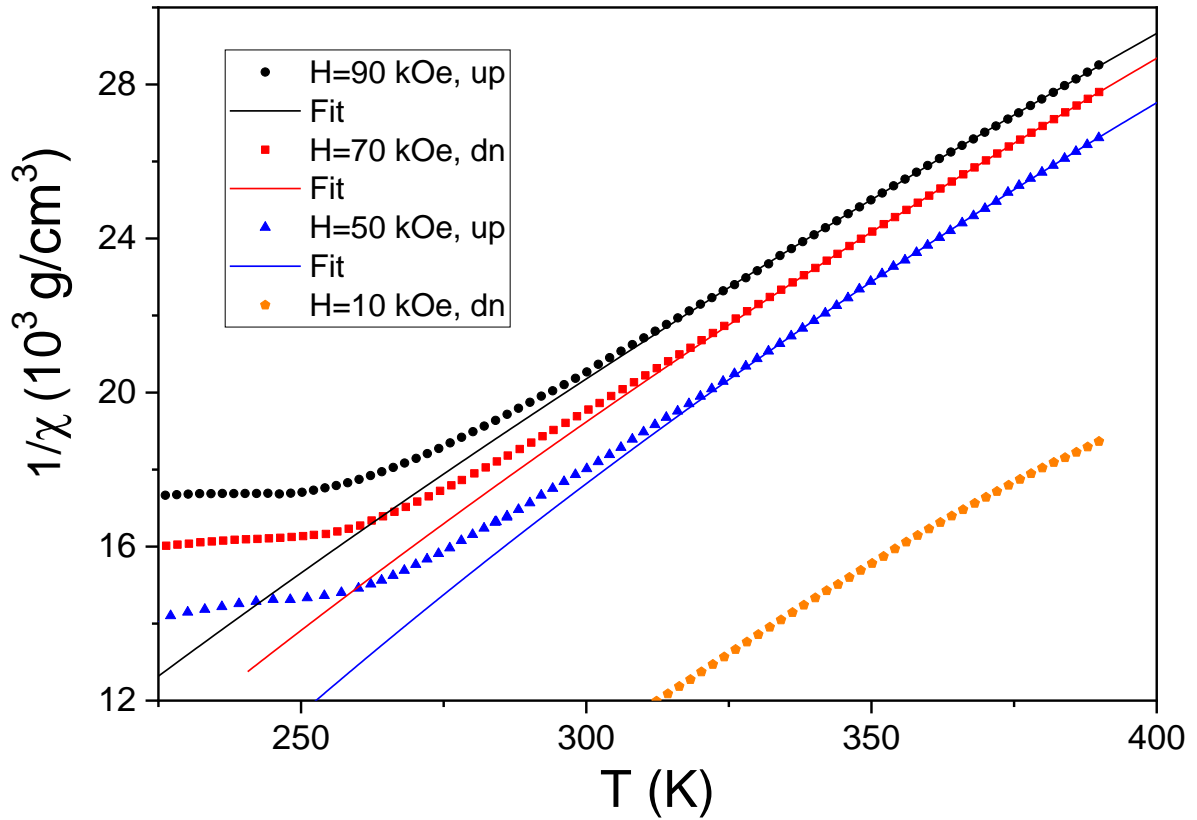


Figure 3. 36: Inverse mass magnetic susceptibility versus temperature of the “0.1 wt.% C” sample at 10, 50, 70 and 90 kOe.

Their linear character reveals presence of a Curie-Weiss type paramagnetic contribution.

Table 3. 8: Summarized fitted parameters to the inversed mass magnetic susceptibility of “0.1 wt.% C” sample at different magnetic field values.

<b>H [kOe]:</b>	<b><math>\theta_{CW}</math> [K]:</b>	<b><math>\chi_0</math> [<math>\cdot 10^{-6} \text{cm}^3/\text{g}</math>]:</b>	<b><math>C</math> [<math>\cdot 10^{-3} \text{cm}^3\text{K}/\text{g}</math>]:</b>	<b><math>\mu_{\text{eff}}</math> [<math>\mu_B/\text{Mn}</math>]:</b>
50	169(5)	9.6(8)	6.2(3)	3.01(8)
70	141(1)	7.7(1)	7.04(5)	3.21(1)
90	120(4)	7.0(5)	7.60(24)	3.34(5)

Based on the equation (3.1) and experimental data presented in Figure 3. 36, Curie-Weiss function were fitted, and obtained parameters are summarized in Table 3. 8 for sample mass: 20.890 mg and molar mass: 52.34 g.

$$\chi_{\sigma} = \chi_0 + C/(T-\theta_{CW}) \quad (3.1)$$

where:  $\chi_{\sigma}$  - volume magnetic susceptibility,  $\chi_0$  – its temperature independent contribution,  $C$  - material-specific Curie constant,  $T$  – temperature and  $\theta_{CW}$  – Weiss constant.

The volume magnetic susceptibility and the corresponding fitted values of the Weiss and Curie constants and the effective magnetic moment vary with the value of the external magnetic field used. This is possibly due to antiferromagnetic correlations, which are gradually suppressed by the increasing applied magnetic field. The value of the paramagnetic moment derived corresponds to about  $3 \mu_B$  per Mn atom, if no magnetic moment of Fe is realized.

In the Figure 3. 37 - Figure 3. 39 heat capacity temperature dependences are presented for the same “0.1 wt.% C” sample ( $m=20.890$  mg,  $M_{\text{mol}}=52.34$  g).

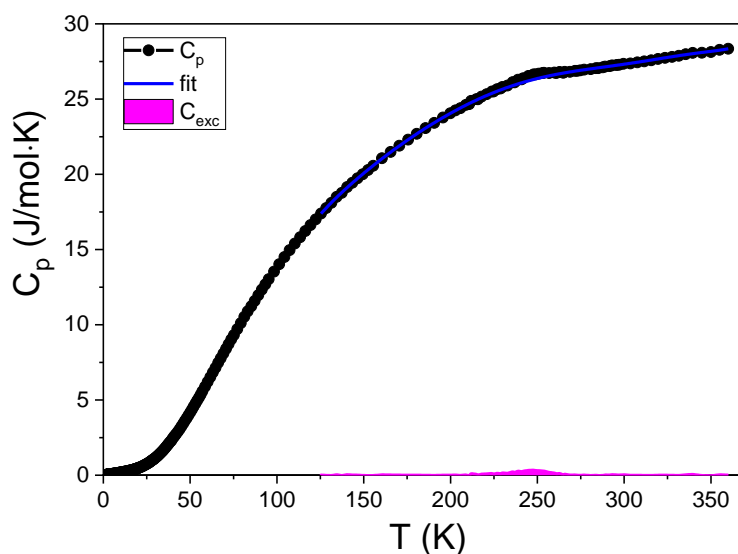


Figure 3. 37: Heat capacity temperature dependence with polynomial fit (blue line) and magnetic heat capacity (pink area).

A typical temperature dependence is observed with an extra peak at about 250 K, where the anomaly in the magnetic susceptibility was found. To check the low temperature behavior the  $C_p/T$  dependence vs.  $T^2$  was plotted.

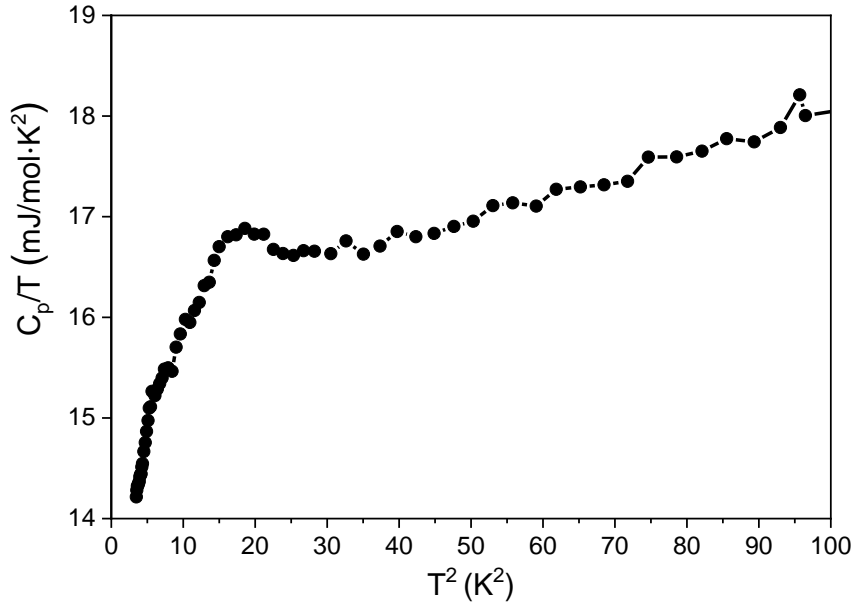


Figure 3.38: Specific heat versus squared temperature dependence for “0.1 wt.% C” sample in the low temperature range.

This dependence shows a deviation from linearity expected for a metal, indicating presence of a considerable nonlinear contribution, possibly of a magnetic origin. The measurements at high temperatures have been carried out also at the applied magnetic field up to 90 kOe and the results are shown below.

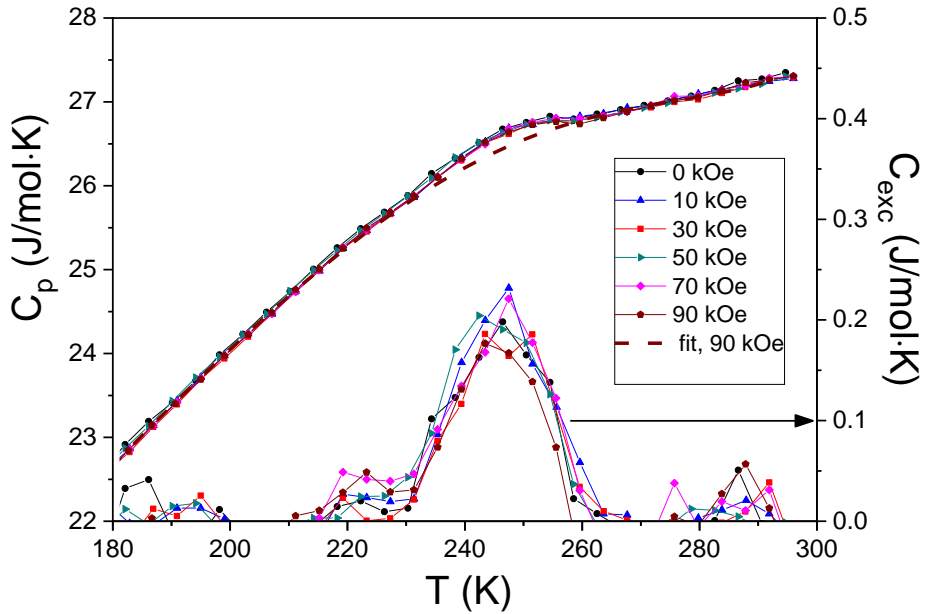


Figure 3.39: Heat capacity temperature dependence measured in different magnetic fields for “0.1 wt.% C” sample.

The excess peak has been subtracted from the data by polynomial fitting. The magnitude of the peak slightly decreases with increasing field and shifts to lower temperatures, indicating antiferromagnetic character of the transition.

Figure 3. 37 presents heat capacity temperature dependence at zero field with polynomial fit and the excess heat capacity of magnetic origin. The curve at zero field was integrated at the temperature range of: 200 – 275 K (see equation 3.2) and the results obtained are presented in the Figure 3. 40.

$$S_{exc} = \int_{T_1}^T \frac{C_{exc}}{T} dT \quad (3.2)$$

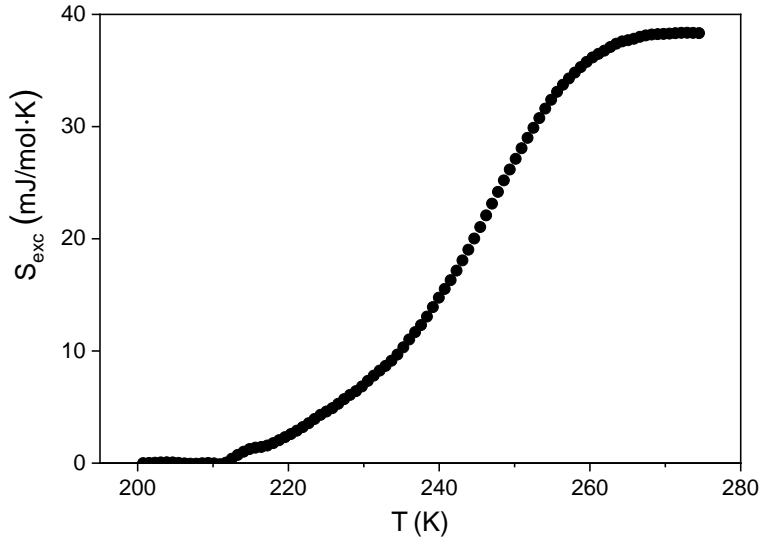


Figure 3. 40: Magnetic entropy temperature dependence measured for “0.1 wt.% C” sample.

Accounting for magnetic origin of the peak in specific heat and the corresponding entropy we can put  $S_{exc} = S_{mag}$  and the calculation procedure allows now for total magnetic moment determination. General expression for magnetic entropy is shown with equation 3.3. Its further transformation is presented in equation 3.4.

$$S_{mag} = R \ln(2J + 1) \quad (3.3)$$

where: J is total magnetic moment, R is ( $R = 8.3144621(75) \frac{J}{mol \cdot K}$ )  $S_{mag} = 0.03833 \frac{J}{mol \cdot K}$

$$J_{Mn} = \left(\frac{1}{2}\right) \left[ \exp\left(\frac{S_{mag}}{0.286R}\right) - 1 \right] = 0.008125 \quad (3.4)$$

where:  $S_{exc}$  is magnetic entropy and R is a gas constant ( $R = 8.3144621(75) \frac{J}{mol \cdot K}$ ).

This allowed for total magnetic moment determination at approximately  $0.016 \mu_B$ .

Temperature dependences of the electrical resistivity for the “As annealed”, “Heated 600 °C” and “0.1 wt.% C” samples are collected in Figure 3. 41.

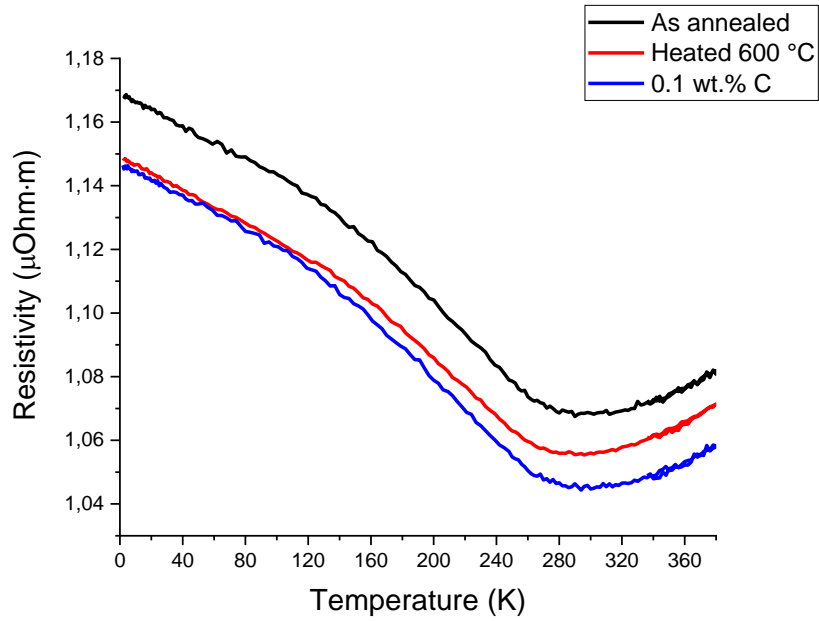


Figure 3. 41: Temperature dependence of the resistivity for: “As annealed”, “Heated 600 °C” and “0.1 wt.% C” samples.

The resistivity shows similar values for all the samples with a strong upturn on lowering the temperature, which has already been attributed in literature to a Kondo-like effect. This upturn starts AT about 280 K, which is slightly higher than the temperature of the magnetic peak in the specific heat.

Magnetoresistance, i.e.  $(R(H)-R(0))/R(0)$  of “As annealed”, “Heated 600 °C” and “0.1 wt.% C” samples was measured at the temperatures: 2 – 300 K and magnetic field range: 0 - 90 kOe. Results are presented in Figure 3. 42.

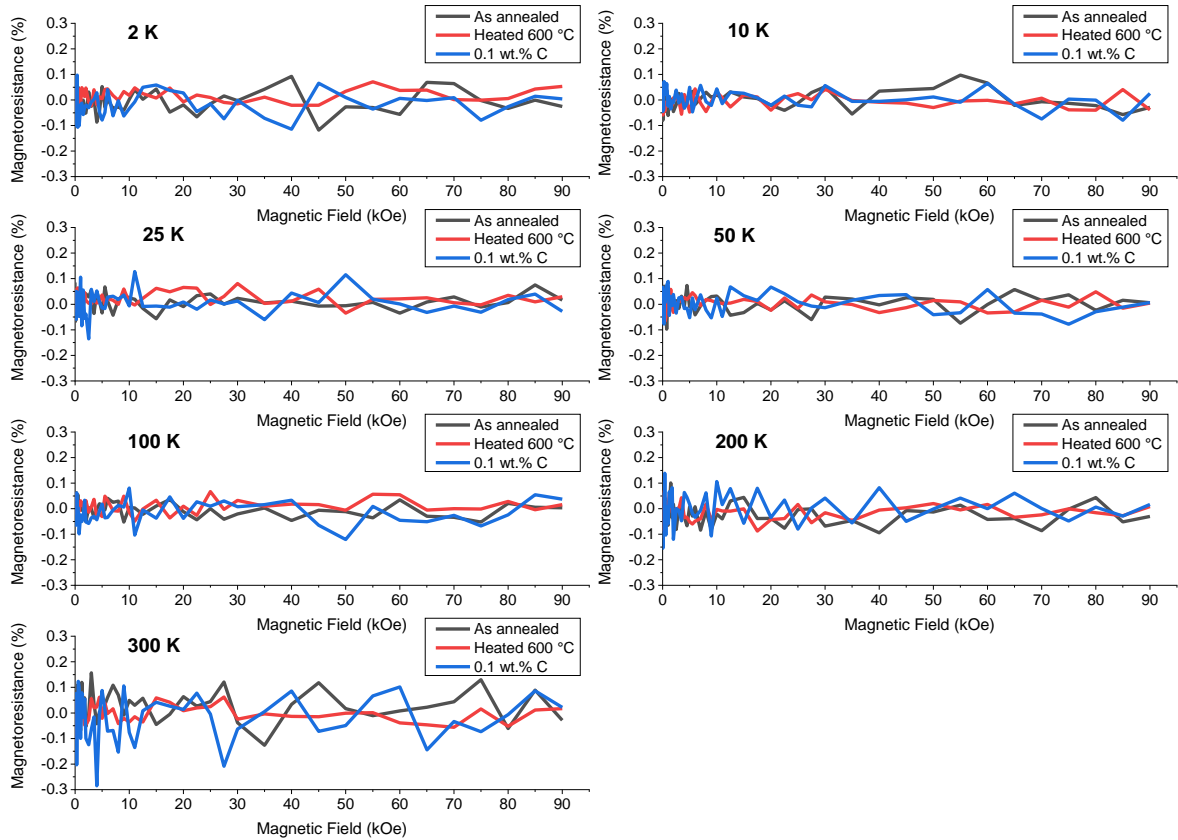


Figure 3.42: Magnetoresistances of “As annealed”, “Heated 600 °C” and “0.1 wt.% C” samples at different temperature.

They are virtually independent on the magnetic field, which indicates an extremely small mean free path of the electrical carriers in the whole temperature range.

### 3.3 Summary of results for Fe-Mn-Si alloys

In the Chapter presented, the influence of heating temperature and small carbon addition on the properties of Fe-30Mn-6Si (wt.%) shape memory alloys was studied. Summarized results are as follows:

- X-Ray Diffraction patterns revealed phase content of the samples and its change after deformation and during heating up to 600 °C. The results are in good agreement with literature.
- No differences are found in the Fe electronic states between all thermally treated samples at room temperature based on XANES. The shape of the absorption edge indicates a metallic character of both Fe and Mn.

- Low temperature and room temperature iron Mössbauer spectra indicate no magnetic moment on iron, thus magnetism of these materials is deduced to be governed by manganese.
- A Curie-Weiss paramagnetic behaviour shows up at higher fields (at low fields it is masked by ferromagnetic contribution until its saturation), indicating existence of localized moments in the materials, in addition to the temperature independent Pauli paramagnetic part due to conduction electrons.
- The ferro- or ferrimagnetic behaviour observed, with exchange bias dependent on the thermal treatment driven reverse martensitic transformation, is attributed to the austenitic fcc phase.
- Nanometric size of the austenitic fcc phase precipitations not detectable by XRD method in the martensite matrix is concluded, based on the exchange bias effect and nucleation of reversed domain character of virgin magnetisation curves.
- Mössbauer spectroscopy measurements show that carbon doped at 0.1 wt.% enters the bulk of the alloy causing the appearance of larger regions of austenite phase and decreasing the Curie-Weiss susceptibility, which reflects a decreased number of paramagnetic Mn atoms.
- Paramagnetic moment of  $3 \mu_B$  per Mn atom is derived from high temperature magnetic susceptibility.
- Specific heat measurements for the alloy with 0.1 wt.% of carbon reveal a peak at 250 K, only slightly sensitive to the applied magnetic field up to 90 kOe, which is attributed to magnetic transition to a glass-like state of the martensite hcp phase with a very small net moment of  $0.016 \mu_B$ .
- Electrical resistivity measurements show an upturn on lowering temperature attributed to a Kondo-like effect. The magnetoresistance is independent on the magnetic field up to 90 kOe at all the temperatures, indicating an extremely small mean free path of the electrical carriers.

## Chapter 4. Cold rolled and annealed NiTi micro-foils – results and discussion.

The study presented in this Chapter focuses on possibility of NiTi shape memory alloy creation by cold rolling method combined with thermal processing. The results give also insights into the diffusion process between nickel/titanium diffusion couples and oxidation – which in the case of preparation of these materials is a very important problem. Sample preparation process (cold rolling of heated foils) performed at Faculty of Non-Ferrous Metals (AGH University of Science and Technology). Results obtained from Scanning Electron Microscope with Energy Dispersive Spectroscopy detector and optical microscope are presented. Optical microscope photographs were obtained at Faculty of Geology, Geophysics and Environmental Protection, AGH University of Science and Technology. More details on these methods are presented in the Chapter 2.

### 4.1 Annealing process

Diffusion couples used in this part of study are presented in Figure 4. 1. Pure nickel and titanium foils of 100 and 50  $\mu\text{m}$  in the thickness were used, respectively. Sandwich like samples were prepared, which provide increased diffusion process volume in comparison with a simple Ni-Ti pair, in view of different diffusion coefficients of nickel/titanium and stronger oxidation of titanium than nickel at elevated temperatures.



Figure 4. 1: Illustrative representation of the cold rolled diffusion couples: a) 50  $\mu\text{m}$  titanium foil between two 100  $\mu\text{m}$  nickel foils and b) 100  $\mu\text{m}$  nickel foil between two 50  $\mu\text{m}$  titanium foils.

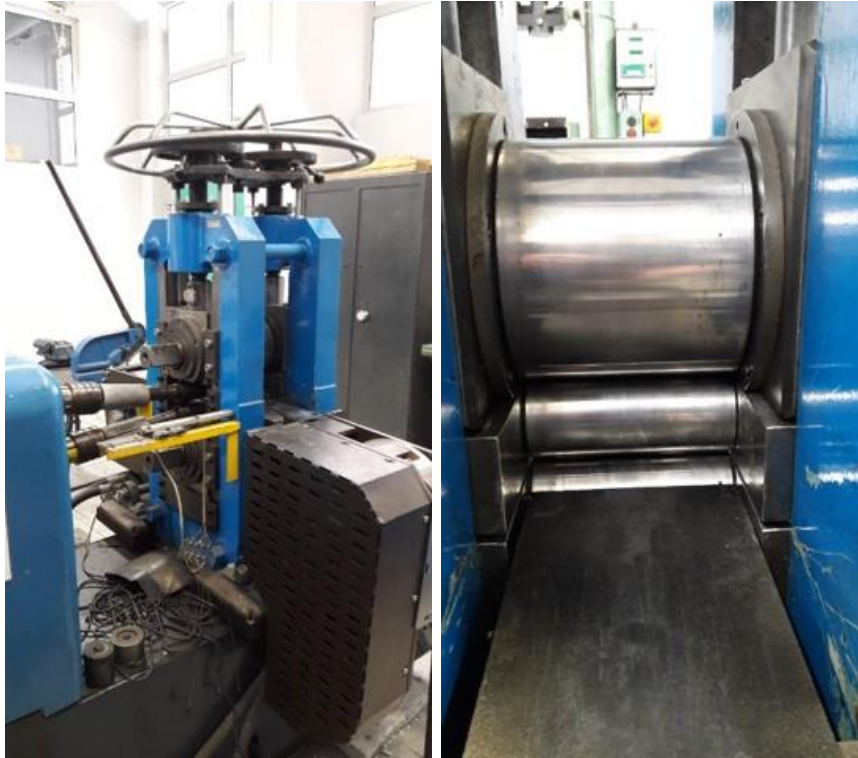


Figure 4. 2: Cold rolling machine at the Faculty of Non-Ferrous Metals, AGH University of Science and Technology.

Table 4. 1: Cold rolling machine specification.

Parameter:	Value:
Thickness of the batch (max):	5 mm
Width of the batch (max)	100 mm
Thickness of the product (min)	0.01 mm
Rolling speed	1.5 to 15 m/min
Rolling force (max)	120 kN
moment of rolling (max)	60 Nm

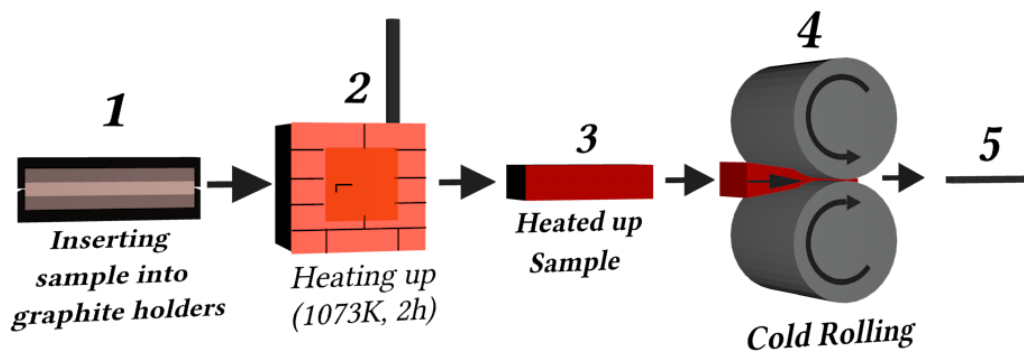


Figure 4. 3: A scheme of the process for heated up and rolled samples: 1. Protection of the sample, 2. heating up to  $\sim 830^{\circ}\text{C}$  (2h), 3. hot sample transfer, 4. Cold rolling and 5. Sample ready for long annealing.

Diffusion couples preparation process involved usage of furnace, graphite dies and cold rolling machine. Foils were put between graphite molds in the way presented in Figure 4. 1. In such a way samples were inserted into hot furnace ( $\sim 830^{\circ}\text{C}$ ) and kept for two hours. After that, graphite was removed and hot diffusion couples were inserted into cold rolling machine – presented in Figure 4. 2. Machine specification is shown in the Table 4. 1. Maximum rolling force was used. Output material foils were found to be well joined, but surface oxidation could be observed by naked eye. A scheme of the process is presented in Figure 4. 3.

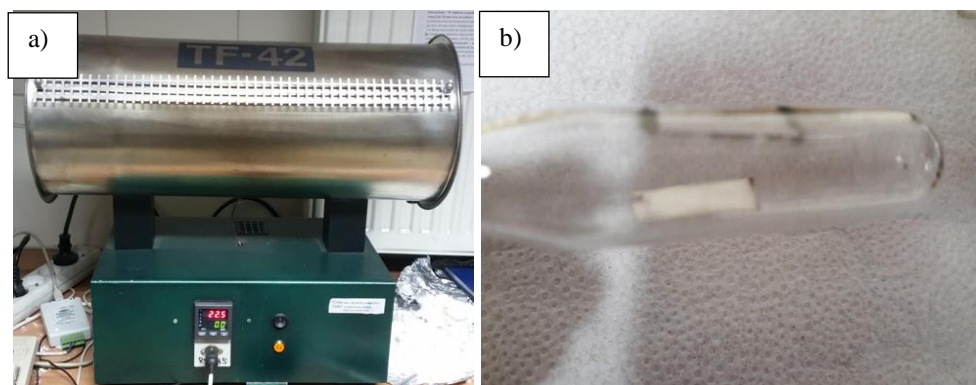


Figure 4. 4: a) Furnace and b) example of the sample sealed in quartz tube in vacuum.

The diffusion couples prepared were further used by annealing with different durations and temperatures. The value of heating step was  $5^{\circ}\text{C}/\text{min}$  and samples were then quenched in water. Each sample was inserted into quartz tube pumped off by turbo-molecular pump (up to  $\sim 2.4 \cdot 10^{-4}$  mbar) and sealed – see Figure 4. 4. It was performed in such a way to prevent

further oxidation process. Making use of the results of previous experiments, the annealing was conducted at temperatures below 1000 °C.

### 4.2 Characterization of materials obtained

Results of annealing of diffusion couples prepared in the process discussed in the previous subchapter are presented. Characterization process is started with surface properties of the samples before annealing and the results are shown in Figure 4. 5 and Figure 4. 7. Images were obtained with optical microscope.

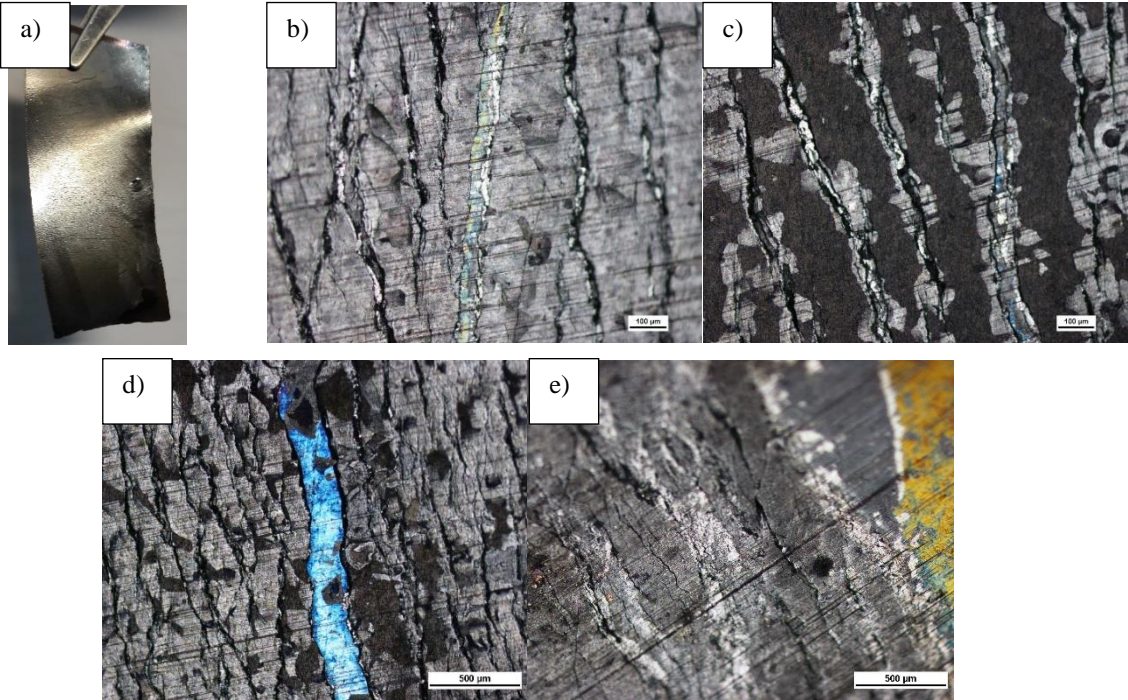


Figure 4. 5: Optical microscope images of 50Ti:100Ni:50Ti sample before annealing.

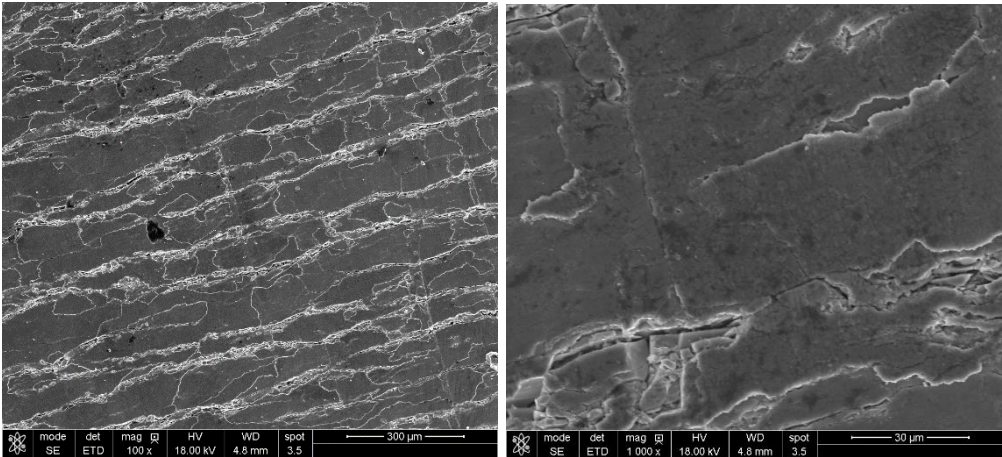


Figure 4. 6: SEM images of 50Ti:100Ni:50Ti before annealing.

Optical microscope images of diffusion couple consisting of 100  $\mu\text{m}$  nickel foil between two 50  $\mu\text{m}$  titanium foils are presented in Figure 4. 5 and Scanning Electron Microscope images are shown in Figure 4. 6. Local oxidation can be observed, which shows up in blue/white/orange color. At the sub-point c) and d), thin black layer can be seen coming possibly from surface contaminated locally by graphite molds during heating sample up before rolling or from the surface of rollers. From the mechanical point of view the foils in the obtained sample are well joined, but the surface looks deformed and wrinkled in the direction perpendicular to rolling direction.



Figure 4. 7: 100Ni:50Ti:100Ni before annealing.

In the case of the sample consisting of 50  $\mu\text{m}$  titanium foil between 100  $\mu\text{m}$  nickel foils - also surface oxidation can be observed as a discoloration – see Figure 4. 7. Nickel external surfaces are very smooth here and not wrinkled, unlike the titanium ones.



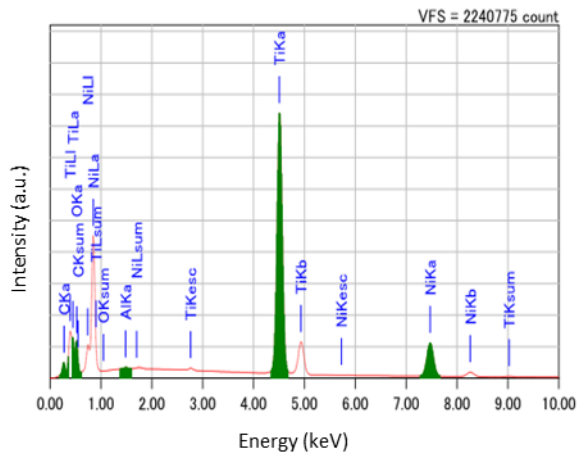
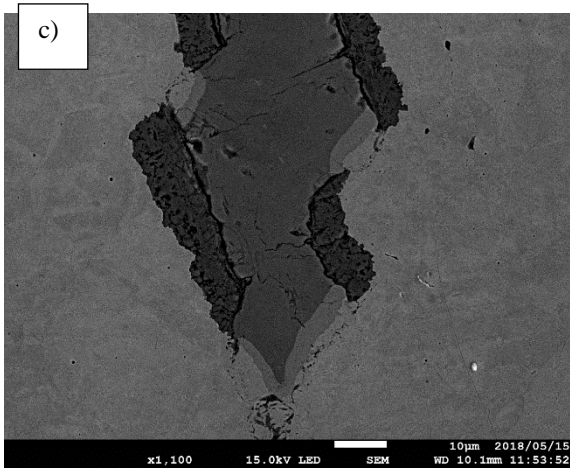
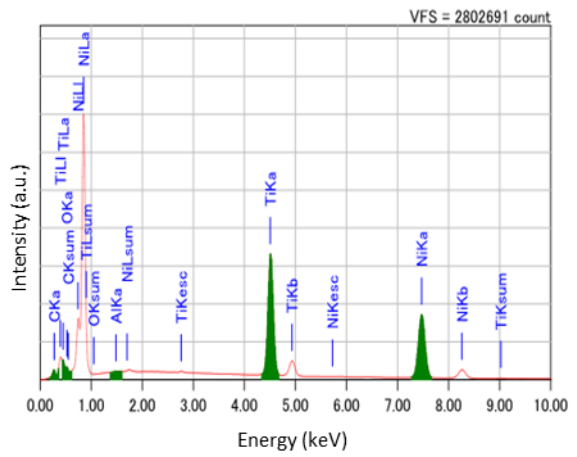
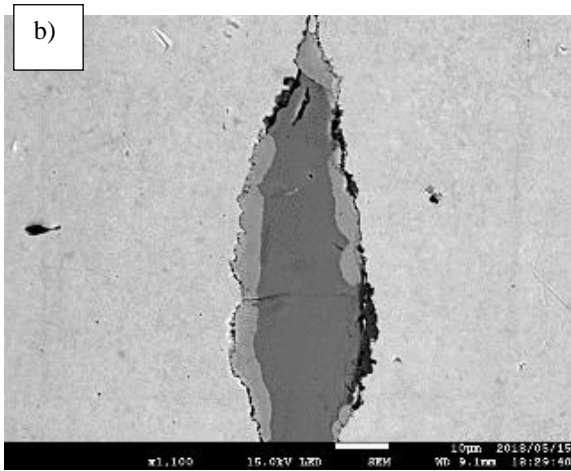
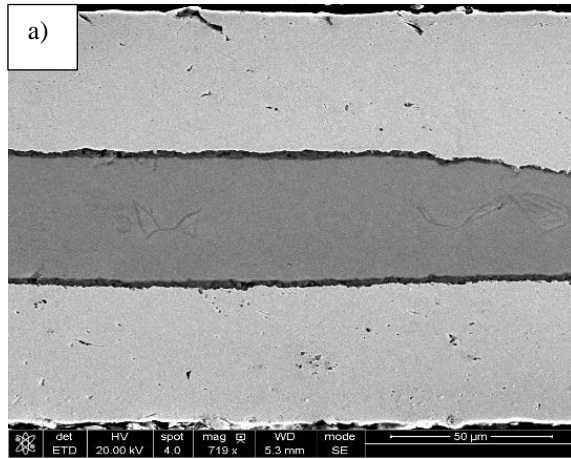
Figure 4. 8: The image of foils cold rolled without prior heating treatment.



Figure 4. 9: The image of foils after secondary cold rolling of cold rolled heated foils.

It is important to note that for the foils cold rolled at room temperature without prior heat treatment their joining failed – see Figure 4. 8. Lowered foils thicknesses can be observed with significant roughness of their inner surfaces (between foils). A similar effect can be observed in secondary cold rolling of previously cold rolled preheated foils – see Figure 4. 9. Effect of foils cracking and wrinkling can also be seen.

In the next part the results of cross-section studies for the diffusion couples prepared by rolling of heated foils, annealed at different temperatures will be discussed. Two general kinds of samples will be discussed:  $100\mu\text{mNi}:50\mu\text{mTi}:100\mu\text{mNi}$  and  $50\mu\text{mTi}:100\mu\text{mNi}:50\mu\text{mTi}$ . Each kind of samples was divided into smaller pieces and subjected to annealing process for 12 h sealed in quartz tubes (in vacuum) in  $700\text{ }^\circ\text{C}$ ,  $800\text{ }^\circ\text{C}$  and  $900\text{ }^\circ\text{C}$ . Next step was the preparation of cross-sectional elemental analysis – see Chapter 2 for samples SEM/EDS analysis preparation process. Results obtained for samples  $100\mu\text{mNi}:50\mu\text{mTi}:100\mu\text{mNi}$  are presented in Figure 4. 10 (SEM images with EDS qualitative analysis), Figure 4. 11 (SEM images with EDS elemental maps), Figure 4. 12 (quantitative map in at.%) and Figure 4. 13 (intensity of elements line and composition dependence), and for  $50\mu\text{mTi}:100\mu\text{mNi}:50\mu\text{mTi}$  in the Figure 4. 14 (SEM images with EDS qualitative analysis), Figure 4. 15 (SEM images with EDS elemental maps), Figure 4. 16 (quantitative map in at.%) and Figure 4. 17 (intensity of elements line and composition dependence). Quantitative elemental maps possess artifacts due to X-Ray scattering and microscope software in place of gap between foils – see Figure 4. 17: c). The spurious effects of sample preparation process: carbon (resin/cross-section surface contamination), aluminum (polishing paste  $\text{Al}_2\text{O}_3$ ) and oxygen (easy surface oxidation process of titanium) have not been taken into account in quantitative analysis.



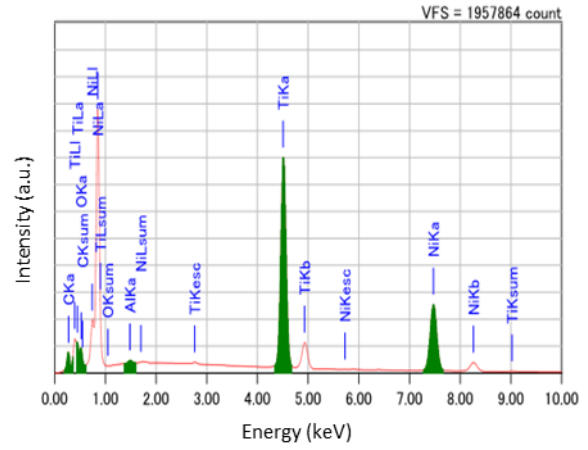
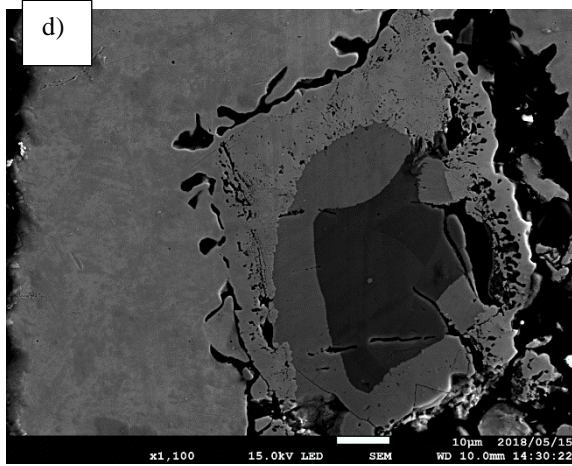
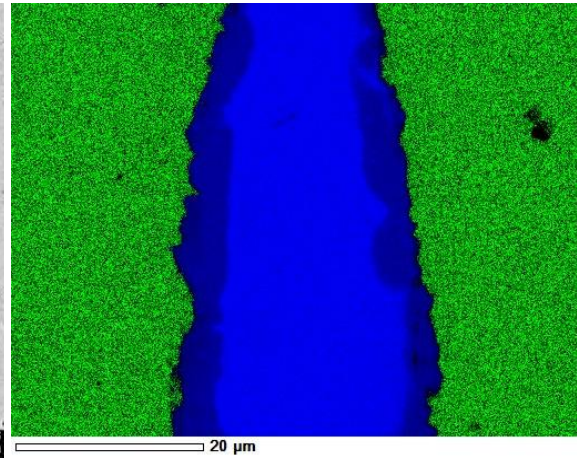
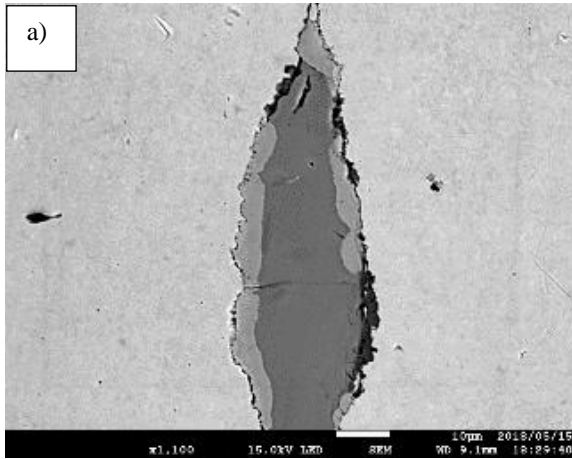


Figure 4. 10: SEM images with EDS maps qualitative graphs for 100µmNi:50µmTi:100µmNi sample a) as rolled and after annealing for 12h in vacuum in: b) 700 °C, c) 800 °C and d) 900 °C.



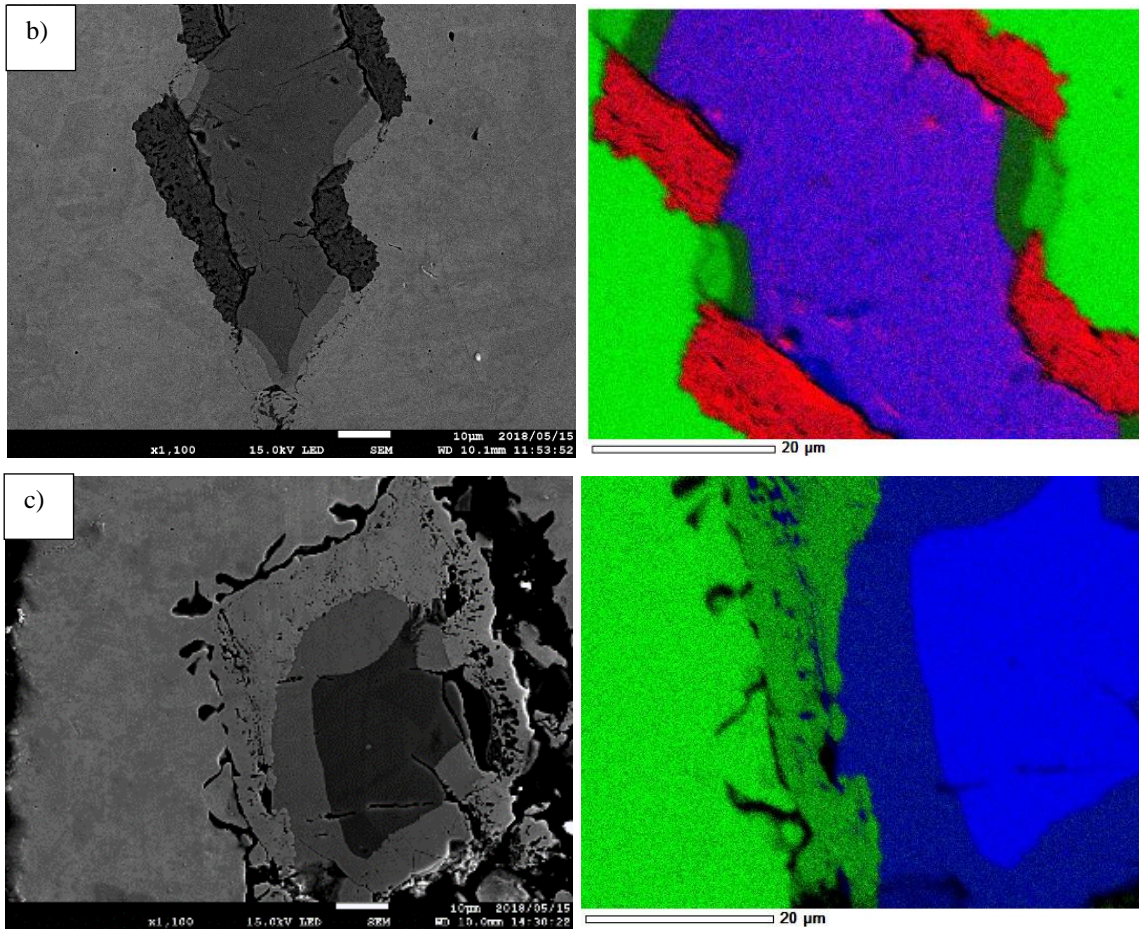
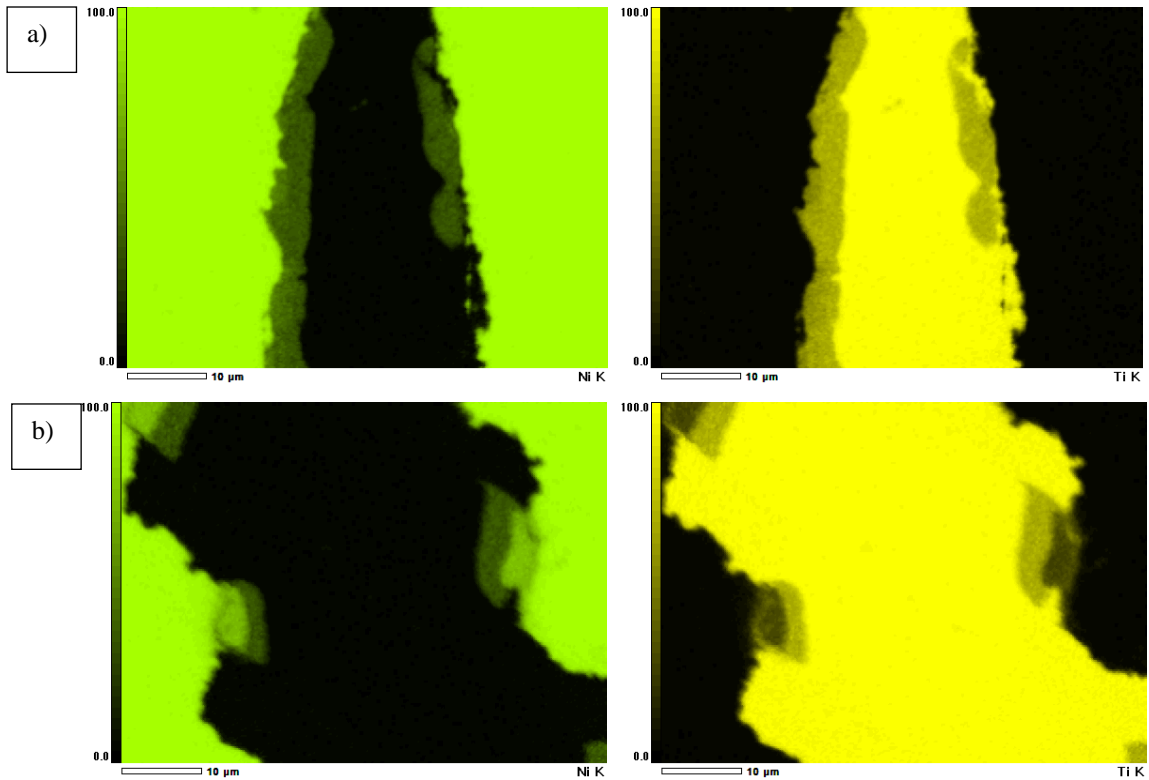


Figure 4. 11: SEM images and EDS maps for 100µmNi:50µmTi:100µmNi sample after annealing for 12h in vacuum in: a) 700 °C, b) 800 °C and c) 900 °C (green color – nickel, blue color – titanium and red - oxygen).



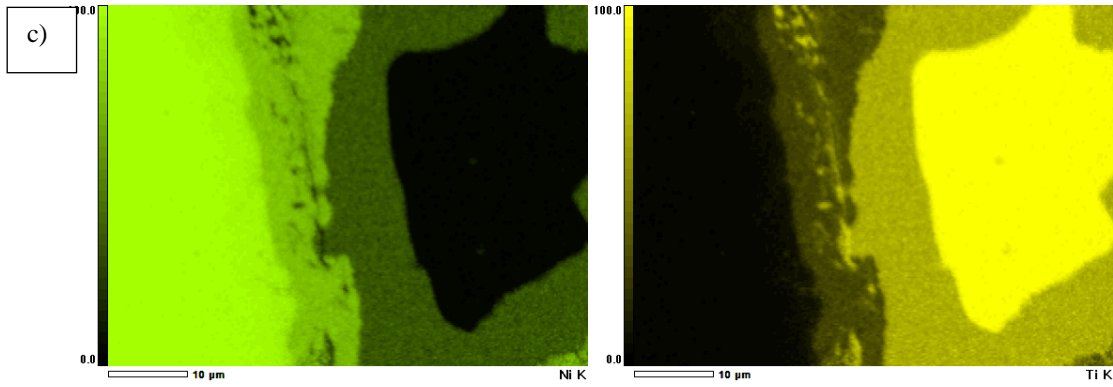


Figure 4.12: EDS quantitative maps for 100µmNi:50µmTi:100µmNi sample after annealing for 12h in vacuum in: a) 700 °C, b) 800 °C and c) 900 °C (green color – nickel and yellow color – titanium) – scale in atomic percentage.

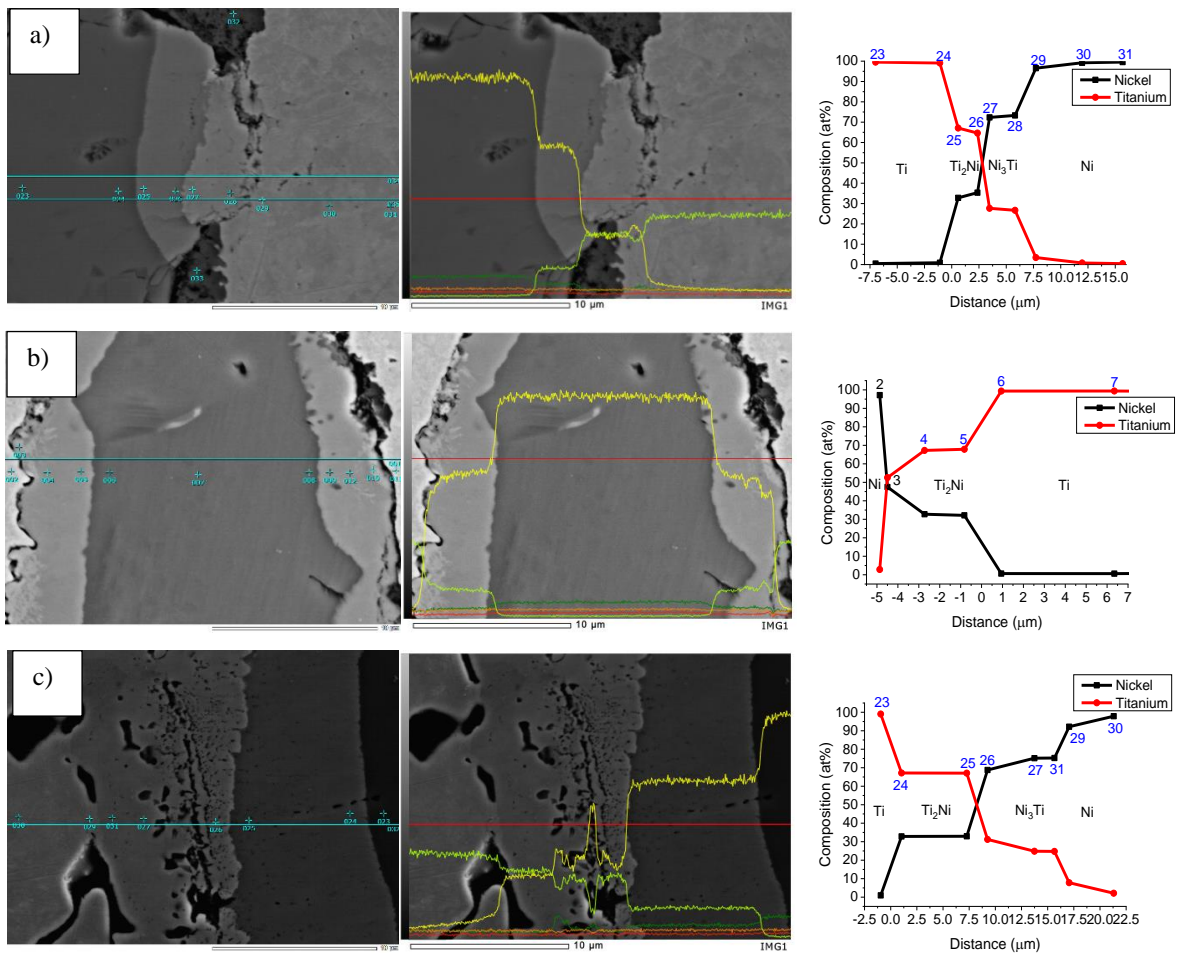
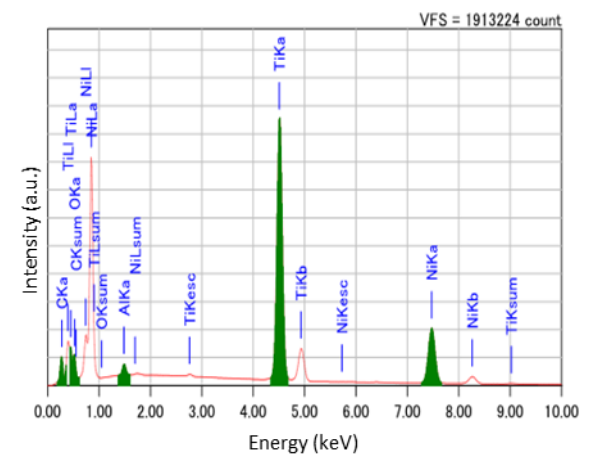
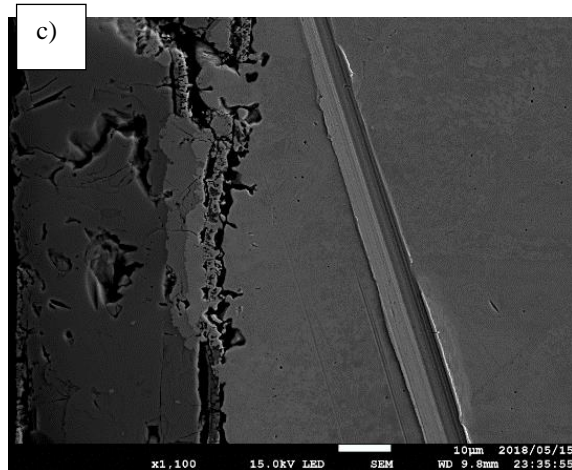
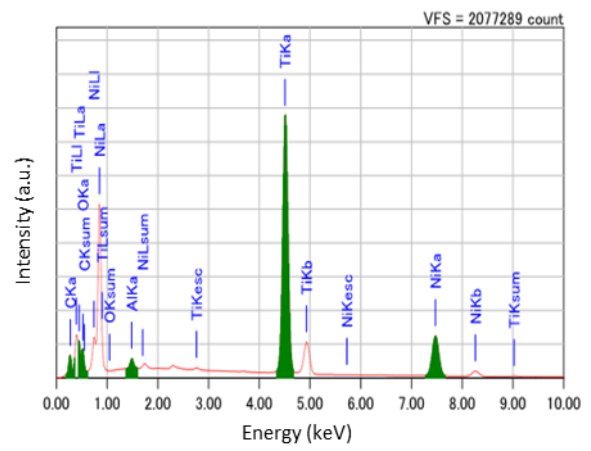
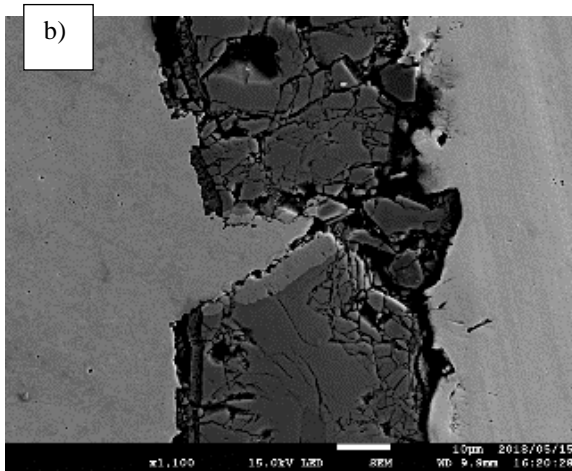
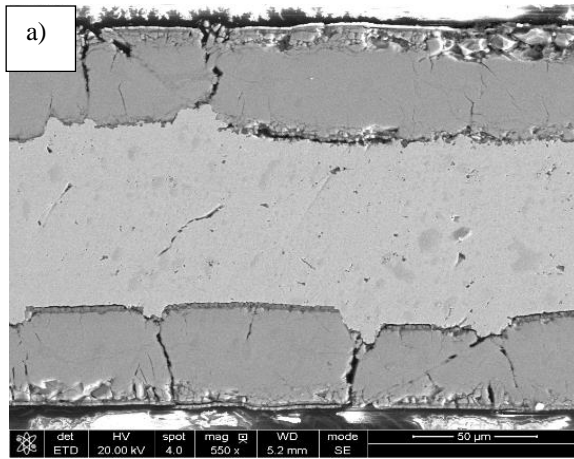


Figure 4.13: SEM image with line measurement and composition dependence with marked points of 100µmNi:50µmTi:100µmNi sample after annealing for 12h in vacuum in: a) 700 °C, b) 800 °C and c) 900 °C (yellow – titanium, light green – nickel, dark green – oxygen, red – carbon and orange – aluminum). Distance is measured from Ti/Ti<sub>2</sub>Ni interface.



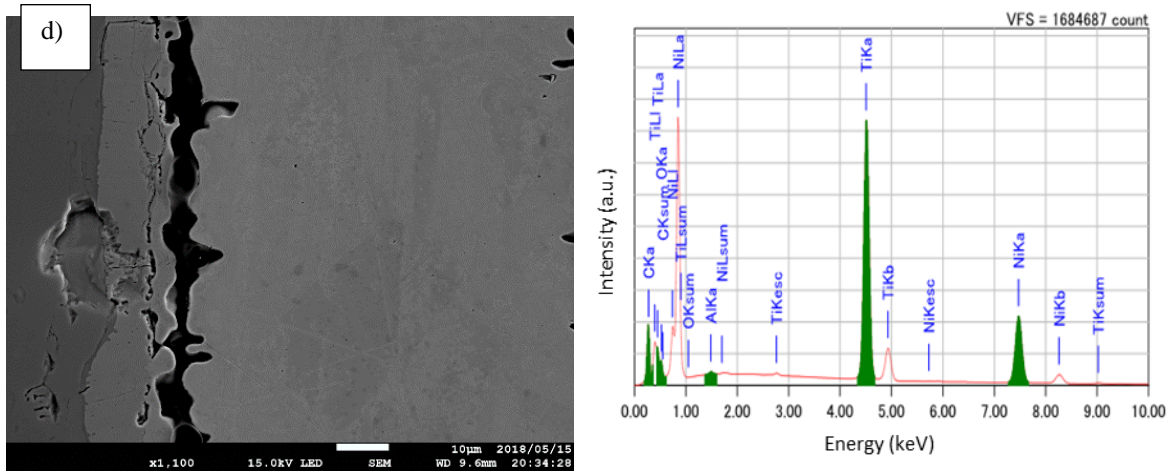
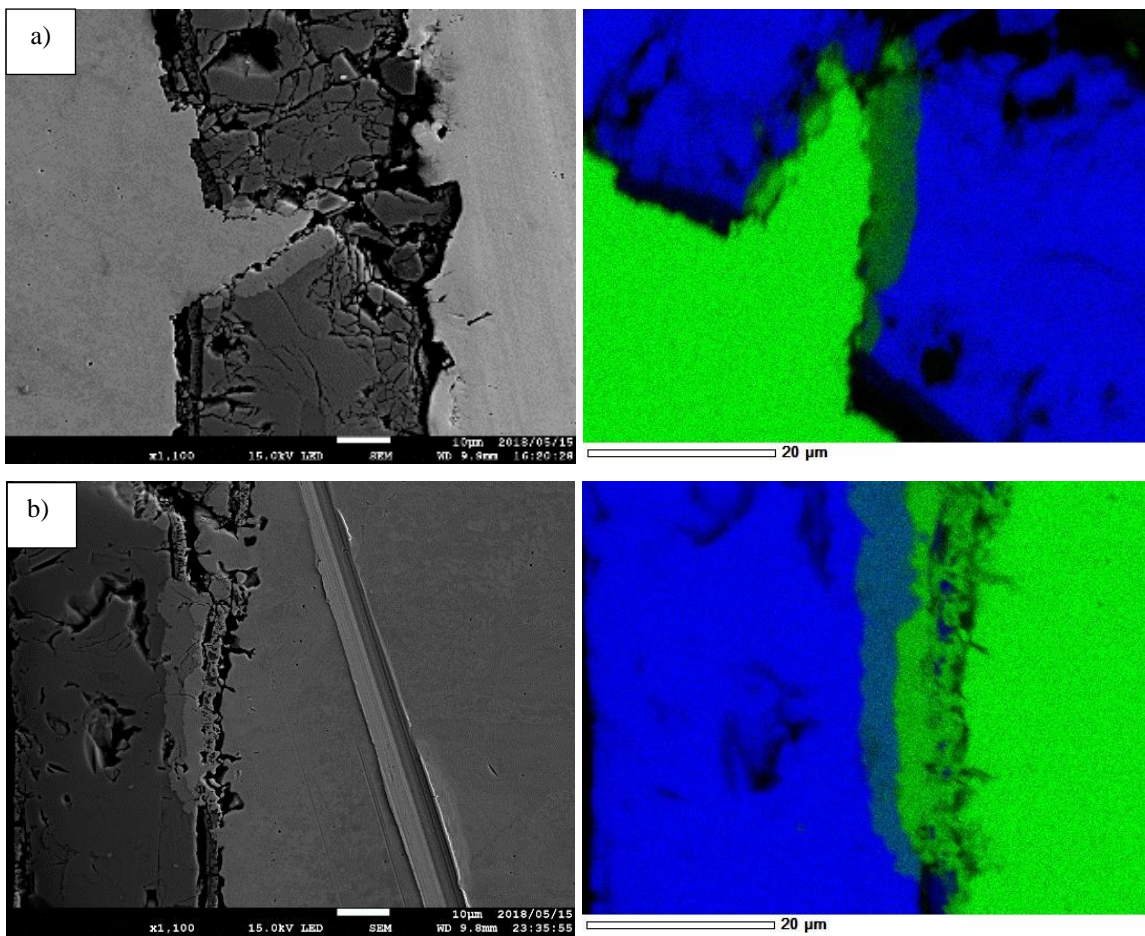


Figure 4. 14: SEM images with EDS maps qualitative graphs for 50µmTi:100µmNi:50µmTi sample a) as rolled and after annealing for 12h in vacuum in: b) 700 °C, c) 800 °C and d) 900 °C.



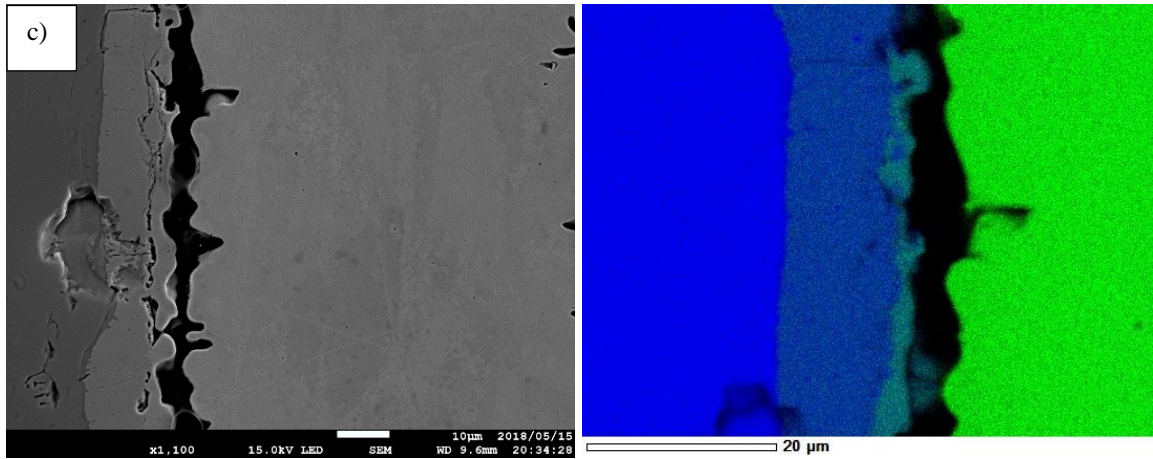


Figure 4. 15: SEM images and EDS maps for 50µmTi:100µmNi:50µmTi sample after annealing for 12h in vacuum in: a) 700 °C, b) 800 °C and c) 900 °C (green color – nickel and blue color - titanium).

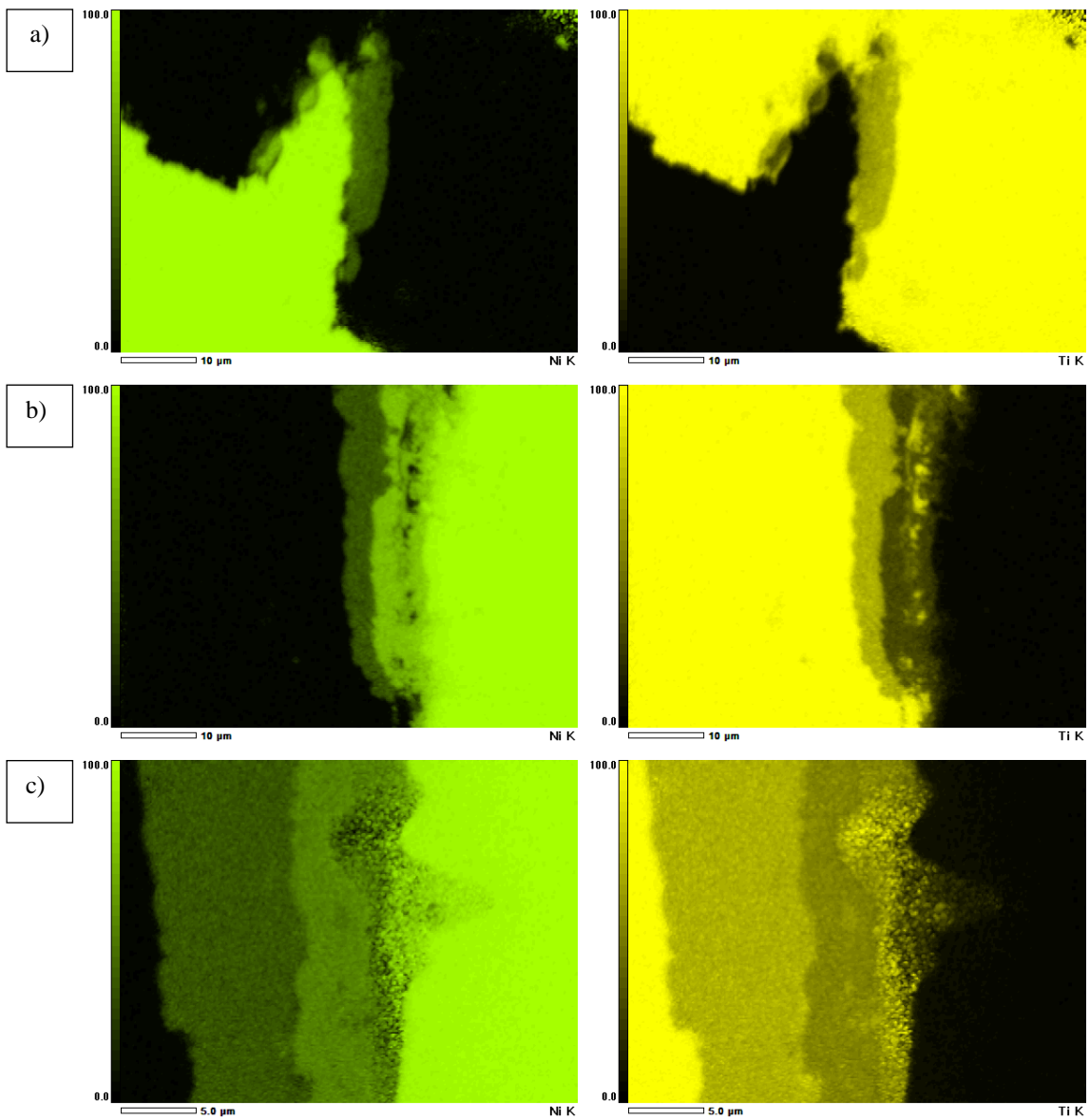


Figure 4. 16: EDS quantitative maps for 50µmTi:100µmNi:50µmTi sample after annealing for 12h in vacuum in: a) 700 °C, b) 800 °C and c) 900 °C (green color – nickel and yellow color – titanium) – scale in atomic percentage.

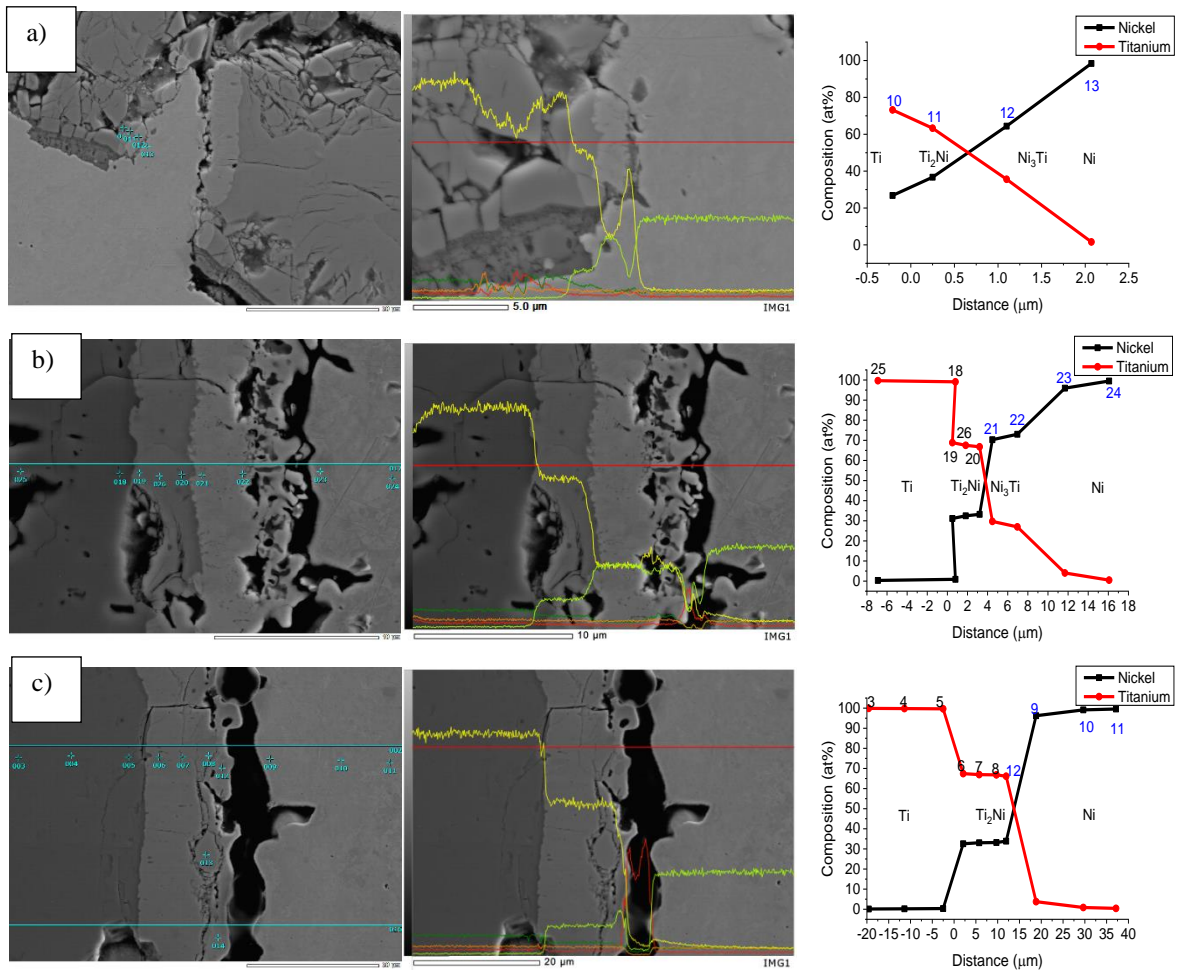


Figure 4. 17: SEM image with line measurement and composition dependence with marked points of 50µmTi:100µmNi:50µmTi sample after annealing for 12h in vacuum in: a) 700 °C, b) 800 °C and c) 900 °C (yellow – titanium, light green – nickel, dark green – oxygen, red – carbon and orange – aluminum). Distance is measured from the Ti/Ti<sub>2</sub>Ni interface.

Based on the inspection of the Figure 4. 10: a) and Figure 4. 14: a) some changes in the foils thickness can be concluded. In the case of 100µmNi:50µmTi:100µmNi sample, nickel foils thickness drop down from initial 100 µm to ~42 µm, and for titanium foil from 50 µm to 41.5 µm. 50µmTi:100µmNi:50µmTi sample shows also changes – nickel foil from initial 100 to ~84 µm and titanium foil from 50 to ~47 µm. Results corresponds to the area with maximal thicknesses.

Graphs in Figure 4. 18, Figure 4. 19 and Figure 4. 20 present collective data of medium thickness of following phases: Ni<sub>3</sub>Ti, Ti<sub>2</sub>Ni and gaps (between foils), respectively.

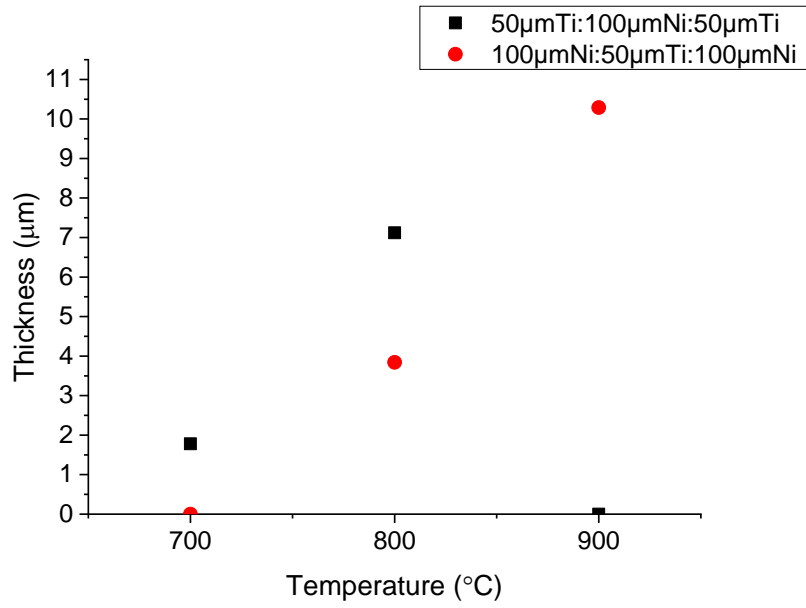


Figure 4. 18: Temperature dependence of medium Ni<sub>3</sub>Ti phase thickness.

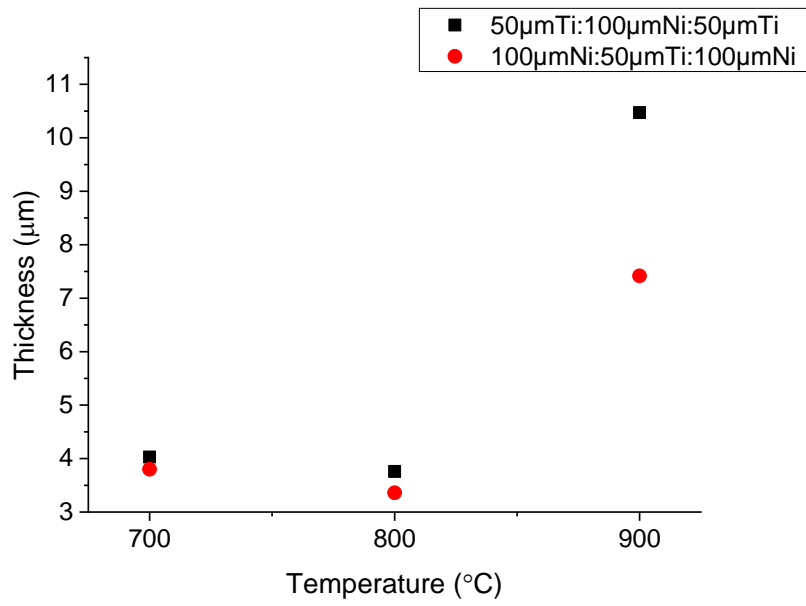


Figure 4. 19: Temperature dependence of medium Ti<sub>2</sub>Ni phase thickness.

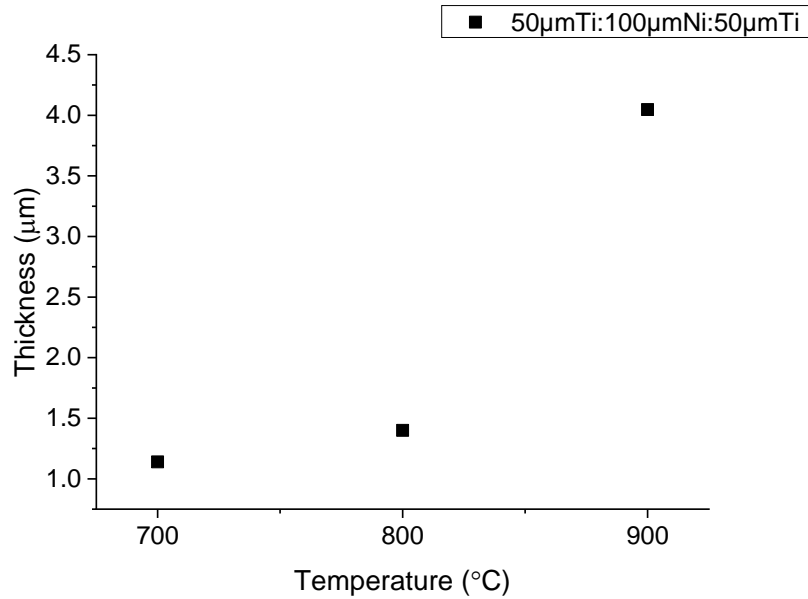


Figure 4. 20: Temperature dependence of medium gap width.

Presence of small area of NiTi phase could be only seen in case of 50µmTi:100µmNi:50µmTi annealed in 900 °C and in 100µmNi:50µmTi:100µmNi in 700 °C. Regarding Ni<sub>3</sub>Ti phase thickness, it increases with temperature in both samples types, but in 50µmTi:100µmNi:50µmTi annealed in 900 °C is not observed. This is connected with creation of Kirkendall voids in titanium/nickel interface and lack of nickel atoms transport from nickel foil. After foil separation, Ni<sub>3</sub>Ti phase at the Ti side transformed into NiTi phase. Based on diffusion process at appropriate conditions (thermal and time), between Ni<sub>3</sub>Ti and Ti<sub>2</sub>Ni phase area should appear NiTi phase. In this situation, it is believed that annealing time was too short and this is a reason why only in two samples (annealing conditions) the NiTi phase can be detected. Ti<sub>2</sub>Ni phase thickness increases with annealing temperature in both samples type, but faster in 50µmTi:100µmNi:50µmTi. Gaps in the interface increase with temperature can be attributed to higher diffusion rate of nickel atoms into titanium foils and with strains created during cold rolling between foils. Based on this, creation of Kirkendall voids can be concluded – presence of very smooth walls around voids is visible. They occur mainly in 50µmTi:100µmNi:50µmTi type samples. In other regions destruction of oxidized material during polishing or sample cutting can be involved (see Figure 4. 15: a)).

From measurements performed the information on the oxidation process can be treated as qualitative one. It is important to note that EDS measurements are not so reliable for light elements quantitative evaluation and titanium is very easy oxidizing element on which thin oxide layer is created. An example of titanium oxidation problem is presented in Figure 4. 21 and Figure 4. 22 - 50µmTi:100µmNi:50µmTi sample annealed for 12h in 700 °C. It can be

seen that oxygen content measured in the direction from nickel foil into titanium increases indicating stronger titanium oxidation – see Figure 4. 21: b).

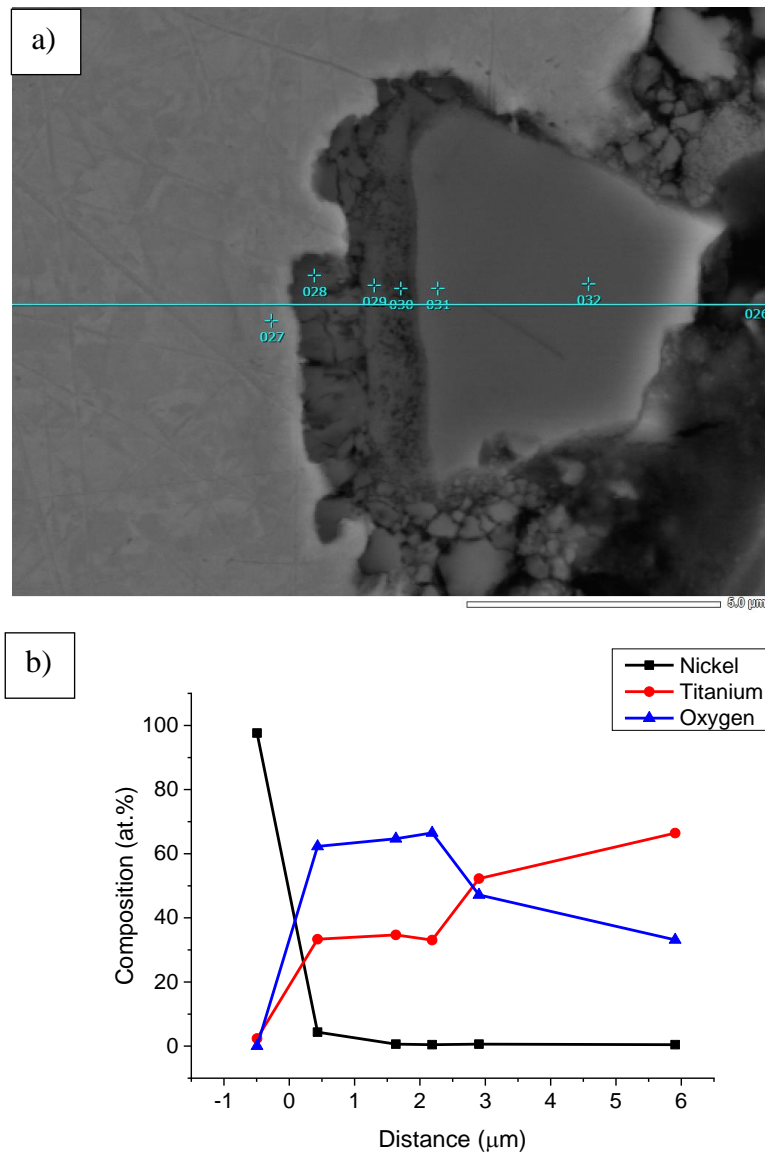


Figure 4. 21: A schematic example of oxidation of 50µmTi:100µmNi:50µmTi sample after annealing in 700 °C for 12h in vacuum.

Line measurement presented in Figure 4. 22 shows intensity dependence of each element along measurement line marked with red line.

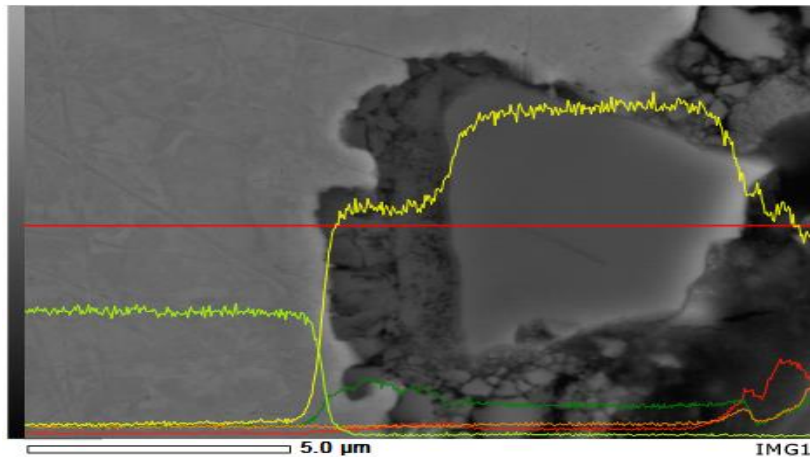


Figure 4. 22: SEM image with line measurement marked by red line and intensities lines represented by following colors: yellow – titanium, light green – nickel, dark green – oxygen, red – carbon and orange – aluminum.

Oxygen content increases on moving from nickel to titanium area. SEM image also confirms brittle phase content in the area with highest oxygen content. It is suspected that described local oxidized holes are created during diffusion couples heating up to ~830 °C before cold rolling. This is caused by a lack of protective atmosphere like argon or high vacuum and not good contact between foils (creation of microvoids).

### 4.3 Summary of results for rolled and annealed NiTi micro-foils

In this Chapter preparation of NiTi shape memory alloys by heated up and rolled foils and annealing was presented. Summarized conclusions are as follows:

- Ti<sub>2</sub>Ni phase thickness increases with annealing temperature in both samples type (faster in 50μmTi:100μmNi:50μmTi samples),
- Ni<sub>3</sub>Ti phase thickness increases with annealing temperature in 100μmNi:50μmTi:100μmNi.
- Ni<sub>3</sub>Ti phase thickness increases up to 800 °C annealing temperature in 50μmTi:100μmNi:50μmTi – at 900 °C annealing it was not observed (creation of Kirkendall voids and transformation into NiTi/Ti<sub>2</sub>Ni phase).
- Titanium oxidation occurs in microvoids appearing between Ni and Ti foils during heating and cold rolling.
- NiTi phase (small area) was observed only in two samples: 50μmTi:100μmNi:50μmTi (900 °C) and 100μmNi:50μmTi:100μmNi (700 °C).
- Gap increase between foils with temperature can be related to higher diffusion rate of nickel into titanium (creation of Kirkendall voids – very smooth walls) mainly in

50 $\mu$ mTi:100 $\mu$ mNi:50 $\mu$ mTi type samples. In other regions, destruction of oxygenated material/fragile phase during polishing can be involved.

The results show a potential for preparation of NiTi shape memory alloys by rolling of preheated foils sandwich, but it is important to introduce protective atmosphere (argon gas or high vacuum) to the preparation process and use much longer annealing time as well as adequate starting composition ratio of nickel and titanium.

## Chapter 5. Sintering of NiTi micro-foils – results and discussion

In this part of the study, pulse-current pressure sintering method was used for Ni-Ti diffusion couples and micro-foils preparation. The equipment of PLASMAN, SS Alloy was used. The next subsections are focusing on Ni-Ti diffusion couples annealing process, micro-foils: types of samples, composition, sintering time and thicknesses. At the end the magnetic, electrical and thermal properties are presented and discussed. Samples preparation and the study of their properties were performed in collaboration with Goto Koki and Yamada Eisuke (Shibaura Institute of Technology students).

### 5.1 Annealing process

Diffusion couples were prepared at the previously mentioned pulsed-current sintering machine – see Figure 5. 1.

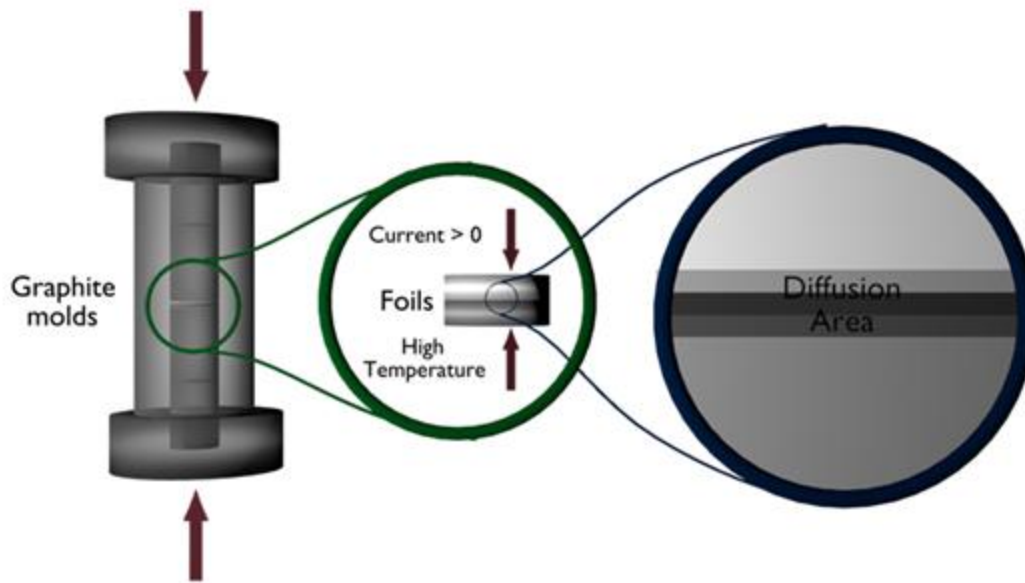


Figure 5. 1: Pulse-current pressure sintering samples preparation process.

Before synthesis, 100  $\mu\text{m}$  thickness nickel and titanium foils with diameter of 20 mm were cleaned in ethanol bath for 20 minutes and put between graphite molds in sintering machine. 9 MPa of external uniaxial compression pressure was used in low vacuum ( $\sim 40$  Pa). Sintering performed in 730  $^{\circ}\text{C}$  for 15 minutes (heating rate of  $\sim 49^{\circ}\text{C}/\text{min}$  and machine cooling). The material obtained was cleaned in ethanol and divided into smaller pieces for further annealing processes. Two annealing temperatures were used: 700 (for: 24, 48 and 72 h) and 800  $^{\circ}\text{C}$  (for: 24 and 72 h). In total, five diffusion couples were prepared. Each one of them was sealed in

separate quartz tube in the high vacuum for annealing. Final stage of the process involved water cooling. Due to small size of diffusion couples and location of diffusion interface, the best analysis option was performing cross-sectional SEM/EDS measurement. Preparation process was described in Chapter 2.

Figure 5. 2 and Figure 5. 3 presents SEM images with EDS cross-sectional line measurements. They were performed for diffusion couples annealed in 700 and 800 °C for different times.

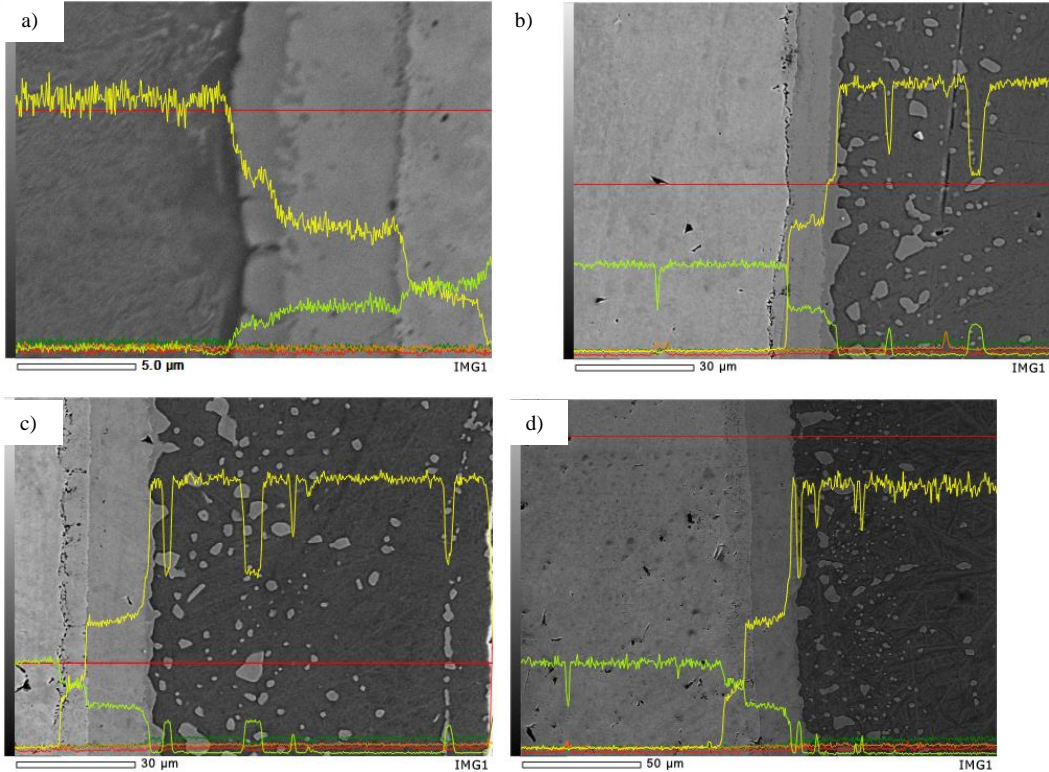


Figure 5. 2: Cross-sectional SEM/EDS line measurements of diffusion couples annealed in 700 °C: a) as sintered, b) 24 h, c) 48 h and d) 72 h (yellow – titanium, light green – nickel, dark green – oxygen, orange – aluminum and red – carbon).

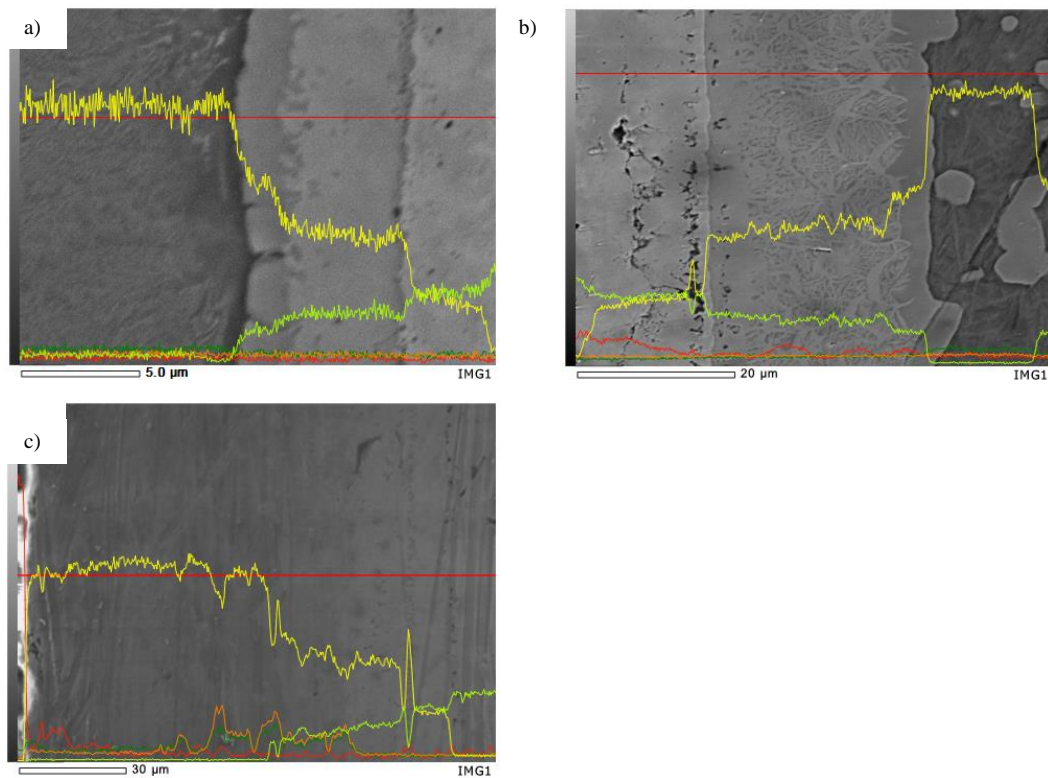


Figure 5. 3: Cross-sectional SEM/EDS line measurements of diffusion couples annealed in 800 °C: a) as sintered, b) 24 and c) 72 h (yellow – titanium, light green – nickel, dark green – oxygen, orange – aluminum and red – carbon).

SEM images are showing interfaces with signs of diffusion for all samples. For the all annealed samples presence of droplet-like features can be observed at titanium side. After annealing, presence of dendritic structures can be seen. They cannot be observed for the as sintered sample. In EDS line measurements five elements were taken into account: titanium, nickel, oxygen, aluminum and carbon (properly marked in the images). Aluminum and carbon presence comes from cross-section sample preparation procedure. Small increase of oxygen level can be noticed on moving from the area of nickel to that of pure titanium. In comparison with rolled samples, no excessively high oxidation is observed.

Figure 5. 4 and Figure 5. 5 presents compositional maps.

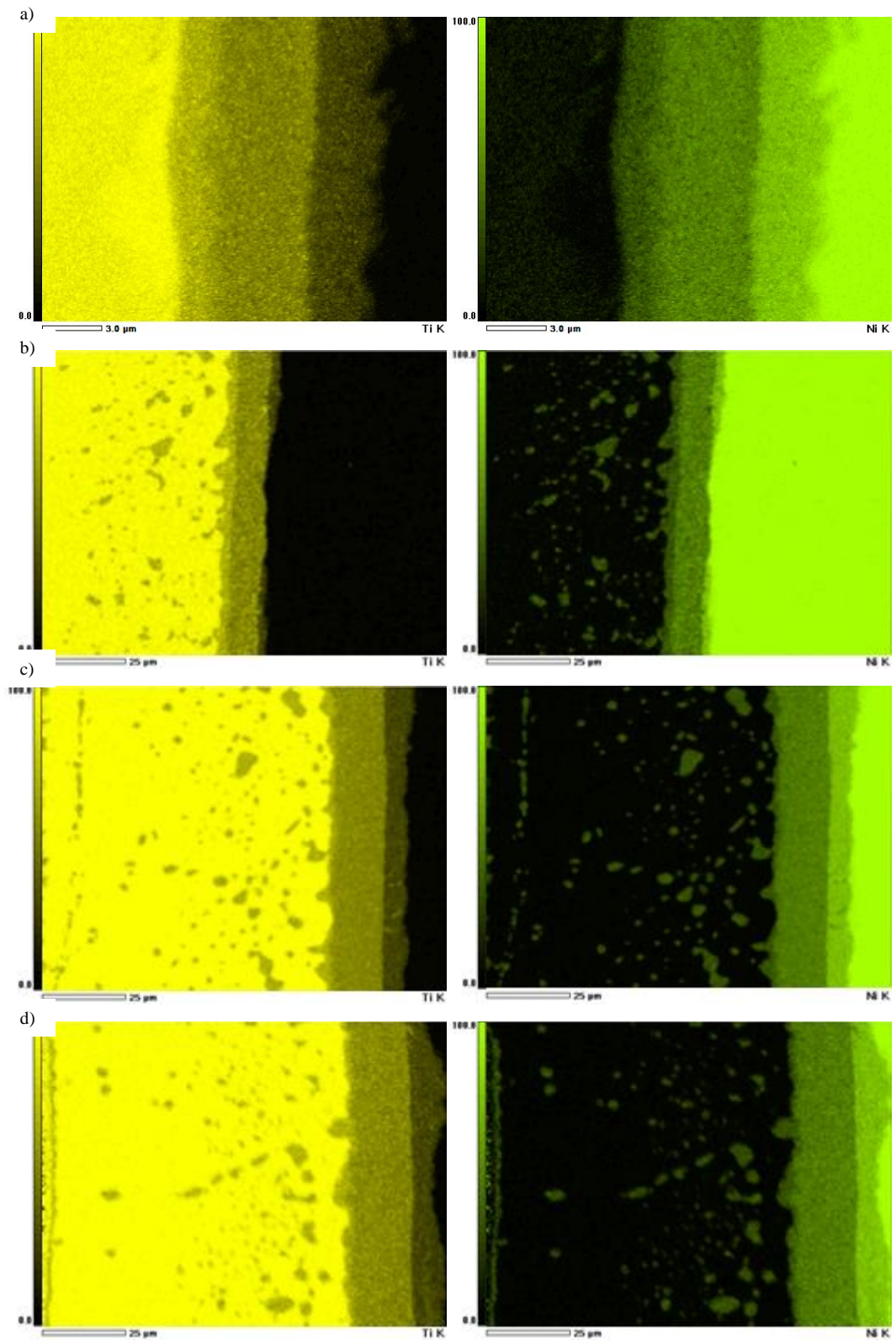


Figure 5. 4: Cross-sectional SEM/EDS map measurements of diffusion couples annealed in 700 °C: a) as sintered, b) 24 h, c) 48 h and d) 72 h (yellow – titanium and light green - nickel).

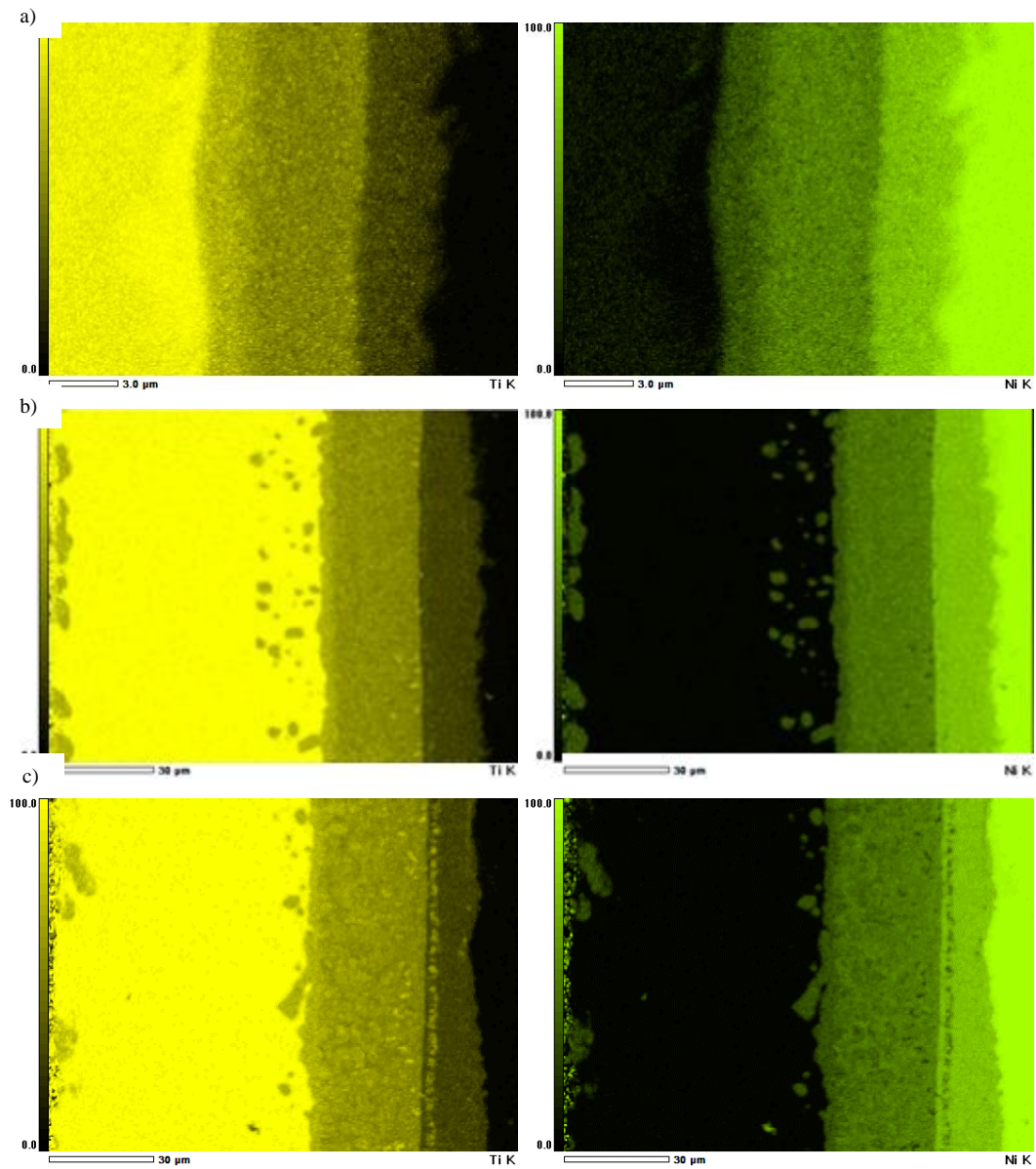
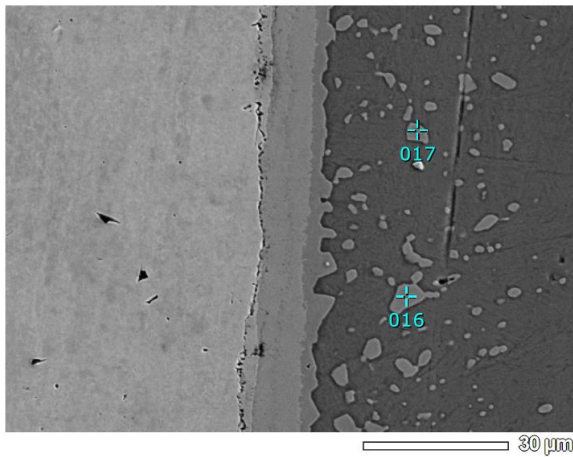


Figure 5. 5: Cross-sectional SEM/EDS map measurements of diffusion couples annealed in 800 °C: a) as sintered, b) 24 h and c) 72 h (yellow – titanium and light green - nickel).

It can be seen that diffusion occurred for all samples. Presence of small droplet-like particles can be observed at the titanium area with their different compositions.



Point number:	Ni (at. %):	Ti (at. %):
017	31.6(6)	68.4(2)
016	31.7(6)	68.3(2)

Figure 5. 6: Cross-sectional SEM/EDS point measurements of droplet-like features and their elemental compositions.

Their formation as a continuous layer at the titanium surface and subsequent “migration” as individual “particles” or their clusters into titanium can be seen in the Figure 5. 6. Their presence is related to sintering method of diffusion couples preparation and electromigration effect of nickel atoms under electric current – they are not observed in the case of rolled samples (see Chapter 4). A possible explanation considers very low melting point of the  $Ti_2Ni$  phase (942 °C), which enables fast diffusion leading to the formation of “droplets” of this phase. In the material three types of intermetallic compounds can be distinguished:  $Ti_2Ni$ ,  $NiTi$  and  $Ni_3Ti$ . In comparison with rolled samples no gaps can be seen which indicates good interface joining. In the Figure 5. 7 layer thicknesses of individual intermetallics obtained with annealing at 700 and 800 °C are presented versus annealing time.

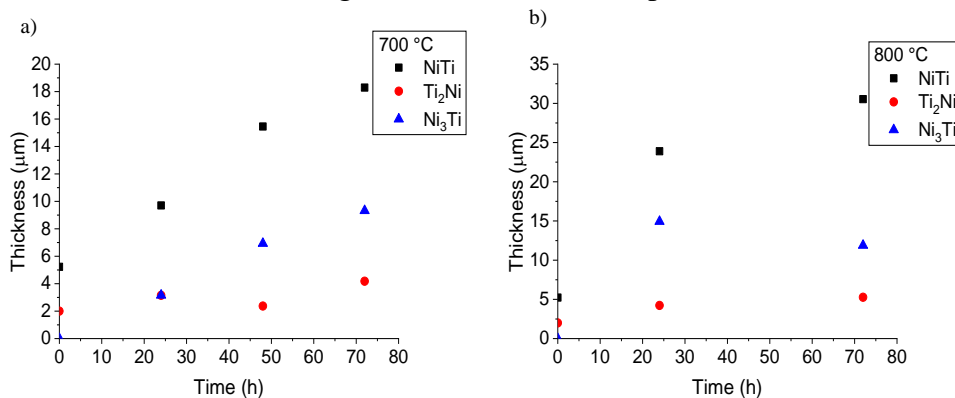


Figure 5. 7: Layer thicknesses of individual intermetallics thicknesses versus annealing time at: a) 700 and b) 800 °C.

It is worth noting that the amount of the  $NiTi$  phase after 24 hours of annealing is more than two times bigger at 800 than at 700 °C.

## 5.2 Characterization of micro-foils

Diffusion couples were prepared by pulse-current pressure sintering. A scheme of the setup is presented in the Figure 5. 8. Samples were placed between 1 mm tantalum (Ta) foil covered with boron nitride thin layers (BN) and graphite molds. Tantalum was used to block carbon diffusion into the samples and BN as anti-adhesive coating material (simplify samples extractions). Trials with graphite paper substitution were also conducted, but they resulted with a sample material stacking inside of it. Samples were prepared at the heating rate of ~50 °C/min and were cooled with machine.

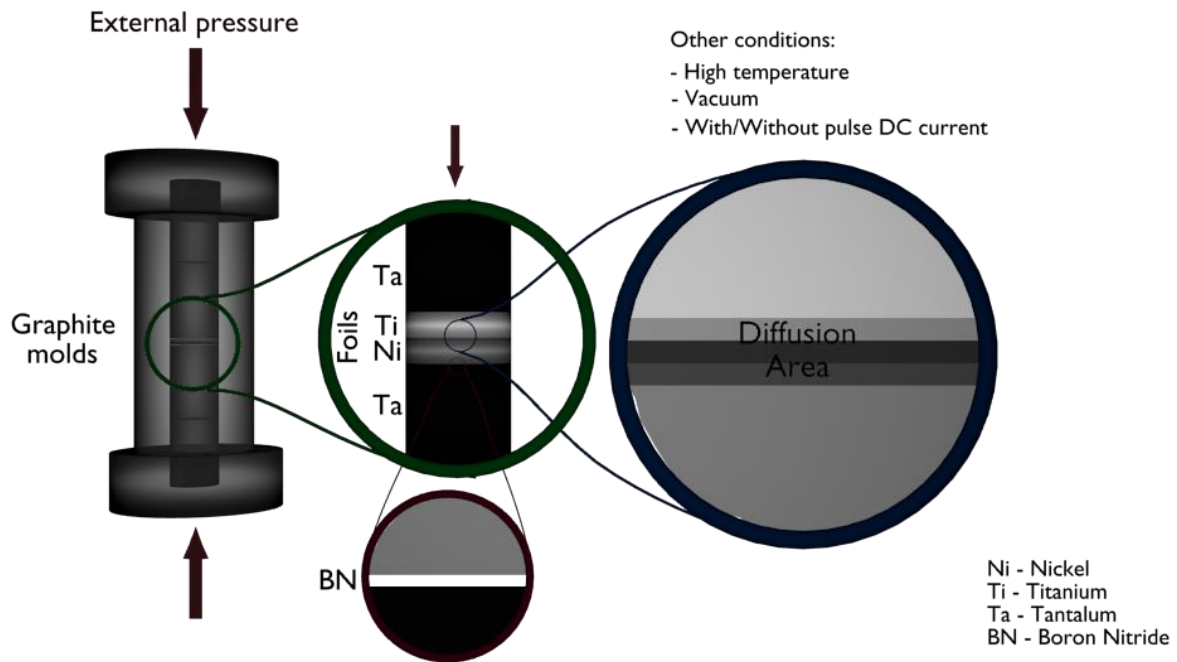


Figure 5. 8: A scheme of the pulse-current pressure sintering sample preparation process.

Prepared samples can be categorized in two types according to starting configurations of the foils: a simple one (one layer of nickel and one layer of titanium) and two sandwich-like configurations: nickel/titanium/nickel and titanium/nickel/titanium - see Figure 5. 9.

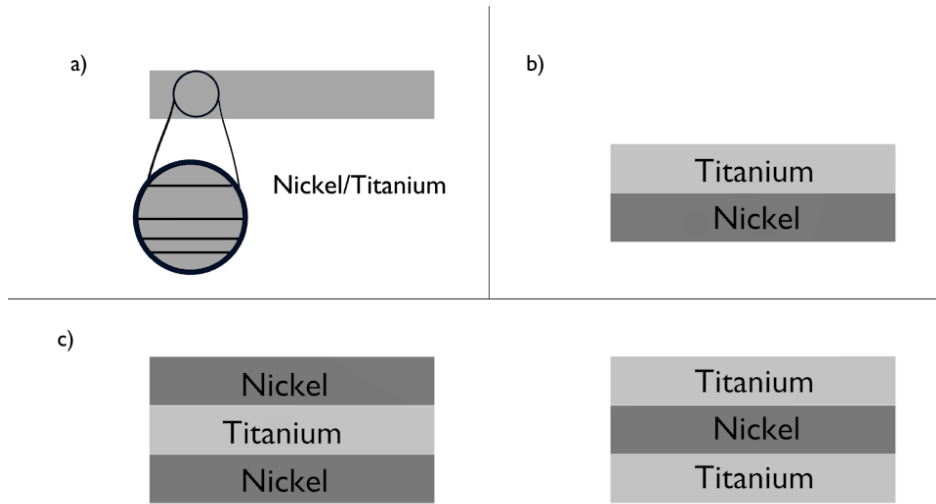


Figure 5. 9: Illustrative representation of the sintered samples types: a) single element layer, b) simple one and c) sandwich-like.

In order to obtain desired thickness of each foil layer, the following pure metals foils thicknesses combinations were used: 1, 2, 5  $\mu\text{m}$  and titanium: 2, 5  $\mu\text{m}$ .

In order to obtain desired weight composition of the elements the respective calculations have been carried out. For this purpose a “Foil Thickness Coefficient (FTC)” (see equation 5.1) was introduced. It connects thicknesses of starting foils with desired compositions of the final compound or alloys. Taking into account the density ratio (Ni/Ti) of 1.98, the FTC can be calculated as follows:

$$FTC = \frac{1.98 \cdot m_{Ti}}{m_{Ni}} = \frac{h_{Ti}}{h_{Ni}} \quad (5.1)$$

Based on this, it is possible to calculate the thicknesses of the input pure metals foils and associate them with NiTi phase diagram. NiTi phase occurs for  $x_{Ni} \in [54, 62]$  wt.% (at  $\sim 1390$  K – the broadest occurrences), which is equivalent to  $FTC \in [1.2, 1.7]$ . Converting it to at.% it occurs for  $x_{Ni} \in [49, 57]$ . It should be applicable for homogenous nickel/titanium distribution in a whole volume, at finished diffusion process between starting metals, negligible contamination, to meet the relevant composition conditions [145].

### 5.2.1 Comparison for different samples types

The two configurations previously mentioned are discussed in this subchapter – the simple one and sandwich-like. Samples prepared in following conditions: compressive pressure of 13 MPa of external uniaxial compression pressure (it increase up to 20 MPa during heating), heating temperature of  $\sim 700$  °C, sintering time of 60 minutes, 5 mm of mold diameter and low vacuum. The samples thickness and input pure metals foils were adjusted to

FTC (~1.7): 16 μm in total, 6 μm of pure nickel and 10 μm of pure titanium. For sandwich type samples outer metal thickness was symmetrically divided (e.g. Ni/Ti/Ni: 3/10/3 μm). Experiment was conducted with following pulse current pattern: 210 A/190 A and 0.5 Hz frequency.

Three methods were used for samples characterization: XRD, SEM/EDS and DSC. Figure 5. 10 presents XRD patterns for all configurations.

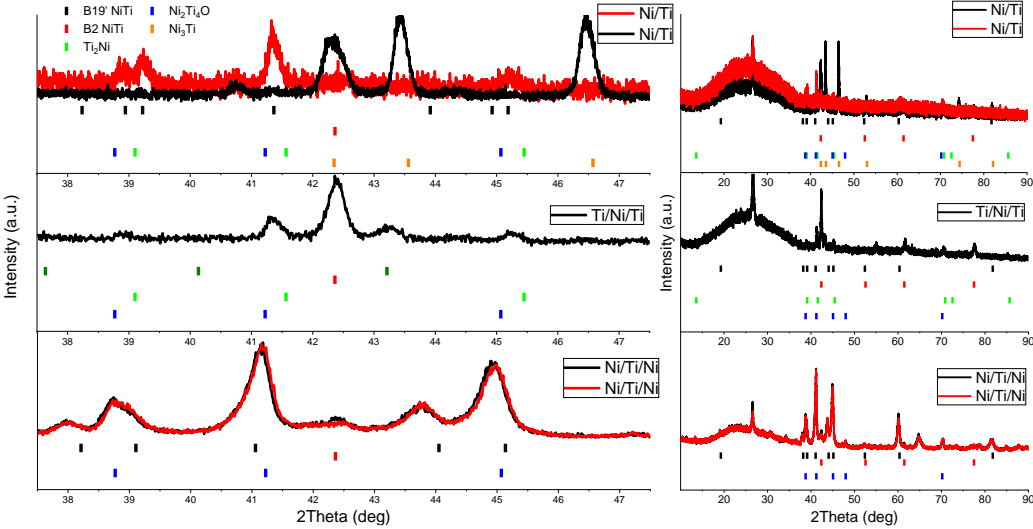


Figure 5. 10: X-Ray Diffraction patterns for Ni/Ti, Ni/Ti/Ni and Ti/Ni/Ti configuration. Right panel shows full range and the left panel is a zoom.

The Ni/Ti configuration exhibits differences between both surfaces: NiTi B19' with Ni<sub>2</sub>Ti<sub>4</sub>O phase from titanium, B2 NiTi and Ni<sub>3</sub>Ti from nickel side. The Ni/Ti/Ni configuration surfaces shows peaks in similar positions of NiTi B19', B2 and Ni<sub>2</sub>Ti<sub>4</sub>O phases. NiTi B2 and Ni<sub>2</sub>Ti<sub>4</sub>O phases are present at both sides of Ti/Ni/Ti configuration. The Ti/Ni/Ti configuration exhibit presence of B2 NiTi, Ti<sub>2</sub>Ni and Ni<sub>2</sub>Ti<sub>4</sub>O phases, with dominance of NiTi B2 phase.

Figure 5. 11, Figure 5. 12 and Figure 5. 13 shows SEM/EDS cross sectional point measurements for all configurations.

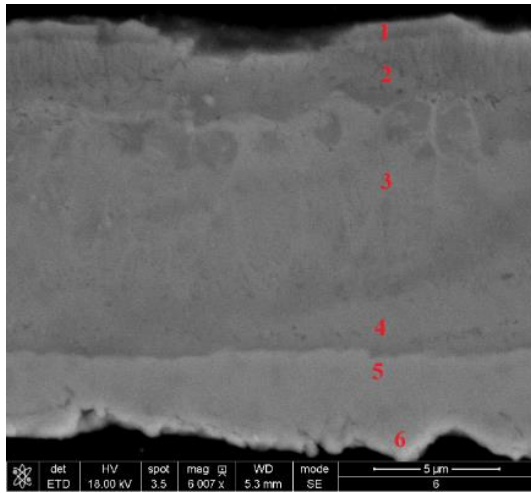


Figure 5. 11: SEM/EDS point measurements of Ni/Ti configuration (distance measured from upper surface).

The uncertainty is of the order of measurement point size. For Ni/Ti configuration partial diffusion process can be observed. From the top of the image almost pure titanium with small addition of nickel ( $\sim 0.6 \mu\text{m}$ ),  $\text{Ti}_2\text{Ni}$  phase ( $\sim 2.4 \mu\text{m}$ ), NiTi (rich in titanium and further in nickel,  $\sim 10.5 \mu\text{m}$  in total) and  $\text{Ni}_3\text{Ti}$  ( $\sim 3-4 \mu\text{m}$ ) phase from the opposite surface. SEM image show dendritic type microstructure in the area of NiTi phase. Based on the contrast, phases with higher composition of nickel result in a brighter color, and titanium - in darker one. It can be seen that higher NiTi phase thickness is produced in the area of initial titanium zone. Also much more homogenized NiTi region is located at  $\text{Ni}_3\text{Ti}$  phase – in the initial pure nickel zone. The titanium zone after diffusion is mainly characterized by dendritic structure of NiTi phase, with its developed, rough boundary at the  $\text{Ti}_2\text{Ni}$  phase region (between point 2 and 3). The last one shows elongated forms perpendicular to the sample surface towards residual Ti, as reported in [71], [165].

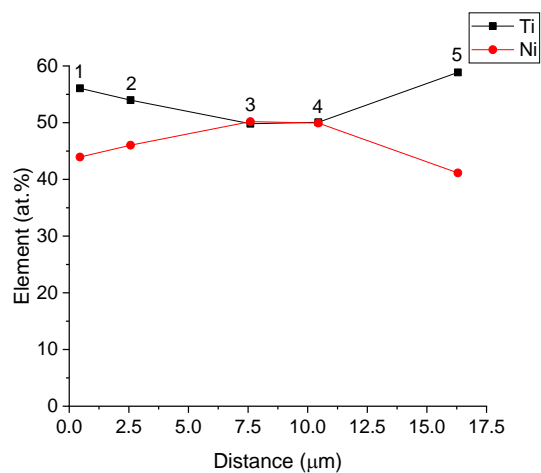
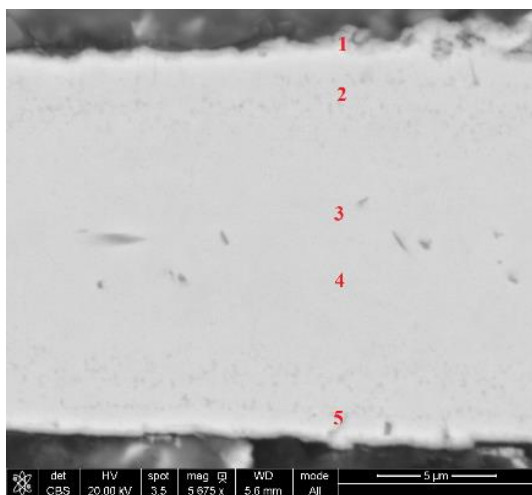


Figure 5. 12: SEM/EDS point measurements of Ni/Ti/Ni configuration (distance measured from upper surface).

Ni/Ti/Ni configuration shows a significant difference in comparison with the previous one. Diffusion occurred in the whole volume, and inhomogeneities are closer to both surfaces (point 2 and 5). Central part of the material is well diffused (about 50:50 of at.% Ti/Ni), and closer to the surfaces increase of titanium content is observed (although below 60 at.%). Microstructure shows an increase of titanium rich particles area along both surfaces. In the middle, small Kirkendall voids are present. During diffusion process, last undiffused phase in such a configuration is  $Ti_2Ni$ , which is in good agreement with composition of observed particles.

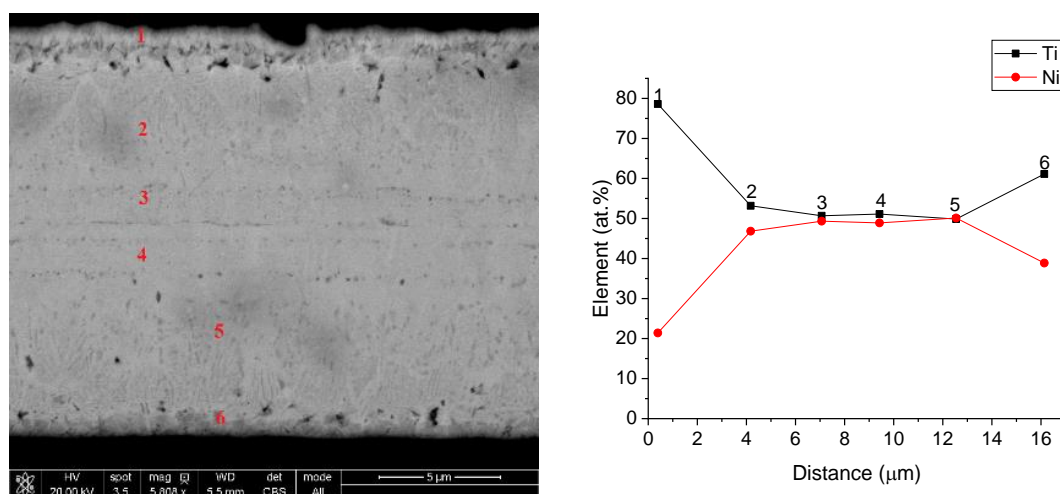


Figure 5. 13: SEM/EDS point measurements of Ti/Ni/Ti configuration (distance measured from upper surface).

The last configuration discussed is Ti/Ni/Ti. Diffusion occurred also in the whole material volume. Higher titanium content is found closer to the surfaces, and small elemental content variations around the 50:50 at.% in the center (see Figure 5. 13). The material show interesting microstructure in comparison with the previous types. It is similar to that in the NiTi area from the Ni/Ti configuration close to the titanium surface. Also small Kirkendall voids in characteristic rows parallel to the sample surfaces can be observed. Higher titanium content corresponds to  $Ti_2Ni$  phase presence at both sample surfaces. Surprisingly, the top surface microstructure is different from the bottom one, where possible oxidation occurred.

In the other part of the foil, undiffused  $Ni_3Ti$  phase area can be seen in the middle of the image (see Figure 5. 14). Image denoted as a) show final steps of  $Ni_3Ti$  area decomposition during the diffusion process. In the image b) higher magnification is shown, where presence of small elongated particles (light grey color) in the NiTi matrix with diameter of 0.1 μm and length of ~0.5 - 1.3 μm. Closer to the surfaces, a collection of  $Ti_2Ni$  (dark grey color) particles of different size between NiTi phase dendrites can be seen. With respect to the shape, these particles are very similar to  $Ni_4Ti_3$  phase obtained after annealing

of Ni-Ti nickel rich compound [166], [167] and powder sintering [80]. Also external stress may be an influence [168]. Interestingly, lighter areas can also be seen in the region of NiTi dendrites. It should be emphasized that, based on Ni-Ti phase diagram (see Figure 1. 6), this particle composition can be specified as Ni<sub>3</sub>Ti phase or, based on the study [80], as Ni<sub>4</sub>Ti<sub>3</sub>. This illustrates a transformation of Ni<sub>3</sub>Ti compound into NiTi phase, by its disintegration into smaller longitudinal particles, which further are transformed into NiTi phase. In a closer look, some similarities of their shape to NiTi dendritic structure can be noted. Due to the NiTi phase growth, the Ni<sub>3</sub>Ti phase content lowers [71]. It is considered that during diffusion process, due to a concentration gradient, titanium from Ti<sub>2</sub>Ni phase diffuses into Ni<sub>3</sub>Ti phase. Nickel diffusion undergoes predominantly in the opposite direction from the rich in nickel dendrites, which then transform into NiTi phase. Taking into account the SEM image, the diffusion and elemental mixing result in appearance of needle-like particles. External pressure creates stress, which additionally influences the process. It is worth noting, that the lowest melting point (at ~942 °C) in the Ni-Ti phase diagram is in Ti - Ti<sub>2</sub>Ni phase area (see Figure 1. 7, red point). Next eutectic point is in the NiTi-Ni<sub>3</sub>Ti zone – at ~1118 °C (see Figure 1. 6, blue point). This may explain why the Ti<sub>2</sub>Ni and Ni<sub>3</sub>Ti phases are initially formed and finally the NiTi phase is created in such a synthesis process.

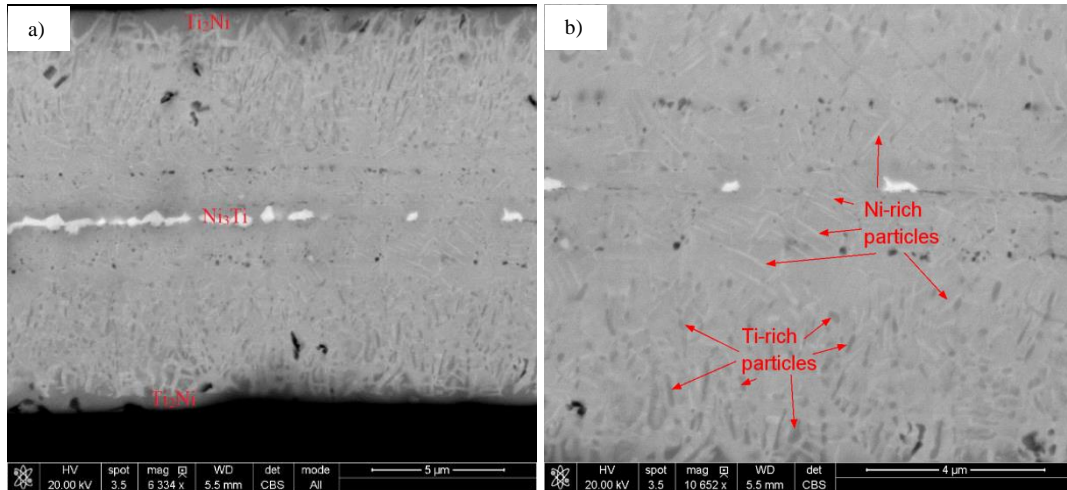


Figure 5. 14: SEM/EDS point measurements of Ti/Ni/Ti configuration in different area: a) whole cross-section and b) zoom on the partial area.

It is worth noting that a possible reason between Ni/Ti/Ni and Ti/Ni/Ti configurations is Ti<sub>2</sub>Ni phase position. When titanium foil is placed between nickel ones, dendritic structures are created from both sides and tend towards interior of the material volume – in the opposite directions. Ni<sub>3</sub>Ti phase located closer to the both surfaces is converted into the NiTi phase due to titanium diffusion. In the interior, dendrites are connecting, which results in faster homogenization. Opposite situation can be seen for the Ti/Ni/Ti configuration, where

dendrites are tending towards both surfaces and the external parts of the material are homogenized poorer than interior.

DSC measurements for the Ni/Ti, Ni/Ti/Ni and Ti/Ni/Ti samples are presented in Figure 5. 15.

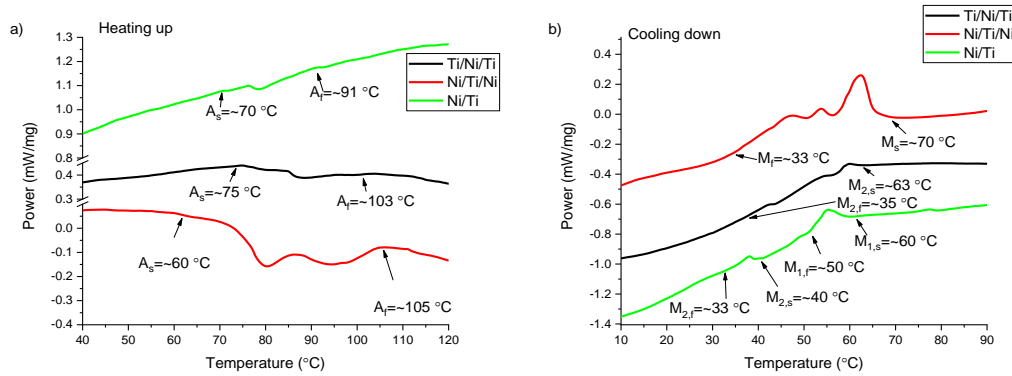


Figure 5. 15 Differential Scanning Calorimetry measurements of the Ti/Ni/Ti (black), Ni/Ti/Ni (red) and Ni/Ti (green) configurations with marked transitions temperatures.

During cooling martensitic transformation can be seen (see Figure 5. 15 b) with marked transition temperatures): they occur in similar temperature range. Ni/Ti and Ti/Ni/Ti samples exhibit very narrow multistage transformations. For Ni/Ti/Ni configuration two peaks can be distinguished. During cooling even three peaks can be observed, which can be attributed to the R-phase occurrence between austenite and martensite. Similar effect was reported for NiTi ageing process [144], [162], [169].

The Ni/Ti/Ni sample in a comparison with other configurations exhibit good plasticity – other cannot be deformed and can be easily broken. It could be attributed to the  $Ti_2Ni$  phase detected close to the surface and the dominant B2 NiTi austenitic phase.

Results obtained for all configurations lead us to the conclusions that the most effective configuration for obtaining a good shape memory micro-foil is Ni/Ti/Ni. It exhibits transformations at the temperatures above room temperature and below 100 °C, which was intended. The Ni/Ti and Ti/Ni/Ti samples show much weaker transitions in similar temperature range.

Figure 5. 16 presents Shape Recovery Rate (SRR) dependence obtained from bending test performed at room temperature. Test were performed for all configurations. The results show that shape recovering starts at 55 °C and finishes at different temperatures depending on the initial strain value. This is consistent with DSC data (see Figure 5. 15), where a multistep transformation can be observed. The sample exhibits 100 % of SRR up to ~100 °C for the maximum value of the used initial bending strain, and up to 85 °C for 1 %. Analogous test has

been attempted for the Ni/Ti and Ti/Ni/Ti sample but it indicated its high elasticity with no signs of plasticity. Its bending to a similar strain value as for the Ni/Ti/Ni sample caused its breaking.

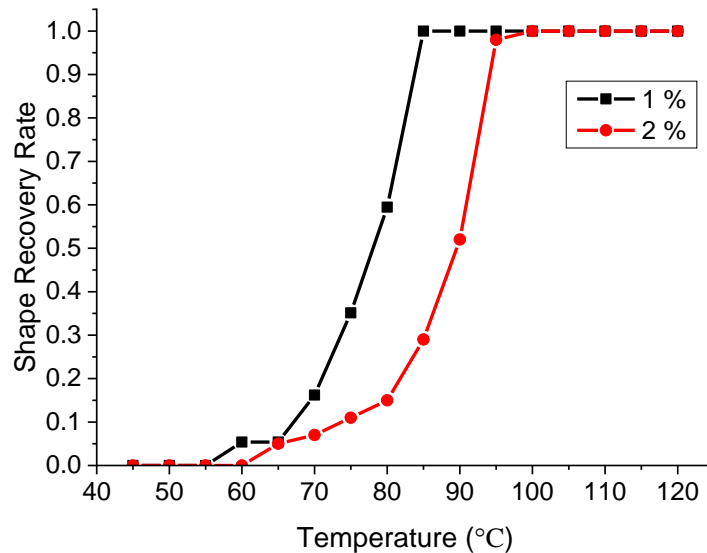


Figure 5. 16: Shape Recovery Rate for Ni/Ti/Ni temperature dependence after bending strain of: 1 and 2 %.

Creation of  $Ti_2Ni$  compound at the surfaces can be positive for applications. Taking into consideration study [170], it was shown that  $Ti_2Ni$  compound in porous compound created during SHS process possess even better biocompatibility than NiTi.

### 5.2.2 Compositional dependence

Based on powder metallurgy and phase diagrams important thing for alloys/compounds preparation is elemental composition. For this purpose six samples were prepared with different foils thickness coefficient (FTC): from 1 to 1.8. Compressive pressure of 13 MPa of external uniaxial compression pressure (it increase up to 20 MPa during heating), heating temperature of  $\sim 700$  °C, sintering time of 60 minutes for all samples (besides 120 min for 1, 1.5 and 180 min for 1.2), 5 mm of mold diameter and low vacuum atmosphere was used. Samples compositions are shown in Table 5. 1 with foils layers thicknesses and used pulse current values with frequency of 0.5 Hz for all materials. This property was evaluated by samples both sides XRD measurements - patterns are presented in Figure 5. 17. SEM/EDS analysis is also presented in Figure 5. 20, Figure 5. 21, Figure 5. 22, Figure 5. 23 and Figure 5. 24, respectively for 1, 1.2, 1.4, 1.7 and 1.8 of FTC values.

Table 5. 1: List of the samples with different elemental compositions – values are estimated.

Nickel foils thickness [μm]:	Titanium foils thickness [μm]:	FTC:	Nickel (at%):	Titanium (at%):	Modulated DC current [A]:
10	10	1.0	61	39	210/190
10	12	1.2	58	42	210/190
5	7	1.4	54	47	230/210
10	15	1.5	52	48	200/180
3	5	1.7	49	51	200/180
5	9	1.8	47	53	230/210

Sample with higher nickel content exhibit presence of Ni<sub>3</sub>Ti phase from both sides. When elemental composition is closer to 50:50 ratio, B2 phase main peak intensity appears. It can be also detected in the samples with lower nickel content (52.5 at%). Only in the sample with foils thickness coefficient equal to 1.7, B19' phase can be detected. Based on SEM/EDS results it can be seen that for FTC lower than 1.4, additional phase (Ni<sub>3</sub>Ti) is created from both surfaces sides – it can be also confirmed by XRD results. Based on sintering time (180 minutes for 1 and 120 min for 1.2) it can be seen that longer annealing time can lower Ni<sub>3</sub>Ti thickness for advance of NiTi phase. Another explanation can be lower initial foils thicknesses (~21 μm for 1 with ~2 μm of Ni<sub>3</sub>Ti phase and ~22 μm for 1.2 with ~3.5 μm of Ni<sub>3</sub>Ti phase based on SEM images). Materials with 1.4 - 1.7 possess high homogeneity of elements distribution in whole material thickness. Foil with FTC of 1.8 exhibits one side higher titanium content, which can be associated with Ti<sub>2</sub>Ni and another with NiTi phase based on SEM/EDS. XRD results confirms presence of mentioned phases and implies content of Ni<sub>4</sub>Ti<sub>3</sub> or BN phase. All samples exhibit small surface oxidation [104], [169], [171], [172] and NiTi compositional phases presence inside of the samples – with different thicknesses. Foils with nearly homogeneous distribution of elements in whole its volume can be obtained based on application of proper foils thicknesses – which can be estimated by FTC. Samples with different FTC value from 1.7 do not exhibit plasticity, but based on mechanical properties are brittle. It can be based on presence of intermetallic compounds and dominant presence of austenite phase. From microstructure point: with nickel increase, particles rich in titanium close to the surfaces can be seen (for FTC: 1.4). Highest content results in separated layers creation (for FTC: 1 and 1.2). Higher titanium

concentration results in  $Ti_2Ni$  phase content. Shape memory effect was also checked on temperature dependent XRD measurements for sample with FTC of 1.7 and 1.5. Sample with 1.7 was measured in three temperatures: 27, 60 and 120 °C – see Figure 5. 18. It can be seen that between 60 and 120 °C phase transformation occurred (between martensite and austenite phase). Patterns in 27 and 60 °C looks very similar – increase of B2 NiTi peak intensity can be observe. For comparison sample with lower value of coefficient (1.5) measured in lower temperatures: 75 (-198 °C) and 300 K – see Figure 5. 19. It is shown that there is no transition between high temperature austenite phase and the low temperature martensite.

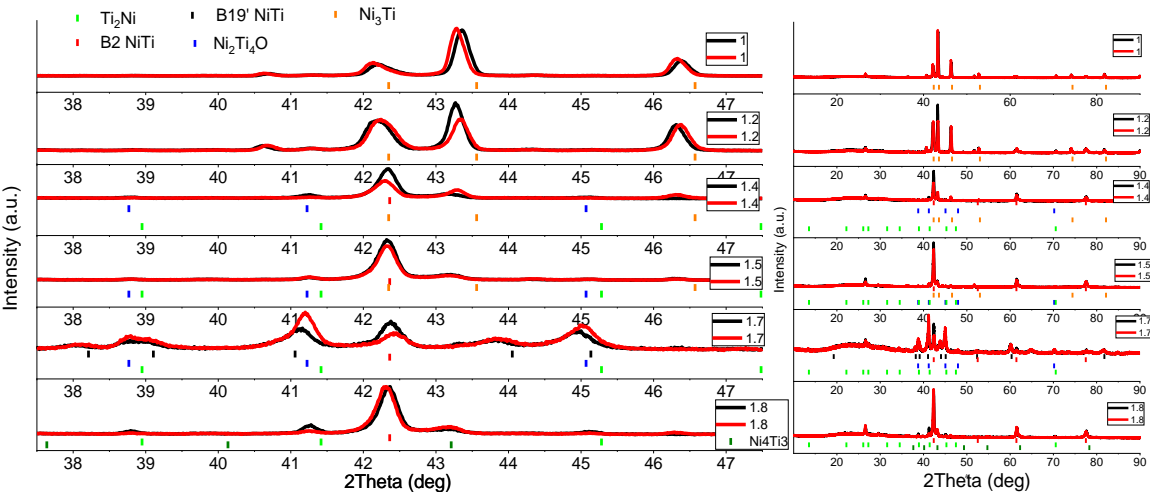


Figure 5. 17: Both sides X-Ray Diffraction patterns for samples with different foils thickness coefficient. Right panel shows full range and the left panel is a zoom.

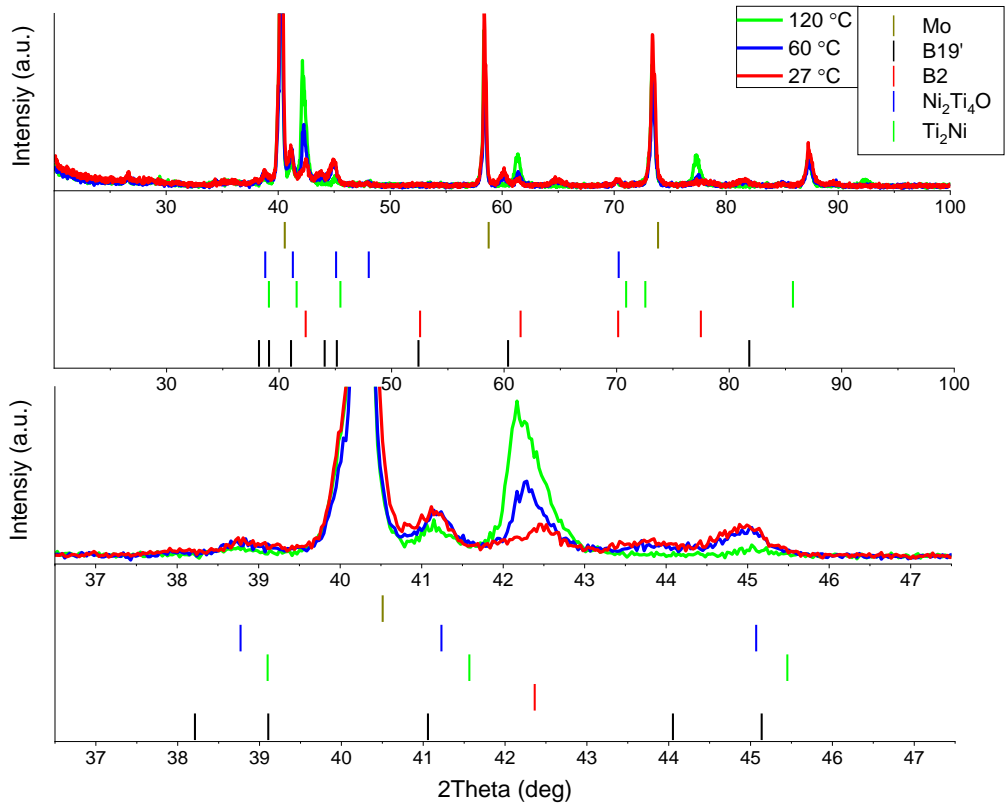


Figure 5. 18: X-Ray Diffraction patterns at various temperatures: red - ambient temperature (27 °C), blue - 60 °C and green - 120 °C for sample with thickness coefficient of 1.7.

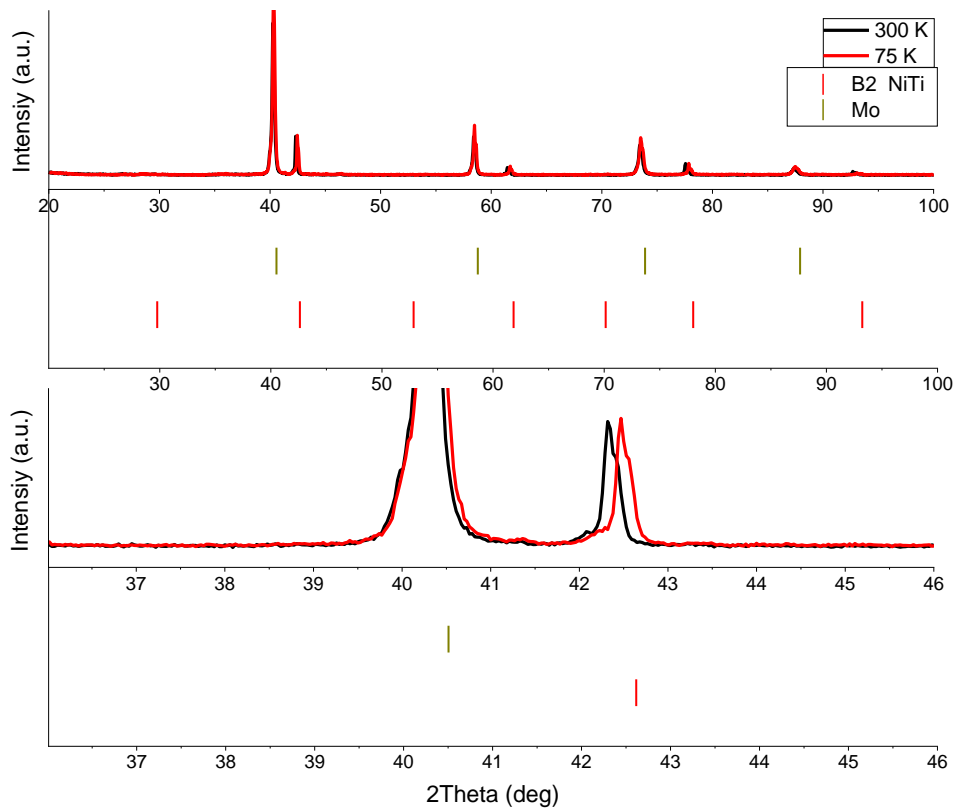


Figure 5. 19: X-Ray Diffraction patterns at various temperatures: black - ambient temperature (300 K) and red - 75 K for sample with thickness coefficient of 1.5.

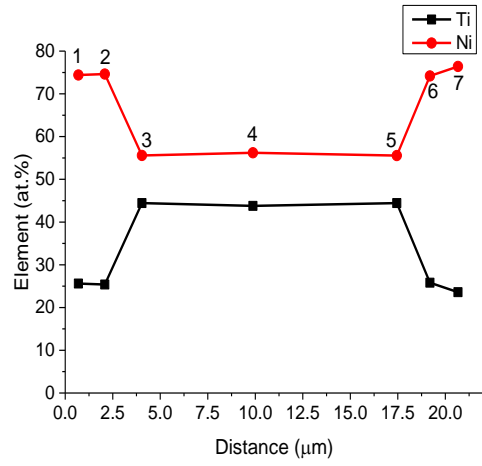
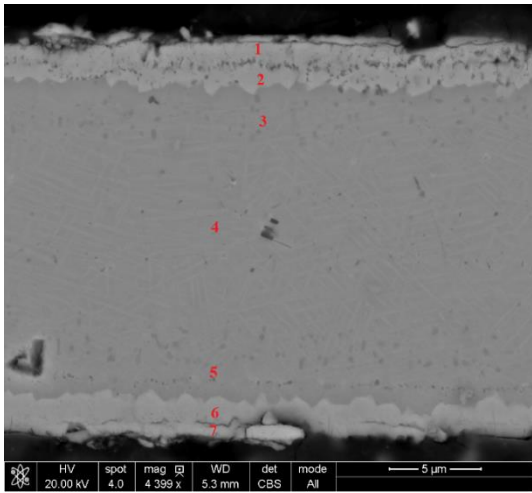


Figure 5. 20: SEM/EDS point measurements of sample with FTC: 1 (distance measured from upper surface).

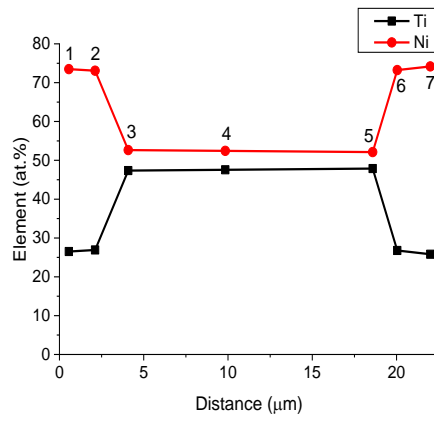
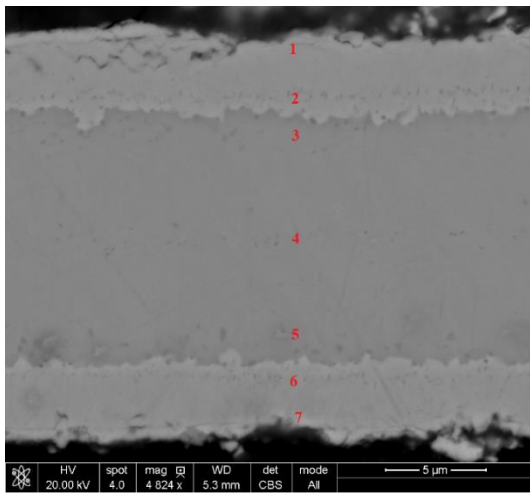


Figure 5. 21: SEM/EDS point measurements of sample with FTC: 1.2 (distance measured from upper surface).

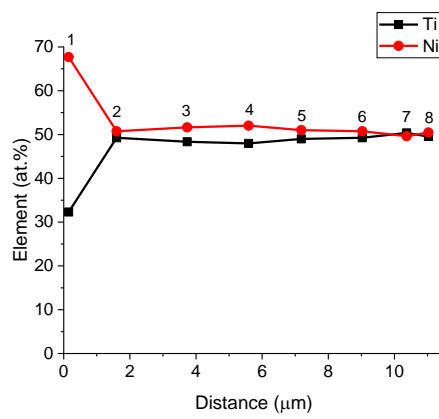
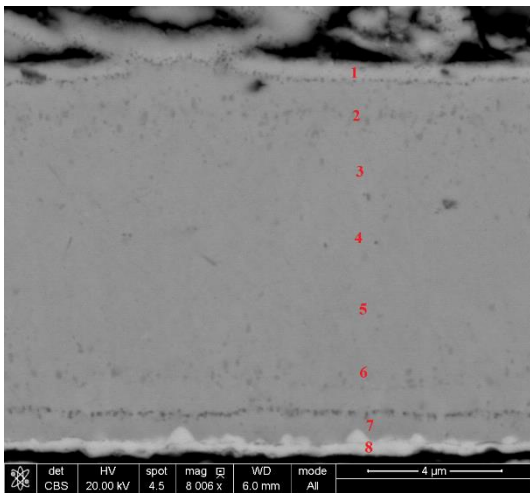


Figure 5. 22: SEM/EDS point measurements of sample with FTC: 1.4 (distance measured from upper surface).

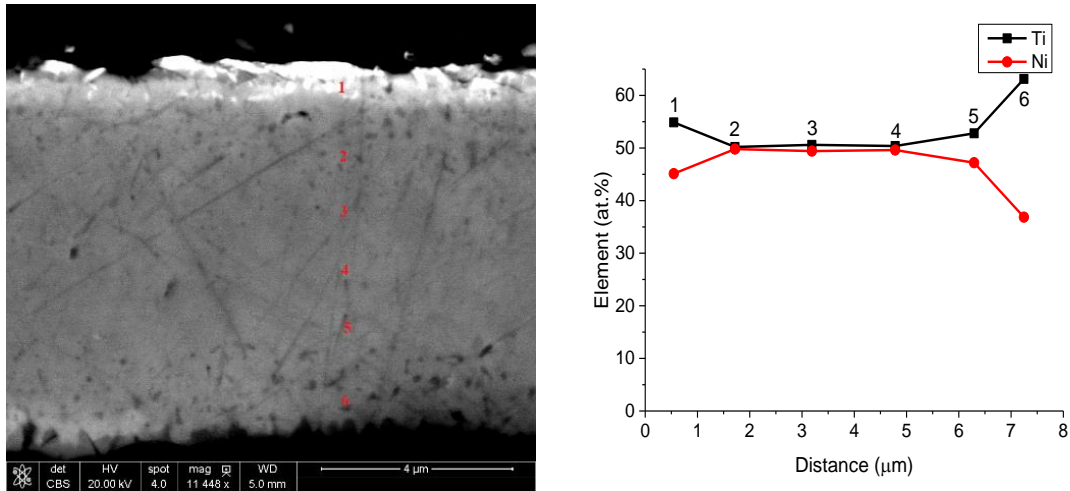


Figure 5. 23: SEM/EDS point measurements of sample with FTC: 1.7 (distance measured from upper surface).

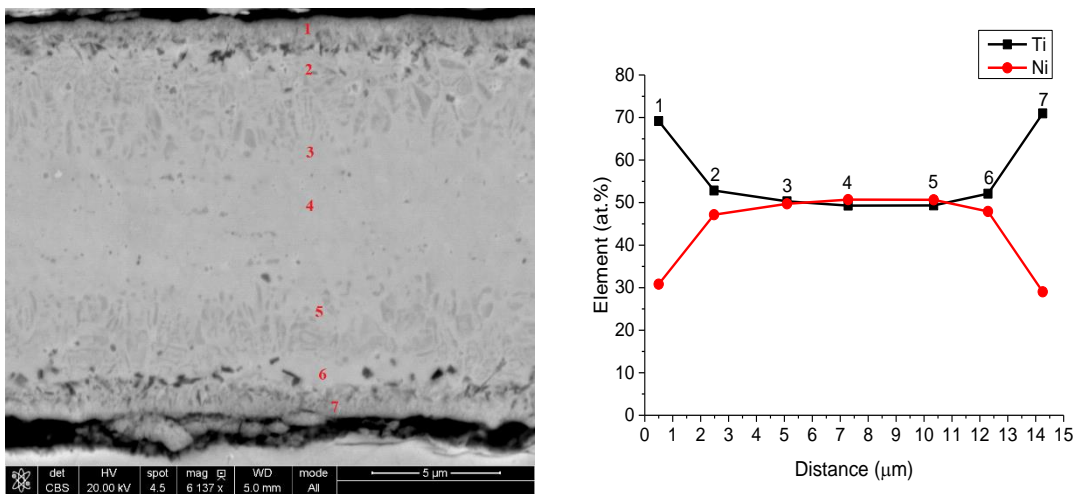


Figure 5. 24: SEM/EDS point measurements of sample with FTC: 1.8 (distance measured from upper surface).

Presented data and results of other studies (e.g. from powder metallurgy) show that initial composition is very important to obtain full volume compound from input materials. Long distance diffusion is more complex phenomenon than it takes in powder sintering. Initial powders are mix together and alloyed in rolling mills, which ensure homogenous element distribution and much shorter diffusion distance. Long distance diffusion require much longer annealing/sintering times. This study shows that it could be good for micro-materials synthesis. Based on the study [68] and obtained results (see point 6 and 7 in the Figure 5. 38), during diffusion in NiTi compound area can be seen different elemental content at different sides of diffusion interface of this phase. It is proposed to subject foils for short annealing process to stabilize elements distribution in lower temperatures. Proposed coefficient can be useful for fast foil thicknesses calculation to obtain compounds with almost desired composition. Mismatch in composition results in multi-phase compounds with laminate-like structures - which were shown – see results for 1, 1.2 and 1.8 of FTC.

Last results in this section are presented in Figure 5. 25. It is a naked eye proof of shape memory effect observed in foil with coefficient value of 1.7. It is in good agreement with literature data describing dependence of transformations temperatures and their compositions [145], [173].

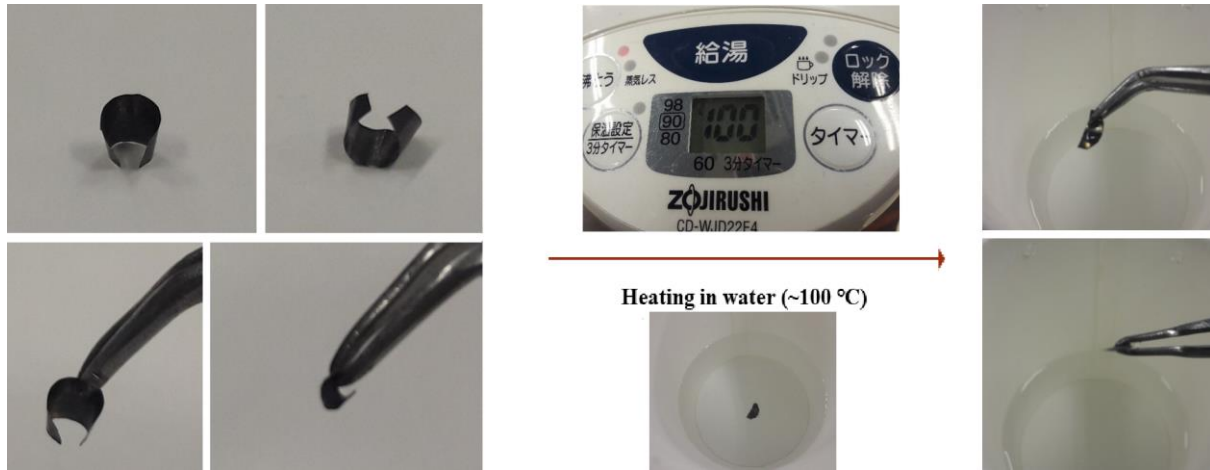


Figure 5. 25: Shape recovery effect observed at heating in boiled water for the sample with thickness coefficient of 1.7.

### 5.2.3 Dependence on sintering time

The study of influence of sintering time (for 20, 40 and 60 min) was also investigated for 8  $\mu\text{m}$  in thickness samples in 700 °C (5 mm of mold diameter) under 13 MPa of external uniaxial compression pressure and pulse current pattern of 220 A/200 A with frequency of 0.5 Hz for all materials in vacuum. XRD patterns for obtained materials are presented in Figure 5. 26. It can be seen that patterns for all sample are similar and main peaks corresponds to B19' phase.

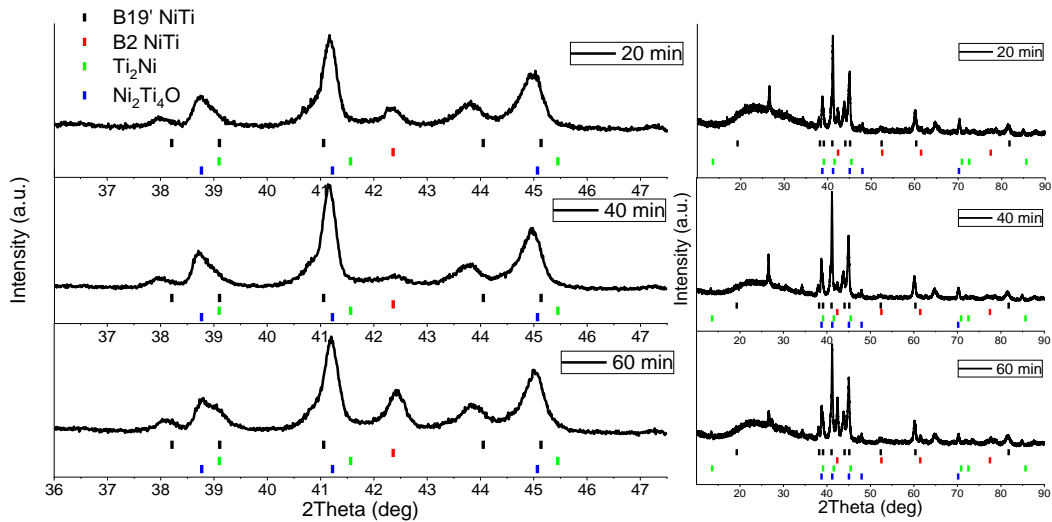


Figure 5. 26: X-Ray Diffraction patterns from both sides of samples after 20,40 and 60 min of sintering time. Right panel shows full range and the left panel is a zoom.

Figure 5. 27, Figure 5. 28 and Figure 5. 29 presents SEM images and EDS cross-sectional point measurements with marked nickel and titanium content. It can be seen that after 40 minutes of sintering elemental distribution is homogenous with small deviations close to the both surfaces – possible due to oxidation process which cannot be stated for sure – polishing process. After 20 minutes two areas can be distinguished with different elemental composition: around 50:50 (NiTi) and 70:30 (Ni<sub>3</sub>Ti) of Ni/Ti. In both regions nickel content is higher, which could be based on the spatial diffusion. The samples thickness changes through sintering time: ~10.34, ~8.34 and ~7.51 μm for 20, 40 and 60 minutes, respectively. It looks like the highest change with signs of cracking can be observed after 20 minutes. Asymmetrical diffusion can be also seen, which is associated with uneven thicknesses of the pure nickel from both materials sides. Changes can be associated with oxygen uptake through the synthesis process and material swelling. Another explanation could be intermetallic compounds creation during the process.

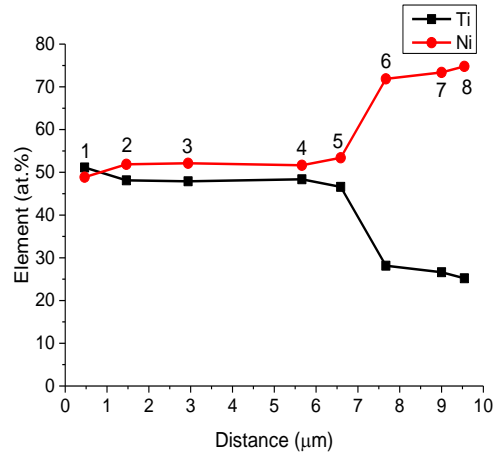
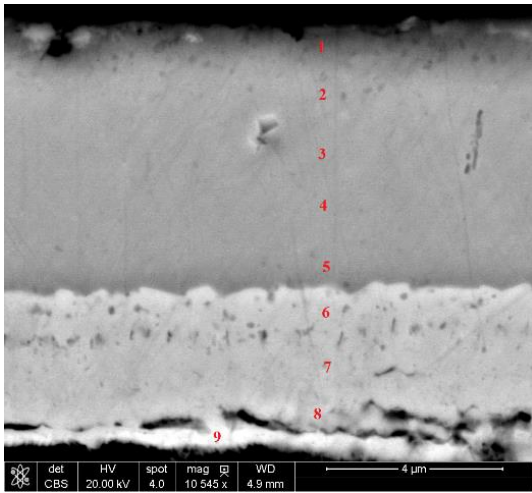


Figure 5. 27: SEM/EDS point measurements of sample after 20 min of sintering (distance measured from upper surface).

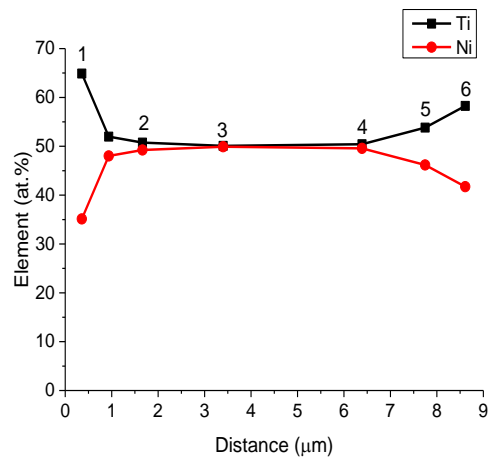
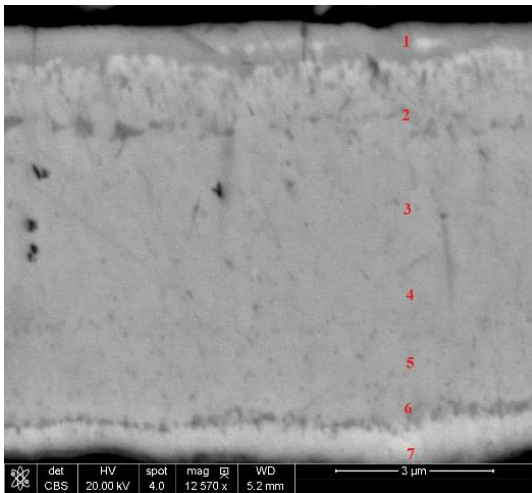


Figure 5. 28: SEM/EDS point measurements of sample after 40 min of sintering (distance measured from upper surface).

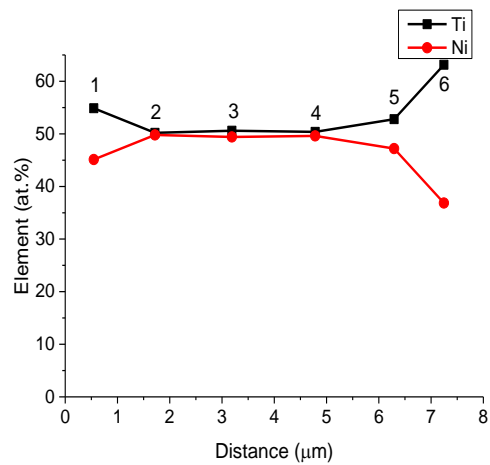
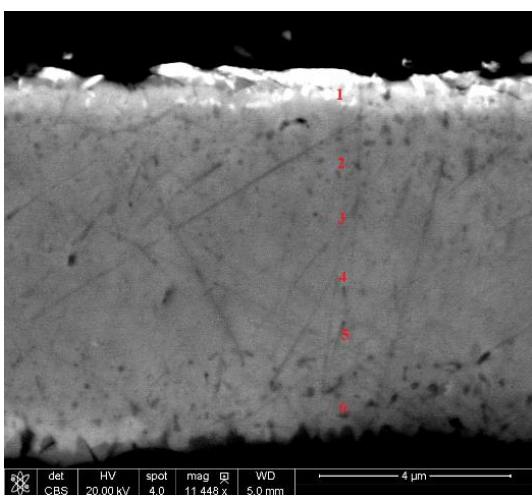


Figure 5. 29: SEM/EDS point measurements of sample after 60 min of sintering (distance measured from upper surface).

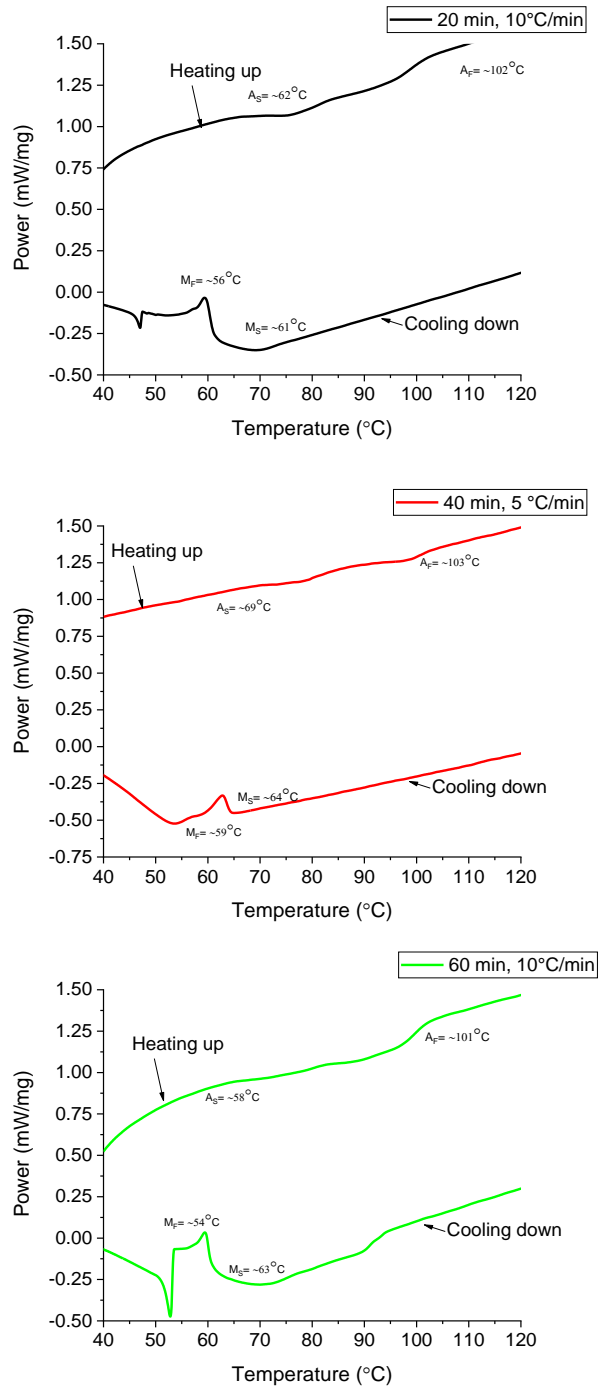


Figure 5. 30: Results of Differential Scanning Calorimetry measurements for samples after 20 (black line), 40 (red line) and 60 (green line) minutes of sintering time with marked transformation temperatures.

DSC measurements performed in air with heating/cooling speed of 10 °C for 20 and 60 min, and 5 °C for 40 min sample. Based on DSC measurements presented in Figure 5. 30, it can be seen that for all samples martensitic transformations and the reverse one occur at temperatures in similar range, which is in good agreement with other results. Multistage transformation also is seen.

## 5.2.4 Dependence on the thickness

This subchapter is focused on properties of foils thickness: 8, 16 and 24  $\mu\text{m}$ . 8  $\mu\text{m}$  foil were prepared from 2/5/1  $\mu\text{m}$  of Ni/Ti/Ni foils, 16  $\mu\text{m}$  from 3/10/3  $\mu\text{m}$  of Ni/Ti/Ni foils, and 24  $\mu\text{m}$  from 5/15/4  $\mu\text{m}$  of Ni/Ti/Ni foils. Compressive pressure of 13 MPa (it increase up to 20 MPa during heating), sintering time of 60 minutes, heating temperature of  $\sim 700$   $^{\circ}\text{C}$ , 5 mm of mold diameter and low vacuum were used. For 8 and 24  $\mu\text{m}$  foils, pulse current pattern of 220 A/200 A, and for 16  $\mu\text{m}$  230A/ 210A with 0.5 Hz frequency. Analysis like before focused on three methods: XRD, SEM/EDS and DSC.

XRD patterns for obtained materials are presented in the Figure 5. 31. It can be seen that patterns for all samples are similar and main peaks corresponds to B19' phase. Material with higher thickness (24  $\mu\text{m}$ ) shows presence of  $\text{Ni}_3\text{Ti}$  phase. It is based on too short sintering process and not homogenous elemental distribution. Markers for  $\text{Ni}_2\text{Ti}_4\text{O}$  and  $\text{Ti}_2\text{Ni}$  phases are also show – possible surface oxidation. 8 and 16  $\mu\text{m}$  foils exhibit difference in intensity of B2 main peak at 42.5 deg have been notice, which is associated with too long synthesis time at chosen temperature [174].

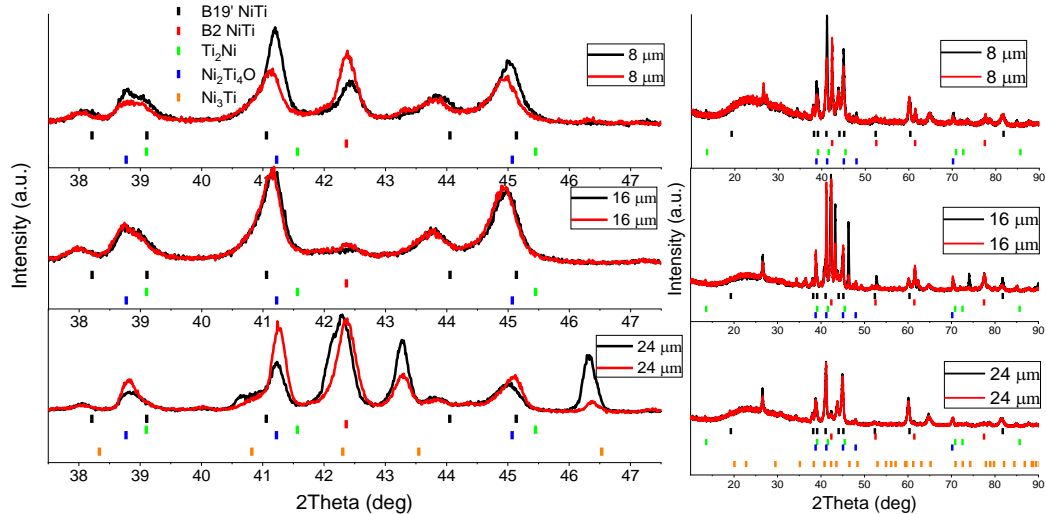


Figure 5. 31: Both sides X-Ray Diffraction patterns of samples with 8, 16 and 24  $\mu\text{m}$  thickness. Right panel shows full range and the left panel is a zoom.

Figure 5. 32, Figure 5. 33 and Figure 5. 34 presents SEM images and EDS cross-sectional point measurements with marked nickel and titanium content. It can be seen that after sintering, elemental distribution is homogenous with small deviations close to the both surfaces. In the center of the foils small void can be observed, and closer to the surface – increase number of droplets. They are making a row-like structure in a similar distance from the surfaces.

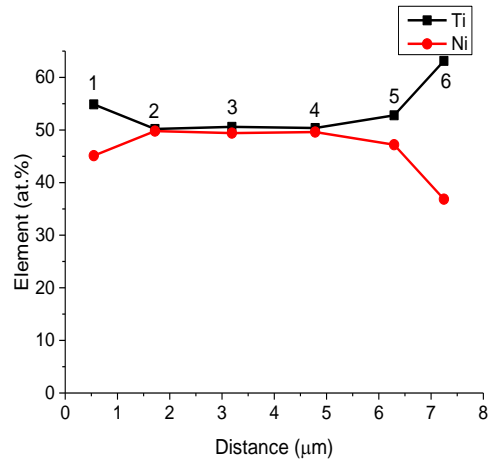
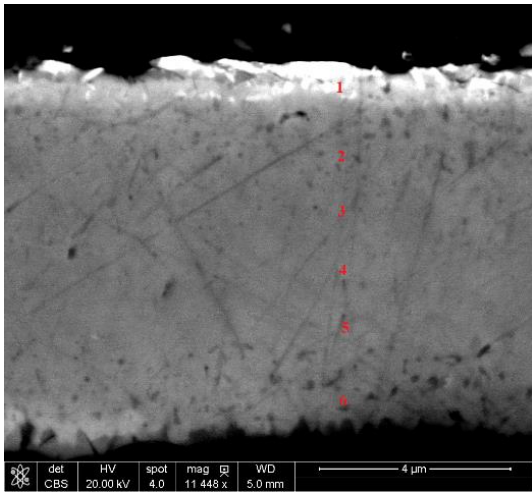


Figure 5. 32: SEM/EDS point measurements of 8 μm foil (distance measured from upper surface).

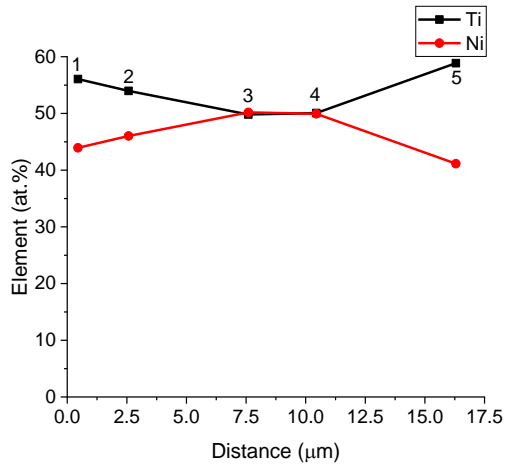
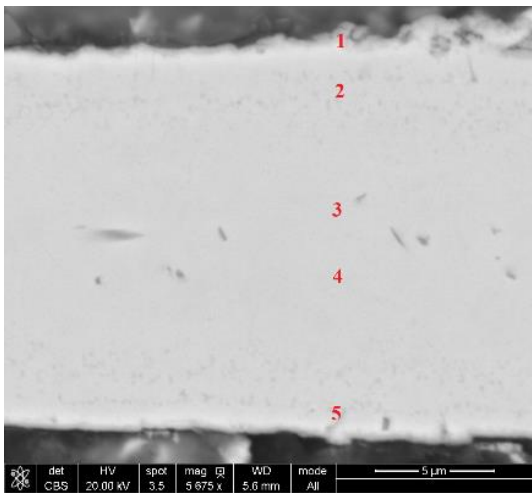


Figure 5. 33: SEM/EDS point measurements of 16 μm foil (distance measured from upper surface).

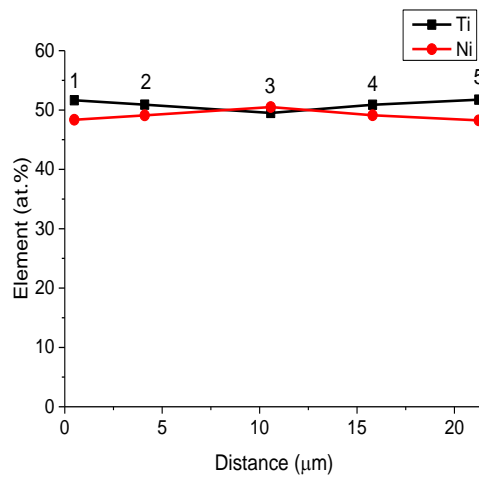
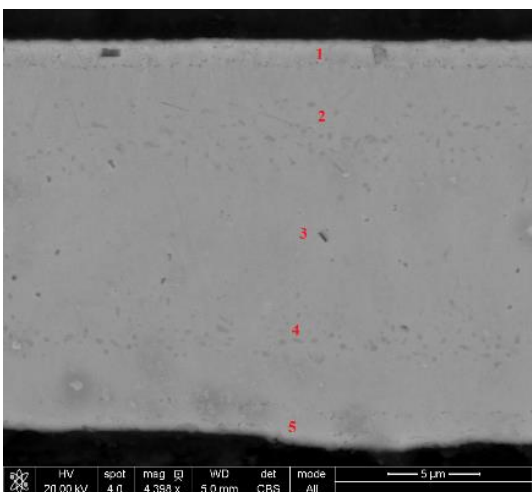


Figure 5. 34: SEM/EDS point measurements of 24 μm foil (distance measured from upper surface).

DSC measurements for all foils can be seen in the Figure 5. 35, with marked transformation temperatures. For 8 and 16  $\mu\text{m}$  heating/cooling speed of 10  $^{\circ}\text{C}/\text{min}$  used, and for 24  $\mu\text{m}$  – 5  $^{\circ}\text{C}/\text{min}$ . 8 and 24  $\mu\text{m}$  measurements performed in air, and 16  $\mu\text{m}$  in argon atmosphere. Their peaks can be observed for all samples. Materials show that austenite/martensite, start/finish temperatures are slightly different with more than one peak. The weakest peaks can be observed for highest foil, which imply longer synthesis time – uneven elemental distribution through whole cross-section.

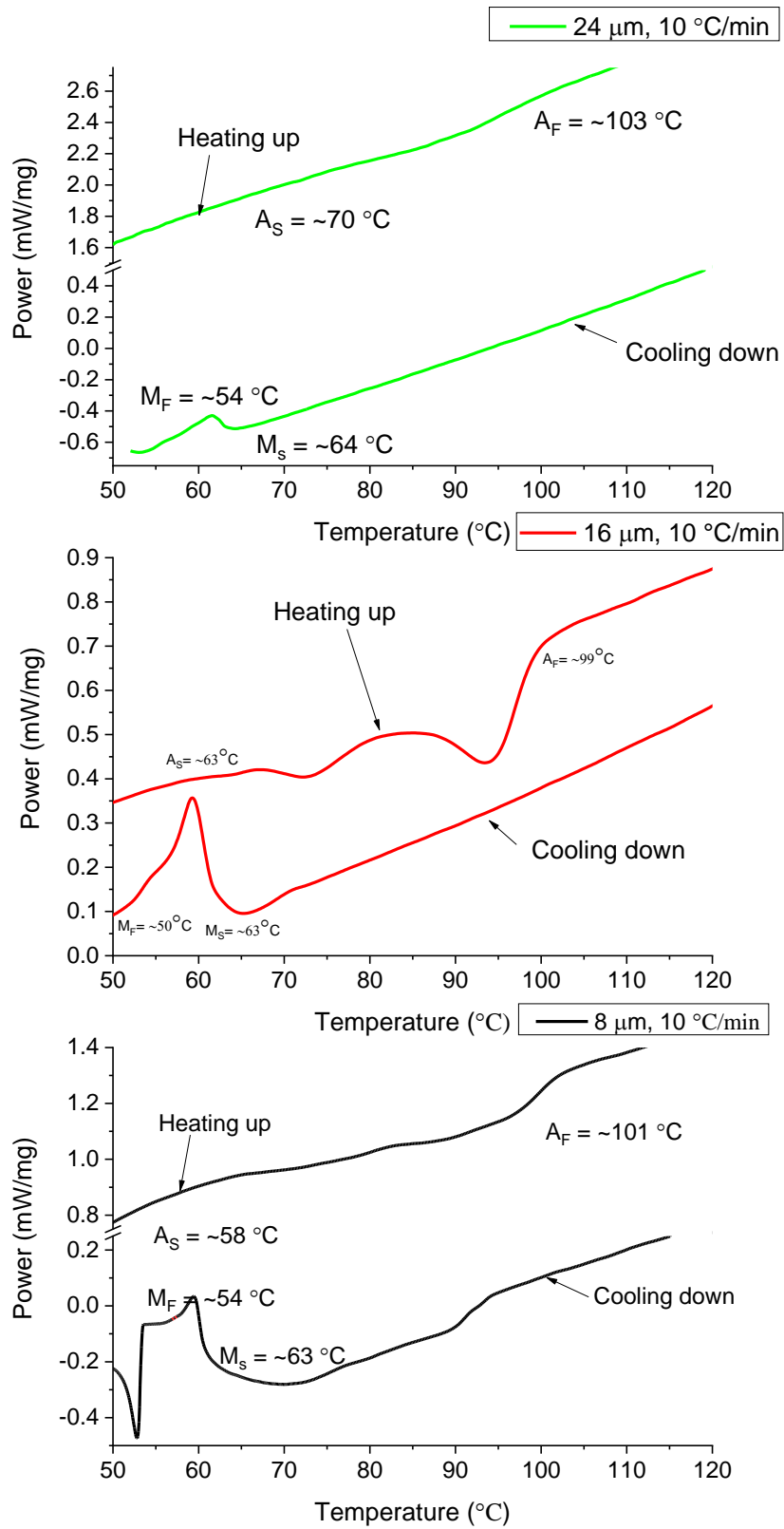


Figure 5. 35: Differential Scanning Calorimetry measurements for samples with 8 (black line), 16 (red line) and 24 (green line)  $\mu\text{m}$  of thickness with marked transformation temperatures.

All collected data show promising results regarding shape memory micro-foil preparation for different thicknesses with multistage transformation and impact on sintering time.

### 5.2.4 Dependence on the time profile of sintering current

This subchapter focuses on comparison of two types of electrical current, namely: direct and pulsed direct used for synthesis. Influence of two current profile types were investigated. It was found that to obtain 700 °C, it is necessary to use 200 A, and for pulsed current 300/20 A at 0.5 Hz frequency. For both samples same foil configuration was used, namely Ni/Ti/Ni (5/10/5 μm), 60 minutes of sintering time under 13 MPa of uniaxial pressure, 5 mm of mold diameter and vacuum of 10 Pa.

Figure 5. 36 presents a SEM/EDS cross-sections of the prepared materials.

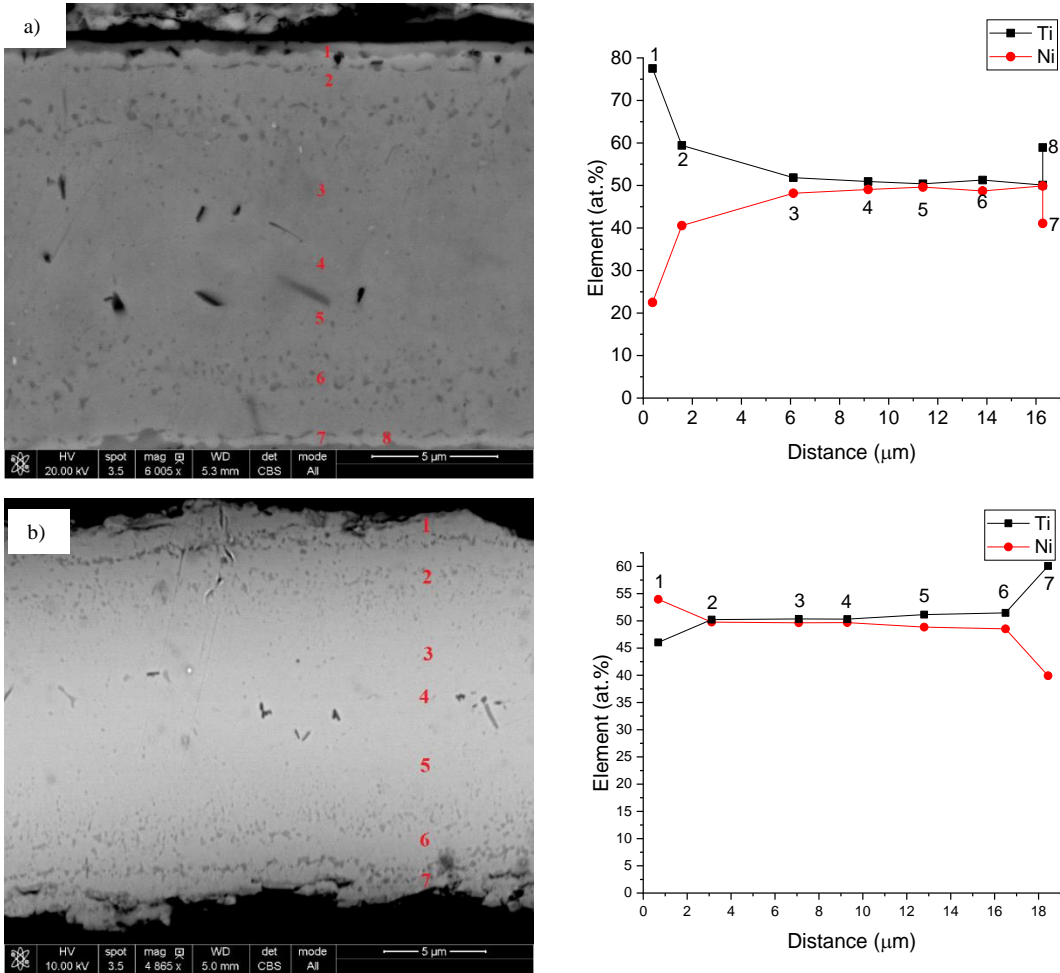


Figure 5. 36: SEM/EDS point measurements of foils prepared by: a) DC and b) pulsed current at 700 °C (points are marked respectively).

It can be seen that for both material similar results were obtained. In the center of the foils, probable small Kirkendall voids are observed with composition close to 50:50. Moving

further to the outer surfaces, increase of  $Ti_2Ni$  particles can be seen, which tends to increase area close to the surfaces. Similar effect obtained in previous section regarding differences between samples configurations. For pulsed current prepared sample, area with high nickel content is presence. For DC material uniform  $Ti_2Ni$  zones are located closely to both surfaces.

Figure 5. 37 presents example of DSC results of Ni/Ti/Ni sandwich type materials by pulsed DC and DC in 700 °C for 60 minutes.

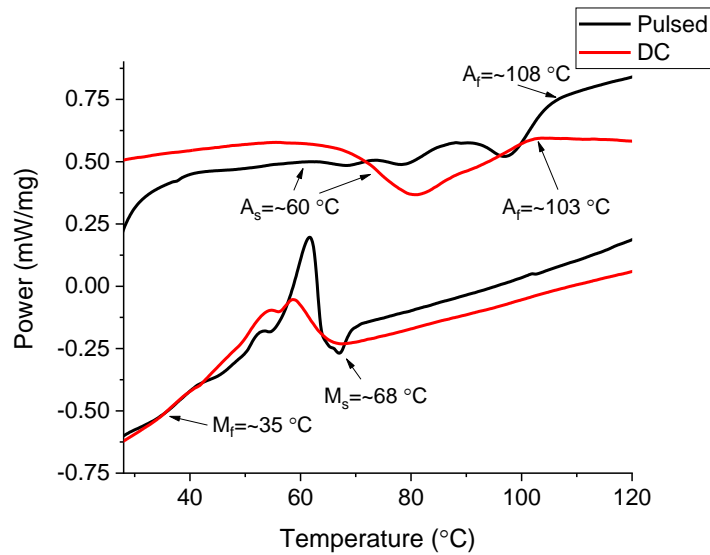


Figure 5. 37: Differential Scanning Calorimetry measurements of foils prepared by DC and pulsed current at 700 °C.

It shows that transformation temperatures are similar, but character of it is different, which suggest that pulses promotes introduction of local inhomogeneities in the bulk of material. Materials produced by DC on the other hand show much more uniform distribution of elements. It is in good agreement with SEM images on which  $Ti_2Ni$  compound layer can be seen next to the surfaces, and in pulsed – much more titanium rich particles spread near the surfaces and no  $Ti_2Ni$  layer presence.

Based on the results presented, differences between prepared samples can be observed. Taking into account necessary direct current effective value to reach each temperature (700 °C by 190 A, respectively) and for pulsed DC (270/20 A with 0.5 Hz for 700 °C), lower value is obtained for the latter one (145 A for 700 °C).

For the importance of the discussion, current flow through a graphite dies which are holding sample foils covered by thin layer of boron nitride. Lubricant material has very good thermal conductivity and at higher temperatures its electrical resistivity decreases [153]–[155]. A comparison with the other studies in which lubricant were not used is now presented.

This study used Ni/Ti diffusion couple at following parameters:  $\sim 267 \frac{A}{cm^2}$ , 13 MPa and 1

hour, and NiTi thickness is  $\sim 10 \mu\text{m}$ . In the first study [71], Ti/Ni/Ti sandwich was used with each foil thickness of  $40 \mu\text{m}$  for 30 minutes of sintering with current density:  $334 \frac{\text{A}}{\text{cm}^2}$  and uniaxial pressure of: 30 MPa, and approximated NiTi thickness is  $\sim 7 \mu\text{m}$ . In the other study [68], diffusion bonding was used in  $900 \text{ }^\circ\text{C}$  under 8 MPa of external pressure for 1 hour between multifoil laminates configuration without current flow. Obtained thickness is  $\sim 7 \mu\text{m}$ . It can be seen that, superior results taking into account used temperature and time is second study. They obtained smaller thickness but in the half of this study sintering time. Second one is this study taking into account that in the last one, much higher temperature was used, and obtained thickness is lower. Taking into account also external pressure, in this study was half of the value of the former one. To sum up, it can be seen additional effect during the diffusion process, which can be assigned to current flow. It have to be emphasized that BN layer is very thin, and used sintering conditions could alter ion conduction. Observed titanium diffusion current dependence in the study [71] is an another argument for the current effect. In the microfoils with Ni/Ti/Ni configuration with appropriate composition, high titanium concentration is present at the surfaces. This may positively influence the elasticity of the material.

### **5.2.5 Magnetic, electrical and thermal properties**

In the present subchapter magnetic, electrical and thermal properties of NiTi microfoils are discussed. For this purpose samples samples with higher diameter (20 mm) were prepared. Used apparatus were described briefly in Chapter 2. Two kind of samples are studied in this subchapter with different thickness, namely:  $26 \mu\text{m}$  (from initial:  $5/16/5 \mu\text{m}$  Ni/Ti/Ni foils) and  $25 \mu\text{m}$  (from initial:  $5/15/5 \mu\text{m}$  Ni/Ti/Ni foils) which are named S1 and S2, respectively. Both samples were sintered for 120 minutes under uniaxial pressure of 3 MPa. S1 obtained in  $630 \text{ }^\circ\text{C}$ , and S2 in  $700 \text{ }^\circ\text{C}$  (Pulse patterns: 500/500 A with 0.5 Hz frequency).

SEM/EDS point measurements obtained from samples cross-sections are presented in Figure 5. 38 and Figure 5. 39. It can be seen that S2 is more homogenous with dotted other intermetallic phases. For the S1 unfinished diffusion can be observed. From the top surface in the image can be seen symmetrical distribution of following phases:  $\text{Ni}_3\text{Ti}$  ( $\sim 1.9/2.5 \mu\text{m}$ ), NiTi ( $\sim 6.4/5.8 \mu\text{m}$ ),  $\text{Ti}_2\text{Ni}$  ( $\sim 1.9/2.2 \mu\text{m}$ ) and in the middle almost pure titanium with the traces of nickel ( $\sim 2.8 \mu\text{m}$ ). Different composition within the NiTi phase is observed between point six (slightly higher titanium content:  $\sim 49.7/50.3 \text{ Ni/Ti at\%}$ ) and seven (higher nickel content:  $\sim 52/48 \text{ Ni/Ti at\%}$ ). Figure 5. 40 show composition of rich titanium particles (point 2

and 3) located close to the both foil surfaces. For both samples detected oxygen level is lower than ~5 at.% and homogenous through whole foil cross-section.

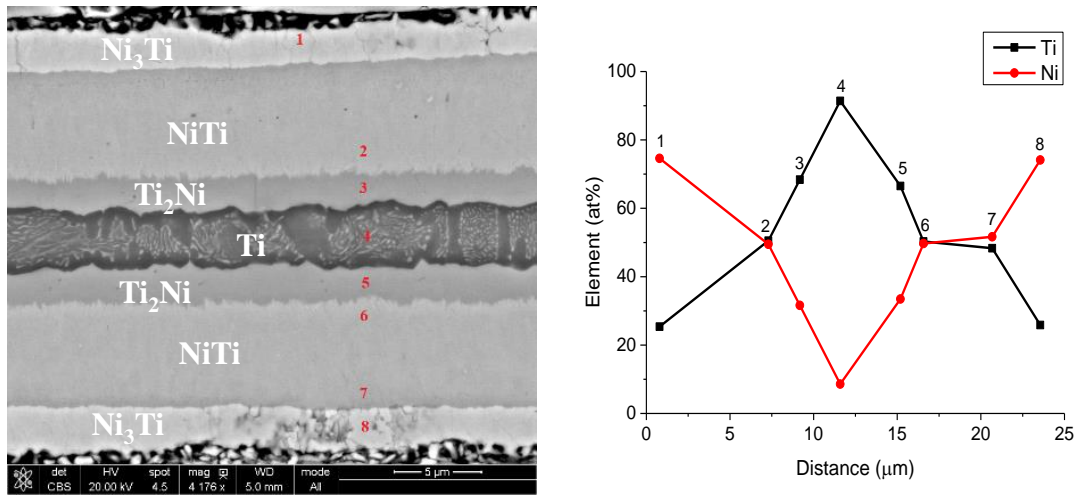


Figure 5. 38: SEM/EDS point measurements of S1 sample.

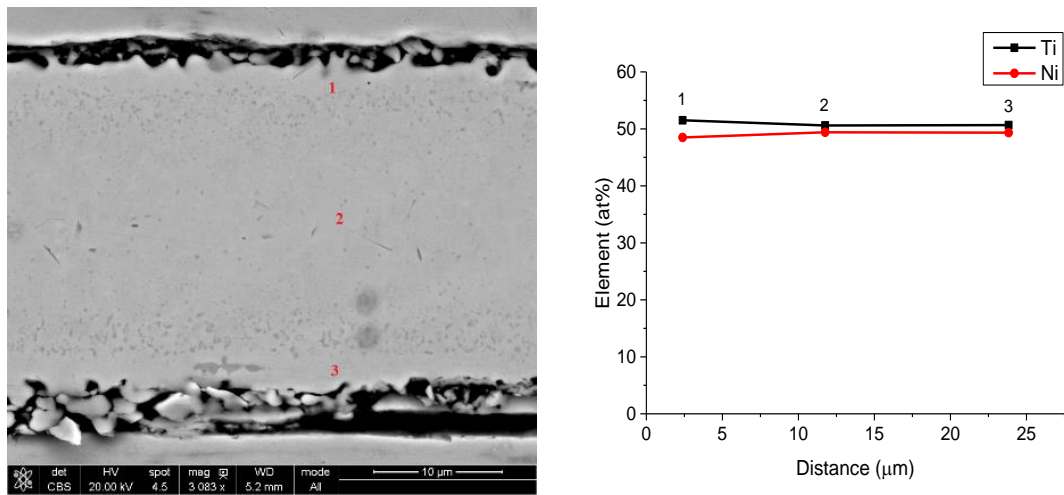
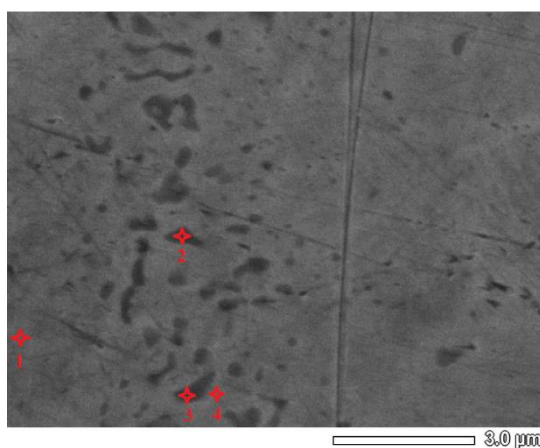


Figure 5. 39: SEM/EDS point measurements of S2 sample.



Point number:	Ni (at%):	Ti (at%):
1	49.2(7)	50.79(2)
2	41.5(6)	58.5(2)
3	39.8(6)	60.3(2)
4	47.1(6)	52.9(2)

Figure 5. 40: BSE-image and EDS results for the cross-sections of sample S2 with marked measurements points and table with elemental composition on the right.

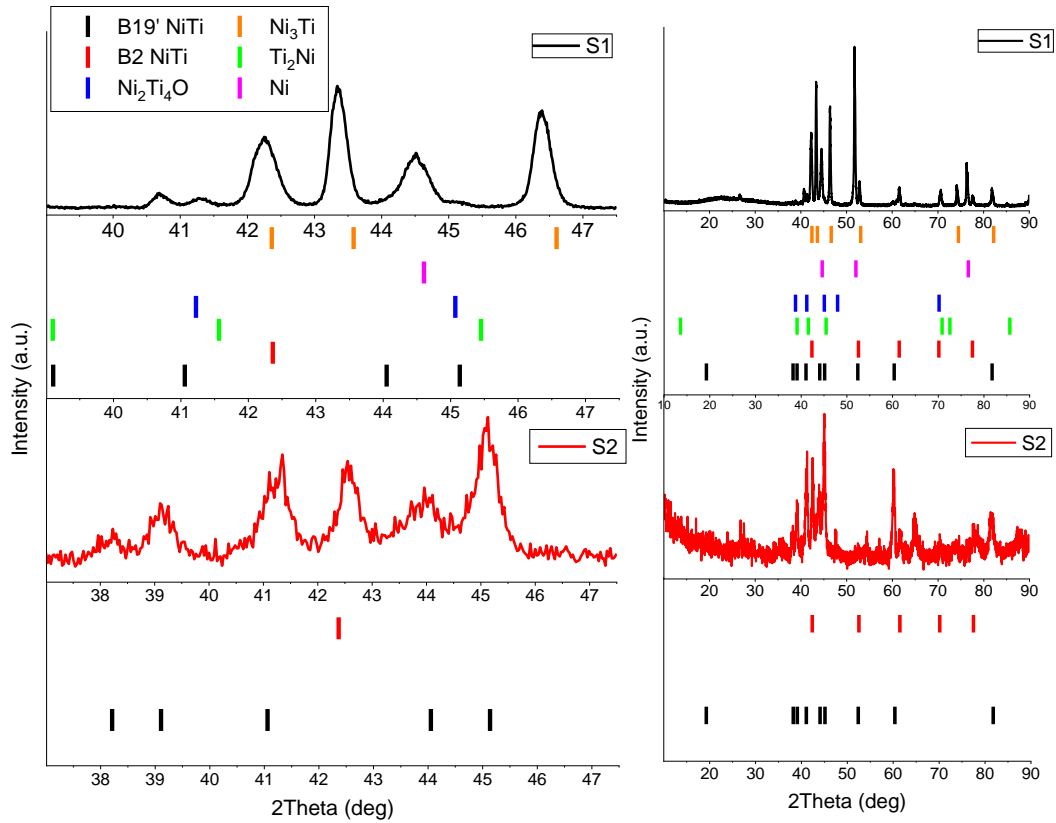


Figure 5. 41: X-Ray Diffraction patterns of a) S1 and b) S2 sample.

XRD patterns for S1 and S2 are presented in the Figure 5. 41. Presence of NiTi B2 and B19' phase peaks can be distinguished for S2. Other phases could not be detected. Opposite situation is for S1 material dominant Ni<sub>3</sub>Ti and Ti<sub>2</sub>Ni phases peaks are present. Weaker peaks of B2, B19' and pure Ni phase peaks are detected. Presented results are in good agreement.

DSC results for the S2 material are presented in the Figure 5. 42.

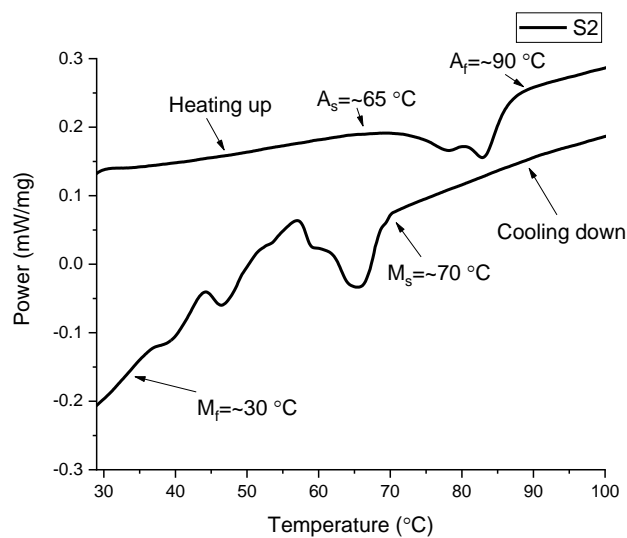


Figure 5. 42: Differential Scanning Calorimetry measurement of S2 material.

They exhibit similar temperature range of thermal transformation during cooling ( $\sim 40/50$  °C).

Figure 5. 43 presents results resistivity measurements for both samples and two foils (pure nickel and titanium 5  $\mu\text{m}$  in thickness) as a reference. It shows, that resistivity for pure metals is lower than for NiTi foils (the lowest for nickel). Differences between S1 and S2 samples can also be observed. Residual resistance of S1 ( $0.201(1) \mu\text{Ohm}\cdot\text{m}$ ) is lower than for S2 ( $0.260(9) \mu\text{Ohm}\cdot\text{m}$ ). For pure metal foils the values are much lower:  $0.0410(3) \mu\text{Ohm}\cdot\text{m}$  and  $0.0065(2) \mu\text{Ohm}\cdot\text{m}$  for titanium and nickel, respectively. Both samples, S1 and S2 exhibit a bump occurring on cooling and is related to R-phase transformation at  $\sim 329$  K/ $\sim 56$  °C and  $\sim 326$  K/ $\sim 53$  °C (maximum) for S1 and S2, respectively. A similar effect was observed in other studies [175]–[177]. For the sample S2 the bump is much higher than for the S1 one.

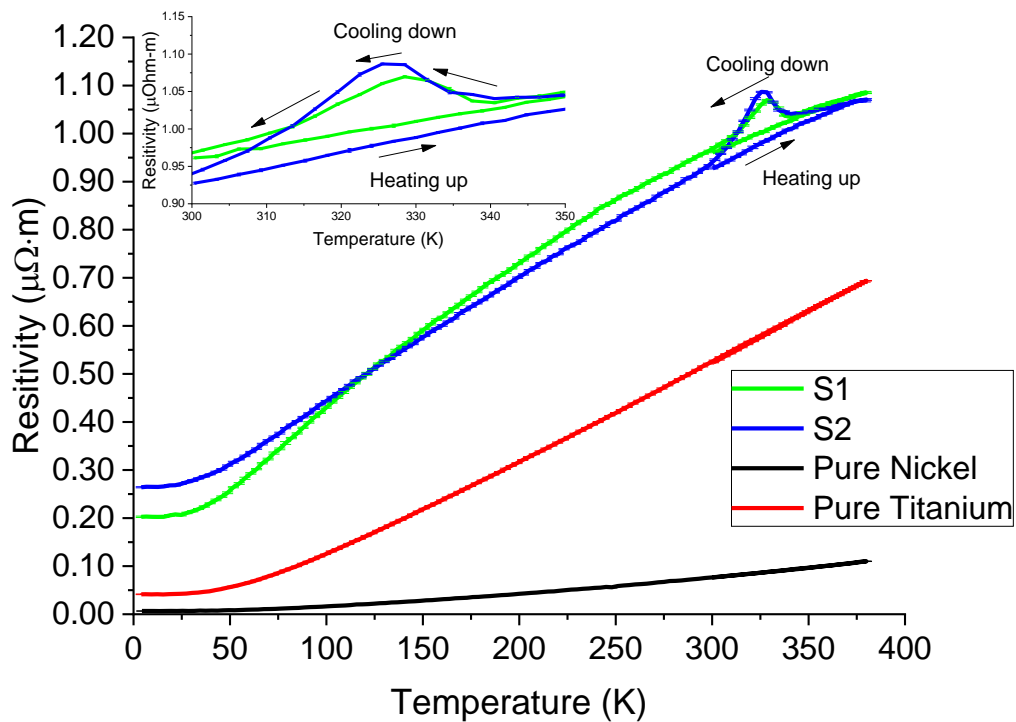


Figure 5. 43: Resistivity results for S1, S2, pure nickel and titanium foils.

Magnetoresistance measurements were performed at different temperatures from 4 to 350 K and magnetic fields from 0 to 89 kOe. Its values were calculated from following equation:  $(R_H - R_0)/R_0$ . Obtained results are shown in Figure 5. 44, Figure 5. 45, Figure 5. 46 and Figure 5. 47 for S1, S2, pure titanium and nickel, respectively. It can be seen that magnetoresistance value for S1 is twice as big as for S2 and similar to that of titanium. Nickel magnetoresistance values are more similar to S2. In Figure 5. 48 comparison of values in 300 and 4 K for all materials are shown. It can be seen that for all the samples, magnetoresistance

values are much higher at 4 K than in 300 K, which reveals a much larger mean free path of the electrical carriers at low temperatures. Between S1 and S2 there is a small difference in values with similar tendency for both temperatures – higher for S1 containing unreacted nickel, which is much better conductive than the NiTi compound or titanium.

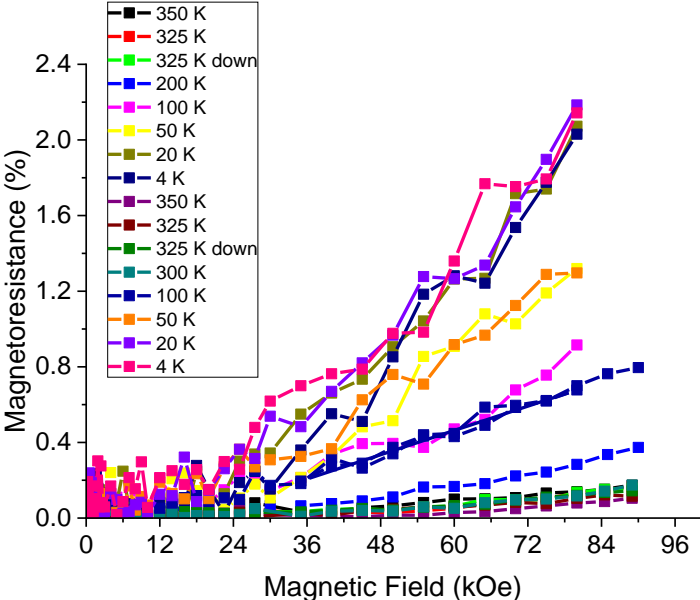


Figure 5. 44: S1 sample magnetoresistance dependences at different temperatures.

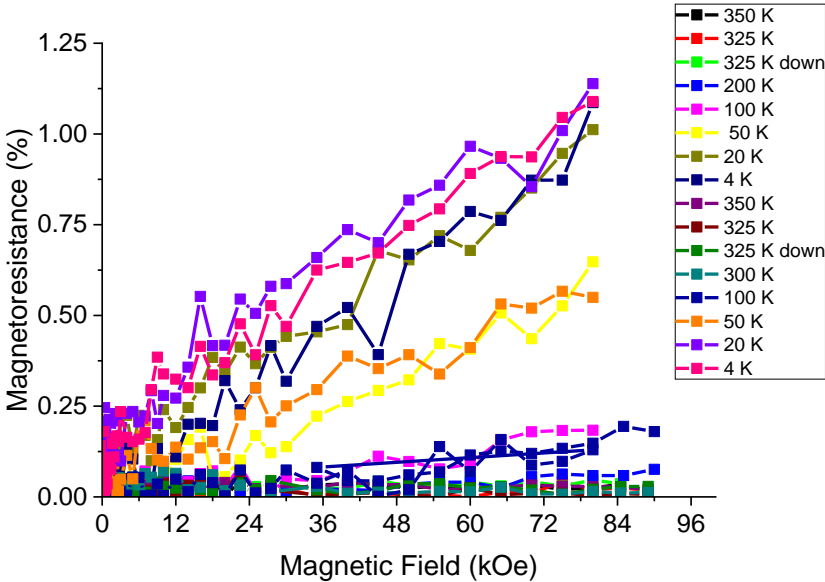


Figure 5. 45: S2 sample magnetoresistance dependences at different temperatures.

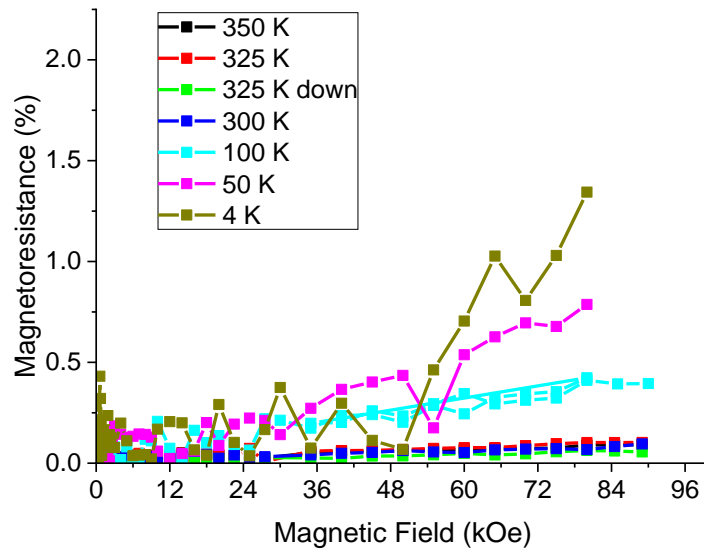


Figure 5. 46: Pure titanium magnetoresistance dependences at different temperatures.

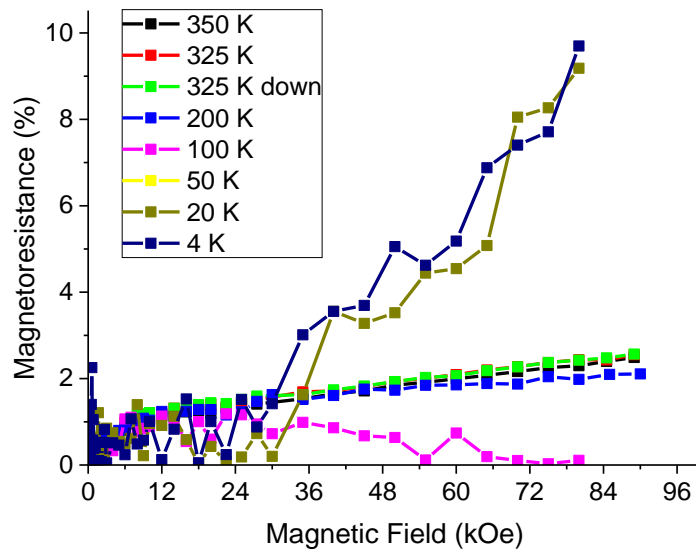


Figure 5. 47: Pure nickel magnetoresistance dependences at different temperatures.

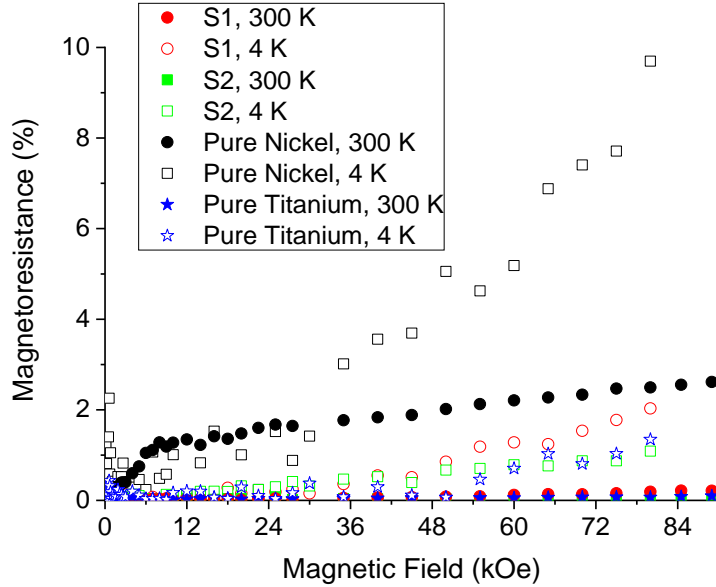


Figure 5. 48: Magnetoresistance of the S1, S2, pure nickel and titanium in the room temperature and 4 K.

Magnetoresistance shows a quadratic function dependence for multiphase sample and nearly linear for homogenous one. For the multiphase material it is higher (well visible at low temperatures) due to presence of unreacted nickel in this material. The quadratic dependence corresponds to the open orbits at the Fermi surface and the linear one indicates the effect of closed orbits. Thus, for the S2 sample, which consists predominantly of the NiTi compound, the contribution from closed orbits can be deduced, which is masked in the S1 sample by magnetoresistance of unreacted nickel.

Applying the Wiedemann–Franz law (equation 5.2) to the electrical conductivity the thermal conductivity was calculated.

$$\frac{\kappa}{\sigma} = LT \quad (5.2)$$

where:  $\kappa$  – thermal conductivity [ $\frac{W}{mK}$ ],  $\sigma$  – resistivity [ $\frac{1}{m \cdot \Omega}$ ],  $L$  - Lorenz number ( $2.44 \cdot 10^{-8} [\frac{W \cdot \Omega}{K^2}]$ ) and  $T$  – temperature [K].

The results obtained are presented in Figure 5. 49.

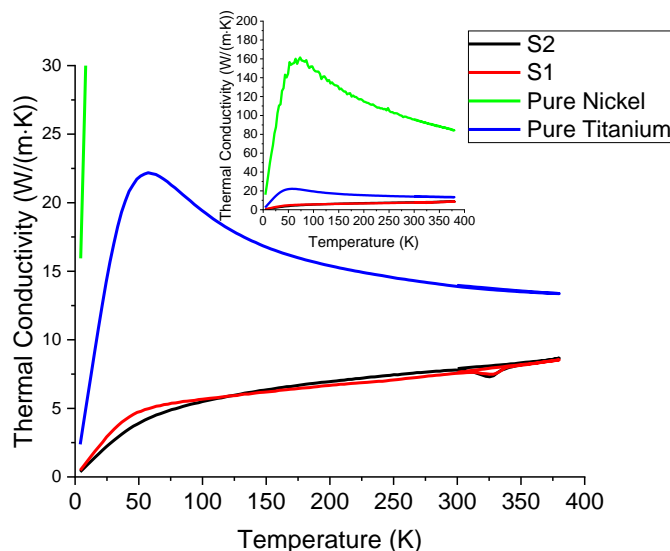


Figure 5.49: Thermal conductivity for all considered materials in this subchapter.

For the materials S1 and S2 the thermal conductivity is similar and much smaller than for pure metals. It indicates presence of structural disorder of atoms in the compounds, also confirmed with a lack of “phonon drag” peak near 50 K usually observed for well crystalline materials.

Last results concern magnetic properties of the materials studied. The data obtained are presented in Figure 5.50 - Figure 5.52. Magnetization dependences curves were obtained after subtraction of diamagnetic part corresponding to plastic sample container from the measurement data. Results are showing a ferromagnetic contribution (hysteresis loop) for S1 in the full temperature range, which is increasing its height (remnant magnetization) and width (coercive field) with temperature decrease. For the S2 material the remnant magnetization is an order of magnitude lower, which is attributed to the presence of unreacted nickel in the S1 sample and a lack of it in the S2 one, in agreement with the XRD and SEM/EDS results.

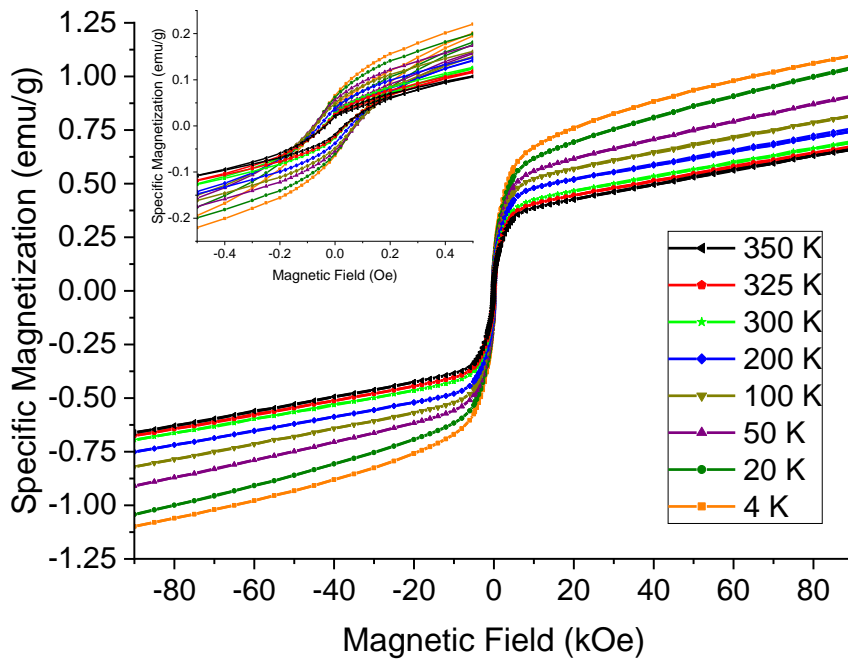


Figure 5. 50: Hysteresis loops at all the temperatures for the S1 sample from 4 to 350 K.

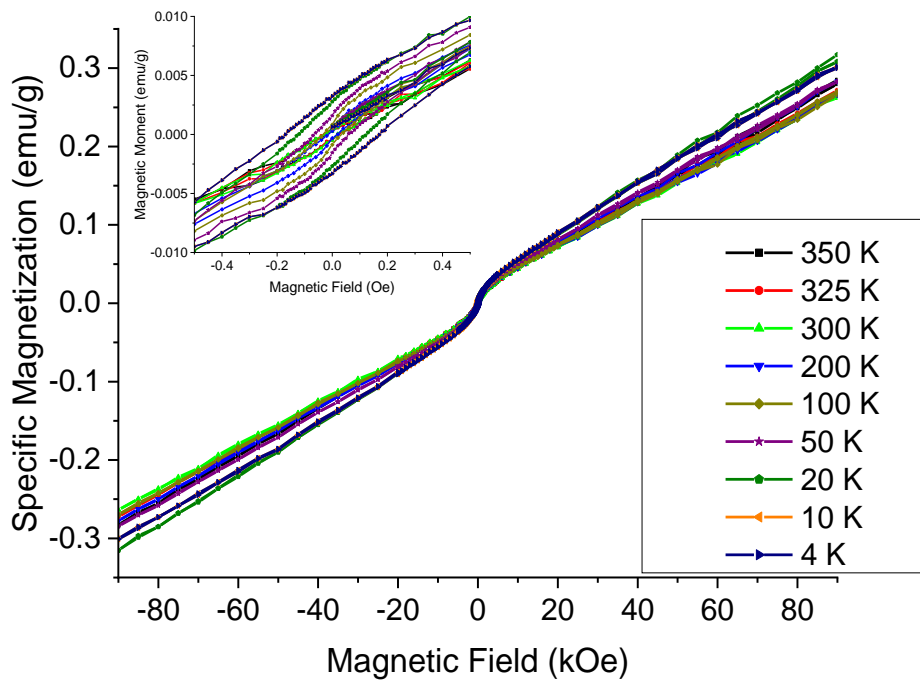


Figure 5. 51: Hysteresis loops at all the temperatures for the S2 sample from 4 to 350 K.

Figure 5. 52 present average susceptibility derived from linear parts of magnetization versus magnetic field curves for S1 and S2.

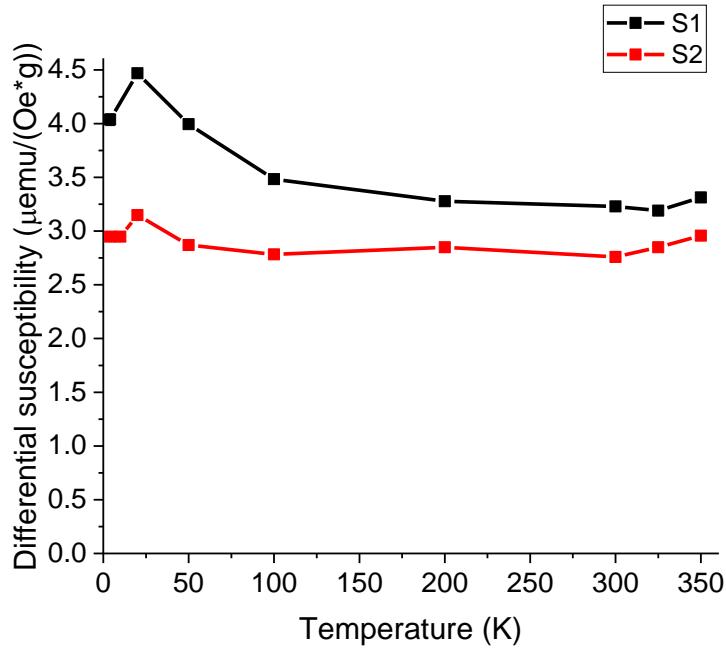


Figure 5.52: Differential susceptibility obtained from mean slope value of linear parts of magnetization vs field dependences for S1 and S2.

Based on these results, except for the small ferromagnetic contributions, the dominant Pauli-like, temperature independent paramagnetism of the NiTi phase in both materials is deduced.

Figure 5.53 presents Shape Recovery Rate (SRR) dependence obtained from bending test performed at room temperature. Tests were performed for all configurations.

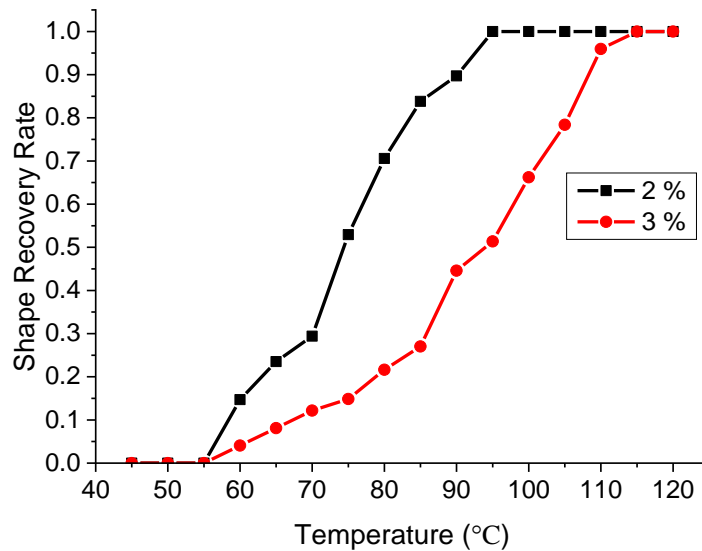


Figure 5.53: Shape Recovery Rate for S2 sample temperature dependence after bending strain of 2 and 3 %.

The results show that shape recovering starts at 55 °C and finishes at different temperatures depending on the initial strain value. This is consistent with DSC data (see

Figure 5. 15), where a multistep transformation could be observed. The sample exhibits 100% of SRR up to  $\sim 115$  °C for the maximum value of the used initial bending strain, i.e. 3%, and up to  $\sim 90$  °C for 2% of it.

### 5.3 Summary of results for sintered NiTi micro-foils

The first part of the Chapter was focused on characterization of diffusion between pure nickel and titanium foils joined with pulse-current pressure sintering, subsequently annealed at 700/800 °C for 24/48/72 hours in vacuum. Measurements of thicknesses of phases appearing were done with SEM/EDS and the following results can be distinguished:

- Good quality of nickel-titanium interface was obtained with no oxidation and enhanced dendrite crystal creation due to diffusion process upon annealing was observed, with smooth diffusion areas near nickel/titanium interface.
- Annealing at 700/800 °C resulted in  $Ti_2Ni$ ,  $Ni_3Ti$  and NiTi phase thickness increase, which was much faster at 800 °C,  $Ti_2Ni$  droplet-like features creation is observed.

Second part of the Chapter was focused on NiTi micro-foils synthesis based on current sintering technique. In a simple annealing process only very low NiTi phase thickness (of 40  $\mu m$  at 800 °C/72 hours) would be obtained. Current sintering ensures faster atom diffusion in the material volume. The results obtained are as follows:

- Ni/Ti/Ni configuration is found to be superior to those of Ni/Ti and Ti/Ni/Ti configuration as it allows for faster diffusion and better homogenization. This is owing to  $Ti_2Ni$  creation and propagation from the middle of the material ensuring more effective and homogeneous dendritic crystal growth of the NiTi phase.
- Shape memory effect is confirmed by XRD (B19' phase peaks and their change to B2 phase due to temperature increase), DSC (martensitic and reverse transformation), EDS (elemental content in the range of the NiTi shape memory alloy composition) and SRR measurements. A full (100 %) shape recovery was obtained in the temperature ranges between room temperature and 115 °C, occurring at lower temperatures for smaller initial strain.
- DC and pulsed DC currents application to Ni/Ti/Ni system sintered at the same temperatures shows slight differences revealed in creation of  $Ti_2Ni$  phase layer close to the surfaces for the DC and promotion of titanium rich particles creation in rows, close to the surfaces. The former ensures smoother thermal transformation, and the latter – multistage one.

- A single step synthesis procedure was formulated and tested. A 16  $\mu\text{m}$  thick, 10 mm in diameter NiTi shape memory foil was successfully obtained in such procedure for 60 minutes sintering at  $\sim 700\text{ }^\circ\text{C}$  and  $\sim 13\text{ MPa}$  uniaxial pressure with 210/190 A pulsed current of 0.5 Hz frequency.
- Electrical resistivity measurements performed for two materials show transition peak on cooling at about  $56\text{ }^\circ\text{C}$  (single phase material – S2) and  $\sim 53\text{ }^\circ\text{C}$  (multiphase material – S1), which is in good agreement with DSC results. A high residual resistivity is observed.
- Magnetoresistance shows a linear dependence from the applied magnetic field for the homogenous micro-foil, which is attributed to the dominant contribution from closed electron orbits at the Fermi surface of the NiTi compound.
- Thermal conductivity derived from resistivity values by application of Wiedemann–Franz law shows a lack of phonon drag peak.
- Magnetic properties show a dominant Pauli paramagnetic behavior of the NiTi phase with some ferromagnetic contribution from unreacted nickel, an order of magnitude smaller for the homogenous sample, than for the multi-phase one.

## Chapter 6. Conclusions

The following main conclusions can be formulated on the basis of the research undertaken in this PhD Thesis:

a) for Fe-Mn-Si alloys:

- Low temperature and room temperature iron Mössbauer spectra indicate no magnetic moment on iron, thus magnetism of these materials is deduced to be governed by manganese.
- A ferromagnetic contribution observed in magnetisation measurements, with exchange bias effect dependent on the thermal treatment driven reverse martensitic transformation, is found to correspond to the austenitic fcc phase. This exchange bias effect reveals nanometric size of the austenitic fcc phase precipitations, not detectable with XRD.
- A Curie-Weiss paramagnetic behaviour showing up at higher fields indicates existence of localized moments of  $3 \mu_B$  per Mn atom, in addition to the temperature independent Pauli paramagnetic part due to conduction electrons.
- Carbon doped at 0.1 wt.% enters the bulk of the alloy causing the appearance of larger regions of austenite phase and decreasing the Curie-Weiss susceptibility, which reflects a decreased number of paramagnetic Mn atoms.
- Specific heat measurements for the alloy with 0.1 wt.% of carbon reveal a peak at 250 K, only slightly sensitive to the applied magnetic field up to 90 kOe, which is attributed to magnetic transition to a glass-like state of the martensite hcp phase with a very small net moment of  $0.016 \mu_B$ .
- Electrical resistivity measurements show its upturn on lowering temperature, attributed to a Kondo-like effect. The magnetoresistance is independent on the magnetic field up to 90 kOe at all the temperatures, indicating an extremely small mean free path of the electrical carriers in these alloys.

b) for the Ni-Ti compound:

- Rolling of preheated Ti/Ni/Ti and Ni/Ti/Ni sets of foils and their subsequent annealing shows their poor joining and low effectiveness of interdiffusion.
- Pulsed-current pressure sintering of Ti/Ni foils provides a good quality of interface with no oxidation and appreciable NiTi dendrite crystal creation upon subsequent annealing is observed, with smooth diffusion areas near nickel/titanium interface. This annealing conducted at 700/800 °C results in  $Ti_2Ni$ ,  $Ni_3Ti$  and NiTi layers thickness

increase, which is much faster at 800 °C.  $Ti_2Ni$  droplet-like features creation is observed.

- For micrometer thick foils, the Ni/Ti/Ni configuration is found to be superior to those of Ni/Ti and Ti/Ni/Ti, as it allows for faster diffusion and better homogenization. This is owing to  $Ti_2Ni$  creation and propagation from the middle of the material, ensuring more effective and homogeneous dendritic crystal growth of the NiTi phase.
- A full (100 %) shape recovery is obtained for the Ni/Ti/Ni configuration derived homogenous NiTi material in the temperature ranges between room temperature and 115 °C, occurring at lower temperatures for smaller initial strain.
- A single step synthesis procedure was formulated and successfully carried out to obtain a 16  $\mu m$  thick NiTi homogenous micro-foil with a 100 % shape recovery rate.
- DC and pulsed DC currents application to Ni/Ti/Ni system sintered at the same temperatures shows slight differences in the microstructure, resulting in a smooth thermal transformation for the former and in the multistage one for the latter.
- A peak in the electrical resistivity measurements corresponding to the R-phase is observed between temperatures which are consistent with those corresponding to the transitions observed with DSC. Thermal conductivity derived from resistivity values by application of Wiedemann–Franz law shows a lack of phonon drag peak.
- Magnetoresistance shows a linear dependence from the applied magnetic field for the homogenous micro-foil, which reveals the contribution from closed electron orbits at the Fermi surface of the NiTi compound.
- Magnetic properties show a dominant Pauli paramagnetic behavior of the NiTi phase with some ferromagnetic contribution from unreacted nickel, an order of magnitude smaller for the homogenous sample, than for the multi-phase one.

## References

- [1] A. Sato, E. Chishima, K. Soma, and T. Mori, "Shape memory effect in  $\gamma \rightleftharpoons \epsilon$  transformation in Fe-30Mn-1Si alloy single crystals," *Acta Metall.*, vol. 30, no. 6, pp. 1177–1183.
- [2] J. Wan and S. Chen, "Martensitic transformation and shape memory effect in Fe-Mn-Si based alloys," *Curr. Opin. Solid State Mater. Sci.*, vol. 9, no. 6, pp. 303–312, 2005.
- [3] T. Sawaguchi, T. Maruyama, H. Otsuka, A. Kushibe, Y. Inoue, and K. Tsuzaki, "Design concept and applications of Fe–Mn–Si-based alloys—from shape-memory to seismic response control," *Mater. Trans.*, vol. 57, no. 3, pp. 283–293, 2016.
- [4] T. Saito, C. Kapusta, and A. Takasaki, "Synthesis and characterization of Fe-Mn-Si shape memory alloy by mechanical alloying and subsequent sintering," *Mater. Sci. Eng. A*, vol. 592, pp. 88–94, 2014.
- [5] T. Saito, K. Gąska, C. Kapusta, and A. Takasaki, "FABRICATION OF Fe-Mn-Si ALLOY BY MECHANICAL ALLOYING AND DIRECT CURRENT SINTERING," no. 30, pp. 62–67, 2010.
- [6] Y. H. Wen, M. Yan, and N. Li, "Effects of carbon addition and aging on the shape memory effect of Fe-Mn-Si-Cr-Ni alloys," *Scr. Mater.*, vol. 50, no. 4, pp. 441–444, 2004.
- [7] H. Liu, "Influence of carbon on martensitic transformation and shape memory effect of Fe-Mn-Si alloys," *Univ. Wollongong Aust.*, 1996.
- [8] K. Tsuzaki, Y. Natsume, T. Maki, and Y. Tomota, "Effect of solution hardening on the shape memory effect of Fe-Mn based alloys," *Scr. Met. Mater.*, p. 33:1087, 1995.
- [9] K. Tsuzaki, Y. Natsume, Y. Kurokawa, and T. Maki, "Improvement of the shape memory effect in Fe-Mn-Si alloys by the addition of carbon," *Scr. Metall. Mater.*, vol. 27, no. 4, pp. 471–473, 1992.
- [10] N. Van Caenegem, L. Duprez, K. Verbeken, B. C. De Cooman, Y. Houbaert, and D. Segers, "Effect of Carbon on the Shape Memory Mechanism in FeMnSiCrNi SMAs," *ISIJ Int.*, vol. 47, no. 5, pp. 723–732, 2007.
- [11] J. Chen, H. B. Peng, Q. Yang, S. L. Wang, F. Song, and Y. H. Wen, "Effect of carbon content on shape memory effect of Fe-Mn-Si-Cr-Ni-based alloys at different deformation temperatures," *Mater. Sci. Eng. A*, vol. 677, no. 20, pp. 133–139, 2016.
- [12] X. Wu and T. Y. Hsu, "Effect of the Neel temperature,  $T_N$ , on martensitic transformation in Fe-Mn-Si-based shape memory alloys," vol. 45, pp. 1–6, 2000.

- [13] Z. X. Qin and Y. S. Zhang, "Study on the magnetism and phase transformation in Fe-Mn-Si-C shape memory alloys," *Acta Metall. Sin. (English Lett.)*, vol. 10, no. 3, pp. 219–223, 1997.
- [14] Z. Qin and Y. Zhang, "Mossbauer effect study of antiferromagnetic Fe – Mn – Si alloys," vol. 116, pp. 225–235, 1998.
- [15] H. Ohno and M. Mekata, "Antiferromagnetism in hcp Iron-Manganese Alloys," *Phys. Soc. Japan*, vol. 31, pp. 102–108, 1970.
- [16] M. Murakami, H. Suzuki, and Y. Nakamura, "Effect of Si on the shape memory effect of polycrystalline Fe-Mn-Si alloys," *Trans. ISIJ*, vol. 27, 1987.
- [17] J. Martínez, G. Aurelio, G. J. Cuello, S. M. Cotes, and J. Desimoni, "Structural properties of FCC and HCP phases in the Fe-Mn-Si system: A neutron diffraction experiment," *Mater. Sci. Eng. A*, vol. 437, no. 2, pp. 323–327, 2006.
- [18] Z. YanSheng, "A study of the Neel transition and the Kondo-like effect of  $\gamma$ -Fe-Mn-Si alloys," *J. Phys. F Met. Phys.*, vol. 18, 1988.
- [19] X. J. Jin, T. Y. Hsu, and X. Zuyao, "Thermodynamic consideration of antiferromagnetic transition on fcc-hcp martensitic transformation in Fe-Mn-Si shape memory alloys," vol. 61, pp. 4–7, 1999.
- [20] M. Murakami, H. Otsuka, H. Suzuki, and S. Matsuda, "Effect of alloying content, phase and magnetic transformation on the shape memory effect of Fe-Mn-Si alloys," *Trans. Iron Steel Inst. Japan*, vol. 27, 1987.
- [21] Q. Zuoxiang, Y. Manping, and Z. Yansheng, "Neel transition and gamma - epsilon transformation in polycrystalline Fe-Mn-Si shape memory alloys," *J. Mater. Sci.*, vol. 31, no. 9, pp. 2311–2315, 1996.
- [22] V. G. Gavriljuk, V. V. Bliznuk, B. D. Shanina, and S. P. Kolesnik, "Effect of silicon on atomic distribution and shape memory in Fe-Mn base alloys," *Mater. Sci. Eng. A*, vol. 406, no. 1–2, pp. 1–10, 2005.
- [23] A. Sheikh, "The structure and magnetic properties of ferromagnetic shape memory alloys containing iron," *Loughbrgh. Univ.*, 2010.
- [24] G. B. KAUFFMAN and I. MAYO, "The Story of Nitinol: The Serendipitous Discovery of the Memory Metal and Its Applications," *Chem. Educ.*, vol. 2, no. 2, pp. 1–21, 1997.
- [25] J. Rynnen *et al.*, "Biocompatibility of nickel-titanium shape memory metal and its corrosion behavior in human cell cultures," *J. Biomed. Mater. Res.*, vol. 35, no. 4, pp. 451–457, 1997.

- [26] P. R. Halani, I. Kaya, Y. C. Shin, and H. E. Karaca, "Phase transformation characteristics and mechanical characterization of nitinol synthesized by laser direct deposition," *Mater. Sci. Eng. A*, vol. 559, pp. 836–843, 2013.
- [27] H. D. Gu *et al.*, "Pulsed laser deposition of NiTi shape memory alloy thin films with optimum parameters," *Thin Solid Films*, vol. 330, no. 2, pp. 196–201, 1998.
- [28] H. Hou, R. F. Hamilton, M. W. Horn, and Y. Jin, "NiTi thin films prepared by biased target ion beam deposition co-sputtering from elemental Ni and Ti targets," *Thin Solid Films*, vol. 570, no. PartA, pp. 1–6, 2014.
- [29] K. K. Ho and G. P. Carman, "Sputter deposition of NiTi thin film shape memory alloy using a heated target," *Thin Solid Films*, vol. 370, pp. 18–29, 2000.
- [30] A. Isalgue, V. Torra, J.-L. Seguin, M. Bendahan, J. . Amigo, and V. Esteve-Cano, "Shape memory NiTi thin films deposited at low temperature," *Mater. Sci. Eng. A*, vol. 273–275, pp. 717–721, 1999.
- [31] W. Tillmann and S. Momeni, "Comparison of NiTi thin films sputtered from separate elemental targets and Ti-rich alloy targets," *J. Mater. Process. Technol.*, vol. 220, pp. 184–190, 2015.
- [32] Y. Fu, W. Huang, H. Du, X. Huang, J. Tan, and X. Gao, "Characterization of TiNi shape-memory alloy thin films for MEMS applications," *Surf. Coatings Technol.*, vol. 145, no. 1–3, pp. 107–112, 2001.
- [33] Y. Fu, H. Du, W. Huang, S. Zhang, and M. Hu, "TiNi-based thin films in MEMS applications: A review," *Sensors Actuators, A Phys.*, vol. 112, no. 2–3, pp. 395–408, 2004.
- [34] A. G. Ramirez, H. Ni, and H. J. Lee, "Crystallization of amorphous sputtered NiTi thin films," *Mater. Sci. Eng. A*, vol. 438–440, no. SPEC. ISS., pp. 703–709, 2006.
- [35] A. Kahn, M. A. Huff, and A. H. Heuer, "The TiNi shape-memory alloy and its applications for MEMS," *J. Micromechanics Microengineering*, vol. 8, no. 3, pp. 213–221, 1998.
- [36] X. Wang and J. J. Vlassak, "Crystallization kinetics of amorphous NiTi shape memory alloy thin films," *Scr. Mater.*, vol. 54, no. 5, pp. 925–930, 2006.
- [37] N. Nayan *et al.*, "Vacuum induction melting of NiTi shape memory alloys in graphite crucible," *Mater. Sci. Eng. A*, vol. 465, pp. 44–48, 2007.
- [38] J. Otubo, O. D. Rigo, C. M. Neto, and P. R. Mei, "The effects of vacuum induction melting and electron beam melting techniques on the purity of NiTi shape memory

- alloys,” *Mater. Sci. Eng. A*, vol. 438–440, pp. 679–682, 2006.
- [39] J. Frenzel, Z. Zhang, K. Neuking, and G. Eggeler, “High quality vacuum induction melting of small quantities of NiTi shape memory alloys in graphite crucibles,” *J. Alloys Compd.*, vol. 385, pp. 214–223, 2004.
- [40] Z. Zhang, J. Frenzel, K. Neuking, and G. Eggeler, “On the reaction between NiTi melts and crucible graphite during vacuum induction melting of NiTi shape memory alloys,” *Acta Mater.*, vol. 53, pp. 3971–3985, 2005.
- [41] Y. Kabiri, A. Kermanpur, and A. Foroozmehr, “Comparative study on microstructure and homogeneity of NiTi shape memory alloy produced by copper boat induction melting and conventional vacuum arc melting,” *Vacuum*, vol. 86, pp. 1073–1077, 2012.
- [42] M. Bram, A. Ahmad-Khanlou, A. Heckmann, B. Fuchs, H. P. Buchkremer, and D. Stöver, “Powder metallurgical fabrication processes for NiTi shape memory alloy parts,” *Mater. Sci. Eng. A*, vol. 337, no. 1–2, pp. 254–263, 2002.
- [43] L. Krone, E. Schüller, M. Bram, O. Hamed, H. P. Buchkremer, and D. Stöver, “Mechanical behaviour of NiTi parts prepared by powder metallurgical methods,” *Mater. Sci. Eng. A*, vol. 378, no. 1–2 SPEC. ISS., pp. 185–190, 2004.
- [44] J. Mentz, M. Bram, H. P. Buchkremer, and D. Stöver, “Improvement of mechanical properties of powder metallurgical NiTi shape memory alloys,” *Adv. Eng. Mater.*, vol. 8, no. 4, pp. 247–252, 2006.
- [45] J. Mentz *et al.*, “Powder metallurgical processing of NiTi shape memory alloys with elevated transformation temperatures,” *Mater. Sci. Eng. A*, vol. 491, no. 1–2, pp. 270–278, 2008.
- [46] E. Schüller, M. Bram, H. P. Buchkremer, and D. Stöver, “Phase transformation temperatures for NiTi alloys prepared by powder metallurgical processes,” *Mater. Sci. Eng. A*, vol. 378, no. 1–2 SPEC. ISS., pp. 165–169, 2004.
- [47] C. P. Frick, A. M. Ortega, J. Tyber, K. Gall, and H. J. Maier, “Multiscale structure and properties of cast and deformation processed polycrystalline NiTi shape-memory alloys,” *Metall. Mater. Trans. A Phys. Metall. Mater. Sci.*, vol. 35 A, no. 7, pp. 2013–2025, 2004.
- [48] A. Ahadi, E. Rezaei, and A. Karimi Taheri, “Effect of hot rolling on microstructure and transformation cycling behaviour of equiatomic NiTi shape memory alloy,” *Mater. Sci. Technol.*, vol. 28, no. 6, pp. 727–732, 2012.

- [49] M. Nastasi, D. M. Parking, and H. Gleiter, “Mechanical Properties and Deformation Behavior of Materials Having Ultra-Fine Microstructures,” *NATO ASI Ser. Ser. E Appl. Sci.*, vol. 233.
- [50] N. Babacan, M. Bilal, C. Hayrettin, J. Liu, O. Benafan, and I. Karaman, “Effects of cold and warm rolling on the shape memory response of Ni<sub>50</sub>Ti<sub>30</sub>Hf<sub>20</sub> high-temperature shape memory alloy,” *Acta Mater.*, vol. 157, pp. 228–244, 2018.
- [51] E. MOHAMMAD SHARIFI and A. KERMANPUR, “Superelastic behavior of nanostructured Ti<sub>50</sub>Ni<sub>48</sub>Co<sub>2</sub> shape memory alloy with cold rolling processing,” *Trans. Nonferrous Met. Soc. China (English Ed.)*, vol. 28, no. 7, pp. 1351–1359, 2018.
- [52] E. M. Sharifi and A. Kermanpur, “Superelastic properties of nanocrystalline NiTi shape memory alloy produced by thermomechanical processing,” *Trans. Nonferrous Met. Soc. China (English Ed.)*, vol. 28, no. 3, pp. 515–523, 2018.
- [53] M. Ataei, A. Zarei-Hanzaki, and A. Shamsolhodaei, “Shape memory response and mechanical properties of warm deformed NiTi intermetallic alloy,” *Mater. Sci. Eng. A*, vol. 680, no. May 2016, pp. 291–296, 2017.
- [54] K. Gall, J. Tyber, G. Wilkesanders, S. W. Robertson, R. O. Ritchie, and H. J. Maier, “Effect of microstructure on the fatigue of hot-rolled and cold-drawn NiTi shape memory alloys,” *Mater. Sci. Eng. A*, vol. 486, no. 1–2, pp. 389–403, 2008.
- [55] K. C. Atli, “The effect of tensile deformation on the damping capacity of NiTi shape memory alloy,” *J. Alloys Compd.*, vol. 679, pp. 260–267, 2016.
- [56] Y. Li *et al.*, “Evolution of microstructure and property of NiTi alloy induced by cold rolling,” *J. Alloys Compd.*, vol. 653, pp. 156–161, 2015.
- [57] M. Pattabi and M. S. Murari, “Effect of Cold Rolling on Phase Transformation Temperatures of NiTi Shape Memory Alloy,” *J. Mater. Eng. Perform.*, vol. 24, no. 2, pp. 556–564, 2014.
- [58] M. H. Parsa and H. Mazaheri, “Finite element and experimental deformation analysis of niti alloy during rolling,” *Int. J. Mater. Form.*, vol. 2, no. SUPPL. 1, pp. 13–16, 2009.
- [59] Z. Lekston, M. Zubko, K. Prusik, and D. Stróz, “Microstructure, phase transformations, and properties of hot-extruded Ni-rich NiTi shape memory alloy,” *J. Mater. Eng. Perform.*, vol. 23, no. 7, pp. 2362–2367, 2014.
- [60] K. Tsuchiya, D. Tomus, M. Umemoto, M. Sasaki, and T. Ohmori, “Property of TiNi Shape Memory Foils Produced by Ultrafine Laminates Method,” *Mater. Sci. Forum*,

- vol. 449–452, pp. 1321–1324, 2004.
- [61] D. Tomus *et al.*, “Fabrication of shape memory TiNi foils via Ti / Ni ultrafine laminates,” *Scr. Mater.*, vol. 48, pp. 489–494, 2003.
- [62] D. Montalvão, Q. Shengwen, and M. Freitas, “A study on the influence of Ni-Ti M-Wire in the flexural fatigue life of endodontic rotary files by using Finite Element Analysis,” *Mater. Sci. Eng. C*, vol. 40, pp. 172–179, 2014.
- [63] E. S. J. Pereira *et al.*, “Mechanical behavior of M-Wire and conventional NiTi wire used to manufacture rotary endodontic instruments,” *Dent. Mater.*, vol. 29, no. 12, pp. e318–e324, 2013.
- [64] E. S. J. Pereira *et al.*, “Physical and mechanical properties of a thermomechanically treated NiTi wire used in the manufacture of rotary endodontic instruments,” *Int. Endod. J.*, vol. 45, no. 5, pp. 469–474, 2012.
- [65] R. Casati, M. Vedani, S. A. M. Tofail, C. Dickinson, and A. Tuissi, “On the preparation and characterization of thin NiTi shape memory alloy wires for MEMS,” *Fract. Struct. ...*, vol. 23, pp. 7–12, 2012.
- [66] G. La Rosa, F. Lo Savio, E. Pedullà, and E. Rapisarda, “A new torquemeter to measure the influence of heat-treatment on torsional resistance of NiTi endodontic instruments,” *Eng. Fail. Anal.*, vol. 82, no. April, pp. 446–457, 2017.
- [67] S. A. Rizvi and T. I. Khan, “A Novel Fabrication Method for Nitinol Shape Memory Alloys,” *Key Eng. Mater.*, vol. 442, pp. 309–315, 2010.
- [68] Y. Zhang, X. Cheng, and H. Cai, “Fabrication, characterization and tensile property of a novel Ti<sub>2</sub>Ni/TiNi micro-laminated composite,” *Mater. Des.*, vol. 92, pp. 486–493, 2016.
- [69] J. E. Garay, U. Anselmi-Tamburini, and Z. A. Munir, “Enhanced growth of intermetallic phases in the Ni-Ti system by current effects,” *Acta Mater.*, vol. 51, no. 15, pp. 4487–4495, 2003.
- [70] Y. Zhou, Q. Wang, D. L. Sun, and X. L. Han, “Co-effect of heat and direct current on growth of intermetallic layers at the interface of Ti-Ni diffusion couples,” *Journal of Alloys and Compounds*, vol. 509, no. 4, pp. 1201–1205, 2011.
- [71] L. Hu, Y. Xue, and F. Shi, “Intermetallic formation and mechanical properties of Ni-Ti diffusion couples,” *Mater. Des.*, vol. 130, no. March, pp. 175–182, 2017.
- [72] O. M. A. Taha, M. B. Bahrom, O. Y. Taha, and M. S. Aris, “EXPERIMENTAL STUDY ON TWO WAY SHAPE MEMORY EFFECT TRAINING PROCEDURE

- FOR NiTiNOL SHAPE MEMORY ALLOY,” *ARNP J. Eng. Appl. Sci.*, vol. 10, no. 17, pp. 7847–7851, 2015.
- [73] A. Takasaki, “Mechanical Alloying of the Ti–Ni System,” *Phys. Status Solidi*, vol. 169, no. 2, pp. 183–191, 1998.
- [74] T. Saito, T. Yokoyama, and A. Takasaki, “Hydrogenation of TiNi shape memory alloy produced by mechanical alloying,” *J. Alloys Compd.*, vol. 509, no. SUPPL. 2, pp. S779–S781, 2011.
- [75] T. Saito and A. Takasaki, “The Influence of Chemical Composition on Shape Memory Effect of TiNi Bulk Alloy Produced by Mechanical Alloying,” vol. 406, 2009.
- [76] T. Birk, S. Biswas, J. Frenzel, and G. Eggeler, “Twinning-Induced Elasticity in NiTi Shape Memory Alloys,” *Shape Mem. Superelasticity*, vol. 2, no. 2, pp. 145–159, 2016.
- [77] D. E. Hodgson, M. H. Wu, and R. J. Biermann, “Shape Memory Alloys,” *ASM Handb.*, vol. 2, pp. 897–902, 2002.
- [78] J. Bhagyaraj, K. V. Ramaiah, C. N. Saikrishna, S. K. Bhaumik, and Gouthama, “Behavior and effect of Ti<sub>2</sub>Ni phase during processing of NiTi shape memory alloy wire from cast ingot,” *J. Alloys Compd.*, vol. 581, pp. 344–351, 2013.
- [79] H. J. Moon, S. J. Chun, T. H. Nam, Y. Liu, H. Yang, and Y. W. Kim, “Thermal stability of the R phase of a rapidly solidified Ti-47.3Ni (at%) alloy,” *Trans. Electr. Electron. Mater.*, vol. 13, no. 1, pp. 19–22, 2012.
- [80] M. Maso’od, M. H. Ismail, R. Razali, and I. Subuki, “Effect of sintering temperatures on microstructural changes and phase transformation of nearly equiatomic microporous NiTi alloy produced by metal injection moulding,” *J. Mech. Eng.*, vol. 5, no. Specialissue6, pp. 115–126, 2018.
- [81] S. Jiang, Y. Zhang, Y. Zhao, S. Liu, L. Hu, and C. Zhao, “Influence of Ni<sub>4</sub>Ti<sub>3</sub> precipitates on phase transformation of NiTi shape memory alloy,” *Trans. Nonferrous Met. Soc. China (English Ed.)*, vol. 25, no. 12, pp. 4063–4071, 2015.
- [82] N. Hatcher, O. Y. Kontsevoi, and A. J. Freeman, “Martensitic transformation path of NiTi,” *Phys. Rev. B - Condens. Matter Mater. Phys.*, vol. 79, no. 2, pp. 2–5, 2009.
- [83] T. W. Duerig and K. Bhattacharya, “The Influence of the R-Phase on the Superelastic Behavior of NiTi,” *Shape Mem. Superelasticity*, vol. 1, no. 2, pp. 153–161, 2015.
- [84] D. M. T. Jafar Khalil-Allafi, Wolfgang W. Schmahl, “Space group and crystal structure of the R-phase in binary NiTi shape memory alloys,” *Acta Mater.*, vol. 54, pp. 3171–3175, 2006.

- [85] M. H. Wu and L. M. Schetky, "Industrial Applications for Shape Memory Alloys," *Int. Conf. Shape Mem. Superelastic Technologies*, vol. 182, pp. 171–182, 2000.
- [86] L. Petrini and F. Migliavacca, "Biomedical Applications of Shape Memory Alloys," *J. Metall.*, vol. 2011, no. Figure 1, pp. 1–15, 2011.
- [87] N. Choudhary and D. Kaur, "Shape memory alloy thin films and heterostructures for MEMS applications: A review," *Sensors Actuators, A Phys.*, vol. 242, pp. 162–181, 2016.
- [88] G. Rondelli, "Corrosion resistance tests on NiTi shape memory alloy," *Biomaterials*, vol. 17, no. 20, pp. 2003–2008, 1996.
- [89] K. Endo and H. Ohno, "Corrosion Behavior of NiTi Alloys in a Physiological Saline Solution," *Shape Mem. Implant.*, pp. 177–193, 2000.
- [90] J. J. Marattukalam *et al.*, "Microstructure and corrosion behavior of laser processed NiTi alloy," *Mater. Sci. Eng. C*, vol. 57, pp. 309–313, 2015.
- [91] J. Zupanc, N. Vahdat-Pajouh, and E. Schäfer, "New thermomechanically treated NiTi alloys - a review," *Int. Endod. J.*, pp. 1088–1103, 2018.
- [92] S. Fukumoto, T. Inoue, S. Mizuno, K. Okita, T. Tomita, and A. Yamamoto, "Friction welding of TiNi alloy to stainless steel using Ni interlayer," *Sci. Technol. Weld. Join.*, vol. 15, no. 2, pp. 124–130, 2010.
- [93] Y. T. Hsu, Y. R. Wang, S. K. Wu, and C. Chen, "Effect of CO<sub>2</sub> laser welding on the shape-memory and corrosion characteristics of TiNi alloys," *Metall. Mater. Trans. A Phys. Metall. Mater. Sci.*, vol. 32, no. 3, pp. 569–576, 2001.
- [94] M. H. Sadati and Y. Javadi, "Investigation of mechanical properties in welding of shape memory alloys," *Procedia Eng.*, vol. 149, no. June, pp. 438–447, 2016.
- [95] W. Wang, X. Yang, H. Li, F. Cong, and Y. Liu, "Effect of laser welding parameters on formation of NiTi shape memory alloy welds," *Adv. Mater. Sci. Eng.*, vol. 2014, 2014.
- [96] M. Cempel and G. Nickel, "Nickel: A review of its sources and environmental toxicology," *Polish J. Environ. Stud.*, vol. 15, no. 3, pp. 375–382, 2006.
- [97] A. Duda-Chodak and U. Blaszczyk, "The Impact of Nickel on Human Health," *J. Elem.*, vol. 13, no. 4, pp. 685–696, 2008.
- [98] W. Jia *et al.*, "Nickel release from orthodontic arch wires and cellular immune response to various nickel concentrations," *J. Biomed. Mater. Res.*, vol. 48, no. 4, pp. 488–495, 1999.
- [99] M. Es-Souni, M. Es-Souni, and H. Fischer-Brandies, "Assessing the biocompatibility

- of NiTi shape memory alloys used for medical applications,” *Anal. Bioanal. Chem.*, vol. 381, no. 3, pp. 557–567, 2005.
- [100] A. Michiardi, C. Aparicio, J. A. Planell, and F. J. Gil, “New oxidation treatment of NiTi shape memory alloys to obtain Ni-free surfaces and to improve biocompatibility,” *J. Biomed. Mater. Res. - Part B Appl. Biomater.*, vol. 77, no. 2, pp. 249–256, 2006.
- [101] J. Frenzel, Z. Zhang, C. Somsen, K. Neuking, and G. Eggeler, “Influence of carbon on martensitic phase transformations in NiTi shape memory alloys,” *Acta Mater.*, vol. 55, no. 4, pp. 1331–1341.
- [102] J. Otubo, O. D. Rigo, A. A. Coelho, C. M. Neto, and P. R. Mei, “The influence of carbon and oxygen content on the martensitic transformation temperatures and enthalpies of NiTi shape memory alloy,” *Mater. Sci. Eng. A*, vol. 481–482, no. 1–2 C, pp. 639–642, 2008.
- [103] Z. Wu, A. Mahmud, J. Zhang, Y. Liu, and H. Yang, “Surface oxidation of NiTi during thermal exposure in flowing argon environment,” *Mater. Des.*, vol. 140, pp. 123–133.
- [104] G. S. Firstov, R. G. Vitchev, H. Kumar, B. Blanpain, and J. Van Humbeeck, “Surface oxidation of NiTi shape memory alloy,” *Biomaterials*, vol. 23, no. 24, pp. 4863–4871, 2002.
- [105] J. H. Zhu, C. T. Liu, and C. H. Chen, “Effect of iron additions on environmental embrittlement of NiTi-base alloys,” *Intermetallics*, vol. 12, no. 7–9 SPEC. ISS., pp. 859–868, 2004.
- [106] X. Zhou, Y. Chen, Y. Huang, Y. Mao, and Y. Yu, “Effects of niobium addition on the microstructure and mechanical properties of laser-welded joints of NiTiNb and Ti6Al4V alloys,” *J. Alloys Compd.*, vol. 735, pp. 2616–2624, 2018.
- [107] Y. ZHANG, S. JIANG, X. ZHU, Y. ZHAO, Y. LIANG, and D. SUN, “Influence of Fe addition on phase transformation behavior of NiTi shape memory alloy,” *Trans. Nonferrous Met. Soc. China (English Ed.)*, vol. 27, no. 7, pp. 1580–1587, 2017.
- [108] H. Otsuka, H. Yamada, T. Maruyama, H. Tanahashi, S. Matsuda, and M. Murakami, “Effects of alloying additions on Fe-Mn-Si shape memory alloys,” *ISIJ Int.*, vol. 30, no. 8, pp. 674–679, 1990.
- [109] J. Wang, Q. Li, C. Xiong, Y. Li, and B. Sun, “Effect of Zr on the martensitic transformation and the shape memory effect in Ti-Zr-Nb-Ta high-temperature shape memory alloys,” *J. Alloys Compd.*, vol. 737, pp. 672–677, 2018.
- [110] G. P. Toker, S. Saedi, E. Acar, O. Ozbulut, and H. E. Karaca, “Shape memory behavior

- of Ni<sub>40.3</sub>Ti<sub>39.7</sub>Hf<sub>15</sub>Pd<sub>5</sub> and Ni<sub>40.3</sub>Ti<sub>44.7</sub>Hf<sub>10</sub>Pd<sub>5</sub> alloys,” *J. Alloys Compd.*, vol. 763, pp. 1012–1017, 2018.
- [111] N. Singh *et al.*, “Effect of ternary additions to structural properties of NiTi alloys,” *Comput. Mater. Sci.*, vol. 112, pp. 347–355, 2016.
- [112] J. Li *et al.*, “The effect of Zr on the transformation behaviors, microstructure and the mechanical properties of Ti-Ni-Cu shape memory alloys,” *J. Alloys Compd.*, vol. 747, pp. 348–353, 2018.
- [113] T. Kurita, H. Matsumoto, K. Sakamoto, K. Tanji, and H. Abe, “Effect of aluminum addition on the transformation of NiTi alloy,” *J. Alloys Compd.*, vol. 396, no. 1–2, pp. 193–196, 2005.
- [114] M. Frotscher, J. Burow, P. Schön, K. Neuking, R. Böckmann, and G. Eggeler, “Characterization of the mechanical properties of ultra-fine grained NiTiCr-wires,” *Materwiss. Werksttech.*, vol. 40, no. 1–2, pp. 17–22, 2009.
- [115] O. Benafan, G. S. Bigelow, and D. A. Scheiman, “Transformation behavior in NiTi-20Hf shape memory alloys – Transformation temperatures and hardness,” *Scr. Mater.*, vol. 146, pp. 251–254, 2018.
- [116] T. Duerig, A. Pelton, and D. Stöckel, “An overview of nitinol medical applications,” *Mater. Sci. Eng. A*, vol. 273–275, pp. 149–160, 1999.
- [117] N. B. Morgan, “Medical shape memory alloy applications - The market and its products,” *Mater. Sci. Eng. A*, vol. 378, no. 1–2 SPEC. ISS., pp. 16–23, 2004.
- [118] S. Shabalovskaya, J. Anderegg, and J. Van Humbeeck, “Critical overview of Nitinol surfaces and their modifications for medical applications,” *Acta Biomater.*, vol. 4, no. 3, pp. 447–467, 2008.
- [119] S. Barbarino, E. L. Saavedra Flores, R. M. Ajaj, I. Dayyani, and M. I. Friswell, “A review on shape memory alloys with applications to morphing aircraft,” *Smart Mater. Struct.*, vol. 23, no. 6, 2014.
- [120] G. Song, N. Ma, and H. N. Li, “Applications of shape memory alloys in civil structures,” *Eng. Struct.*, vol. 28, no. 9, pp. 1266–1274, 2006.
- [121] S. Saadat *et al.*, “An Overview of Vibration and Seismic Application of NiTi Shape Memory Alloy,” *Smart Mater. Struct.*, vol. 11, no. 2, pp. 218–229, 2002.
- [122] L. Janke, C. Czaderski, M. Motavalli, and J. Ruth, “Applications of shape memory alloys in civil engineering structures - Overview, limits and new ideas,” *Mater. Struct. Constr.*, vol. 38, no. 279, pp. 578–592, 2005.

- [123] J. M. Jani, M. Leary, A. Subic, and M. A. Gibson, “A review of shape memory alloy research, applications and opportunities,” *Mater. Des.*, vol. 56, pp. 1078–1113, 2014.
- [124] S. M. Kumar and M. Vanitha Lakshmi, “Applications of Shape Memory Alloys in Mems Devices,” *Int. J. Adv. Res. Comput. Commun. Eng.*, vol. 2, no. 2, pp. 1122–1127, 2013.
- [125] S. Mishra, “Applications of Shape Memory Alloys: A Review,” vol. 2, no. 2, pp. 1–7, 2015.
- [126] A. Soroka, A. Sozinov, N. Lanska, M. Rameš, L. Straka, and K. Ullakko, “Composition and temperature dependence of twinning stress in non-modulated martensite of Ni-Mn-Ga-Co-Cu magnetic shape memory alloys,” *Scr. Mater.*, vol. 144, pp. 52–55, 2018.
- [127] M. Rameš, O. Heczko, A. Sozinov, K. Ullakko, and L. Straka, “Magnetic properties of Ni-Mn-Ga-Co-Cu tetragonal martensites exhibiting magnetic shape memory effect,” *Scr. Mater.*, vol. 142, pp. 61–65, 2018.
- [128] A. Pérez-Checa *et al.*, “Study of the critical parameters for magnetic field-induced strain in high temperature Ni-Mn-Ga-Co-Cu-Fe single crystals,” *Scr. Mater.*, vol. 158, pp. 16–19, 2019.
- [129] A. Pérez-Checa, J. Feuchtwanger, J. M. Barandiaran, A. Sozinov, K. Ullakko, and V. A. Chernenko, “Ni-Mn-Ga-(Co, Fe, Cu) high temperature ferromagnetic shape memory alloys: Effect of Mn and Ga replacement by Cu,” *Scr. Mater.*, vol. 154, pp. 131–133, 2018.
- [130] M. J. Szczerba, J. Przewoźnik, J. Żukrowski, C. Kapusta, M. S. Szczerba, and B. Major, “THE INFLUENCE OF HIGH TEMPERATURE PLASTIC DEFORMATION ON MAGNETIC PROPERTIES OF Ni<sub>2</sub>MnGa TYPE SINGLE CRYSTALS,” *Arch. Metall. Mater.*, vol. 54, no. 2, 2009.
- [131] C. F. Lin and J. B. Yang, “Martensitic transformation and magnetic properties of ferromagnetic shape memory Fe<sub>66</sub>Pd<sub>30</sub>Rh<sub>4</sub> alloys,” *J. Magn. Magn. Mater.*, vol. 323, no. 22, pp. 2792–2796, 2011.
- [132] P. Czaja *et al.*, “Martensitic transition, structure and magnetic anisotropy of martensite in Ni-Mn-Sn single crystal,” *Acta Mater.*, vol. 118, pp. 213–220, 2016.
- [133] M. P. Caputo, A. E. Berkowitz, A. Armstrong, P. Müllner, and C. V. Solomon, “4D printing of net shape parts made from Ni-Mn-Ga magnetic shape-memory alloys,” *Addit. Manuf.*, vol. 21, no. December 2017, pp. 579–588, 2018.

- [134] X. Wang *et al.*, “Selective laser melting produced layer-structured NiTi shape memory alloys with high damping properties and Elinvar effect,” *Scr. Mater.*, vol. 146, pp. 246–250, 2018.
- [135] S. Saedi *et al.*, “Shape memory response of porous NiTi shape memory alloys fabricated by selective laser melting,” *J. Mater. Sci. Mater. Med.*, vol. 29, no. 4, 2018.
- [136] J. Li *et al.*, “The effect of Zr on the transformation behaviors, microstructure and the mechanical properties of Ti-Ni-Cu shape memory alloys,” *J. Alloys Compd.*, vol. 747, pp. 348–353, 2018.
- [137] E. Bronstein, E. Faran, and D. Shilo, “A new experimental method for measuring stress-temperature phase diagram in shape memory alloys,” *Scr. Mater.*, vol. 154, pp. 145–148, 2018.
- [138] K. Otsuka and C. M. Wayman, “Shape Memory Materials,” *Cambridge Univ. Press*, 1999.
- [139] A. M. C. LTD., “Characteristics and applications of Fe-Mn-Si-based shape memory alloys,” no. 1, 1999.
- [140] B. Liu, Y. F. Zheng, and L. Ruan, “In vitro investigation of Fe<sub>30</sub>Mn<sub>6</sub>Si shape memory alloy as potential biodegradable metallic material,” *Mater. Lett.*, vol. 65, no. 3, pp. 540–543, 2011.
- [141] M. N. Mokgalaka, S. L. Pityana, P. A. I. Popoola, and T. Mathebula, “NiTi intermetallic surface coatings by laser metal deposition for improving wear properties of Ti-6Al-4V substrates,” *Adv. Mater. Sci. Eng.*, vol. 2014, no. February 2016, 2014.
- [142] X. Shao, X. Guo, Y. Han, W. Lu, J. Qin, and D. Zhang, “Characterization of the diffusion bonding behavior of pure Ti and Ni with different surface roughness during hot pressing,” *Mater. Des.*, vol. 65, pp. 1001–1010, 2015.
- [143] G. F. Bastin and G. D. Rieck, “Diffusion in Titanium-Nickel System .1. Occurrence and Growth of Various Intermetallic Compounds,” *Metall. Trans.*, vol. 5, no. 8, pp. 1817–1826, 1974.
- [144] Y. Zhou, Q. Wang, D. L. Sun, and X. L. Han, “Co-effect of heat and direct current on growth of intermetallic layers at the interface of Ti-Ni diffusion couples,” *J. Alloys Compd.*, vol. 509, no. 4, pp. 1201–1205, 2011.
- [145] J. Frenzel, E. P. George, A. Dlouhy, C. Somsen, M. F. X. Wagner, and G. Eggeler, “Influence of Ni on martensitic phase transformations in NiTi shape memory alloys,” *Acta Mater.*, vol. 58, no. 9, pp. 3444–3458, 2010.

- [146] M. Johnson, "Nitinol Technical Properties." [Online]. Available: <http://jmmedical.com/resources/221/Nitinol-Technical-Properties.html>. [Accessed: 19-Sep-2018].
- [147] G. F. Bastin and G. D. Rieck, "Diffusion in Titanium-Nickel System .2. Calculations of Chemical and Intrinsic Diffusion-Coefficients," *Metall. Trans.*, vol. 5, no. 8, pp. 1827–1831, 1974.
- [148] S. Moustafa, W. Daoush, A. Ibrahim, and E. Neubaur, "Hot Forging and Hot Pressing of AlSi Powder Compared to Conventional Powder Metallurgy Route," *Mater. Sci. Appl.*, vol. 02, no. 08, pp. 1127–1133, 2011.
- [149] B. Henriques, D. Soares, J. C. Teixeira, and F. . Silva, "Effect of hot pressing variables on the microstructure, relative density and hardness of sterling silver (Ag-Cu alloy) powder compacts," *Mater. Res.*, vol. 17, no. 3, pp. 664–671, 2014.
- [150] Z. Chunping and Z. Kaifeng, "Pulse Current Auxiliary Sintering," *IntechOpen*, 2013.
- [151] J. R. Heinz U. Kessel, Jürgen Hennicke, Jürgen Schmidt, Thomas Weißgärber, Bernd F. Kieback, Matthias Herrmann, "Chapter 17 Fabrication and Processing of Engineering Materials," no. 1, pp. 1–45.
- [152] RHP-TechnologyGmbH, "Inductive Hot Pressing." [Online]. Available: <http://www.rhp-technology.com/en/technologies/inductive-hot-pressing/>. [Accessed: 20-Sep-2018].
- [153] X. Chen, Y. Cheng, X. Xie, W. Feng, and K. Wu, "Calculation of the ionic conductivity of h-BN and its effect on the dielectric loss," *J. Phys. D Appl. Phys.*, vol. 40, p. 846, 2007.
- [154] M. Lu, A. Bousetta, and A. Bensaoula, "Electrical properties of boron nitride thin films grown by neutralized nitrogen ion assisted vapor deposition," *Appl. Phys. Lett.*, no. January, pp. 132–135, 1996.
- [155] L. G. Carpenter and P. J. Kirby, "The electrical resistivity of boron nitride over the temperature range 700 degrees C to 1400 degrees C," *J. Phys. D. Appl. Phys.*, vol. 15, p. 1143, 1982.
- [156] "Shibaura Institute of Technology, Tokyo, Japan." [Online]. Available: [techno-plaza.shibaura-it.ac.jp](http://techno-plaza.shibaura-it.ac.jp). [Accessed: 31-Aug-2018].
- [157] T. Straczek and C. Kapusta, *Analiza symulacyjna widm XAFS selenu w preparatach z grzyba shiitake*. Kraków: AGH University of Science and Technology, 2012.
- [158] FEI, "Nova NanoSEM 50 Series." [Online]. Available: [www.fei.co.jp](http://www.fei.co.jp). [Accessed: 01-

- Sep-2018].
- [159] Q. Design, *Physical Property Measurement System Vibrating Sample Magnetometer (VSM) Option User's Manual*. .
- [160] Q. Design, *Physical Property Measurement System Resistivity Option User's Manual*. .
- [161] ShimadzuScientificInstruments, "Shimadzu." [Online]. Available: [www.ssi.shimadzu.com](http://www.ssi.shimadzu.com). [Accessed: 31-Aug-2018].
- [162] S.-F. Ou, B.-Y. Peng, Y.-C. Chen, and M.-H. Tsai, "Manufacturing and Characterization of NiTi Alloy with Functional Properties by Selective Laser Melting," *Metals (Basel)*, vol. 8, no. 5, p. 342, 2018.
- [163] W. Prendota, K. Goc, S. Miyazawa, A. Takasaki, D. Rybicki, and C. Kapusta, "Influence of carbon addition to Fe-Mn-Si type alloy on the structure and shape memory effect," *Adv. Mater. Sci. Eng.*, 2018.
- [164] W. PRENDOTA *et al.*, "Magnetic study of the Fe-Mn-Si shape memory alloys," *AGH Univ. Sci. Technol. Press. EURO THERM-2016 7th Eur. Therm. Conf. ISBN 978-83-7464-869-1*, pp. 67–71, 2016.
- [165] K. Topolski, P. Wieceński, Z. Szulc, A. Gałka, and H. Garbacz, "Progress in the characterization of explosively joined Ti/Ni bimetals," *Materials and Design*, vol. 63, pp. 479–487, 2014.
- [166] T. Bartel and K. Hackl, "Multiscale modeling of martensitic phase transformations : On the numerical determination of heterogeneous mesostructures within shape-memory alloys induced by precipitates," no. January, pp. 324–342, 2010.
- [167] B. Chad Hornbuckle, X. X. Yu, R. D. Noebe, R. Martens, M. L. Weaver, and G. B. Thompson, "Hardening behavior and phase decomposition in very Ni-rich Nitinol alloys," *Mater. Sci. Eng. A*, vol. 639, pp. 336–344, 2015.
- [168] C. B. Ke, S. S. Cao, X. Ma, and X. P. Zhang, "Modeling of Ni<sub>4</sub>Ti<sub>3</sub> precipitation during stress-free and stress-assisted aging of bi-crystalline NiTi shape memory alloys," *Trans. Nonferrous Met. Soc. China (English Ed.)*, vol. 22, no. 10, pp. 2578–2585, 2012.
- [169] G. S. Firstov, R. G. Vitchev, H. Kumar, B. Blanpain, and J. Van Humbeeck, "Surface oxidation of NiTi shape memory alloy," *Biomaterials*, vol. 23, no. 24, pp. 4863–4871, 2002.
- [170] P. Bassani *et al.*, "Porous NiTi shape memory alloys produced by SHS: microstructure and biocompatibility in comparison with Ti<sub>2</sub>Ni and TiNi<sub>3</sub>," *J. Mater. Sci. Mater. Med.*, vol. 25, no. 10, pp. 2277–2285, 2014.

- [171] Z. Wu, A. Mahmud, J. Zhang, Y. Liu, and H. Yang, "Surface oxidation of NiTi during thermal exposure in flowing argon environment," *Mater. Des.*, vol. 140, pp. 123–133, 2018.
- [172] K. Aniołek, "The influence of thermal oxidation parameters on the growth of oxide layers on titanium," *Vacuum*, vol. 144, pp. 94–100, 2017.
- [173] C. Velmurugan, V. Senthilkumar, S. Dinesh, and D. Arulkirubakaran, "Review on phase transformation behavior of NiTi shape memory alloys," *Mater. Today Proc.*, vol. 5, no. 6, pp. 14597–14606, 2018.
- [174] G. Satoh, A. Birnbaum, and Y. L. Yao, "EFFECT OF ANNEALING PARAMETERS ON THE SHAPE MEMORY PROPERTIES OF NITI," 2008.
- [175] V. Antonucci, G. Faiella, M. Giordano, F. Mennella, and L. Nicolais, "Electrical resistivity study and characterization during NiTi phase transformations," *Thermochim. Acta*, vol. 462, no. 1–2, pp. 64–69, 2007.
- [176] G. Airoidi, T. Ranucci, and G. R. Mechanical, "Mechanical and Electrical Properties of A NiTi Shape Memory Alloy," *J. Phys. IV*, vol. 01, pp. 439–444, 1991.
- [177] A. I. Kovalev, A. V. Logunov, N. V. Petrushin, and L. S. Egorova, "Thermal conductivity and electrical resistivity of NiTi in the temperature interval 90–450 K," *J. Eng. Phys.*, vol. 32, no. 2, pp. 183–185, 1977.

## List of tables

Table 1. 1: Selected Shape Memory Alloys and their important characteristics. Taken from: [77].	6
Table 1. 2: Comparison of selected properties of NiTi and FeMnSiCr alloys. Taken from:[122], [138].	9
Table 3. 1: Overview of the samples.	31
Table 3. 2: Elemental cell parameters obtained after Rietveld refinements for XRD patterns of “As annealed” and “Heated 600 °C” sample.	35
Table 3. 3: Crystallographic unit cell parameters obtained after Rietveld refinements for XRD patterns of “0.1 wt.% C” sample at 75, 295 and 423 K.	38
Table 3. 4: Summarized Isomer Shifts and FWHM values for all samples in low and room temperature. At the lower part temperature dependence FWHM of “As annealed” sample.	41
Table 3. 5: Isomer shift values at room temperature and 80K.	44
Table 3. 6: Mean values of saturation magnetization at 80 kOe.	47
Table 3. 7: Values of remnant- remnant+ and mean remnant magnetization for “0.1 wt.% C” sample.	48
Table 3. 8: Summarized fitted parameters to the inversed mass magnetic susceptibility of “0.1 wt.% C” sample at different magnetic field values.	56
Table 4. 1: Cold rolling machine specification.	64
Table 5. 1: List of the samples with different elemental compositions – values are estimated.	96

## List of figures

Figure 1. 1: Illustrative representation of the thermally induced shape memory effect in Ni-Ti alloys. ....	4
Figure 1. 2: SMA stress-strain curves: green – austenite, blue - martensite and orange - superelastic behavior. ....	5
Figure 1. 3: General examples of Ni-Ti applications: a) eyeglass frame, b) cellular phone antenna [85], c), d) orthodontic wires and e), f) neurosurgical stent. Taken from: [86].	7
Figure 1. 4: Ni-Ti applications as (micro) devices. Taken from: [87]. ....	8
Figure 1. 5: Fe-Mn-Si alloy as: a), b) pipes connecting material and c), d) fishplate connector. Taken from: [139].....	10
Figure 1. 6: Phase diagram of the Ti–Ni system, taken from: [141]. Red dot – lowest melting point for titanium rich alloy and blue dot - lowest melting point for nickel rich alloy. ....	12
Figure 1. 7: A comparison between: a) well-chosen volume of input materials and b) wrong chosen for similar diffusion time and c) wrong when diffusion process is completed. Based on [67], [69]–[71], [142]–[144].....	13
Figure 1. 8: Illustrative representation of phases creation during diffusion process between pure nickel and titanium input materials: a) at the temperature range of NiTi phase. b) and c) lower temperature or too short diffusion time. ....	14
Figure 1. 9: Table summarizing direct current heating effects. Adapted from [150]...	15
Figure 1. 10: a) Boron Nitride (BN) spray and b) example of output foil obtained after synthesis process. ....	15
Figure 1. 11: Pulse-current pressure sintering equipment (PLASMAN, SS Alloy): a) main, b) sintering in high temperature and c) chamber inside view. ....	16

Figure 2. 1: Image of: on the left SmartLab, Rigaku Corporation (Technoplaza, Shibaura) [156] and characterization table on the right. ....	18
Figure 2. 2: Image of: on the left Siemens d5000 (SSPD, AGH) and characterization table on the right.....	18
Figure 2. 3: Images of: a) sample between fixation clip, b) resin holder with fixation clip and sample inside and c) resin holder with samples cross-sections after grinding and polishing process. ....	20
Figure 2. 4: Image of: on the left FEI Nova NanoSEM 450 Scanning (at Faculty of Metals Engineering and Industrial Computer Science, AGH University of Science and Technology) and characterization table on the right. Taken from [158]. ....	21
Figure 2. 5: Image of: on the left JSM-7100F (JEOL Ltd., at Technoplaza, Shibaura Institute of Technology) and characterization table on the right. [156].....	21
Figure 2. 6: Illustrative representation of Mössbauer spectrums: a) single line (singlet) b) two lines (doublet) and c) six lines (sextet). ....	22
Figure 2. 7: Mössbauer Spectroscopy sample preparation process. ....	23
Figure 2. 8: a) Sample inside holder, b) gas flow cryostat and c) Mössbauer Spectroscopy measurement setup.....	24
Figure 2. 9: Images of Physical Properties Measurement System with 9 T superconducting magnet: a) PC with PPMS electronics cabinet and b) Dewar/probe (with mounted VSM module, Quantum Design).....	24
Figure 2. 10: VSM sample holder with inserted sample (foil). ....	25
Figure 2. 11: Illustration of four point method: black lines – wires and red numbers – pressing pin positions. ....	26

Figure 2. 12: Images of resistivity option sample: puck a), b) upper part (connection pin board from the top and bottom respectively), c) lower part: three channel sample puck, d) assembled and e) in the user bridge board. ....	26
Figure 2. 13: Image of DSC-60 (SHIMADZU) device (on the left) and characterization table (on the right). Taken from [161]. ....	27
Figure 2. 14: Example of DSC curve with following transitions marked: a) melting, b) crystallization and c) glass transition for exothermal and endothermal reactions. ....	28
Figure 2. 15: Example of shape memory alloy DSC curve with marked transformation temperatures: $A_S$ – austenite start, $A_F$ – austenite finish, $M_S$ – martensitic start and $M_F$ – martensitic finish. ....	28
Figure 2. 16: Bending test diagram. Taken from [162]. ....	29
Figure 3. 1: Samples preparation process. ....	31
Figure 3. 2: Dependence of shape recovery strain on C content of the alloys. (A) As-annealed state. (B) After one cycle of training, Prendota et al. [163] ....	32
Figure 3. 3: Mössbauer spectra for “0.1 wt.% C” powders after MA for 10 h, Prendota et al. [163]. ....	32
Figure 3. 4: Mössbauer spectra for “0.1 wt.% C” powders after MA for 30h, Prendota et al. [163]. ....	33
Figure 3. 5: X-Ray Diffraction patterns for “As annealed” (black line) and “0.1 wt.% C” (red line) after 30 h of mechanical alloying. ....	33
Figure 3. 6: Room temperature X-Ray Diffraction patterns for “As annealed” sample. Detected phase: $\epsilon$ -hcp (hexagonal close-packed). ....	34
Figure 3. 7: Room temperature X-Ray Diffraction patterns for “Heated 600 °C” sample. Detected phase: $\epsilon$ -hcp (hexagonal close-packed). ....	34

Figure 3. 8: X-Ray Diffraction patterns for “0.1 wt.% C” in 75 K (experimental data - black dots, differential pattern - red line and blue line – fitted pattern).....	35
Figure 3. 9: X-Ray Diffraction patterns for “0.1 wt.% C” in 295 K (experimental data - black dots, differential pattern - red line and blue line – fitted pattern). .....	36
Figure 3. 10: X-Ray Diffraction patterns for “0.1 wt.% C” in 423 K (experimental data - black dots, differential pattern - red line and blue line – fitted pattern). .....	36
Figure 3. 11: X-Ray Diffraction patterns for “0.1 wt.% C” in 75 (black line), 295 (red line) and 423 K (blue line). .....	37
Figure 3. 12: XANES (on the left side) and EXAFS (on the right side) for iron (upper images) and manganese (lower images) K edge measurements of “As annealed” and “Heated 600 °C” samples. ....	39
Figure 3. 13: Mössbauer spectra for all samples obtained at room temperature.....	40
Figure 3. 14: Mössbauer spectra for all samples obtained at low temperature. The right panel shows a zoom of the spectra at low velocity range. ....	40
Figure 3. 15: Mössbauer spectra for sample “As annealed” obtained in different temperatures. The right panel shows a zoom of the spectra at low velocity range.....	41
Figure 3. 16: Isomer shift for all samples at ambient (black squares) and liquid helium temperature (red dots). .....	42
Figure 3. 17: Isomer Shift for “As annealed” and “Heated 600 °C”.....	42
Figure 3. 18: Mössbauer spectra: a) room temperature and b) 80K for “As annealed” and “0.1 wt.% C” alloys. ....	43
Figure 3. 19: CEMS spectra for “As annealed” (black dots), “Heated 200 °C” (red dots), “Heated 400 °C” (blue dots) and “Heated 500 °C” (cyan dots) sample (dark yellow line –fit).....	44
Figure 3. 20: Hysteresis loops for the “As annealed” sample at all the temperatures..	45

Figure 3. 21: Virgin magnetization curves for the “As annealed” sample at all the temperatures. ....	46
Figure 3. 22: Hysteresis loops for “As annealed” sample at all the temperatures without paramagnetic contribution.....	46
Figure 3. 23: Hysteresis loops for “0.1 wt.% C” sample at all the temperatures. ....	47
Figure 3. 24: Hysteresis loops for “0.1 wt.% C” sample at all the temperatures - zoomed. ....	48
Figure 3. 25: Temperature dependence of slope values for paramagnetic contributions (linear part). Dashed lines are guides for eyes. ....	49
Figure 3. 26: Coercivity values for “As annealed” sample. ....	50
Figure 3. 27: Coercivity values for “Heated 200 °C” sample. ....	50
Figure 3. 28: Coercivity values for “Heated 500 °C” sample. ....	51
Figure 3. 29: Coercivity values for “Heated 600 °C” sample. ....	51
Figure 3. 30: Coercivity values for “0.1 wt.% C” sample.....	52
Figure 3. 31: Saturation Magnetization corresponding to the field of 80 kOe after subtraction of paramagnetic (linear) contribution from magnetization curves at various temperatures. ....	53
Figure 3. 32: ZFC and 100 Oe FC of “0.1 wt.% C”. ....	53
Figure 3. 33: Inverse magnetic susceptibility versus temperature of all samples in the magnetic field of 100 Oe.....	54
Figure 3. 34: Inverse magnetic susceptibility versus temperature of all samples in the magnetic field of 10 kOe.....	54
Figure 3. 35: Inverse magnetic susceptibility versus temperature of all samples in the magnetic field of 80 kOe (besides 0.1 wt.% C). ....	55

Figure 3. 36: Inverse mass magnetic susceptibility versus temperature of the “0.1 wt.% C” sample at 10, 50, 70 and 90 kOe.....	56
Figure 3. 37: Heat capacity temperature dependence with polynomial fit (blue line) and magnetic heat capacity (pink area).....	57
Figure 3. 38: Specific heat versus squared temperature dependence for “0.1 wt.% C” sample in the low temperature range.....	58
Figure 3. 39: Heat capacity temperature dependence measured in different magnetic fields for “0.1 wt.% C” sample. ....	58
Figure 3. 40: Magnetic entropy temperature dependence measured for “0.1 wt.% C” sample.....	59
Figure 3. 41: Temperature dependence of the resistivity for: “As annealed”, “Heated 600 °C” and “0.1 wt.% C” samples.....	60
Figure 3. 42: Magnetoresistances of “As annealed”, “Heated 600 °C” and “0.1 wt.% C” samples at different temperature.....	61
Figure 4. 1: Illustrative representation of the cold rolled diffusion couples: a) 50 μm titanium foil between two 100 μm nickel foils and b) 100 μm nickel foil between two 50 μm titanium foils. ....	63
Figure 4. 2: Cold rolling machine at the Faculty of Non-Ferrous Metals, AGH University of Science and Technology. ....	64
Figure 4. 3: A scheme of the process for heated up and rolled samples: 1. Protection of the sample, 2. heating up to ~830°C (2h), 3. hot sample transfer, 4. Cold rolling and 5. Sample ready for long annealing.....	65
Figure 4. 4: a) Furnace and b) example of the sample sealed in quartz tube in vacuum. ....	65

Figure 4. 5: Optical microscope images of 50Ti:100Ni:50Ti sample before annealing. .....	66
Figure 4. 6: SEM images of 50Ti:100Ni:50Ti before annealing.....	66
Figure 4. 7: 100Ni:50Ti:100Ni before annealing.....	67
Figure 4. 8: The image of foils cold rolled without prior heating treatment.....	67
Figure 4. 9: The image of foils after secondary cold rolling of cold rolled heated foils. .....	68
Figure 4. 10: SEM images with EDS maps qualitative graphs for 100 $\mu$ mNi:50 $\mu$ mTi:100 $\mu$ mNi sample a) as rolled and after annealing for 12h in vacuum in: b) 700 °C, c) 800 °C and d) 900 °C.....	70
Figure 4. 11: SEM images and EDS maps for 100 $\mu$ mNi:50 $\mu$ mTi:100 $\mu$ mNi sample after annealing for 12h in vacuum in: a) 700 °C, b) 800 °C and c) 900 °C (green color – nickel, blue color – titanium and red - oxygen). .....	71
Figure 4. 12: EDS quantitative maps for 100 $\mu$ mNi:50 $\mu$ mTi:100 $\mu$ mNi sample after annealing for 12h in vacuum in: a) 700 °C, b) 800 °C and c) 900 °C (green color – nickel and yellow color – titanium) – scale in atomic percentage.....	72
Figure 4. 13: SEM image with line measurement and composition dependence with marked points of 100 $\mu$ mNi:50 $\mu$ mTi:100 $\mu$ mNi sample after annealing for 12h in vacuum in: a) 700 °C, b) 800 °C and c) 900 °C (yellow – titanium, light green – nickel, dark green – oxygen, red – carbon and orange – aluminum). Distance is measured from Ti/Ti <sub>2</sub> Ni interface. .....	72
Figure 4. 14: SEM images with EDS maps qualitative graphs for 50 $\mu$ mTi:100 $\mu$ mNi:50 $\mu$ mTi sample a) as rolled and after annealing for 12h in vacuum in: b) 700 °C, c) 800 °C and d) 900 °C.....	74

Figure 4. 15: SEM images and EDS maps for 50 $\mu$ mTi:100 $\mu$ mNi:50 $\mu$ mTi sample after annealing for 12h in vacuum in: a) 700 °C, b) 800 °C and c) 900 °C (green color – nickel and blue color - titanium).....	75
Figure 4. 16: EDS quantitative maps for 50 $\mu$ mTi:100 $\mu$ mNi:50 $\mu$ mTi sample after annealing for 12h in vacuum in: a) 700 °C, b) 800 °C and c) 900 °C (green color – nickel and yellow color – titanium) – scale in atomic percentage.....	75
Figure 4. 17: SEM image with line measurement and composition dependence with marked points of 50 $\mu$ mTi:100 $\mu$ mNi:50 $\mu$ mTi sample after annealing for 12h in vacuum in: a) 700 °C, b) 800 °C and c) 900 °C (yellow – titanium, light green – nickel, dark green – oxygen, red – carbon and orange – aluminum). Distance is measured from the Ti/Ti <sub>2</sub> Ni interface.....	76
Figure 4. 18: Temperature dependence of medium Ni <sub>3</sub> Ti phase thickness.....	77
Figure 4. 19: Temperature dependence of medium Ti <sub>2</sub> Ni phase thickness.....	77
Figure 4. 20: Temperature dependence of medium gap width.....	78
Figure 4. 21: A schematic example of oxidation of 50 $\mu$ mTi:100 $\mu$ mNi:50 $\mu$ mTi sample after annealing in 700 °C for 12h in vacuum. ....	79
Figure 4. 22: SEM image with line measurement marked by red line and intensities lines represented by following colors: yellow – titanium, light green – nickel, dark green – oxygen, red – carbon and orange – aluminum. ....	80
Figure 5. 1: Pulse-current pressure sintering samples preparation process.....	82
Figure 5. 2: Cross-sectional SEM/EDS line measurements of diffusion couples annealed in 700 °C: a) as sintered, b) 24 h, c) 48 h and d) 72 h (yellow – titanium, light green – nickel, dark green – oxygen, orange – aluminum and red – carbon). ....	83

Figure 5. 3: Cross-sectional SEM/EDS line measurements of diffusion couples annealed in 800 °C: a) as sintered, b) 24 and c) 72 h (yellow – titanium, light green – nickel, dark green – oxygen, orange – aluminum and red – carbon).....	84
Figure 5. 4: Cross-sectional SEM/EDS map measurements of diffusion couples annealed in 700 °C: a) as sintered, b) 24 h, c) 48 h and d) 72 h (yellow – titanium and light green - nickel).....	85
Figure 5. 5: Cross-sectional SEM/EDS map measurements of diffusion couples annealed in 800 °C: a) as sintered, b) 24 h and c) 72 h (yellow – titanium and light green - nickel).....	86
Figure 5. 6: Cross-sectional SEM/EDS point measurements of droplet-like features and their elemental compositions.....	87
Figure 5. 7: Layer thicknesses of individual intermetallics thicknesses versus annealing time at: a) 700 and b) 800 °C.....	87
Figure 5. 8: A scheme of the pulse-current pressure sintering sample preparation process.....	88
Figure 5. 9: Illustrative representation of the sintered samples types: a) single element layer, b) simple one and c) sandwich-like.....	89
Figure 5. 10: X-Ray Diffraction patterns for Ni/Ti, Ni/Ti/Ni and Ti/Ni/Ti configuration. Right panel shows full range and the left panel is a zoom. ....	90
Figure 5. 11: SEM/EDS point measurements of Ni/Ti configuration (distance measured from upper surface).....	91
Figure 5. 12: SEM/EDS point measurements of Ni/Ti/Ni configuration (distance measured from upper surface).....	91
Figure 5. 13: SEM/EDS point measurements of Ti/Ni/Ti configuration (distance measured from upper surface).....	92

Figure 5. 14: SEM/EDS point measurements of Ti/Ni/Ti configuration in different area: a) whole cross-section and b) zoom on the partial area.....	93
Figure 5. 15 Differential Scanning Calorimetry measurements of the Ti/Ni/Ti (black), Ni/Ti/Ni (red) and Ni/Ti (green) configurations with marked transitions temperatures.....	94
Figure 5. 16: Shape Recovery Rate for Ni/Ti/Ni temperature dependence after bending strain of: 1 and 2 % . .....	95
Figure 5. 17: Both sides X-Ray Diffraction patterns for samples with different foils thickness coefficient. Right panel shows full range and the left panel is a zoom.....	97
Figure 5. 18: X-Ray Diffraction patterns at various temperatures: red - ambient temperature (27 °C), blue - 60 °C and green - 120 °C for sample with thickness coefficient of 1.7.....	98
Figure 5. 19: X-Ray Diffraction patterns at various temperatures: black - ambient temperature (300 K) and red - 75 K for sample with thickness coefficient of 1.5.....	98
Figure 5. 20: SEM/EDS point measurements of sample with FTC: 1 (distance measured from upper surface).....	99
Figure 5. 21: SEM/EDS point measurements of sample with FTC: 1.2 (distance measured from upper surface).....	99
Figure 5. 22: SEM/EDS point measurements of sample with FTC: 1.4 (distance measured from upper surface).....	99
Figure 5. 23: SEM/EDS point measurements of sample with FTC: 1.7 (distance measured from upper surface).....	100
Figure 5. 24: SEM/EDS point measurements of sample with FTC: 1.8 (distance measured from upper surface).....	100
Figure 5. 25: Shape recovery effect observed at heating in boiled water for the sample with thickness coefficient of 1.7. ....	101

Figure 5. 26: X-Ray Diffraction patterns from both sides of samples after 20,40 and 60 min of sintering time. Right panel shows full range and the left panel is a zoom. ....	102
Figure 5. 27: SEM/EDS point measurements of sample after 20 min of sintering (distance measured from upper surface). ....	103
Figure 5. 28: SEM/EDS point measurements of sample after 40 min of sintering (distance measured from upper surface). ....	103
Figure 5. 29: SEM/EDS point measurements of sample after 60 min of sintering (distance measured from upper surface). ....	103
Figure 5. 30: Results of Differential Scanning Calorimetry measurements for samples after 20 (black line), 40 (red line) and 60 (green line) minutes of sintering time with marked transformation temperatures.....	104
Figure 5. 31: Both sides X-Ray Diffraction patterns of samples with 8, 16 and 24 $\mu\text{m}$ thickness. Right panel shows full range and the left panel is a zoom. ....	105
Figure 5. 32: SEM/EDS point measurements of 8 $\mu\text{m}$ foil (distance measured from upper surface).....	106
Figure 5. 33: SEM/EDS point measurements of 16 $\mu\text{m}$ foil (distance measured from upper surface).....	106
Figure 5. 34: SEM/EDS point measurements of 24 $\mu\text{m}$ foil (distance measured from upper surface).....	106
Figure 5. 35: Differential Scanning Calorimetry measurements for samples with 8 (black line), 16 (red line) and 24 (green line) $\mu\text{m}$ of thickness with marked transformation temperatures. ....	108
Figure 5. 36: SEM/EDS point measurements of foils prepared by: a) DC and b) pulsed current at 700 $^{\circ}\text{C}$ (points are marked respectively).....	109

Figure 5. 37: Differential Scanning Calorimetry measurements of foils prepared by DC and pulsed current at 700 °C. ....	110
Figure 5. 38: SEM/EDS point measurements of S1 sample.....	112
Figure 5. 39: SEM/EDS point measurements of S2 sample.....	112
Figure 5. 40: BSE-image and EDS results for the cross-sections of sample S2 with marked measurements points and table with elemental composition on the right.....	112
Figure 5. 41: X-Ray Diffraction patterns of a) S1 and b) S2 sample. ....	113
Figure 5. 42: Differential Scanning Calorimetry measurement of S2 material.....	113
Figure 5. 43: Resistivity results for S1, S2, pure nickel and titanium foils.....	114
Figure 5. 44: S1 sample magnetoresistance dependences at different temperatures..	115
Figure 5. 45: S2 sample magnetoresistance dependences at different temperatures..	115
Figure 5. 46: Pure titanium magnetoresistance dependences at different temperatures. ....	116
Figure 5. 47: Pure nickel magnetoresistance dependences at different temperatures.	116
Figure 5. 48: Magnetoresistance of the S1, S2, pure nickel and titanium in the room temperature and 4 K. ....	117
Figure 5. 49: Thermal conductivity for all considered materials in this subchapter. .	118
Figure 5. 50: Hysteresis loops at all the temperatures for the S1 sample from 4 to 350 K.....	119
Figure 5. 51: Hysteresis loops at all the temperatures for the S2 sample from 4 to 350 K.....	119
Figure 5. 52: Differential susceptibility obtained from mean slope value of linear parts of magnetization vs field dependences for S1 and S2.....	120
Figure 5. 53: Shape Recovery Rate for S2 sample temperature dependence after bending strain of 2 and 3 %.....	120

